Relativistic dissipative causal magnetohydrodynamics from kinetic theory and the effect of electric fields on bulk observables in high-energy heavy-ion collisions

By

ANKIT KUMAR PANDA

PHYS11202004002

National Institute of Science Education and Research, Bhubaneswar

A thesis submitted to the

Board of Studies in Physical Sciences

(as applicable)

In partial fulfillment of requirements

for the Degree of

DOCTOR OF PHILOSOPHY
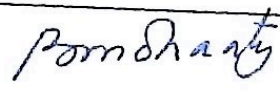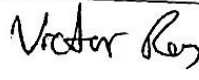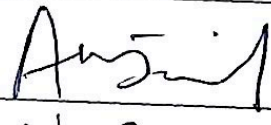
of

HOMI BHABHA NATIONAL INSTITUTE

25th October, 2024

Homi Bhaba National Institute

Recommendations of the Viva Voce Committee

As members of the Viva Voce Committee, we certify that we have read the dissertation prepared by **Ankit Kumar Panda** entitled **Relativistic dissipative causal magnetohydro-dynamics from kinetic theory and the effect of electric fields on bulk observables in high-energy heavy-ion collisions** and recommend that it may be accepted as fulfilling the thesis requirement for the award of Degree of Doctor of Philosophy.

Chairman - Prof. Bedangadas Mohanty   _Bedangadas Mohanty_   25/10/2024

Guide / Convener - Dr. Victor Roy   _Victor Roy_   25.10.24

Examiner - Prof. Rishi Sharma   _Rishi Sharma_   25/10/2024.

Member 1 - Dr. Amaresh Kumar Jaiswal   _Amaresh_   25/10/2024

Member 2 - Dr. Najmul Haque   _Haque_   25.10.2024

Member 3 - Dr. Santosh Kumar Das   _Santosh Kumar Das_   25/10/24

Final approval and acceptance of this thesis is contingent upon the candidate's submission of the final copies of the thesis to HBNI.

I/We hereby certify that I/we have read this thesis prepared under my/our direction and recommend that it may be accepted as fulfilling the thesis requirement.

Date : 25.10.24
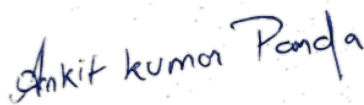
Place : NISER, Bhubaneswor

Signature

Co-guide (if any)

Victor Roy.

Signature

Guide

i

STATEMENT BY AUTHOR

This dissertation has been submitted in partial fulfillment of requirements for an advanced degree at Homi Bhabha National Institute (HBNI) and is deposited in the Library to be made available to borrowers under rules of the HBNI.
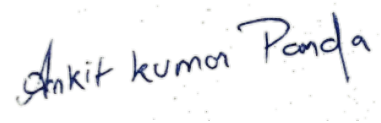
Brief quotations from this dissertation are allowable without special permission, provided that accurate acknowledgement of source is made. Requests for permission for extended quotation from or reproduction of this manuscript in whole or in part may be granted by the Competent Authority of HBNI when in his or her judgment the proposed use of the material is in the interests of scholarship. In all other instances, however, permission must be obtained from the author.

Ankit Kumar Panda

DECLARATION

I hereby declare that I am the sole author of this thesis in partial fulfillment of the requirements for a Doctorate degree from National Institute of Science Education and Research (NISER). I authorize NISER to lend this thesis to other institutions or individuals for the purpose of scholarly research.

Ankit Kumar Panda

List of Publications

Publications arising from the current thesis :

1. Relativistic non-resistive viscous magnetohydrodynamics from the kinetic theory: a relaxation time approach. **Ankit Kumar Panda**, Ashutosh Dash, Rajesh Biswas, Victor Roy. (**JHEP 03 (2021) 216**).

2. Relativistic resistive dissipative magnetohydrodynamics from the relaxation time approximation. **Ankit Kumar Panda**, Ashutosh Dash, Rajesh Biswas, Victor Roy. (**Phys.Rev.D 104 (2021) 5, 054004**).

3. Investigating the role of electric fields on flow harmonics in heavy-ion Collisions. **Ankit Kumar Panda**, Reghukrishnan Gangadharan, Victor Roy. (**J.Phys.G 50 (2023) 7, 075102**).

4. Charged participants and their electromagnetic fields in an expanding fluid, Ashutosh Dash, **Ankit Kumar Panda**. (**Phys.Lett.B 848 (2024) 138342**).

5. Electromagnetic fields in low-energy heavy-ion collisions with baryon stopping, **Ankit Kumar Panda**, Partha Bagchi, Hiranmaya Mishra, Victor Roy. (**Phys. Rev. C 110 (2024) 024902**).

Other publications not included in the thesis :

1. Study of early time attractor with longitudinal forces with Bjorken symmetry, Reghukrishnan Gangadharan, **Ankit Kumar Panda**, Victor Roy. (**Phys. Rev. D 109, 074020 (2024)**).

Arxived paper :

1. Wave Phenomena In General Relativistic Magnetohydrodynamics, **Ankit Kumar Panda**, Victor Roy. (**2205.03107**).

2. Enhanced ψ' yield and $\psi'/(J/\psi)$ yield ratio as a possible signature of QGP formation in high multiplicity $p + p$ collisions, Partha Bagchi, Arpan Das, Ananta P. Mishra, **Ankit Kumar Panda**. (**2407.07073**).

Conference proceedings :

1. Dynamics of Hot QCD Matter – Current Status and Developments, Santosh K. Das(Indian Inst. Tech. Goa), Prabhakar Palni(Unlisted, IN), Jhuma Sannigrahi(Indian Inst. Tech. Goa), Jan-e Alam(Calcutta, VECC), Cho Win Aung(Indian Inst. Tech., Bhilai) et al. (Aug 29, 2022) Published in: Int.J.Mod.Phys.E 31 (2022) 12, **Int.J.Mod.Phys.E** • e-Print: 2208.13440.

2. Relativistic resistive dissipative magnetohydrodynamics from the relaxation time approximation, Ankit Kumar Panda(NISER, Jatni), Ashutosh Dash(NISER, Jatni), Rajesh Biswas(NISER, Jatni), Victor Roy(NISER, Jatni) (2022) Contribution to: 65th DAE BRNS Symposium on nuclear physics, **700-701**.

3. Wave Phenomena in General Relativistic Magnetohydrodynamics, Ankit Kumar Panda (NISER, Jatni), Victor Roy (NISER, Jatni) (2024) Contribution to: Springer Proc. Phys., **625-626**.

Ankit Kumar Panda

DEDICATED TO

All the PhD students who want to pursue their career as a researcher and to all the depressing moments one has to go through during these times.

ACKNOWLEDGEMENTS

ABSTRACT

In high-energy heavy-ion collisions, two heavy nuclei, moving at relativistic velocities, undergo Lorentz contraction and collide onto one another. Within these collisions, certain nucleons, known as participants, contribute to the collision process, depositing a significant amount of energy within a small volume. This leads to the formation of hot, dense matter composed of a deconfined state of quarks and gluons, termed Quark Gluon Plasma (QGP). Initially, this matter exists in a highly non-equilibrium state, with its constituents colliding rapidly until reaching a near-equilibrium stage. This is then accurately described by relativistic viscous hydrodynamics formalism. The QGP subsequently expands and cools, transitioning back to colorless hadrons in a process known as hadronization. Even after hadronization, the hadrons continue to collide, both elastically and non-elastically, until reaching a point where all collisions cease, and the particles freely stream into the detector for detection. In addition to the QGP formed by the participants, there is also an intense transient magnetic field generated, primarily by the relativistically moving spectators who do not participate in the collision process. Theoretical calculations suggest that the initial magnitude of the magnetic field resulting from a non-central Au+Au collision at $\sqrt{s_{NN}} = 200$ GeV ranges from 10^{14} to 10^{15} Tesla. This intense magnetic field offers a unique opportunity to explore various novel phenomena such as Chiral Magnetic Effect (CME), Chiral Separation Effect (CSE), and Chiral Magnetic Wave (CMW). Since the QGP consists of freely moving charges, it exhibits finite conductance and is highly responsive to electromagnetic fields. Consequently, the QGP induces additional responses to the electromagnetic fields, thereby altering the fields themselves. This underscores the importance of studying the interplay between electromagnetic fields and fluid dynamics. The most effective approach to this study is through relativistic magnetohydrodynamics formalism.

During the cooling and expansion process, constituent degrees of freedom, namely quarks and gluons, collide with each other and transfer momentum, energy and mass. This is why the study of transport properties is crucial. In the first part of the thesis, we will primarily examine the impact of external electromagnetic fields, originating from spectators, on the transport coefficients and evolution equations of various dissipative stresses (shear, bulk, and diffusion). This is carried out by solving relativistic magnetohydrody-

namic (RMHD) equations and determining the transport coefficients through underlying microscopic theory, specifically from relativistic kinetic theory. We find here that second-order evolution equations pick up additional contributions due to external electromagnetic fields, and the Navier-Stokes relations change, making the primary transport coefficients (shear and diffusion) anisotropic. Additionally, we delve into how these additional transport coefficients arising from the external electromagnetic fields are influenced by variations in temperature, mass, and magnetic field. Understanding these dissipative stresses, such as shear, bulk, and diffusion, is critical in the context of high-energy collisions as they govern the non-equilibrium behavior of the QGP formed in these collisions.

Next, we study the generation of the electromagnetic fields in heavy-ion collisions. There are essentially two sources of electromagnetic fields: the spectators and the participants. Here, we will focus on contributions from participants only. We study here the full 3+1D spatio-temporal evolution of electromagnetic fields, taking into account the participants flowing with the fluid. We discuss the results for two specific cases: point charges and a more realistic scenario with transverse charge distribution. We found that unlike the electromagnetic field by the spectators, fields by participants increase and then decrease with time post collisions. Also, a naive comparison about the strength of the field from both sources suggests that the fields at a later stage are mainly due to the participant charges.

As we transition to low-energy heavy-ion collisions, experimental observations reveal the emergence of nuclear stopping, where an increasing number of nucleons congregate the mid-rapidity region. As there is a stopping we can affirm that there should be deceleration of the charges occuring. These deceleration should be taken into account while calculating the electromagnetic fields at the low centre-of-mass energies. This motivates us to investigate the effect of baryon stopping on the electromagnetic fields at low center-of-mass energy collisions. We do this by introducing a energy-dependent stopping power and hence parameterizing the participants velocity profile in a Monte-Carlo Glauber model. Here we see clear effects of stopping on the various components of EM fields at later times after the collisions.

Finally, in the last part of this thesis, we conduct a detailed investigation into the impact of electric fields on bulk observables such as spectra and flow harmonics. Here we consider four different configurations of electric fields on the transverse plane of the freeze-out

surface (kinetic freeze-out) and analyze the bulk observables (spectra and flows). This analysis is performed using a blast wave model where we parameterize the flow velocity and temperature on the freeze-out hypersurface and incorporate Cooper-Frey prescriptions for the particlization process. One of the most important result is the effect of electric fields on the behavior of Δv_2 of the identified particles (proton and pion for our case) with respect to transverse momentum (p_T) of the particles. It initially increases and then nearly saturates at some higher p_T at around 3 GeV.

Contents

List of Figures

1

4

List of Tables

Chapter 1

Introduction

Approximately fourteen billion years ago, the universe came into existence, and since then, it has cooled down to a level that allows for our existence [1]. Scientists have conducted extensive research to explore and understand the universe by studying its fundamental building blocks, which involves investigating the elementary particles and their interactions. By the early nineteen hundred's, it was discovered that atoms consist of a positively charged nucleus around which negatively charged electrons orbit. The nucleus is further composed of positively charged protons and charge-neutral neutrons [2]. However, one would expect that the protons inside the nucleus would undergo strong electric repulsion [3], which would lead to the instability of the nucleus. This puzzle led to the development of theories proposing an additional force known as the strong nuclear force [4, 5]. In addition to the electromagnetic and strong nuclear forces, there are two other fundamental forces: the gravitational and the weak force. The gravitational force is a long-range force that manifests its effect at a macroscopic scale, such as the motion of planets. The weak force [6, 7], on the other hand, is responsible for the radioactive decay of the nucleus, such as beta decay. For a long time, protons, neutrons, and electrons were considered the fundamental building blocks of matter. Protons and neutrons, which are spin-half particles, are known as baryons, while there is another category of integral spin particles known as mesons. Collectively, these baryons and mesons are known as hadrons. In the late twentieth century, Murray Gell-Mann and George Zweig independently proposed that hadrons are made up of quarks, known as the quark model of hadrons [4, 8]. Later, it was also theorized that quarks themselves are bound together by gluons, which act as a mediating particle for the

strong nuclear force [9]. Along with the electrical charges corresponding to electromagnetic interactions, analogous color charges corresponding to the strong nuclear force were introduced. Quarks possess color charges but come together to form color-neutral hadrons. Due to confinement within the hadrons, experiments cannot observe free quarks. However, quarks can briefly become liberated (typically of the order of 10^{-23} seconds) within the nuclear volume through high-energy collisions between two nuclei or by compressing nuclear matter to create regions of high baryon densities. This phenomenon, termed asymptotic freedom of quarks, was proposed by Gross, Wilczek, and Politzer [10, 11, 12].

These theoretical models, in conjunction with collider experiments [13, 14], facilitated the discovery of fundamental particles such as quarks and gluons. This breakthrough paved the way for the development of the Standard Model of particle physics, which encompasses three generations of quarks and leptons, in addition to the four fundamental gauge bosons (gluons, photons, $W^{\pm}$ and Z bosons), and the Higgs boson [15] which gives masses to all the fundamental particles in the standard model. The challenge of understanding the nature and properties of quarks and gluons spurred the exploration of high-energy collider experiments. As discussed above, these experiments create brief periods of deconfined regions, leading to the formation of a novel state of matter known as quark-gluon plasma (QGP) [16, 17]. These experiments involve the collision of two heavy nuclei, traveling at nearly the speed of light, which yields extremely high energy densities, replicating conditions akin to the early universe and facilitating the formation of QGP [18, 19]. Along with quarks and gluons, one fascinating aspect of these collisions is the generation of the strongest magnetic fields known in the universe, resulting from the motion of charged protons in the nucleus [20], which are of the order of 10^{18} to 10^{19} G [21] for a typical non-central Au + Au or Pb + Pb collision at RHIC ($\sqrt{s_{NN}} = 200$ GeV) and LHC ($\sqrt{s_{NN}} = 2.76$ TeV) energies, respectively.

At very high energy densities, such as that achieved in heavy-ion collisions, chiral sym-

metry is approximately restored [22, 23], meaning there is almost no difference in the number of left-handed and right-handed quarks. However, the presence of topological fluctuations leads to chiral imbalance [24, 25]. This imbalance, along with the intense magnetic fields, may lead to the separation of positively and negatively charged quarks, resulting in a charge current along the direction of the magnetic fields. This phenomenon is known as the chiral magnetic effect [26, 27], which is expected to exist in such systems. Other novel and fascinating effects like chiral separation effect [28], chiral Hall effect [29], chiral vortical effect [30], etc., are also expected to be experienced in heavy-ion collisions.

Previous studies [31, 32, 33] have demonstrated that quark-gluon plasma (QGP) achieves thermal equilibrium and exhibits collective motion. Such phenomena are well-captured by relativistic viscous hydrodynamics formulations (discussed further in Sections 1.0.3 and 2.1). Consequently, the coexistence of intense magnetic fields and the QGP medium in high-energy collision experiments allows us to comprehensively describe the evolution process using relativistic magnetohydrodynamics formulations. This constitutes the central focus of the present thesis.

Moving forward, this chapter primarily serves as a formal introduction to the system and processes involved in heavy-ion collisions. This is organized as follows: In Section.(1.0.1), we explore the nature and characteristics of the QGP. Following that, Section.(1.0.2) focuses on the intricacies of heavy-ion collisions, examining the collision dynamics. Subsequently, Section.(1.0.3) will provide insights into the various stages involved in the heavy-ion collision process, elucidating the evolution from initial to final states. Given our primary emphasis on studying the novel state of matter, Quark-Gluon Plasma, in heavy-ion collision experiments, we will further discuss various signatures hinting at its existence in such collisions in Section.(1.0.4). Finally, in Section.(1.0.5), we will discuss the generation of the electromagnetic fields and its characteristics in heavy-ion collisions, as well as a few of the experimental attempts to measure them.

1.0.1 Quark Gluon Plasma

The conceptualization of quark-gluon plasma (QGP) arises from a profound understanding that under extreme thermal and density conditions, strongly interacting hadrons described by Quantum Chromodynamics (QCD), undergoes a phase transition. This pivotal insight traces its origins back to the 1970s when physicists envisioned that interactions among quarks and gluons would significantly weaken under such extremes, indicated by the weakening of the strong coupling constant (α_s) with increasing momentum transfer (Q) [34, 35]. α_s is related to the momentum transfer (Q) through the following relation:

$$\alpha_s(Q^2) \quad = \quad \frac{12\pi}{(11N_c - 2N_f)\ln(\frac{Q^2}{\Lambda_{\text{QCD}}^2})},\tag{1.1}$$

where N_c is the number of color charges and N_f denoting the number of flavors. Here Λ_{QCD} acts as a scale parameter for QCD calculation [36].

Fig.(1.1) presents a comparison of theoretical and experimental findings for α_s versus Q, showing consistency within the error bars. This observation suggests that in the limit $Q^2 \to \Lambda_{\text{QCD}}^2$, the value of α_s is large and increases monotonically, whereas in the other limit that is at $Q^2 \to \infty$, α_s becomes smaller and smaller which is known as the asymptotic freedom of quarks and gluons. QCD mainly has two distinct regimes of application based on the strength of the strong coupling constant α_s, that is the perturbative and non-perturbative. Firstly, in the perturbative realm, where α_s is small, QCD calculations excellently align with experimental determinations, particularly evident in high-momentum transfer parton collisions [10]. Conversely, as α_s becomes large, the perturbative framework collapses, necessitating alternative approaches. Within the non-perturbative regime, numerical simulations on a space-time lattice serve as a primary method for first-principle calculations. This non-perturbative domain further boils down into two conditions. At zero temperature, lattice QCD (lQCD) computations effectively predict hadron masses and thus breaks the chiral symmetry. Conversely, in the high-temperature limit, perturbative QCD foresees the

9
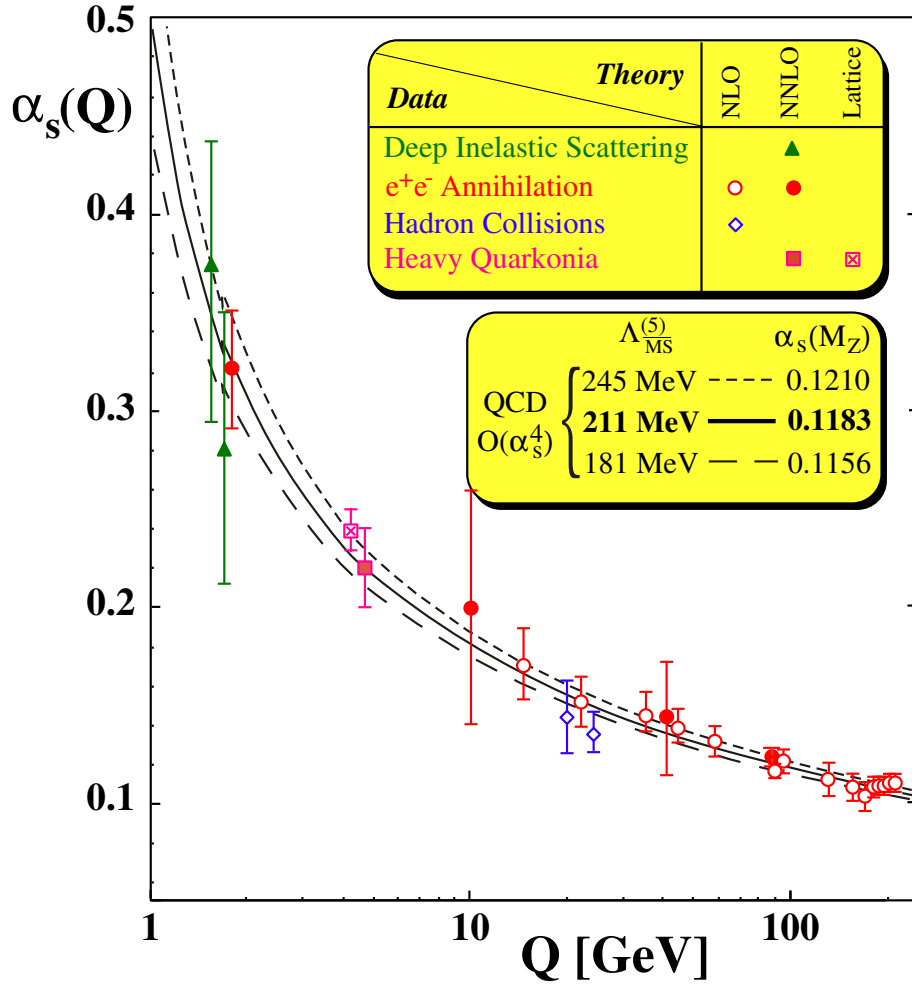
Figure 1.1: Variation of α_s with Q from [34]. Measurements of $\alpha_s(Q^2)$ with the results obtained through fits of $\alpha_s(M_Z)$ to data within specific ranges of Q.

restoration of chiral symmetry. The lQCD analyses incorporating realistic quark masses suggested a quark-hadron transition occurring around a crossover temperature of around 150 MeV [37] for vanishing chemical potential. Lattice calculations further predict the behaviour of scaled Energy density ($\frac{\epsilon}{T^4}$), Pressure ($\frac{P}{T^4}$) and entropy density ($\frac{s}{T^4}$). Fig.(1.2) demonstrates the variation of all scaled quantities mentioned above as a function of temperature (T). Here we can see a sharp increase in these quantities at around a crossover temperature (T_c) of 150 MeV (yellow band shown in the figure). Calculating the effective degrees of freedom in a pion gas reveals an approximate value of 3. Conversely, for

a composite system involving quarks with 3 distinct flavors, alongside their corresponding anti-particles and gluons, the effective degrees of freedom can be expressed as:

$$g_{\text{eff}} = (g_{\text{gluon}} + \frac{7}{8}g_{\text{quark}}) = (8 \times 2 + \frac{7}{8}N_c N_f N_s N_a) = 47.5.$$

Here, N_c signifies the number of colors ($N_c = 3$), N_f denotes the number of flavors ($N_f = 3$), N_s denotes the spin degrees of freedom ($N_s = 2$), and $N_a = 2$ stands for the degrees of freedom attributed to both particles and anti-particles. We find that degrees of freedom increases in QGP medium formation. This can be clearly seen from the sudden rise in the scaled quantities around T_c suggesting a transition from a state where degrees of freedom are hadrons at lower temperatures (T < T_c) to a state where quarks and gluons become the relevent degrees of freedom at higher temperatures (T > T_c). We also note that these quantities do not achieve the Stefan-Boltzmann limit (that is the non-interacting limit shown at the right top of the plot in dashed line) even for a system of massless quarks and gluons at high temperatures which indicates towards its strongly interacting nature.
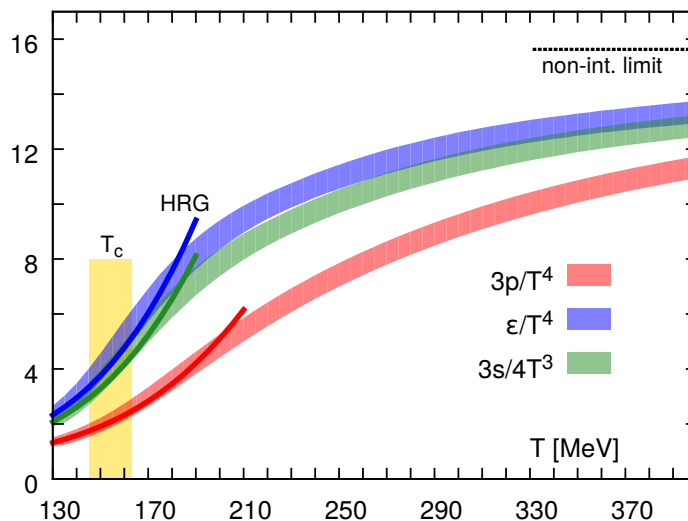
Figure 1.2: Variation of $\frac{\epsilon}{T^4}$, $\frac{3p}{T^4}$, $\frac{3s}{T^4}$ vs T from lattice QCD results [37].

QGP thus embodies a captivating state of matter that exhibits attributes reminiscent of a strongly interacting medium [17]. Next, we move onto the heavy-ion collision experiments,

which produces such a medium.

1.0.2 Heavy-ion collisions and other collision experiments

From cosmological side the understanding of the early universe is mainly based on analyzing remnants of the Big Bang through cosmic microwave background radiation (CMBR) [38] studies or observing natural phenomena like neutron star mergers [39], which often present complex observational and interpretative challenges, along with statistical limitations. As an alternative approach, scientists recreate early universe conditions in laboratory settings, often referred to as a "little bang". This provides an opportunity to statistically enrich our findings. Colliding heavy-ions at high-energies, as performed at research facilities such as Relativistic Heavy-Ion Collider (RHIC) and Large Hadron Collider (LHC), generates energy densities comparable to those encountered microseconds after the Big Bang. This enables researchers to explore the properties and behavior of the QGP, providing valuable insights into the conditions of the early universe.

The initial experimental confirmation of QGP came to light at the Relativistic Heavy-Ion Collider (RHIC) in the early 2000s, situated at the Brookhaven National Laboratory. Here, collisions between heavy-ions, specifically gold nuclei (Au), were conducted at ultra-relativistic speeds (peak energies of $\sqrt{s_{NN}} = 200$ GeV). Subsequent exploration took place at the Large Hadron Collider (LHC) located at CERN, where collisions involving heavy-ions, particularly lead nuclei (Pb), were performed at even higher energies (peak energies of $\sqrt{s_{NN}} = 13$ TeV). Both LHC and RHIC played crucial roles in meticulously scrutinizing the characteristics of the QGP medium. Through precise measurement and analysis of various observables such as jet quenching, elliptic flow, and strangeness enhancement (discussed later in Section.(1.0.4)), these experiments not only confirmed the existence of QGP but also provided profound insights into its properties [40].

While heavy-ion collisions are centered on investigating the properties of the QGP, al-
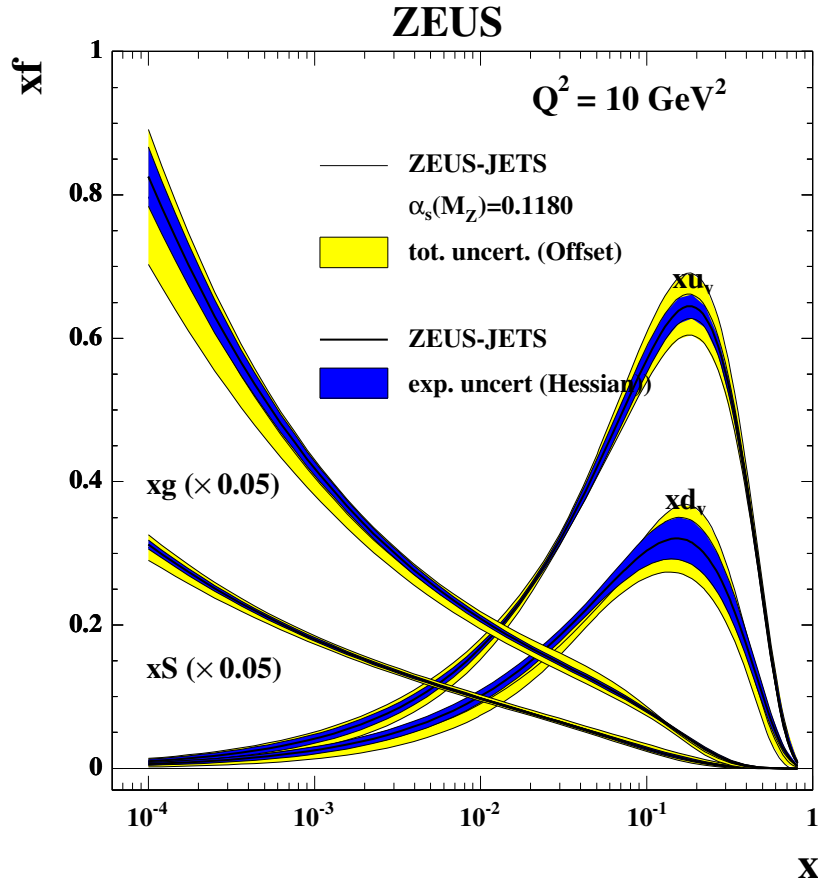
Figure 1.3: PDFs at $Q^2 = 10 GeV^2$, obtained from the ZEUS analysis of HERA data performed by the Offset and the Hessian methods [41].

ternative experiments such as ZEUS at HERA were designed to assess the nuanced characteristics of nucleons (protons and neutrons). This was achieved through the collision of leptons with protons using deep inelastic scattering techniques. One crucial aspect of this study is the investigation of parton distribution functions (PDFs), which provide insights into the distribution and arrangement of partons (quarks and gluons) within a nucleon. Fig.(1.3) illustrates the PDFs for up (u), down (d), and strange (s) quarks, as well as gluons, obtained from the HERA experiment at a specific scale of momentum transfer ($Q^2 = 10 GeV^2$). Here x is the Bjorken x, which simply denotes the fraction of momentum carried by a parton (quark or gluon) inside a proton. So at large x values (close to 1), quarks dominate the

nucleon's composition, while at small x values (close to 10^{-4}), there is a rise in gluon and strangeness content, indicating their increased contribution to the nucleon's structure at very high energies. This gives us an idea that at very high energies, the probability of finding gluons and sea quarks carrying a significant fraction of the nucleon's momentum becomes very high. Thus, we can affirm that gluons play a vital role in the overall structure and dynamics of the nucleon in this regime. Furthermore, this indefinite growth of gluon PDFs in the low x regime looks counterintuitive, as the volume of a nucleon is finite, which in turn should imply that the gluons should also exhibit saturation, famously called the "Gluon Saturation" problem, one of the main aims of future EIC experiments [42]. Moreover, based on the above idea initial model (CGC or color glass condenstate) has been developed and implemented in heavy-ion collision simulations [43, 44]. Therefore, by studying the PDFs at different momentum fractions in experiments like ZEUS at HERA or upcoming EIC experiments [42] might provide us with valuable insights into the distribution and behavior of partons within nucleons, complementing the research conducted in heavy-ion collision experiments.

1.0.3 Stages of heavy-ion collision

During the collision, certain nucleons from the colliding nuclei actively participate in the interaction, while others remain passive. The nucleons that are engaged in the interactions are termed as "participants", whereas the inactive ones are called as "spectators". The participants deposits an enormous amount of energy into a very confined space, leading to the formation of QGP. After this, QGP will undergo an evolution which can be broadly categorized into three stages: the pre-hydrodynamic stage, the hydrodynamic stage, and the freezout stage, each playing a crucial role in its development. Fig.(1.4) shows a schematic view of different stages of heavy-ion collisions which we will discuss below in some details.
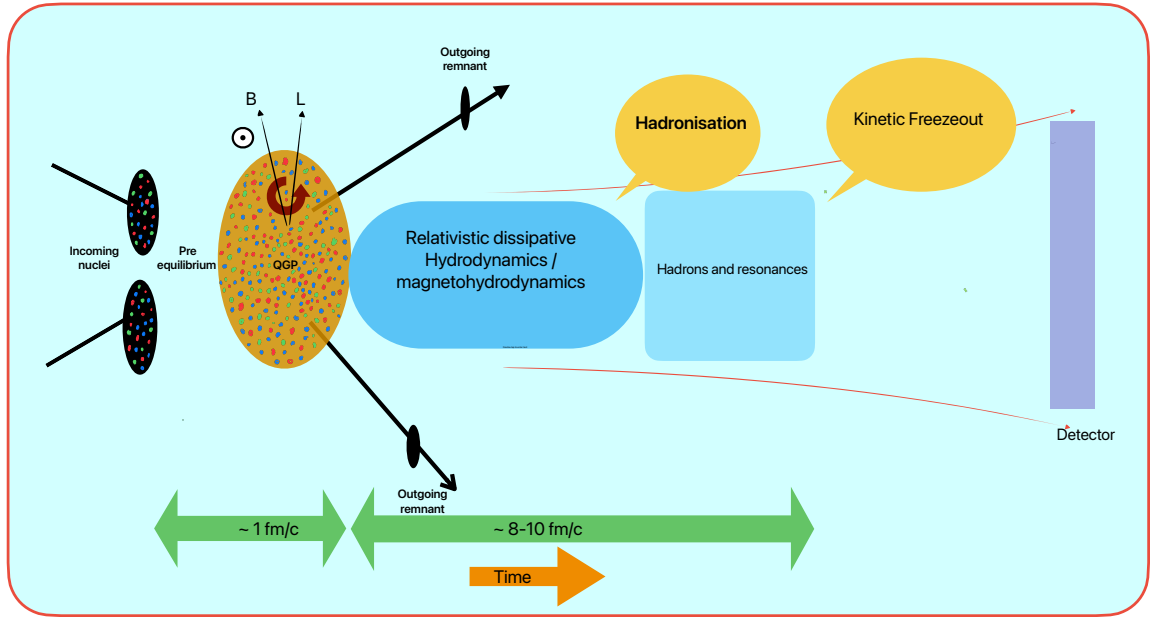
Figure 1.4: Stages of heavy-ion collisions.

Pre-hydrodynamic stage :

As shown in Fig.(1.4), the pre-hydrodynamic stage of heavy-ion collisions refers to the period immediately after the collision (at proper time $\tau > 0$) until local thermal equilibrium is reached, during which the created medium is far away from thermal equilibrium. During this stage, the medium can be effectively described by a free streaming mechanism. The high kinetic energy of the incoming nucleons leads to the production of a substantial number of heavy quark pairs, such as $c\bar{c}$, $s\bar{s}$, and $b\bar{b}$, as well as highly energetic photons. These particles are generated mainly through initial hard scatterings. During the pre-hydrodynamic stage, these highly energetic, but weakly coupled, partons start interacting among themselves. These interactions gradually lead to the equilibration of the system, where the partons reach a state of thermal equilibrium. This equilibration eventually gives rise to the formation of the strongly coupled QGP (sQGP) phase, characterized by the collective behavior of quarks and gluons. The duration of the pre-hydrodynamic stage, denoted by τ, is less than 1 fm (at RHIC or LHC energies). Although there are ongoing discussions and in-

vestigations concerning the existence of attractor solutions that might provide some answer to this very early isotropisation process [45, 46, 47, 48, 49, 50, 51, 52, 53, 54, 55, 56, 57]. In hydrodynamic simulations of heavy-ion collisions at the energies of LHC and RHIC, the pre-hydrodynamic stage is typically modeled to have a duration of around 0.2-0.6 fm [58]. The specific duration is chosen to reproduce the mean transverse momentum ($\langle p_T \rangle$) distribution of identified particles measured in experiments. This choice ensures that the hydrodynamic evolution accurately describes the experimental data and provides valuable information about the properties and dynamics of the created medium. The transition from the pre-hydrodynamic stage to the hydrodynamic stage marks the onset of the QGP phase. Additionally a large transient electromagnetic (EM) field is generated during the collision, primarily due to the spectator nucleons [59, 60, 61, 62, 63] which is of the order of $10^{18} - 10^{19}$G (the production of which is discussed later in Section.(1.0.5)). Also along with that a large initial angular momentum is also produced of the order of $10^3 - 10^5$ $\hbar$ (see Fig.(1.4)) [64, 65, 66]. We now move to the next stage of the collision that is the hydrodynamic stage.

Hydrodynamic stage :

There is ample evidence, such as the mass ordering of transverse momentum spectra for identified particles (such as pions, kaons, and protons), as well as flow patterns like elliptic flow (discussed later in this chapter), suggesting that the Quark-Gluon Plasma (QGP) formed in heavy-ion collisions undergoes collective motion. These findings have been validated by comparing results from relativistic hydrodynamics simulations with experimental data [67, 68, 69, 70]. However, relatively little attention has been paid, especially in the heavy-ion community, to the inclusion of electromagnetic fields in these simulations. Such inclusion should be a natural extension and should lead to a consistent formulation of relativistic magnetohydrodynamics [21], providing insight into the evolution of the QGP,

as depicted in Fig.(1.4). In this stage, the QGP experiences expansion and cooling. The expansion and cooling effects can be intuitively understood through the first law of thermodynamics, expressed as:

$$dQ = dU + P \, dV \tag{1.2}$$

where dQ is the heat supplied to the system, dU is the change in the internal energy of the system, P is the pressure and dV is the change in the volume of the system. If dQ = 0 (i.e., no external heat is supplied), then the work done by the system, P dV , will only change the internal energy of the system. That is, dU = −P dV. So if the volume increases (dV > 0), it will reduce the internal energy of the system. This shows that expansion will reduce the temperature of the system. This expansion and cooling causes the local energy density to decrease which after certain time drops below the cross-over (transition) energy density. This transition, known as hadronization(1.4), which marks the beginning of a stage where degrees of freedom from quarks and gluons get converted into hadrons, with pions, kaons, and protons being the dominant hadrons produced. Even after hadronization, the expansion and cooling of the system continues, and their behavior can still be effectively described using hydrodynamics formalism. As the medium further cools down, particle production through inelastic scattering eventually ceases at a specific temperature referred to as the chemical freeze-out temperature. However, elastic interactions between the particles persist, contributing to the overall dynamics of the system. It is important to note that the fluid description of the medium is valid in regions where the mean free path of particles, denoted as λ, is much smaller than the characteristic size of the system, denoted as L, i.e., $\frac{\lambda}{L} << 1$ [68, 71, 72]. When $\lambda \approx L$, the fluid description becomes no longer applicable. The transition from a QGP to hadrons represents a gradual evolution from a fluid to a particle-like picture, wherein interactions are primarily dictated by hadron-hadron interactions. In realistic scenarios, replicated through simulations, individualistic interactions among hadrons are captured using

various transport models [73, 74, 75, 76, 77, 78, 79, 80, 81]. These models incorporate the interactions mainly through different particle interaction cross-sections. It is however crucial to note that the precise timing of this transition depends on the specific collision systems, impact parameters, and center-of-mass energies ($\sqrt{s_{NN}}$) of the collisions. Furthermore, these models naturally include a freeze-out stage, which we discuss below.

Freezeout stage :

After the hydrodynamic stage, the system progresses into the freezeout stage, where the mean-free path between individual particles becomes appreciable compared to the system size. This is usually the stage between chemical and kinetic freezeout. The entire heavy-ion collision process in the most central case typically spans until 10-15 femtoseconds [82] (depends one the collision energies and system sizes), out of which this last stage spans for about 5-6 femtoseconds. By examining short-lived resonance particles decaying through strong interactions, we can investigate the properties of the hadronic phase. Short-lived resonances with a lifetime comparable to that of the hadronic phase, lead to the involvement of their decay products in regeneration and rescattering processes [83, 84, 85]. These interactions significantly contributed to the final particle spectra, correlations, and other experimental observables. The entire process comes to a halt when the mean free path between particles becomes greater than the system size. At this point, kinetic freezeout occurs, and the particles free-stream to the detectors for detection.

1.0.4 Probes to detect QGP in heavy-ion collisions

The typical lifetime of QGP is of the order of 10^{-23} seconds [86], so it is practically impossible to get direct access to the medium formed in order to understand its dynamics and properties. Hence, we need some indirect probes or signatures to conclude whether a QGP medium has been formed. There are many signatures, and here we discuss some of them.

- **Elliptic flow :** In a non-central heavy-ion collision, the nuclear overlap region typically assumes an almond-shaped geometry, exhibiting spatial anisotropy. The evolution of the medium is predominantly governed by fluid dynamics, driven by pressure gradients.
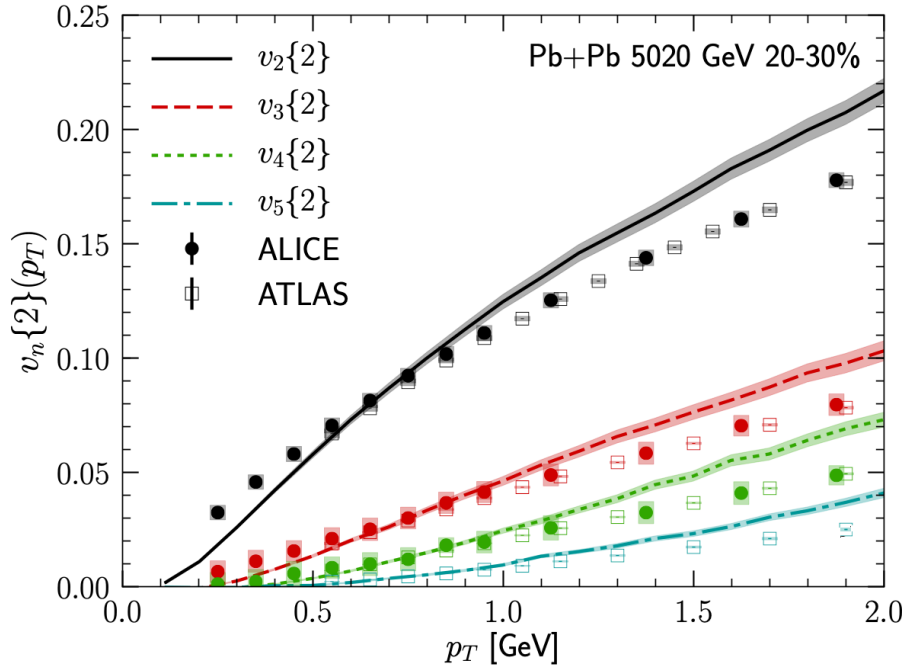
Figure 1.5: Various flow harmonics calculated using two particle correlation vs p_T for Pb-Pb 5.02 TeV at 20-30 % centrality [87]

These pressure gradients act to transform the initial spatial anisotropy into momentum anisotropy. Considering nuclei moving along the z-direction (beam direction) and the impact parameter (b, defined as the distance between the centers of the two nuclei) assumed along the x-axis, the azimuthal distribution of the produced particle multiplicity can be expressed in terms of a Fourier expansion as follows:

$$E\frac{d^3N}{dp^3} = \frac{d^2N}{2\pi p_T dp_T dy}(1 + \sum_{n=1}^{\infty} v_n \cos n(\varphi - \Psi_n)). \tag{1.3}$$

Here $E\frac{d^3N}{dp^3}$ on the LHS of the equation Eq.(1.3) is known as the invariant yield and this has been written in terms of different flow coefficients (v_n's), where the v_n can

be defined as :

$$v_n(p_T) \quad = \quad \frac{\int_{-\pi}^{\pi} d\varphi \cos n \left(\varphi - \Psi_n\right) \frac{d^3 N}{d^2 p_T dy}}{\int_{-\pi}^{\pi} d\varphi \frac{d^3 N}{d^2 p_T dy}}, \tag{1.4}$$

where N, p_T, and y are Multiplicity, transverse momentum, and rapidity of the produced particle (momentum rapidity), respectively. Here, the elliptic flow is defined as $v_2 = \langle \cos 2(\varphi - \Psi_2) \rangle$, where φ represents the azimuthal angle of the particles produced in the lab frame, and Ψ_2 is the second-order reaction plane angle. Here the $\langle \cdot \rangle$ represents the average over events and also over all particles in these events. While other geometric fluctuations may also exist, giving rise to higher-order flow harmonics such as v_3, v_4, v_5, etc. The positivity of the elliptic flow occurs when particles are predominantly produced in the in-plane (the plane defined by the impact parameter (b) and the beam axis), i.e., in the $x - z$ plane, rather than in the out-of-plane ($y - z$ plane).

Some of the early experimental results showcasing the results of flow harmonics can be found in [88, 18, 89, 90]. Figure.(1.5) shows the various flow harmonics calculated using two particle correlation for Pb-Pb collisions at $\sqrt{s_{\mathrm{NN}}} = 5.02$ TeV with 20-30% centrality. The symbols represent data from experiments (ALICE and AT-LAS), while the lines with bands are from hydrodynamical models. We observe that the elliptic flow (depicted in black) calculated here is the dominant contributor, and the viscous hydrodynamics governing the description of the evolution of the fluid agrees well with the experimental data, indicating the collective nature of the medium (QGP) thus formed. However, the magnitude of the observed v_n (p_T) depends on the initial eccentricities ϵ_n (anisotropies in space), with the second harmonic eccentricity defined as $\epsilon_2 = \frac{\langle\langle y^2 - x^2 \rangle\rangle}{\langle\langle y^2 + x^2 \rangle\rangle}$ and the specific shear viscosity ($\frac{\eta}{s}$) values, where η is the dynamical shear viscosity coefficient and s is the entropy density.

The magnitude of the elliptic flow $v_2(p_T)$ indicates the presence of an expanding
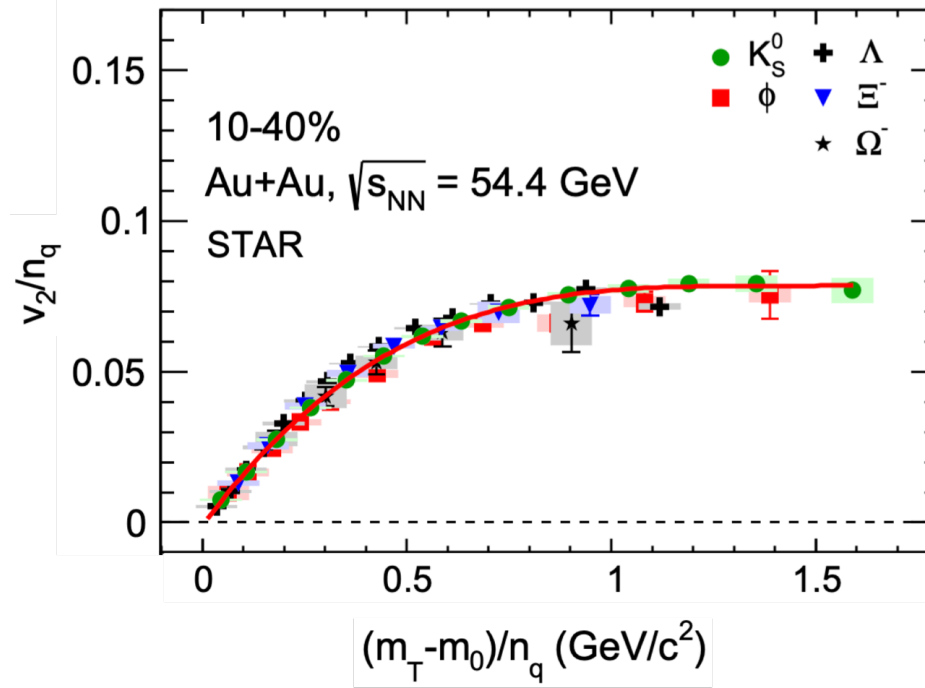
Figure 1.6: Scaled elliptic flow for $\sqrt{s_{NN}} = 54.4$ GeV at 10-40 % centrality for various particle species [91].

medium but does not directly signify the formation of such a medium at the quark level. The explanation for this lies in the concept of quark coalescence or recombination. This mechanism involves the production of hadrons, where quarks (q) and anti-quarks ($\bar{q}$) located at nearby phase space combine to form ($q\bar{q}$) for mesons and (qqq) for baryons. By employing this mechanism and plotting v_2/n_q, where n_q is the number of valence quarks/anti-quarks (2 for mesons and 3 for baryons), against p_T, it is observed that at low p_T (< 3 GeV), the scaling holds, whereas at higher p_T, there is a clear deviation from the scaling, indicating that particle production at higher p_T is primarily due to fragmentation [92].

Figure.(1.6) displays the plot for $\frac{v_2}{n_q}$ versus transverse kinetic energy scaled with n_q, i.e., $(m_T - m_0)/n_q$, at $\sqrt{s_{NN}} = 54.4$ GeV for Au+Au collisions at 10-40% centrality class for five different particle species ($K_s^0, \phi, \Lambda, \Omega^-, \Xi^-$). The various symbols rep-

resent data from STAR experiments, while the solid red line denotes the fit to the K_s^0 data. It is evident that different species aptly follow the scaling behavior. The consistent scaling behavior, observed regardless of whether the charged particles are mesons or baryons, underscores the effectiveness of the recombination model at low p_T. This indicates that colored quarks exhibit hydrodynamic flow and subsequently coalesce into colorless hadrons, thereby aptly capturing the fluid nature of the medium.

- **Quarkonia suppression :** The suppression of quarkonia, such as the J/Ψ bound state composed of charm and anti-charm quarks ($c\bar{c}$), in heavy-ion collision experiments is considered a key indicator of QGP formation. These heavy quarks and antiquarks, predominantly generated during the initial stages of the collision, interact through a potential described by $V = -\frac{\alpha_s}{r} + kr$ [93]. The first term of the potential is the Coulombic term due to two color charges (of q and q̄) with α_s being the strong coupling constant and r is the distance between the quark-anti-quark pair but the second one is the linear term which increases as the q is separated from q̄ thus increasing the potential which makes it impossible to obtain a single free quark [93]. In the presence of a surrounding medium, such as a QGP, the formed quarkonia interact with the surrounding charges, leading to interactions between the heavy quarkonia and the surrounding light quarks. The presence of surrounding light quarks effectively screens the heavy quarkonia, hindering their survival, a phenomenon known as Debye screening. As a result, the potential between the heavy quarks is modified by a factor $e^{-\frac{r}{\Lambda_D}}$, where Λ_D is the Debye screening length. If the length scale of the bound state exceeds Λ_D, it becomes more prone to dissociation. The dissociated heavy quarks subsequently undergo hadronization by interacting with other light quarks, forming pairs such as q$\bar{s}$, q̄s, q$\bar{d}$, etc. As they dissociate in the presence of the medium, there is a suppression in their number compared to that of without

22

the medium. This suppression in their production, as observed in [94, 95], hints at the production of QGP in heavy-ion experiments. Experimentally, the effect of these processes can be observed through a quantity named R_{AA}, also known as the nuclear modification factor. This factor is generally defined as:

$$R_{AA}(p_T, y) = \frac{\frac{d^2N}{d^2p_T dy}\big|_{A+A}}{\langle N_{\text{coll}} \rangle \frac{d^2N}{d^2p_T dy}\big|_{p+p}}, \tag{1.5}$$

where $\langle N_{coll} \rangle$ is the number of binary collisions usually taken from the Glauber model calculations. This R_{AA} is the ratio of multiplicity of heavy q$\bar{\text{q}}$ pair in heavy-ion collision to that produced in the p-p collisions where no QGP is assumed to be produced. The suppression in the number of quarkonia mainly is seen when R_{AA} is less than 1. This suggests that there is a medium formation. Initially, it was anticipated that the most pronounced suppression would occur at low quarkonium momenta, where the q$\bar{\text{q}}$ pair, quasi-statically embedded within the QGP, experiences the full impact of Debye screening. However, at high p_T, it was predicted that the suppression of J/Ψ would diminish and eventually vanish. This expectation arose from the fact that the c$\bar{\text{c}}$ bound state forms outside the QGP and thus is unaffected by color screening. This perception has since evolved in light of numerous theoretical and experimental findings. It has been acknowledged that additional mechanisms contribute to quarkonium melting beyond the static q$\bar{\text{q}}$ potential. As the temperature of the medium increases, different quarkonium states experience varying degrees of suppression. The binding energy of each state determines its susceptibility to dissociation in the QGP which is known as the sequential melting of quarkonia. Several investigations, exemplified by studies on charmonium [96] and bottomonium [97], affirm that the concept of sequential melting transcends the oversimplified paradigm of color screening.

Recent advancements both experimental and model predictions have shedded light on

the fact that the properties of the quarkonia could also be affected by the regeneration effects, that is regeneration of low p_T quarkonia at LHC energies [98].

- **Jet quenching :** Jets are colimated spray of particles coming from the initial high p_T partons produced in the initial stage of heavy-ion collision. These jets while traversing the thermal medium losses energy due to interaction with the dense matter. This thus results in the supression of the high p_T particles which is generally measured via the same nuclear modification factor R_{AA} which was defined above in Eq.(1.5) with the exception that the multiplicity (N) here is for the individual light and heavy quarks as opposed to the quarkonia in the previous case. It was observed initially at RHIC [99, 100, 101, 102] and was subsequently observed at LHC as well [103, 104]. $R_{AA} \sim 1$ implies no suppression whereas $R_{AA} < 1$ hints at suppression of jets. Fig.(1.7) shows the plot of nuclear modification factor R_{AA} for direct photons and other light mesons for Au+Au collision at $\sqrt{s_{NN}} = 200$ GeV and also for $\pi^{\pm}$ for d+Au collisions at the same centre of mass energy. We can see that at about 5-10 GeV the ϕ, π, η mesons all show a similar level of suppression, which can be attributed as the effect of interaction with dense thermal medium. As a thermal medium is usually attributed for low p_T particle production, this jet quenching can thus be thought of as a final state effect rather than from the initial state. However the R_{AA} for the direct γ show no suppression indicating the fact that photons interaction with medium is negligible. $\pi^{\pm}$ from the d+Au collisions also show almost no suppression. This indicate towards the fact that medium induced suppression is not seen in those systems possibly due to no medium formation. Along with the light hadrons the heavy flavour hadrons also serve as a potential candidate for identifying suppression as these are also generally formed at an early stage of the collision process and traces out the full medium along its evolution.
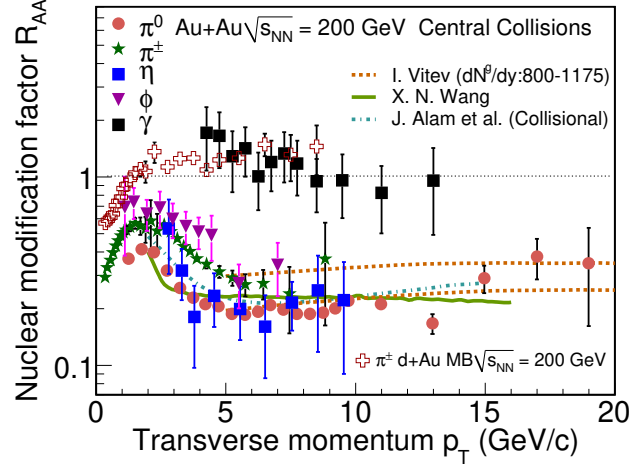
Figure 1.7: R_{AA} for direct photons and other mesons for Au+Au collision at $\sqrt{s_{NN}} = 200$ GeV [92]. Also the result for $\pi^{\pm}$ is given for d+ AU collisions at $\sqrt{s_{NN}} = 200$ GeV.
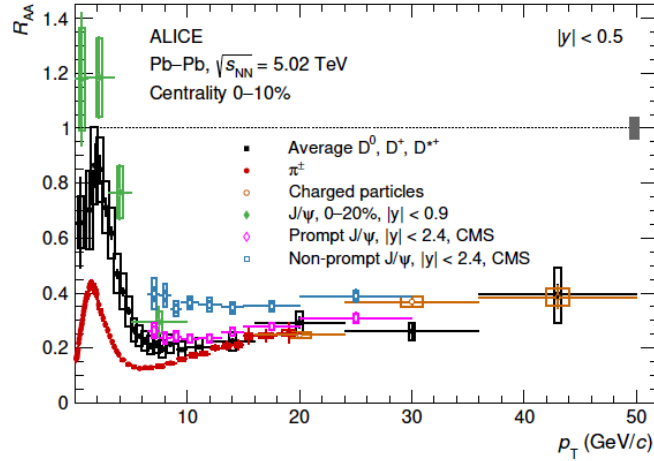
Figure 1.8: R_{AA} is depicted for prompt D-mesons, charged pions, charged particles, and J/Ψ particles by ALICE [105]. Additionally, R_{AA} results for both prompt and non-prompt J/Ψ particles from CMS are included [106]. These measurements were conducted in central Pb+Pb collisions at mid-rapidity with specific energy conditions noted in the legend.

Fig.(1.8) shows R_{AA} vs p_T for various heavy mesons (D mesons), charged pions ($\pi^{\pm}$) from ALICE experiments and quarkonia (J/Ψ both prompt and non prompt) from CMS experiment for Pb+Pb at $\sqrt{s_{NN}} = 5.02$ TeV at 0-10% centrality. We can see that at higher p_T over 10 GeV/c, the suppression of both heavy and light charged

hadrons almost show a similar level of suppression which is indeed due to the medium effect. There are also other measurements, such as the ratio of the yields, performed on different heavy quarks, can be found in [107, 108].

- **Strangeness enhancement :** The strangeness enhancement is one of the most important signature of the QGP medium formation. Among the oldest signatures proposed to indicate the presence of QGP in heavy-ion collisions is the observation of enhancement in the strange particle production [109, 110]. Nucleons inside the nuclei before the collisions lack valence strange quarks, yet $s\bar{s}$ pairs can be generated in the initial hard scattering, subsequent QGP or hadronic phase formed during high-energy heavy-ion collisions. In the event of QGP formation, an elevated production of s and $\bar{s}$ quarks is anticipated compared to normal hadronic interactions. This is due to the competitive nature between the production of $s\bar{s}$ pairs and $u\bar{u}$ and $d\bar{d}$ pairs. This indicates towards seeing an enhancement in strangeness production via taking the ratio of the yields of multi-strange to light hadrons both at hadronic as well as partonic sector which is usually given by:

$$\frac{\text{multi-strange particles multiplicity } (\Lambda, \Omega)}{\text{light particles } (\pi^+, \pi^-).} \qquad (1.6)$$

  In addition to examining this ratio for different system sizes, such as p+p, p+Pb, and Pb+Pb collisions, the relative comparison across these sizes can also serve as an indicator of QGP phase formation. The validation of this phenomenon as a hallmark of QGP formation was initially provided by the WA97 experiment [111]. Fig.(1.9) presents the data showing the ratios of yields of multi-strange baryons (Λ, Ξ^-, $\Omega^- + \bar{\Omega}^+$) for different system sizes relative to production at p+Be versus N_{part}, obtained from the NA57 experiment [112]. The plot on the right side corresponds to the antiparticle counterpart shown on the left. The plot reveals that at lower N_{part} the plots for p-Be and p-Pb (small systems have low multiplicity), remain consistent with unity,

26
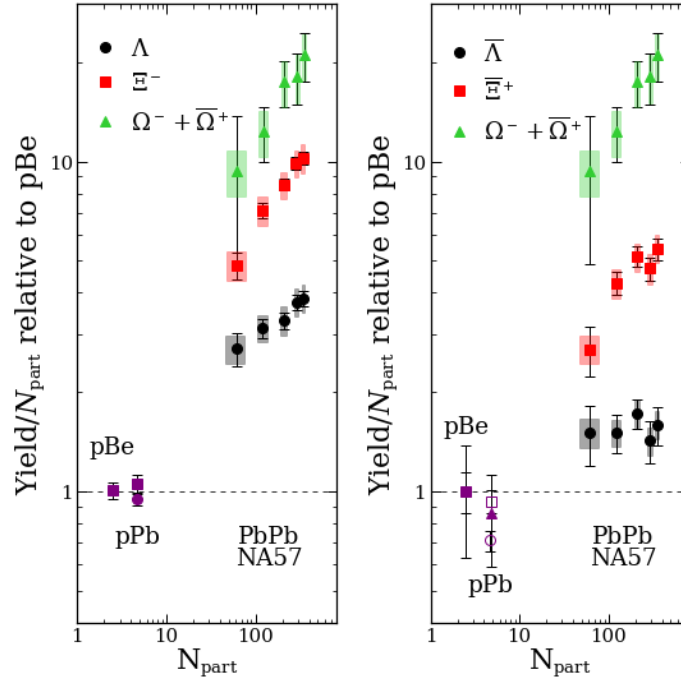
Figure 1.9: Multistrange baryon enhancement measured by NA57 in Pb+Pb collisions at $\sqrt{s_{NN}} = 17.3$ GeV as a function of the number of participant nucleons (N_{part}) [112].

whereas in the higher N_{part} region, the results for Pb+Pb show an increasing trend with respect to the increase in the number of participating nucleons. This increasing trend in the ratios of multi-strange baryons in Pb+Pb to that in p+p or p+Be hints at the formation of QGP medium in the nuclear-nuclear collisions. These findings were subsequently supported by results from both STAR and ALICE experiments [113, 114].

- **The direct photon measurement :** Photons serve as electromagnetic probes, offering crucial insights about the presence of a dense partonic medium. They are generated at various stages of heavy-ion collisions, spanning from the pre-equilibrium phase to the freeze-out stage, through processes such as $q + \bar{q} \to \gamma + \gamma$, $q + \bar{q} \to \gamma + g$, and $\pi^+ + \pi^- \to \gamma + \rho^0$. Direct photons are the photons that are not produced from hadronic decays. Fig.(1.10) shows the p_T spectra for direct photons for Pb+Pb collision at $\sqrt{s_{NN}} = 2.76$ TeV for different centrality classes (0–20 %, 20–40 %, 40–80
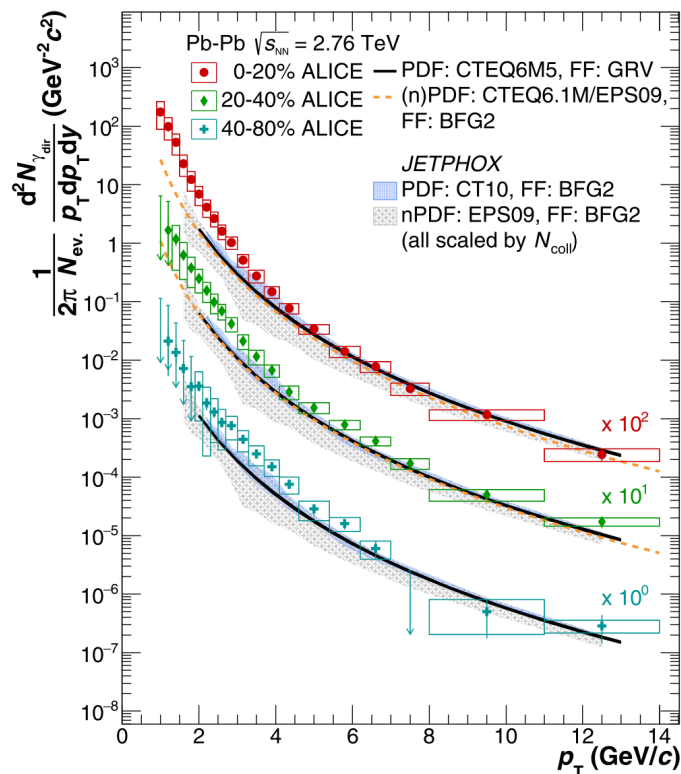
Figure 1.10: Comparison between the direct photon p_T-spectra in Pb+Pb collisions at $\sqrt{s_{NN}} = 2.76$ TeV across different centrality windows (0–20%, 20–40%, and 40–80%), each scaled by specific factors (100, 10, and 1 respectively). These spectra are contrasted with next-to-leading order pQCD predictions for direct photon yields in p+p collisions at the same energy level, but scaled individually by the number of binary nucleon collisions corresponding to each centrality window, as referenced in [115].

%) along with the pQCD predictions in case of p+p collisions at the similar energy. It is clear that at high transverse momentum that is for $p_T > 4$ GeV/c both the data from Pb+Pb and scaled pQCD predictions for p+p collisions matches really well, whereas there is a disagreement between them at low p_T regime ($p_T < 4$ GeV/c). This disagreement is more evident in the most central collisions that is for 0–20 % centrality range. At high p_T regime that is beyond 4 GeV/c the direct photon spectra obeys a power law whereas at low p_T, the Pb+Pb data obeys an exponential distribution proportional to $e^{-\frac{p_T}{T_{\text{eff}}}}$, where T_{eff} is the effective temperature of the medium and p_T is the

usual transverse momentum of the particle. This exponential behaviour clearly indicates the thermal behaviour of the direct photons. From this exponential fit we can get the slope whose inverse will give us the temperature of the initial thermal medium that is formed. There has been several attempts to extract the initial temperatures of the medium using ideal and viscous hydrodynamics models [116, 117] which roughly estimates τ_{ini}= 0.2 fm/c with initial temperature at the centre to be T_{ini}= 682 MeV and τ_{ini}= 0.4 fm/c with T_{ini}= 385 MeV respectively. Recently, employing Bayesian fits, researchers attempted to constrain the combination $\tau_{\text{ini}}^{1/3}T_{\text{ini}}$. Their findings yielded a value of 450^{+100}_{-70} fm$^{1/3}$MeV for Pb+Pb collisions at $\sqrt{s_{NN}} = 2.76$ TeV and 350^{+130}_{-60} fm$^{1/3}$MeV for Au+Au collisions at $\sqrt{s_{NN}} = 200$ GeV [118].

- **QGP droplet in small systems:** Till now all the signatures were indicating the formation of dense QGP medium in large systems like Pb, Au where we also assumed that smaller systems like p+p, p+Au, d+Au do not produced QGP medium. However, it was seen that even high-energy proton-proton collisions could produce a statistical system that might exhibit aspects of hydrodynamic behavior. The question then arises: Are the energy densities in small systems sufficiently high to produce a QGP medium, or is there a lower bound on the droplet size of the QGP that we can also anticipate for smaller systems.

  CMS provided the initial clear evidence of the behavior resembling a collective flow pattern in p-p collisions at $\sqrt{s_{NN}} = 7$ TeV [119]. Subsequent angular correlation measurements at $\sqrt{s_{NN}} = 2.76$ and 13 TeV further supported this finding [120, 121]. Similar observations of collective flow patterns have been documented in p+Pb collisions at the LHC as well as in p+Au, d+Au, and ^{3}He+Au collisions at RHIC [122, 123, 124, 125, 126, 127]. There have also been attempts from the computational side involving viscous hydrodynamics to try and understand the situation across var-
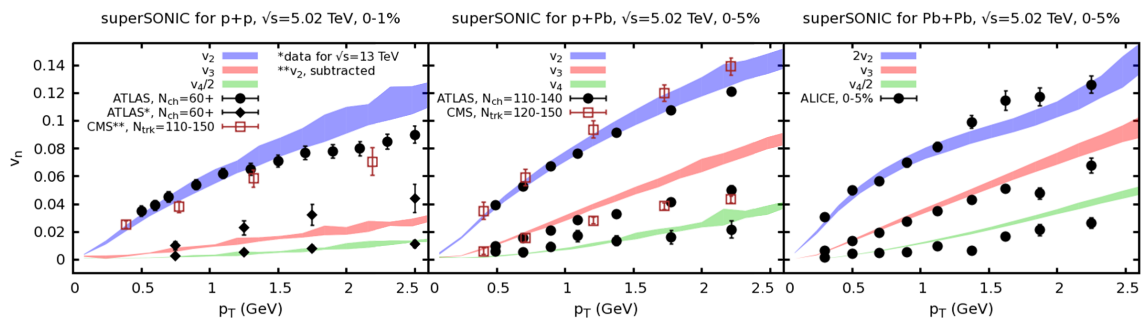
Figure 1.11: The hydrodynamic (superSONIC) simulations (bands) are compared with experimental data from ATLAS, CMS, and ALICE (symbols) for the elliptic (v_2), triangular (v_3), and quadrupolar (v_4) flow coefficients across various collision systems: p+p (left panel), p+Pb (center panel), and Pb+Pb (right panel) collisions at $\sqrt{s} = 5.02$ TeV. Simulations were conducted using $\eta/s = 0.08$ and $\zeta/s = 0.01$ for all systems. Notably, ATLAS results for v_3 and v_4 are available solely for $\sqrt{s} = 13$ TeV, whereas all simulation outcomes are based on $\sqrt{s} = 5.02$ TeV. The figure originates from [128].

ious system sizes. One such attempt is through the comparison of flow harmonics. Fig.(1.11) shows v_n's for three different system sizes that is for p+p (left most), p+Pb (middle) and Pb+Pb (right most) for $\sqrt{s_{NN}} = 5.02$ TeV for the most central case. The symbols represents the data from various experiments whereas the bands are the simulation results using the superSONIC code which uses viscous hydrodynamics for the medium evolution. We can observe that the model calculations remarkably reproduces the results across various system sizes. This suggests the possibility that a QGP-like system may be formed in all such system sizes.

We will now discuss one of the intriguing aspects, which also constitutes the primary focus of the current thesis that is studying the effects and behavior of intense electromagnetic fields produced in heavy-ion collision experiments. We now begin here by exploring their generation in such collisions.

1.0.5   Electromagnetic field production in heavy-ion collisions

In non-central heavy-ion collisions, the rapid motion of nuclei results in the generation of intense electromagnetic fields. Due to the fast moving spectators moving along z-direction, with impact parameter along the x-axis, the yth-component of magnetic field will be the dominant contributor to the overall field production. Mathematically it can be written in units of m_π^2 as [129]:

$$e \cdot \langle B_y \rangle \propto \frac{\sqrt{s}}{2m_p} \frac{Z}{A^{2/3}} \frac{b}{2R_A}, \quad \text{for } b < 2R_A, \tag{1.7}$$

where m_p, Z, A, b, R_A are mass of proton, atomic number, mass number, impact parameter, radius of the nuclei respectively. This shows that the fields will increase with increase in the $\sqrt{s}$, Z and b. Studies have demonstrated that while these magnetic fields are transient in vacuum, they may persist for longer durations in the presence of a conducting medium. Fig.(1.12) illustrates the scenario where two highly Lorentz contracted nuclei moving at
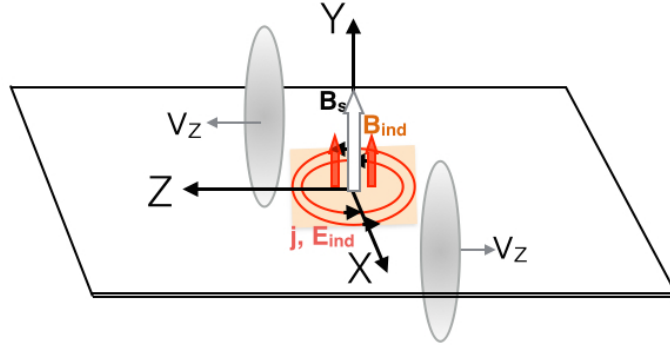
Figure 1.12: Pictorial depiction of electromagnetic fields produced in a non-central heavy-ion collision [130].

relativistic velocities in the beam direction (z-axis), with non-zero impact parameter along the x-axis. The magnetic fields at $(x, y, z) = (0, 0, 0)$ (shown by $\mathbf{B}_s$) are produced predominantly in the y-direction that is perpendicular to the reaction plane (that is the plane formed by the impact-parameter (x-axis) and the beam direction (z-axis)). According to the

Maxwell's equation $\nabla \times \mathbf{E} = -\partial_t \mathbf{B}$, this time varying magnetic fields will induce an electric, which in turn produces a current $\mathbf{J}$ (shown by red circles). According to $\nabla \times \mathbf{B} = \mu_0 \mathbf{J}$, these currents indeed will induce a magnetic field again in the same direction (y-axis) as was produced by the moving spectators. This will enhance the contribution of the magnetic field along the y-direction and this enhancement is primarily due to the medium induced effects. This makes the magnetic fields to sustain more in the presence of a medium. This sustained presence of magnetic fields increase their chances of being detected in high-energy heavy-ion collision experiments [21]. The temporal behaviour of the magnetic field in presence of a medium is illustrated in Fig.(1.13). Here we observe that the B_y decays rapidly and reaches a very low value within a short period of time, around 2 fm (shown in blue) in vaccum. However, in the presence of a conductive medium (shown in red), the field sustains for a longer period and maintains an appreciable strength.
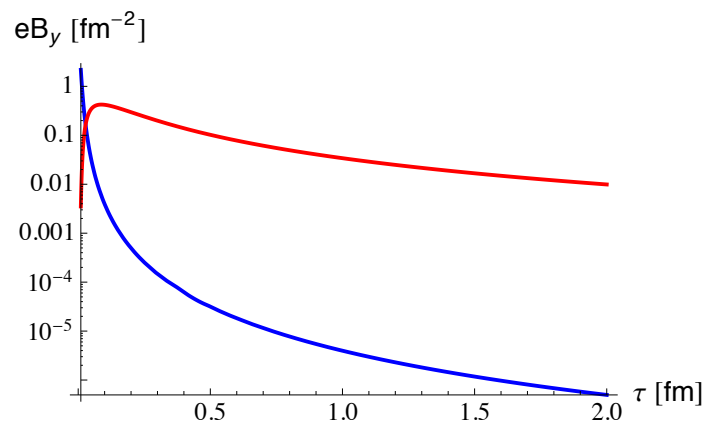
Figure 1.13: Evolution of magnetic field with (red solid line) and without (blue solid line) conductivity at RHIC energies[21].

Although a smooth distribution of protons inside a nucleus (calculated from optical Glauber model) yields electric and magnetic fields predominantly in x- and y-direction respectively, but in reality a calculation on an event-by-event basis indicates that due to the fluctuations in the positions of the protons inside the nuclei, all the components of the electromagnetic fields can exhibit comparable strengths [59, 60]. This phenomena is also

illustrated in chapter.(5). However the predictions on the magnitude and calculation of the strength of the electromagnetic fields are mere theoretical. Nonetheless, there have been few attempts from the experimental side to measure and determine the effect of electromagnetic fields, which we briefly describe below.

Observables for electromagnetic fields in heavy-ion collisions

Experimental progress and measurements that has been conducted to investigate the impact of electromagnetic fields on the medium in heavy-ion collisions, is either by examining the Chiral Magnetic Effect (CME) or by studying differential directed flow [131, 132, 133]. The CME is primarily observed in parity odd medium. It presents an unusual scenario
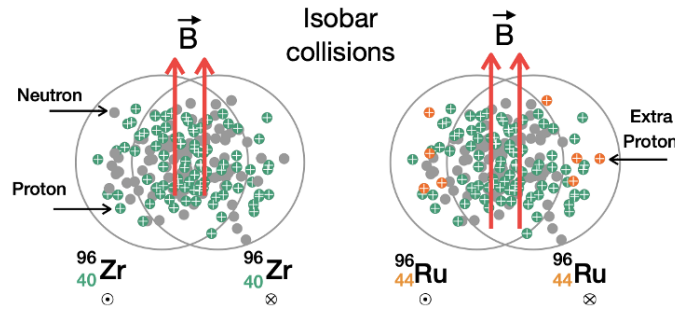
Figure 1.14: Visual representation of isobaric collisions involving Zr + Zr and Ru + Ru.

where an electric current emerges along the direction of an external magnetic field, induced by a disparity in chirality (the difference in the number of left-handed and right-handed particles). These anomalies are also anticipated in heavy-ion collisions, characterized by highly intense magnetic fields and chirality imbalances within the generated medium. In the quest for the CME search in heavy-ion collisions, investigations are chiefly conducted through isobaric collisions. These collisions involve comparing the outcomes between collisions of different ions, such as Zr or Ru, which share the same mass number but have different atomic numbers (as depicted in Fig.(1.14)). Comparisons here are made between

Zr+Zr and Ru+Ru collision systems to analyze the effects of varying atomic numbers while keeping the mass number constant. As the magnetic fields are proportional to the atomic number (Z), the one's with greater Z will experience more magnetic fields, which will lead to a greater separation between particles. The background contributions in both the systems are kept constant via same mass number A (96 in this case). Thereby, indicating the fact that any additional effects observed from comparing these collisions may stem from electromagnetic fields. The observable employed to detect this phenomenon is the γ correlator defined as:

$$\gamma = \langle \cos(\phi_\alpha + \phi_\beta - 2\Psi_{RP}) \rangle, \tag{1.8}$$

where ϕ_α and ϕ_β represent the azimuthal angles of particles of interest (POIs), and Ψ_{RP} denotes the reaction plane angle. CME searches and its progress have been extensively documented in the literature [132, 133].
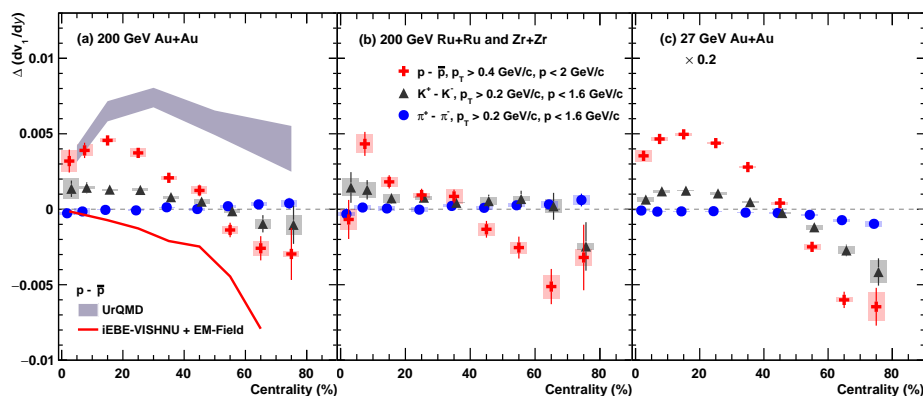
Figure 1.15: Comparison between experimental data and model predictions for the differential slope of elliptic flow ($\Delta \frac{dv_1}{dy}$) is conducted for pions, kaons, and protons in Au + Au collisions at center-of-mass energies of $\sqrt{s_{NN}}$ = 200 GeV and 27 GeV, as well as for isobaric collisions at $\sqrt{s_{NN}}$ = 200 GeV [131].

Another observable that is used to measure the effect of electromagnetic fields are through differential directed flow. Recent experiments have investigated the observable $\Delta \frac{dv_1}{dy}$ for all identified charged particles (pions, protons, kaons). $\Delta \frac{dv_1}{dy}$ is typically defined

as the difference in the contribution from the particle and anti-particle's the directed flow slope values calculated at mid-rapidity (y=0). This phenomenon is primarily observed with centrality, as the effect of the electromagnetic field is expected to increase in more peripheral collisions (70 - 80 %), mainly due to a large number of spectators. In Fig.(1.15), data points for different systems and energies are represented by various symbols where colors red, blue, and black corresponds to protons, pions, and kaons, respectively. The plots from various models, such as UrQMD (depicted in the violet band) and VISHNU + EM field (indicated by the red line), are also included. The notable observation indicating the presence of the electromagnetic field is the negative slope of the aforementioned observable. It can be seen that the model with the electromagnetic field (represented by the red line) roughly reproduces the trajectory of the slope, whereas the model without electromagnetic fields does not.

With that now we focus on the primary objective of this thesis:

- Calculation of evolution equations for the dissipative stresses (bulk, diffusion and shear) in presence of external electromagnetic fields from kinetic theory.

- Generation of electromagnetic fields by the participant charges in heavy-ion collisions.

- Effect of baryon stopping on the temporal evolution of all the components of electromagnetic fields.

- The effect of electric fields on the bulk observables (spectra, v_n's).

1.0.6 Thesis motivation

It is well known that the relativistic generalization of non-relativistic Navier-Stokes relations possesses an acausality issue, also discussed in chapter.(2). Specifically, it yields a

group velocity v_g that diverges at large k limit, where $k = |\mathbf{k}|$ with $\mathbf{k}$ being the wave vector. To circumvent this issue, Israel and Stewart [134, 135, 136] proposed the formulation of relaxation-type equations for dissipative stresses (bulk, shear, heat current) by going to a higher order in derivative expansion. These equations can be written in the following form:

$$\Pi = -\frac{1}{3}\zeta \left(\partial_\mu u^\mu + \beta_0 \dot{\Pi} - \alpha_0 \partial_\mu q^\mu \right), \tag{1.9}$$

$$q^\lambda = \kappa T \Delta^{\lambda\mu} \left[\partial_\mu \alpha \cdot nT/(\epsilon + P) - \beta_1 \dot{q}_\mu + \alpha_0 \partial_\mu \Pi + \alpha_1 \partial_\nu \pi^\nu_\mu \right], \tag{1.10}$$

$$\pi_{\lambda\mu} = -2\eta \left(u_{<\lambda|\mu>} + \beta_2 \dot{\pi}_{\lambda\mu} - \alpha_1 q_{<\lambda|\mu>} \right), \tag{1.11}$$

where u^μ, Π, q^λ, $\pi_{\lambda\mu}$ denote the fluid's four-velocity, bulk, heat current, and shear stress, respectively. Meanwhile, ζ, κ, and η primarily represent the first-order transport coefficients, defined as bulk viscosity, thermal conductivity, and shear viscosity, respectively.

Bulk viscosity describes how a substance responds when it's compressed or rarefied. Shear viscosity explains how it reacts to tangential forces, while thermal conductivity tells us how it responds to the heat moving from a high-temperature to a low-temperature region. The dissipative stresses (Π, q^λ, $\pi_{\lambda\mu}$) are zeroth, first, and second-rank tensors, respectively. Their formation arises from the comprehensive expansion of the full energy-momentum tensor across all potential tensor ranks. A symmetric $T^{\mu\nu}$ can thus be written as:

$$T^{\mu\nu} = A_1 u^\mu u^\nu + A_2 g^{\mu\nu} + A_3 \Pi + A_4 \pi^{\mu\nu} + A_5 \left(u^\mu q^\nu + u^\nu q^\mu \right), \tag{1.12}$$

where the A's are the unknown coefficients. The shear stress is a symmetric second-rank tensor derived from the symmetric component of the $T^{\mu\nu}$ tensor. Both the heat current and shear stress naturally exhibit orthogonality to the fluid's four-velocity u^μ. The dimensionless transport coefficients ($\frac{\eta}{s}$ and $\frac{\zeta}{s}$), where 's' is entropy density, hold significant importance in determining the magnitude of flow harmonics (v_2). Moreover, their temperature dependence underscores the system's identification as a strongly coupled liquid rather than a weakly coupled gas. Holographic calculations have proposed lower bounds on the $\frac{\eta}{s}$ value,

typically around $\frac{1}{4\pi}$ [137]. Furthermore, Bayesian estimates suggest that this value stands as the lowest among known fluids, such as liquid helium and water, offering valuable insights into the temperature-dependent behavior of both $\frac{\eta}{s}$ and $\frac{\varsigma}{s}$ [138].

Reflecting on the right-hand side of Eqs.(1.9)-(1.11), the first term in each equation represents the Navier-Stokes relationships for the corresponding stresses. It's worth noting that these terms are all first-order in gradient expansion, treating u^μ and T as zeroth or-der in the gradient expansion. However, upon progression to higher orders, new transport coefficients denoted by α's and β's come into play. Eqs.(1.9)-(1.11) typically treat the in-dividual dissipative stresses (Π, q^λ, $\pi_{\lambda\mu}$) as separate entities, diverging from their role as dependent quantities in the Navier-Stokes limit, thereby providing an evolution equation for each. In the Navier-Stokes limit these dissipative stresses or fluxes are related to the thermodynamics forces by the following relation:

$$\mathbf{J} = \gamma\mathbf{X}, \tag{1.13}$$

where $\mathbf{X}$ is the thermodynamic force which acts on the medium and $\mathbf{J}$ is the flux generated, with γ being the transport coefficient. Here $\mathbf{J}$ can be Π, q^λ, and $\pi_{\lambda\mu}$ and the $\mathbf{X}$ be deriva-tive of zeroth order fluid variables like u^μ, T, and α, with the γ being their corresponding transport coefficients. The thorough derivation of these equations through entropy current analysis is further given in chapter.(2). Obtaining these equations and estimating the nec-essary transport coefficients required a meticulous derivation from a microscopic theory, with relativistic kinetic theory as the foundation. At its core lies the relativistic Boltzmann equation [139], expressed as:

$$p^\mu\partial_\mu f + F^\mu\frac{\partial f}{\partial p^\mu} = C[f], \tag{1.14}$$

where p^μ represents the four-momentum of an individual particle, F^μ accounts for all exter-nal forces, and the right-hand side encompasses contributions from collisions. The function

f denotes the one-particle distribution function derived from this equation for various processes. In an $2 \leftrightarrow 2$ elastic collisions like $pp^{'} \leftrightarrow kk^{'}$, the term $C[f]$ is expressed as:

$$C[f] = \frac{1}{2} \int dp^{'} dk dk^{'} W_{pp^{'} \to kk^{'}} \left(f_k f_{k^{'}} \tilde{f}_p \tilde{f}_{p^{'}} - f_p f_{p^{'}} \tilde{f}_k \tilde{f}_{k^{'}} \right), \qquad (1.15)$$

where p, $p^{'}$ and k, $k^{'}$ denote the four-momenta of the involved particles before and after the collision respectively. $W_{pp^{'} \to kk^{'}}$ represents the transition rate for the collisions between individual particles. This equation's first and second terms (given in the bracket) denote the gain and loss terms for a collision happening locally at a given point. However, this form of collision kernel introduces a challenge by converting the relativistic Boltzmann equation into an integro-differential form, which is very challenging to solve. Therefore, several approximations were introduced by linearizing $C[f]$ [140, 141, 142], with the relaxation time approximation (RTA) being one of the most popular methods. RTA simplifies the entire right-hand side to $-\frac{u \cdot p}{\tau_c} \delta f$, where $\delta f = f - f_0$, denotes the small deviation from the equilibrium distribution function f_0, and τ_c represents the relaxation time (further lights on this is provided in chapter.(2)). Moreover, Eqs. (1.9)-(1.11) have been derived multiple times from the underlying relativistic kinetic theory using various approximations of collision kernels [143, 144, 145, 146, 147, 148, 149, 150, 151, 152], commonly employed in numerical simulations. However, modifications to these evolution equations were necessary in the presence of electromagnetic fields, accounting for the contribution from F^{μ}.

In this thesis, we formulate such evolution equations using relativistic kinetic theory, employing the RTA within the collision kernel while considering the influence of external electromagnetic fields. These equations are formulated to encompass contributions from both particles and antiparticles. Additionally, we conduct a comparative analysis with results obtained through the 14-moment method [153, 154]. Furthermore, we extend our investigation to explore the impact of these fields on bulk observables, such as spectra and flow harmonics (v_n), employing a blast-wave model. This model incorporates a

parametrized velocity profile with azimuthal anisotropy and temperature variation at the freezeout hypersurface, allowing for a comprehensive assessment of the effects of the electromagnetic field (only electric fields in the present thesis).

So far, the fields considered were external, originating predominantly from spectator charges. Numerous studies have explored the effect of such fields by considering that the fields from the participants are very small compared to those produced by the spectators. However, a detailed investigation regarding this was lacking. Hence, we aim to investigate the behavior of electromagnetic fields primarily sourced from participant charges.

As the electromagnetic fields generated during the initial phase of heavy-ion collisions evolve, they interact with the QGP medium, influencing its behavior by altering the fluid's velocity. This modification in velocity, in turn, induces further alterations in the fields, highlighting the necessity for a consistent magnetohydrodynamics (MHD) formulation. Integrating these effects into the code necessitates a consistent Magnetohydrodynamics (MHD) simulation, typically initialized with field components derived from Glauber model calculations assuming a constant velocity for the charged nucleons (protons). However, experimental findings from low-energy heavy-ion collisions indicate the stopping of participant nucleons around the mid-rapidity region, prompting adjustments to initial conditions. In another study, we addressed this by parameterizing the velocity of participant protons such that after the collisions, the fields undergo deceleration, exhibiting a stopping effect. We systematically evaluated all electromagnetic field components and discussed their temporal evolution.

1.0.7 Organisation of the thesis

The current thesis is organized as follows. Firstly, in chapter.(2), we present a theoretical overview of relativistic hydrodynamics, magnetohydrodynamics, and kinetic theory, which serve as the foundation for the subsequent chapters of the thesis.

Following that, in chapter.(3), we delve into formulating a second-order non-resistive and resistive magnetohydrodynamics (MHD) theory from relativistic kinetic theory, employing the RTA as the collision kernel. This section investigates the evolution of various dissipative stresses, encompassing the effects of electric and magnetic fields. Furthermore, we analyze the transport coefficients resulting from including electromagnetic fields, considering their dependence on magnetic field strength, temperature, and mass at the Navier-Stokes and the second-order in gradient expansion limit.

In chapter.(4), we focus solely on the contributions from participants where we derive the expressions for all the components of electromagnetic fields under two distinct scenarios, one for a point charge and another for a more realistic scenario as possible in the case of heavy-ion collisions.

Chapter.(5) primarily addresses the incorporation of baryon stopping effects via parametrizing the participant proton velocity in the Glauber model and exploring their impact on the temporal evolution of all the electromagnetic field components at low energies.

Lastly, in chapter.(6), by employing the blastwave model to parameterize fluid velocity and temperature on the freezeout (kinetic) hypersurface and adopting the Cooper-Frye particlization prescription, we investigate the influence of electric fields on bulk observables such as spectra and flow harmonics (v_n's).

We finally conclude the thesis in chapter.(7), where we summarize all the results obtained, outline the conclusions drawn from the research presented in this thesis, and present some of the avenues that can be further explored.

Throughout this thesis, we will be working in the natural units that are $\hbar = c = k_B = \epsilon_0 = \mu_0 = 1$ and the metric tensor in flat space-time is $g^{\mu\nu} = \text{diag}(+1, -1, -1, -1)$ unless otherwise specified.

References

[1] G. Lemaitre, "Republication of: The beginning of the world from the point of view of quantum theory," *Nature* **127**, 706 (1931) doi:10.1007/s10714-011-1214-6.

[2] E. Rutherford, "The scattering of alpha and beta particles by matter and the structure of the atom," *Phil. Mag. Ser. 6* **21**, 669-688 (1911) doi:10.1080/14786440508637080.

[3] J.J. Thomson, "XL. Cathode Rays," *Philosophical Magazine Letters* **87**(5), 303-326 (2007), doi: 10.1080/09500830701306165.

[4] M. Gell-Mann, "A Schematic Model of Baryons and Mesons," *Phys. Lett.* **8**, 214-215 (1964) doi: 10.1016/S0031-9163(64)92001-3.

[5] F. Wilczek, "Quantum Chromodynamics (QCD): The Modern Theory of the Strong Interaction," Ann. Rev. Nucl. Part. Sci. **32**, 177-209 (1982) doi:10.1146/annurev.ns.32.120182.001141

[6] E. Fermi, "An attempt of a theory of beta radiation. 1.," Z. Phys. **88**, 161-177 (1934) doi:10.1007/BF01351864.

[7] S. Weinberg, "A Model of Leptons," *Phys. Rev. Lett.* **19**, 1264-1266 (1967) doi: 10.1103/PhysRevLett.19.1264.

[8] G. Zweig, "An SU(3) model for strong interaction symmetry and its breaking. Version 1," CERN-TH-401.

[9] H. Fritzsch and M. Gell-Mann, "Current algebra: Quarks and what else?," eConf **C720906V2**, 135-165 (1972) [arXiv:hep-ph/0208010 [hep-ph]].

[10] D. J. Gross and F. Wilczek, "Ultraviolet Behavior of Nonabelian Gauge Theories," *Phys. Rev. Lett.* **30**, 1343-1346 (1973) doi: 10.1103/PhysRevLett.30.1343.

[11] H. David Politzer, "Asymptotic freedom: An approach to strong interactions," *Physics Reports* **14**(4), 129–180 (1974), publisher: *Elsevier*.

[12] David J. Gross and Frank Wilczek, "Asymptotically free gauge theories. II," *Physical Review D* **9**(4), 980 (1974), publisher: *APS*.

[13] R. Brandelik *et al.* [TASSO], "Evidence for Planar Events in e+ e- Annihilation at High-Energies," Phys. Lett. B **86**, 243-249 (1979) doi:10.1016/0370-2693(79)90830-X

[14] D. P. Barber, U. Becker, H. Benda, A. Boehm, J. G. Branson, J. Bron, D. Buikman, J. Burger, C. C. Chang and H. S. Chen, *et al.* "Discovery of Three Jet Events and a Test of Quantum Chromodynamics at PETRA Energies," Phys. Rev. Lett. **43**, 830 (1979) doi:10.1103/PhysRevLett.43.830

[15] P. W. Higgs, "Broken Symmetries and the Masses of Gauge Bosons," *Phys. Rev. Lett.* **13**, 508-509 (1964) doi: 10.1103/PhysRevLett.13.508.

[16] E. V. Shuryak, "Quark-Gluon Plasma and Hadronic Production of Leptons, Photons and Psions," Phys. Lett. B **78**, 150 (1978) doi:10.1016/0370-2693(78)90370-2

[17] K. Rajagopal and F. Wilczek, "The Condensed matter physics of QCD," doi: 10.1142/9789812810458_0043 [arXiv:hep-ph/0011333 [hep-ph]].

[18] J. Adams *et al.* [STAR], "Experimental and theoretical challenges in the search for the quark gluon plasma: The STAR Collaboration's critical assessment of the evidence from RHIC collisions," *Nucl. Phys. A* **757**, 102-183 (2005) doi: 10.1016/j.nuclphysa.2005.03.085 [arXiv:nucl-ex/0501009 [nucl-ex]].

[19] I. Arsene *et al.* [BRAHMS], "Quark gluon plasma and color glass condensate at RHIC? The Perspective from the BRAHMS experiment," Nucl. Phys. A **757**, 1-27 (2005) doi:10.1016/j.nuclphysa.2005.02.130 [arXiv:nucl-ex/0410020 [nucl-ex]].

[20] V. Skokov, A. Y. Illarionov and V. Toneev, "Estimate of the magnetic field strength in heavy-ion collisions," *Int. J. Mod. Phys. A* **24**, 5925-5932 (2009) doi:10.1142/S0217751X09047570 [arXiv:0907.1396 [nucl-th]].

[21] U. Gursoy, D. Kharzeev and K. Rajagopal, "Magnetohydrodynamics, charged currents and directed flow in heavy ion collisions," *Phys. Rev. C* **89**(5), 054905 (2014) doi:10.1103/PhysRevC.89.054905 [arXiv:1401.3805 [hep-ph]].

[22] T. Hatsuda and T. Kunihiro, "Critical Phenomena Associated with Chiral Symmetry Breaking and Restoration in QCD," Prog. Theor. Phys. **74**, 765 (1985) doi:10.1143/PTP.74.765

[23] G. E. Brown and M. Rho, "Chiral restoration in hot and/or dense matter," Phys. Rept. **269**, 333-380 (1996) doi:10.1016/0370-1573(95)00067-4 [arXiv:hep-ph/9504250 [hep-ph]].

[24] D. E. Kharzeev, "Topologically induced local P and CP violation in QCD x QED," Annals Phys. **325**, 205-218 (2010) doi:10.1016/j.aop.2009.11.002 [arXiv:0911.3715 [hep-ph]].

[25] D. E. Kharzeev, "Chern-Simons current and local parity violation in hot QCD matter," Nucl. Phys. A **830**, 543C-546C (2009) doi:10.1016/j.nuclphysa.2009.10.049 [arXiv:0908.0314 [hep-ph]].

[26] D. Kharzeev, "Parity violation in hot QCD: Why it can happen, and how to look for it," *Phys. Lett. B* **633**, 260-264 (2006) doi: 10.1016/j.physletb.2005.11.075 [arXiv:hep-ph/0406125 [hep-ph]].

[27] K. Fukushima, D. E. Kharzeev and H. J. Warringa, "The Chiral Magnetic Effect," *Phys. Rev. D* **78**, 074033 (2008) doi: 10.1103/PhysRevD.78.074033 [arXiv:0808.3382 [hep-ph]].

[28] D. T. Son and A. R. Zhitnitsky, "Quantum anomalies in dense matter," *Phys. Rev. D* **70**, 074018 (2004) doi: 10.1103/PhysRevD.70.074018 [arXiv:hep-ph/0405216 [hep-ph]].

[29] S. Pu, S. Y. Wu and D. L. Yang, "Chiral Hall Effect and Chiral Electric Waves," *Phys. Rev. D* **91**(2), 025011 (2015) doi: 10.1103/PhysRevD.91.025011 [arXiv:1407.3168 [hep-th]].

[30] N. Banerjee, J. Bhattacharya, S. Bhattacharyya, S. Dutta, R. Loganayagam and P. Surowka, "Hydrodynamics from charged black branes," *JHEP* **01**, 094 (2011) doi: 10.1007/JHEP01(2011)094 [arXiv:0809.2596 [hep-th]].

[31] L. P. Csernai and H. Stoecker, Central heavy ion collisions by nuclear hydrodynamics," Phys. Rev. C **25**, 3208 (1981) doi:10.1103/PhysRevC.25.3208.,

[32] L. P. Csernai and B. Lukacs, A VISCOUS HYDRODYNAMICAL MODEL FOR RELATIVISTIC HEAVY ION REACTIONS," Acta Phys. Polon. B **15**, 149-165 (1984).

[33] U. W. Heinz, H. Song and A. K. Chaudhuri, "Dissipative hydrodynamics for viscous relativistic fluids," Phys. Rev. C **73**, 034904 (2006) doi:10.1103/PhysRevC.73.034904 [arXiv:nucl-th/0510014 [nucl-th]].

[34] S. Bethke, "α_s 2002," *Nucl. Phys. B Proc. Suppl.* **121**, 74-81 (2003) doi: 10.1016/S0920-5632(03)01817-6 [arXiv:hep-ex/0211012 [hep-ex]].

44

[35] L. D. McLerran and R. Venugopalan, "Computing quark and gluon distribution functions for very large nuclei," *Phys. Rev. D* **49**, 2233-2241 (1994) doi: 10.1103/PhysRevD.49.2233 [arXiv:hep-ph/9309289 [hep-ph]].

[36] M. Gockeler, R. Horsley, A. C. Irving, D. Pleiter, P. E. L. Rakow, G. Schierholz and H. Stuben, "A Determination of the Lambda parameter from full lattice QCD," Phys. Rev. D **73**, 014513 (2006) doi:10.1103/PhysRevD.73.014513 [arXiv:hep-ph/0502212 [hep-ph]].

[37] H. T. Ding, F. Karsch and S. Mukherjee, "Thermodynamics of strong-interaction matter from Lattice QCD," Int. J. Mod. Phys. E **24**, no.10, 1530007 (2015) doi:10.1142/S0218301315300076 [arXiv:1504.05274 [hep-lat]].

[38] J. Chluba, M. H. Abitbol, N. Aghanim, Y. Ali-Haimoud, M. Alvarez, K. Basu, B. Bolliet, C. Burigana, P. de Bernardis and J. Delabrouille, *et al.* "New horizons in cosmology with spectral distortions of the cosmic microwave background," *Exper. Astron.* **51**(3), 1515-1554 (2021) doi: 10.1007/s10686-021-09729-5 [arXiv:1909.01593 [astro-ph.CO]].

[39] B. P. Abbott *et al.* [LIGO Scientific and Virgo], "GW170817: Observation of Gravitational Waves from a Binary Neutron Star Inspiral," Phys. Rev. Lett. **119**, no.16, 161101 (2017) doi:10.1103/PhysRevLett.119.161101 [arXiv:1710.05832 [gr-qc]].

[40] J. Schukraft, "Results from the first heavy ion run at the LHC," *J. Phys. Conf. Ser.* **381**, 012011 (2012) doi: 10.1088/1742-6596/381/1/012011 [arXiv:1112.0550 [hep-ex]].

[41] A. Cooper-Sarkar and C. Gwenlan, "Comparison and combination of ZEUS and H1 PDF analyses: HERA - LHC workshop proceedings," [arXiv:hep-ph/0508304 [hep-ph]].

[42] A. Accardi, J. L. Albacete, M. Anselmino, N. Armesto, E. C. Aschenauer, A. Bacchetta, D. Boer, W. K. Brooks, T. Burton and N. B. Chang, *et al.* "Electron Ion Collider: The Next QCD Frontier: Understanding the glue that binds us all," *Eur. Phys. J. A* **52**(9), 268 (2016) doi: 10.1140/epja/i2016-16268-9 [arXiv:1212.1701 [nucl-ex]].

[43] L. D. McLerran and R. Venugopalan, "Boost covariant gluon distributions in large nuclei," Phys. Lett. B **424**, 15-24 (1998) doi:10.1016/S0370-2693(98)00214-7 [arXiv:nucl-th/9705055 [nucl-th]].

[44] M. Luzum and P. Romatschke, "Conformal Relativistic Viscous Hydrodynamics: Applications to RHIC results at s(NN)**(1/2) = 200-GeV," Phys. Rev. C **78**, 034915 (2008) [erratum: Phys. Rev. C **79**, 039903 (2009)] doi:10.1103/PhysRevC.78.034915 [arXiv:0804.4015 [nucl-th]].

[45] P. Romatschke, "Relativistic Hydrodynamic Attractors with Broken Symmetries: Non-Conformal and Non-Homogeneous," *JHEP* **12**, 079 (2017) doi: 10.1007/JHEP12(2017)079 [arXiv:1710.03234 [hep-th]].

[46] S. Jaiswal, C. Chattopadhyay, A. Jaiswal, S. Pal and U. Heinz, "Exact solutions and attractors of higher-order viscous fluid dynamics for Bjorken flow," *Phys. Rev. C* **100**(3), 034901 (2019) doi: 10.1103/PhysRevC.100.034901 [arXiv:1907.07965 [nucl-th]].

[47] C. Chattopadhyay, S. Jaiswal, L. Du, U. Heinz and S. Pal, "Non-conformal attractor in boost-invariant plasmas," *Phys. Lett. B* **824**, 136820 (2022) doi: 10.1016/j.physletb.2021.136820 [arXiv:2107.05500 [nucl-th]].

[48] S. Jaiswal, J. P. Blaizot, R. S. Bhalerao, Z. Chen, A. Jaiswal and L. Yan, "From moments of the distribution function to hydrodynamics: The nonconformal case," *Phys. Rev. C* **106**(4), 044912 (2022) doi: 10.1103/PhysRevC.106.044912 [arXiv:2208.02750 [nucl-th]].

[49] J. Jankowski and M. Spaliński, "Hydrodynamic attractors in ultrarelativistic nuclear collisions," *Prog. Part. Nucl. Phys.* **132**, 104048 (2023) doi: 10.1016/j.ppnp.2023.104048 [arXiv:2303.09414 [nucl-th]].

[50] S. Kamata, J. Jankowski and M. Martinez, "Novel features of attractors and transseries in nonconformal Bjorken flows," *Phys. Rev. D* **107**(11), 116004 (2023) doi: 10.1103/PhysRevD.107.116004 [arXiv:2206.00653 [physics.flu-dyn]].

[51] A. Dash and V. Roy, "Hydrodynamic attractors for Gubser flow," *Phys. Lett. B* **806**, 135481 (2020) doi: 10.1016/j.physletb.2020.135481 [arXiv:2001.10756 [nucl-th]].

[52] C. Chattopadhyay and U. W. Heinz, "Hydrodynamics from free-streaming to thermalization and back again," *Phys. Lett. B* **801**, 135158 (2020) doi: 10.1016/j.physletb.2019.135158 [arXiv:1911.07765 [nucl-th]].

[53] G. Giacalone, A. Mazeliauskas and S. Schlichting, "Hydrodynamic attractors, initial state energy and particle production in relativistic nuclear collisions," *Phys. Rev. Lett.* **123**(26), 262301 (2019) doi: 10.1103/PhysRevLett.123.262301 [arXiv:1908.02866 [hep-ph]].

[54] J. P. Blaizot and L. Yan, "Emergence of hydrodynamical behavior in expanding ultra-relativistic plasmas," *Annals Phys.* **412**, 167993 (2020) doi: 10.1016/j.aop.2019.167993 [arXiv:1904.08677 [nucl-th]].

[55] M. Strickland, "The non-equilibrium attractor for kinetic theory in relaxation time approximation," *JHEP* **12**, 128 (2018) doi: 10.1007/JHEP12(2018)128 [arXiv:1809.01200 [nucl-th]].

[56] J. P. Blaizot and L. Yan, "Fluid dynamics of out of equilibrium boost invariant plasmas," *Phys. Lett. B* **780**, 283-286 (2018) doi: 10.1016/j.physletb.2018.02.058 [arXiv:1712.03856 [nucl-th]].

[57] A. Behtash, C. N. Cruz-Camacho and M. Martinez, "Far-from-equilibrium attractors and nonlinear dynamical systems approach to the Gubser flow," *Phys. Rev. D* **97**(4), 044041 (2018) doi: 10.1103/PhysRevD.97.044041 [arXiv:1711.01745 [hep-th]].

[58] C. Shen and S. Alzhrani, "Collision-geometry-based 3D initial condition for relativistic heavy-ion collisions," *Phys. Rev. C* **102**(1), 014909 (2020) doi: 10.1103/PhysRevC.102.014909 [arXiv:2003.05852 [nucl-th]].

[59] A. Bzdak and V. Skokov, "Event-by-event fluctuations of magnetic and electric fields in heavy ion collisions," *Phys. Lett. B* **710**, 171-174 (2012) doi: 10.1016/j.physletb.2012.02.065 [arXiv:1111.1949 [hep-ph]].

[60] W. T. Deng and X. G. Huang, "Event-by-event generation of electromagnetic fields in heavy-ion collisions," *Phys. Rev. C* **85**, 044907 (2012) doi: 10.1103/PhysRevC.85.044907 [arXiv:1201.5108 [nucl-th]].

[61] K. Tuchin, "Particle production in strong electromagnetic fields in relativistic heavy-ion collisions," *Adv. High Energy Phys.* **2013**, 490495 (2013) doi: 10.1155/2013/490495 [arXiv:1301.0099 [hep-ph]].

[62] V. Roy and S. Pu, "Event-by-event distribution of magnetic field energy over initial fluid energy density in $\sqrt{s_{NN}}$= 200 GeV Au-Au collisions," *Phys. Rev. C* **92**, 064902 (2015) doi: 10.1103/PhysRevC.92.064902 [arXiv:1508.03761 [nucl-th]].

48

[63] H. Li, X. l. Sheng and Q. Wang, "Electromagnetic fields with electric and chiral magnetic conductivities in heavy ion collisions," *Phys. Rev. C* **94**, no.4, 044903 (2016) doi: 10.1103/PhysRevC.94.044903 [arXiv:1602.02223 [nucl-th]].

[64] W. T. Deng and X. G. Huang, "Vorticity in Heavy-Ion Collisions," *Phys. Rev. C* **93**, no.6, 064907 (2016) doi: 10.1103/PhysRevC.93.064907 [arXiv:1603.06117 [nucl-th]].

[65] Y. Jiang, Z. W. Lin and J. Liao, "Rotating quark-gluon plasma in relativistic heavy ion collisions," *Phys. Rev. C* **94**, no.4, 044910 (2016) [erratum: *Phys. Rev. C* **95**, no.4, 049904 (2017)] doi: 10.1103/PhysRevC.94.044910 [arXiv:1602.06580 [hep-ph]].

[66] X. Wang, M. Wei, Z. Li and M. Huang, "Quark matter under rotation in the NJL model with vector interaction," *Phys. Rev. D* **99**, no.1, 016018 (2019) doi: 10.1103/PhysRevD.99.016018 [arXiv:1808.01931 [hep-ph]].

[67] A. K. Chaudhuri, "A short course on Relativistic Heavy Ion Collisions," IOPP, 2014, ISBN 978-0-7503-1061-1, 978-0-7503-1060-4 doi: 10.1088/978-0-750-31060-4 [arXiv:1207.7028 [nucl-th]].

[68] U. Heinz and R. Snellings, "Collective flow and viscosity in relativistic heavy-ion collisions," *Ann. Rev. Nucl. Part. Sci.* **63**, 123-151 (2013) doi: 10.1146/annurev-nucl-102212-170540 [arXiv:1301.2826 [nucl-th]].

[69] C. Gale, S. Jeon and B. Schenke, "Hydrodynamic Modeling of Heavy-Ion Collisions," *Int. J. Mod. Phys. A* **28**, 1340011 (2013) doi: 10.1142/S0217751X13400113 [arXiv:1301.5893 [nucl-th]].

[70] P. Romatschke and U. Romatschke, "Relativistic Fluid Dynamics In and Out of Equilibrium," Cambridge University Press, 2019, ISBN 978-1-108-48368-1, 978-1-108-75002-8 doi: 10.1017/9781108651998 [arXiv:1712.05815 [nucl-th]].

[71] H. Song and U. W. Heinz, "Extracting the QGP viscosity from RHIC data - A Status report from viscous hydrodynamics," *J. Phys. G* **36**, 064033 (2009) doi: 10.1088/0954-3899/36/6/064033 [arXiv:0812.4274 [nucl-th]].

[72] C. Gale, S. Jeon, B. Schenke, P. Tribedy and R. Venugopalan, "Event-by-event anisotropic flow in heavy-ion collisions from combined Yang-Mills and viscous fluid dynamics," *Phys. Rev. Lett.* **110**, no.1, 012302 (2013) doi: 10.1103/PhysRevLett.110.012302 [arXiv:1209.6330 [nucl-th]].

[73] Z. W. Lin, C. M. Ko, B. A. Li, B. Zhang and S. Pal, "A Multi-phase transport model for relativistic heavy ion collisions," *Phys. Rev. C* **72**, 064901 (2005) doi: 10.1103/PhysRevC.72.064901 [arXiv:nucl-th/0411110 [nucl-th]].

[74] M. Bleicher, E. Zabrodin, C. Spieles, S. A. Bass, C. Ernst, S. Soff, L. Bravina, M. Belkacem, H. Weber and H. Stoecker, *et al.* "Relativistic hadron hadron collisions in the ultrarelativistic quantum molecular dynamics model," *J. Phys. G* **25**, 1859-1896 (1999) doi: 10.1088/0954-3899/25/9/308 [arXiv:hep-ph/9909407 [hep-ph]].

[75] B. Andersson, G. Gustafson, G. Ingelman and T. Sjostrand, "Parton Fragmentation and String Dynamics," *Phys. Rept.* **97**, 31-145 (1983) doi: 10.1016/0370-1573(83)90080-7.

[76] K. Werner, "Strings, pomerons, and the venus model of hadronic interactions at ultrarelativistic energies," *Phys. Rept.* **232**, 87-299 (1993) doi: 10.1016/0370-1573(93)90078-R.

[77] N. S. Amelin, K. K. Gudima and V. D. Toneev, "Quark - Gluon String Model and Ultrarelativistic Heavy Ion Interactions. (In German)," *Sov. J. Nucl. Phys.* **51**, 327-333 (1990).

[78] H. Sorge, H. Stoecker and W. Greiner, "Poincare Invariant Hamiltonian Dynamics: Modeling Multi - Hadronic Interactions in a Phase Space Approach," *Annals Phys.* **192**, 266-306 (1989) doi: 10.1016/0003-4916(89)90136-X.

[79] M. Gyulassy and X. N. Wang, "HIJING 1.0: A Monte Carlo program for parton and particle production in high-energy hadronic and nuclear collisions," *Comput. Phys. Commun.* **83**, 307 (1994) doi: 10.1016/0010-4655(94)90057-4 [arXiv:nucl-th/9502021 [nucl-th]].

[80] J. Aichelin and H. Stoecker, "Quantum molecular dynamics. A Novel approach to N body correlations in heavy ion collisions," *Phys. Lett. B* **176**, 14-19 (1986) doi: 10.1016/0370-2693(86)90916-0.

[81] K. Geiger, *Phys. Rept.* **258**, 237-376 (1995) doi: 10.1016/0370-1573(95)96931-Z.

[82] F. Gastineau and J. Aichelin, "Hanbury Brown-tTiss correlation functions from event generators: A Reliable approach to determine the size of the emitting source in ultrarelativistic heavy ion collisions?," Phys. Rev. C **65**, 014901 (2002) doi:10.1103/PhysRevC.65.014901 [arXiv:nucl-th/0007049 [nucl-th]].

[83] B. I. Abelev *et al.* [STAR], "Strange baryon resonance production in s(NN)**(1/2) = 200-GeV p+p and Au+Au collisions," *Phys. Rev. Lett.* **97**, 132301 (2006) doi: 10.1103/PhysRevLett.97.132301 [arXiv:nucl-ex/0604019 [nucl-ex]].

[84] S. Acharya *et al.* [ALICE], "Evidence of rescattering effect in Pb-Pb collisions at the LHC through production of $K^*(892)^0$ and $\phi(1020)$ mesons," *Phys. Lett. B* **802**, 135225 (2020) doi: 10.1016/j.physletb.2020.135225 [arXiv:1910.14419 [nucl-ex]].

[85] J. Adams *et al.* [STAR], "K(892)* resonance production in Au+Au and p+p collisions at s(NN)**(1/2) = 200-GeV at STAR," *Phys. Rev. C* **71**, 064902 (2005) doi: 10.1103/PhysRevC.71.064902 [arXiv:nucl-ex/0412019 [nucl-ex]].

[86] L. Adamczyk *et al.* [STAR], "Global Λ hyperon polarization in nuclear collisions: evidence for the most vortical fluid," *Nature* **548**, 62-65 (2017) doi: 10.1038/nature23004 [arXiv:1701.06657 [nucl-ex]].

[87] J. W. Harris and B. Müller, "QGP Signatures" Revisited," [arXiv:2308.05743 [hep-ph]].

[88] B. B. Back *et al.* [PHOBOS], "The PHOBOS perspective on discoveries at RHIC," *Nucl. Phys. A* **757**, 28-101 (2005) doi: 10.1016/j.nuclphysa.2005.03.084 [arXiv:nucl-ex/0410022 [nucl-ex]].

[89] K. Adcox *et al.* [PHENIX], "Formation of dense partonic matter in relativistic nucleus-nucleus collisions at RHIC: Experimental evaluation by the PHENIX collaboration," *Nucl. Phys. A* **757**, 184-283 (2005) doi: 10.1016/j.nuclphysa.2005.03.086 [arXiv:nucl-ex/0410003 [nucl-ex]].

[90] B. Muller, J. Schukraft and B. Wyslouch, "First Results from Pb+Pb collisions at the LHC," *Ann. Rev. Nucl. Part. Sci.* **62**, 361-386 (2012) doi: 10.1146/annurev-nucl-102711-094910 [arXiv:1202.3233 [hep-ex]].

[91] M. Abdallah *et al.* [STAR], "Azimuthal anisotropy measurement of (multi)strange hadrons in Au+Au collisions at $\sqrt{S_{NN}} = 54.4 GeV$," *Phys. Rev. C* **107**, no.2, 024912 (2023) doi: 10.1103/PhysRevC.107.024912 [arXiv:2205.11073 [nucl-ex]].

[92] B. Mohanty, "Exploring the QCD landscape with high-energy nuclear collisions," *New J. Phys.* **13**, 065031 (2011) doi: 10.1088/1367-2630/13/6/065031 [arXiv:1102.2495 [nucl-ex]].

[93] E. Eichten, K. Gottfried, T. Kinoshita, J. B. Kogut, K. D. Lane and T. M. Yan, "The Spectrum of Charmonium," *Phys. Rev. Lett.* **34**, 369-372 (1975) [erratum: *Phys. Rev. Lett.* **36**, 1276 (1976)] doi: 10.1103/PhysRevLett.34.369.

[94] M. C. Abreu *et al.* [NA38], "J / psi, psi-prime and Drell-Yan production in S U interactions at 200-GeV per nucleon," *Phys. Lett. B* **449**, 128-136 (1999) doi: 10.1016/S0370-2693(99)00057-X.

[95] M. C. Abreu *et al.* [NA50], "Evidence for deconfinement of quarks and gluons from the J / psi suppression pattern measured in Pb + Pb collisions at the CERN SPS," *Phys. Lett. B* **477**, 28-36 (2000) doi: 10.1016/S0370-2693(00)00237-9.

[96] A. Jakovac, P. Petreczky, K. Petrov and A. Velytsky, "Quarkonium correlators and spectral functions at zero and finite temperature," *Phys. Rev. D* **75**, 014506 (2007) doi: 10.1103/PhysRevD.75.014506 [arXiv:hep-lat/0611017 [hep-lat]].

[97] P. Petreczky, S. Sharma and J. H. Weber, "Bottomonium melting from screening correlators at high temperature," *Phys. Rev. D* **104**, no.5, 054511 (2021) doi: 10.1103/PhysRevD.104.054511 [arXiv:2107.11368 [hep-lat]].

[98] S. Acharya *et al.* [ALICE], "Measurements of inclusive J/ψ production at midrapidity and forward rapidity in Pb–Pb collisions at sNN = 5.02 TeV," *Phys. Lett. B* **849**, 138451 (2024) doi: 10.1016/j.physletb.2024.138451 [arXiv:2303.13361 [nucl-ex]].

[99] K. Adcox *et al.* [PHENIX], "Suppression of hadrons with large transverse momentum in central Au+Au collisions at $\sqrt{s_{NN}}$ = 130-GeV," *Phys. Rev. Lett.* **88**, 022301 (2002) doi: 10.1103/PhysRevLett.88.022301 [arXiv:nucl-ex/0109003 [nucl-ex]].

[100] C. Adler *et al.* [STAR], "Centrality dependence of high p_T hadron suppression in Au+Au collisions at $\sqrt{s_{NN}}$ = 130-GeV," *Phys. Rev. Lett.* **89**, 202301 (2002) doi: 10.1103/PhysRevLett.89.202301 [arXiv:nucl-ex/0206011 [nucl-ex]].

[101] I. Arsene *et al.* [BRAHMS], "Transverse momentum spectra in Au+Au and d+Au collisions at s**(1/2) = 200-GeV and the pseudorapidity dependence of high p(T) suppression," *Phys. Rev. Lett.* **91**, 072305 (2003) doi: 10.1103/PhysRevLett.91.072305 [arXiv:nucl-ex/0307003 [nucl-ex]].

[102] B. B. Back *et al.* [PHOBOS], "Centrality dependence of charged hadron transverse momentum spectra in Au + Au collisions from s(NN)**(1/2) = 62.4-GeV to 200-GeV," *Phys. Rev. Lett.* **94**, 082304 (2005) doi: 10.1103/PhysRevLett.94.082304 [arXiv:nucl-ex/0405003 [nucl-ex]].

[103] K. Aamodt *et al.* [ALICE], "Suppression of Charged Particle Production at Large Transverse Momentum in Central Pb-Pb Collisions at $\sqrt{s_{NN}} = 2.76$ TeV," *Phys. Lett. B* **696**, 30-39 (2011) doi: 10.1016/j.physletb.2010.12.020 [arXiv:1012.1004 [nucl-ex]].

[104] S. Chatrchyan *et al.* [CMS], "Study of High-pT Charged Particle Suppression in PbPb Compared to *pp* Collisions at $\sqrt{s_{NN}} = 2.76$ TeV," *Eur. Phys. J. C* **72**, 1945 (2012) doi: 10.1140/epjc/s10052-012-1945-x [arXiv:1202.2554 [nucl-ex]].

[105] S. Acharya *et al.* [ALICE], "Prompt D^0, D^+, and D^{*+} production in Pb–Pb collisions at $\sqrt{s_{NN}} = 5.02$ TeV," *JHEP* **01**, 174 (2022) doi: 10.1007/JHEP01(2022)174 [arXiv:2110.09420 [nucl-ex]].

[106] A. M. Sirunyan *et al.* [CMS], "Measurement of prompt and nonprompt charmonium suppression in PbPb collisions at 5.02 TeV," *Eur. Phys. J. C* **78**, no.6, 509 (2018) [erratum: *Eur. Phys. J. C* **83**, 145 (2023)] doi: 10.1140/epjc/s10052-018-5950-6 [arXiv:1712.08959 [nucl-ex]].

[107] S. Acharya *et al.* [ALICE], "Measurement of beauty-strange meson production in Pb–Pb collisions at sNN=5.02TeV via non-prompt Ds+ mesons," *Phys. Lett. B* **846**, 137561 (2023) doi: 10.1016/j.physletb.2022.137561 [arXiv:2204.10386 [nucl-ex]].

[108] A. Tumasyan *et al.* [CMS], "Observation of Bs0 mesons and measurement of the Bs0/B+ yield ratio in PbPb collisions at Image 1 TeV," *Phys. Lett. B* **829**, 137062 (2022) doi: 10.1016/j.physletb.2022.137062 [arXiv:2109.01908 [hep-ex]].

[109] J. Rafelski, "Formation and Observables of the Quark-Gluon Plasma," *Phys. Rept.* **88**, 331 (1982) UFTP-80-1982.

[110] J. Rafelski and B. Muller, "Strangeness Production in the Quark - Gluon Plasma," *Phys. Rev. Lett.* **48**, 1066 (1982) [erratum: *Phys. Rev. Lett.* **56**, 2334 (1986)] doi: 10.1103/PhysRevLett.48.1066.

[111] E. Andersen *et al.* [WA97], "Strangeness enhancement at mid-rapidity in Pb Pb collisions at 158-A-GeV/c," *Phys. Lett. B* **449**, 401-406 (1999) doi: 10.1016/S0370-2693(99)00140-9.

[112] F. Antinori *et al.* [NA57], "Enhancement of hyperon production at central rapidity in 158-A-GeV/c Pb-Pb collisions," *J. Phys. G* **32**, 427-442 (2006) doi: 10.1088/0954-3899/32/4/003 [arXiv:nucl-ex/0601021 [nucl-ex]].

[113] B. I. Abelev *et al.* [STAR], "Enhanced strange baryon production in Au + Au collisions compared to p + p at s(NN)**(1/2) = 200-GeV," *Phys. Rev. C* **77**, 044908 (2008) doi: 10.1103/PhysRevC.77.044908 [arXiv:0705.2511 [nucl-ex]].

[114] J. Adam *et al.* [ALICE], "Enhanced production of multi-strange hadrons in high-multiplicity proton-proton collisions," *Nature Phys.* **13**, 535-539 (2017) doi: 10.1038/nphys4111 [arXiv:1606.07424 [nucl-ex]].

[115] J. Adam *et al.* [ALICE], "Direct photon production in Pb-Pb collisions at $\sqrt{s_{NN}} =$ 2.76 TeV," *Phys. Lett. B* **754**, 235-248 (2016) doi: 10.1016/j.physletb.2016.01.020 [arXiv:1509.07324 [nucl-ex]].

[116] H. van Hees, M. He and R. Rapp, "Pseudo-critical enhancement of thermal photons in relativistic heavy-ion collisions?," *Nucl. Phys. A* **933**, 256-271 (2015) doi: 10.1016/j.nuclphysa.2014.09.009 [arXiv:1404.2846 [nucl-th]].

[117] J. F. Paquet, C. Shen, G. S. Denicol, M. Luzum, B. Schenke, S. Jeon and C. Gale, "Production of photons in relativistic heavy-ion collisions," *Phys. Rev. C* **93**, no.4, 044906 (2016) doi: 10.1103/PhysRevC.93.044906 [arXiv:1509.06738 [hep-ph]].

[118] J. F. Paquet and S. A. Bass, "Electromagnetic measurement of the temperature of quark-gluon plasma produced in central ultrarelativistic nuclear collisions," [arXiv:2205.12299 [nucl-th]].

[119] V. Khachatryan *et al.* [CMS], "Observation of Long-Range Near-Side Angular Correlations in Proton-Proton Collisions at the LHC," *JHEP* **09**, 091 (2010) doi: 10.1007/JHEP09(2010)091 [arXiv:1009.4122 [hep-ex]].

[120] G. Aad *et al.* [ATLAS], "Observation of Long-Range Elliptic Azimuthal Anisotropies in $\sqrt{s}$ =13 and 2.76 TeV *pp* Collisions with the ATLAS Detector,"

Phys. Rev. Lett. **116**, no.17, 172301 (2016) doi: 10.1103/PhysRevLett.116.172301 [arXiv:1509.04776 [hep-ex]].

[121] V. Khachatryan *et al.* [CMS], "Measurement of long-range near-side two-particle angular correlations in pp collisions at $\sqrt{s} = 13$ TeV," *Phys. Rev. Lett.* **116**, no.17, 172302 (2016) doi: 10.1103/PhysRevLett.116.172302 [arXiv:1510.03068 [nucl-ex]].

[122] B. Abelev *et al.* [ALICE], "Long-range angular correlations on the near and away side in p-Pb collisions at $\sqrt{s_{NN}} = 5.02$ TeV," *Phys. Lett. B* **719**, 29-41 (2013) doi: 10.1016/j.physletb.2013.01.012 [arXiv:1212.2001 [nucl-ex]].

[123] G. Aad *et al.* [ATLAS], Phys. Rev. Lett. **110**, no.18, 182302 (2013) doi:10.1103/PhysRevLett.110.182302 [arXiv:1212.5198 [hep-ex]].

[124] S. Chatrchyan *et al.* [CMS], Phys. Lett. B **718**, 795-814 (2013) doi:10.1016/j.physletb.2012.11.025 [arXiv:1210.5482 [nucl-ex]].

[125] V. Khachatryan *et al.* [CMS], Phys. Rev. Lett. **115**, no.1, 012301 (2015) doi:10.1103/PhysRevLett.115.012301 [arXiv:1502.05382 [nucl-ex]].

[126] C. Aidala *et al.* [PHENIX], Nature Phys. **15**, no.3, 214-220 (2019) doi:10.1038/s41567-018-0360-0 [arXiv:1805.02973 [nucl-ex]].

[127] J. L. Nagle and W. A. Zajc, Ann. Rev. Nucl. Part. Sci. **68**, 211-235 (2018) doi:10.1146/annurev-nucl-101916-123209 [arXiv:1801.03477 [nucl-ex]].

[128] R. D. Weller and P. Romatschke, "One fluid to rule them all: viscous hydrodynamic description of event-by-event central p+p, p+Pb and Pb+Pb collisions at $\sqrt{s} = 5.02$ TeV," *Phys. Lett. B* **774**, 351-356 (2017) doi: 10.1016/j.physletb.2017.09.077 [arXiv:1701.07145 [nucl-th]].

[129] X. G. Huang, "Electromagnetic fields and anomalous transports in heavy-ion collisions — A pedagogical review," Rept. Prog. Phys. **79**, no.7, 076302 (2016) doi:10.1088/0034-4885/79/7/076302 [arXiv:1509.04073 [nucl-th]].

[130] V. Roy, S. Pu, L. Rezzolla and D. H. Rischke, "Effect of intense magnetic fields on reduced-MHD evolution in $\sqrt{s_{\mathrm{NN}}}$ = 200 GeV Au+Au collisions," Phys. Rev. C **96**, no.5, 054909 (2017) doi:10.1103/PhysRevC.96.054909 [arXiv:1706.05326 [nucl-th]].

[131] M. I. Abdulhamid *et al.* [STAR], "Observation of the electromagnetic field effect via charge-dependent directed flow in heavy-ion collisions at the Relativistic Heavy Ion Collider," Phys. Rev. X **14**, no. 1, 011028 (2024) doi:10.1103/PhysRevX.14.011028 [arXiv:2304.03430 [nucl-ex]].

[132] M. Abdallah *et al.* [STAR], "Search for the chiral magnetic effect with isobar collisions at $\sqrt{s_{NN}}$=200 GeV by the STAR Collaboration at the BNL Relativistic Heavy Ion Collider," Phys. Rev. C **105**, no. 1, 014901 (2022) doi:10.1103/PhysRevC.105.014901 [arXiv:2109.00131 [nucl-ex]].

[133] C. Zhang [STAR], "An overview of new measurements of flow, chirality and vorticity from STAR experiment," Int. J. Mod. Phys. E **32**, no. 11, 2341001 (2023) doi:10.1142/S021830132341001X [arXiv:2203.13106 [nucl-ex]].

[134] W. Israel and J. M. Stewart, "Transient relativistic thermodynamics and kinetic theory," Annals Phys. **118**, 341-372 (1979) doi: 10.1016/0003-4916(79)90130-1

[135] H. Grad, "On the kinetic theory of rarefied gases," Commun. Pure Appl. Math. **2**, no. 4, 331-407 (1949) doi: 10.1002/cpa.3160020403

[136] W. Israel, "Nonstationary irreversible thermodynamics: A Causal relativistic theory," Annals Phys. **100**, 310-331 (1976) doi: 10.1016/0003-4916(76)90064-6

[137] P. Kovtun, D. T. Son and A. O. Starinets, "Viscosity in strongly interacting quantum field theories from black hole physics," Phys. Rev. Lett. **94**, 111601 (2005) doi:10.1103/PhysRevLett.94.111601 [arXiv:hep-th/0405231 [hep-th]].

[138] J. E. Bernhard, J. S. Moreland and S. A. Bass, "Bayesian estimation of the specific shear and bulk viscosity of quark–gluon plasma," Nature Phys. **15**, no.11, 1113-1117 (2019) doi:10.1038/s41567-019-0611-8

[139] Cercignani, Carlo, The Boltzmann equation and its applications, doi=10.1007/978-1-4612-1039-9,

[140] P. L. Bhatnagar, E. P. Gross and M. Krook, "A Model for Collision Processes in Gases. 1. Small Amplitude Processes in Charged and Neutral One-Component Systems," Phys. Rev. **94**, 511-525 (1954) doi:10.1103/PhysRev.94.511.

[141] R. L. Anderson and B. R. Ikenberry, "A relativistic relaxation-time model for the Boltzmann equation," Physica **74**, 466-488 (1974) doi:10.1016/0031-8914(74)90355-3.

[142] Charles-Michel Marle, "Sur l'établissement des équations de l'hydrodynamique des fluides relativistes dissipatifs. I. — L'équation de Boltzmann relativiste," Annales De L Institut Henri Poincare-physique Theorique **10**, 67-126 (1969) url: `https://api.semanticscholar.org/CorpusID:124097847`.

[143] B. Betz, D. Henkel, and D. H. Rischke, "From kinetic theory to dissipative fluid dynamics," *Prog. Part. Nucl. Phys.* **62**, 556-561 (2009), doi: 10.1016/j.ppnp.2008.12.018 [arXiv:0812.1440 [nucl-th]].

[144] G. S. Denicol, T. Koide, and D. H. Rischke, "Dissipative relativistic fluid dynamics: a new way to derive the equations of motion from kinetic theory," *Phys. Rev. Lett.* **105**, 162501 (2010), doi: 10.1103/PhysRevLett.105.162501 [arXiv:1004.5013 [nucl-th]].

[145] A. Muronga, "Relativistic Dynamics of Non-ideal Fluids: Viscous and heat-conducting fluids. II. Transport properties and microscopic description of relativistic nuclear matter," *Phys. Rev. C* **76**, 014910 (2007), doi: 10.1103/PhysRevC.76.014910 [arXiv:nucl-th/0611091 [nucl-th]].

[146] G. S. Denicol, H. Niemi, E. Molnar, and D. H. Rischke, "Derivation of transient relativistic fluid dynamics from the Boltzmann equation," *Phys. Rev. D* **85**, 114047 (2012), doi: 10.1103/PhysRevD.85.114047 [arXiv:1202.4551 [nucl-th]].

[147] G. S. Denicol, E. Molnár, H. Niemi, and D. H. Rischke, "Derivation of fluid dynamics from kinetic theory with the 14-moment approximation," *Eur. Phys. J. A* **48**, 170 (2012), doi: 10.1140/epja/i2012-12170-x [arXiv:1206.1554 [nucl-th]].

[148] B. Betz, D. Henkel, and D. H. Rischke, "Complete second-order dissipative fluid dynamics," *J. Phys. G* **36**, 064029 (2009), doi: 10.1088/0954-3899/36/6/064029.

[149] M. A. York and G. D. Moore, "Second order hydrodynamic coefficients from kinetic theory," *Phys. Rev. D* **79**, 054011 (2009), doi: 10.1103/PhysRevD.79.054011 [arXiv:0811.0729 [hep-ph]].

[150] A. Jaiswal, R. S. Bhalerao, and S. Pal, "New relativistic dissipative fluid dynamics from kinetic theory," *Phys. Lett. B* **720**, 347-351 (2013), doi: 10.1016/j.physletb.2013.02.025 [arXiv:1204.3779 [nucl-th]].

[151] A. Jaiswal, "Relativistic dissipative hydrodynamics from kinetic theory with relaxation time approximation," *Phys. Rev. C* **87**, no.5, 051901 (2013), doi: 10.1103/PhysRevC.87.051901 [arXiv:1302.6311 [nucl-th]].

[152] W. Florkowski and R. Ryblewski, "Highly-anisotropic and strongly-dissipative hydrodynamics for early stages of relativistic heavy-ion collisions," *Phys. Rev. C* **83**, 034907 (2011), doi: 10.1103/PhysRevC.83.034907 [arXiv:1007.0130 [nucl-th]].

[153] G. S. Denicol, X. G. Huang, E. Molnár, G. M. Monteiro, H. Niemi, J. Noronha, D. H. Rischke, and Q. Wang, "Nonresistive dissipative magnetohydrodynamics from the Boltzmann equation in the 14-moment approximation," *Phys. Rev. D* **98**, no.7, 076009 (2018), doi: 10.1103/PhysRevD.98.076009 [arXiv:1804.05210 [nucl-th]].

[154] G. S. Denicol, E. Molnár, H. Niemi, and D. H. Rischke, "Resistive dissipative magnetohydrodynamics from the Boltzmann-Vlasov equation," *Phys. Rev. D* **99**, no.5, 056017 (2019), doi: 10.1103/PhysRevD.99.056017 [arXiv:1902.01699 [nucl-th]].

Chapter 2

Revisiting Theoretical Frameworks: From Macroscopic to Microscopic

The two main theories we focus on are fluid dynamics and kinetic theory. Fluid dynamics encompasses the study of fluid motion and behavior, from blood flow in the human circulatory system to the collective dynamics of fundamental particles like quarks and gluons forming Quark-Gluon Plasma (QGP). Fundamentally, fluid dynamics relies on conservation laws and the Navier-Stokes equation to describe fluid motion. At the same time, its relativistic counterpart incorporates special relativity principles and is governed by the conservation of the energy-momentum tensor and charge current. On the other hand, relativistic kinetic theory offers a robust statistical framework in which the macroscopic quantities are expressed in terms of single-particle distribution function. At its core lies the relativistic Boltzmann equation, which dictates the evolution of the distribution function of particles in phase space.

This chapter is organized as follows: firstly, we delve into the mathematical construct of the macroscopic theory, specifically the relativistic version of fluid dynamics in Section.(2.1). Building upon our previous discussion on the intense magnetic field generation in the chapter.(1), we briefly introduce the concept of relativistic magnetohydrodynamics in Section.(2.2). Lastly, in Section.(2.3), we talk about the relativistic kinetic theory, setting the stage for its application in the subsequent chapters of the current thesis.

2.1 Relativistic Hydrodynamics

Our current understanding of fluid dynamics relies heavily on the concept of scales. Fluid dynamics, or hydrodynamics, operates on effectively long wavelengths (that is at large length scales), assuming a collective behavior of the fluid. This collective behavior can be quantified by a dimensionless quantity represented by the ratio of two length scales: one microscopic and another macroscopic. If this ratio, denoted as Knudsen number $=$ $\frac{\text{microscopic scale}}{\text{macroscopic scale}}$, is less than 1, fluid dynamics provides a reasonable description. In this section, we commence with a review of the mathematical formulation of ideal (non-dissipative) and dissipative relativistic hydrodynamics [1].

2.1.1 Ideal Hydrodynamics

In a relativistic framework, energy and momentum are encapsulated within the energy-momentum tensor $T^{\mu\nu}$, which represents a system's response to perturbations in the metric tensor $g^{\mu\nu}$. Classical fluid dynamics, in the absence of thermal fluctuations, constructs the energy-momentum tensor at leading order (ideal case) from a rank-one timelike tensor u^{μ} and a rank-two tensor $g^{\mu\nu}$, where u^{μ} denotes the fluid four-velocity. These tensors are the only available constructs for such construction with u^{μ} and $g^{\mu\nu}$ taking arbitrarily any form and are quite general. By applying a suitable Lorentz boost, the equilibrium energy-momentum tensor can be transformed into the local rest frame (LRF), characterized by $u^{\mu} = (1, \mathbf{0})$. In this frame, $T^{\mu\nu}$ takes the following form:

$$T^{\mu\nu} = \begin{pmatrix} \epsilon & 0 & 0 & 0 \\ 0 & \mathrm{P} & 0 & 0 \\ 0 & 0 & \mathrm{P} & 0 \\ 0 & 0 & 0 & \mathrm{P} \end{pmatrix}. \tag{2.1}$$

Where:

- $T^{00} = \epsilon$, represents the energy density of the fluid.

- T^{0i} where i = (1,2,3), represents the momentum density.

- T^{i0} where i= (1,2,3), represents the energy flux.

- T^{ii} = P, with i not summed over, represents the Pressure.

- T^{ij} where i $\neq$ j is shear stress.

In an arbitrary frame with four-velocity, $u^\mu = \gamma(1, v)$, the general form of the energy-momentum tensor in the case of an ideal fluid is given by:

$$T^{\mu\nu}_{(0)} = (\epsilon + P)u^\mu u^\nu - P g^{\mu\nu}. \tag{2.2}$$

In this context, the subscript '0' signifies the 0$^{\text{th}}$-order in gradient expansion. Also 'In equilibrium' indicates a state of local thermal equilibrium, implying dependence of all the thermodynamic variables on both space and time ($x^\mu = (t, x, y, z)$). Both ϵ and P denote quantities in the local rest frame of the fluid, where the observer moves with the fluid, and are also time- and position-dependent functions. Consequently, the space-time evolution of the ideal fluid adheres to the conservation equations of energy and momentum given as:

$$\partial_\mu T^{\mu\nu}_{(0)} = 0. \tag{2.3}$$

Additionally, the conservation of net charges, such as baryon, strangeness, and electric charges, follows the conservation equation for the particle four-current:

$$\partial_\mu N^\mu_{j(0)} = 0, \quad j = 1, 2, 3. \tag{2.4}$$

In this representation, the zeroth component N^0 symbolizes the net number density n whereas the remaining three components N^i_j ($i = 1, 2, 3$) represent the respective current carried by the jth particle, where the subscript 'j' denotes various conserved charges. Hence for an ideal fluid in local thermal equilibrium, the quantities $T^{\mu\nu}$ and N^μ take the following form:

$$T^{\mu\nu}_{(0)} = (\epsilon(x) + P(x)) u^\mu u^\nu - P(x) g^{\mu\nu}, \tag{2.5}$$

$$N^\mu_{(0)} = n u^\mu. \tag{2.6}$$

Counting the number of equations, we find 5 conservation equations (4 from the conserva-tion of energy-momentum tensor and 1 from the net particle number conservation equation), but the number of unknowns is six: $\epsilon(x)$, $P(x)$, $n(x)$, and the three components of u^μ (three because $u^\mu u_\mu = 1$ is a constraint). Therefore, we need one additional constraint to close the equation, which comes from the equation of state, relating the pressure, energy density, and number density, given as $P(x) = f(\epsilon(x), n(x))$.

To gain physical insight from the conservation equations, we introduce the spatial pro-jector operator $\Delta^\mu_\nu = (g^\mu_\nu - u^\mu u_\nu)$. The operator Δ^μ_ν is orthogonal to the fluid four-velocity u^μ, that is $\Delta^\mu_\nu u^\nu = 0$. Projecting out the component along the direction of the fluid velocity, we obtain:

$$u_\nu \partial_\mu T^{\mu\nu}_{(0)} = 0 \Rightarrow D\epsilon + (\epsilon + P)\partial_\mu u^\mu = 0, \tag{2.7}$$

where $D = u^\mu \partial_\mu$. Next, projecting the conservation equation along the direction perpen-dicular to the fluid velocity gives us:

$$\Delta^\alpha_\nu \partial_\mu T^{\mu\nu}_{(0)} = 0 \Rightarrow (\epsilon + P)u^\mu \partial_\mu u^\alpha - \Delta^{\mu\alpha}\partial_\mu P = 0 \Rightarrow (\epsilon + P)Du^\alpha - \nabla^\alpha P = 0, \tag{2.8}$$

where $\nabla^\alpha = \Delta^{\mu\alpha}\partial_\mu$. Eq.(2.7) and Eq.(2.8) are the relativistic versions of the continuity and Euler equations respectively. In the non-relativistic limit ($v \ll c$), D and ∇^α essentially reduce to time and space derivatives, and the energy density ϵ closely approximates the mass density (ρ) as $\epsilon \approx \rho$, neglecting the kinetic terms. Thus, the relativistic conservation equation in the non-relativistic limit simplifies to the following conservation of mass and Euler equations:

$$\partial_t \rho + \nabla \cdot (\rho \mathbf{v}) = 0, \tag{2.9}$$

$$\partial_t \mathbf{v} + \mathbf{v} \cdot \nabla \mathbf{v} = -\frac{1}{\rho}\nabla P. \tag{2.10}$$

These equations are quite well-known and are widely used.

Again, recalling the first law of thermodynamics (as discussed previously in chapter 1), we have:

$$dQ = dU + PdV - \mu dN, \tag{2.11}$$

where dQ represents the amount of heat change in the system, which can alternatively be expressed as TdS, with T denoting the temperature and dS the change in entropy of the system. Here, dU signifies the change in internal energy, dV the change in volume, P the pressure, μ the chemical potential, and dN the change in number of particles in the system. Dividing the above equation by volume yields:

$$ds = \beta du + \beta P \frac{dV}{V} - \alpha dn, \tag{2.12}$$

where $ds = dS/V$ denotes the entropy density, $\beta = \frac{1}{T}$, $du = dU/V$ represents the internal energy density, $\alpha = \frac{\mu}{T}$, and $dn = dN/V$ signifies the number density. The covariant generalization of the above equation is written as:

$$dS^\mu_{(0)} = \beta^\nu dT^\mu_{\nu(0)} - \alpha dN^\mu_{(0)}. \tag{2.13}$$

Here, the subscript '0' denotes equilibrium conditions. Also, note that thermodynamic analysis is typically conducted under equilibrium or very close to equilibrium conditions. Rewriting Eq.(2.13) in terms of partial derivatives we have:

$$\partial_\mu S^\mu_{(0)} = \beta^\nu \partial_\mu T^\mu_{\nu(0)} - \alpha \partial_\mu N^\mu_{(0)}. \tag{2.14}$$

Given the conditions $\partial_\mu T^{\mu\nu}_{(0)} = 0$ and $\partial_\mu N^\mu_{(0)} = 0$, we arrive at:

$$\partial_\mu S^\mu_{(0)} = 0. \tag{2.15}$$

This equation represents the second law of thermodynamics, showing that no entropy is produced when the system is in equilibrium.

2.1.2 Viscous Hydrodynamics

In the previous section, we explored the ideal hydrodynamics formulation. However, reality often deviates from these ideal conditions. Dissipative effects in a fluid stem from irreversible thermodynamic processes occurring during fluid motion. Typically, individual fluid elements may not be in complete equilibrium with the entire fluid body. To approach equilibrium, they exchange heat with their surroundings or may dissipate energy through friction during their relative motion with the surroundings. Accounting for all these phenomena is essential for constructing a realistic description of a relativistic fluid. Mathematically we can write $T^{\mu\nu}$ and N^μ taking all the dissipative effects into account as follows:

$$T^{\mu\nu} = T^{\mu\nu}_{(0)} + \Pi^{\mu\nu} = \epsilon u^\mu u^\nu - P\Delta^{\mu\nu} + \Pi^{\mu\nu}, \tag{2.16}$$

$$N^\mu = N^\mu_{(0)} + V^\mu = n u^\mu + V^\mu, \tag{2.17}$$

where the additional terms arise due to the inclusion of dissipative effects (which can contain any order of force gradient terms). The term encompassing all the dissipative contributions in the energy-momentum tensor is denoted by $\Pi^{\mu\nu}$, and in the number current, it is denoted by V^μ. Moving forward we need to decompose the $\Pi^{\mu\nu}$ into scalars, vectors, and tensors so we use the following projection operator to do it. That is

$$\Delta^{\mu\nu}_{\alpha\beta} = \frac{1}{2}\left(\Delta^\mu_\alpha \Delta^\nu_\beta + \Delta^\mu_\beta \Delta^\nu_\alpha - \frac{2}{3}\Delta^{\mu\nu}\Delta_{\alpha\beta}\right), \tag{2.18}$$

which is orthogonal to both u^μ and $\Delta^{\mu\nu}$. Now we can write the full $\Pi^{\mu\nu}$ only in terms of the available irreducible tensors u^μ, $\Delta^{\mu\nu}$ and the above mentioned $\Delta^{\mu\nu}_{\alpha\beta}$. This reads as:

$$\Pi^{\mu\nu} = -\Pi\Delta^{\mu\nu} + 2u^{(\mu}h^{\nu)} + \pi^{\mu\nu}, \tag{2.19}$$

where Π is bulk viscous pressure, h^μ is heat current and $\pi^{\mu\nu}$ is shear viscous pressure and are defined as:

$$\Pi \equiv -\frac{1}{3}\Delta_{\alpha\beta}\Pi^{\alpha\beta},$$

$$h^\mu \equiv \Delta_\alpha^\mu u_\beta \Pi^{\alpha\beta},$$

$$\pi^{\mu\nu} \equiv \Delta_{\alpha\beta}^{\mu\nu}\Pi^{\alpha\beta}.$$

The term $u^{(\mu}h^{\nu)}$ represents the following symmetric form $(u^\mu h^\nu + u^\nu h^\mu)/2$. Also V^μ can be indicated as diffusion current with $V^\mu = \Delta_\alpha^\mu N^\alpha$. With this, we again do a counting of variables and the number of independent components available. We know that $T^{\mu\nu}$ constitutes a symmetric second-rank tensor with ten independent components, while N^μ represents a four-vector, resulting in a total of fourteen independent components. Upon examining the tensor decompositions of $T^{\mu\nu}$ and N^μ, we recognize that V^μ and h^μ, being orthogonal to u^μ, possess only three independent components each. The shear-stress tensor $\pi^{\mu\nu}$, symmetric, traceless, and orthogonal to u^μ, inherently harbors five independent components. Alongside u^μ, ϵ, n, and Π, totaling six independent components (where pressure P is related with ϵ through the equation of state), we thus have a total sum of seventeen independent components, surpassing the anticipated count by three. This can be solved by defining our velocity four-vector or in short by a frame definition.

So far, the hydrodynamic four-velocity u^μ has been left unspecified. By choosing a suitable frame for u^μ, it becomes possible to define important macroscopic properties such as energy density, number density, heat flow, and entropy density for any fluid. Two widely used definitions of u^μ originate from the formulations of Eckart and Landau-Lifshitz [2, 3, 4]. Under the Eckart definition, u^μ aligns with the particle four-flow N^μ, expressed as:

$$u^\mu \equiv \frac{N^\mu}{\sqrt{N_\nu N^\nu}}. \tag{2.20}$$

In the local rest frame of the fluid, it's observed that the spatial component of N^μ becomes zero. On the contrary, Landau-Lifshitz's approach aligns u^μ with the energy flow, expressed

as:

$$u^\mu \equiv \frac{T_\nu^\mu u^\nu}{\sqrt{u_\alpha T^{\alpha\beta} T_{\beta\gamma} u^\gamma}}. \tag{2.21}$$

When projecting $T^{\mu\nu} u_\nu$ with the projection operator, we obtain:

$$\Delta_\mu^\sigma T^{\mu\nu} u_\nu = 0. \tag{2.22}$$

As a result, the energy flow vanishes in the local rest frame of the fluid element, indicating $h^\mu \equiv 0$ in this frame. Essentially, in the Landau-Lifshitz frame, we observe a non-vanishing diffusion current V^μ alongside a vanishing heat current h^μ, whereas the reverse occurs in the Eckart frame. By making this selection, we ensure consistency with the required and available number of independent components, which is 14. Therefore, for the remainder of the thesis, we will exclusively adopt the Landau frame choice.

First-Order Theory for Viscous Hydrodynamics

As mentioned earlier, ideal hydrodynamics represents a zeroth-order gradient expansion. However, accounting for dissipative effects involves incorporating terms that are gradients of known hydrodynamic variables such as u^μ and T. Here, first-order refers to the inclusion of terms up to the first-order in the gradient expansion of the above-mentioned fluid variables. In the presence of dissipation, entropy production occurs, denoted by $\partial_\mu S^\mu \neq 0$. By generalizing the entropy current, we can express it in the following form:

$$S^\mu = P\beta^\mu + \beta_\nu T_\nu^\mu - \alpha N^\mu. \tag{2.23}$$

Here, $\alpha = \frac{\mu}{T}$, where T represents the local temperature of the system and μ denotes the chemical potential. Additionally, $\beta^\nu = \frac{u^\nu}{T}$, and $T^{\mu\nu}$ along with N^μ include both equilibrium and dissipative terms. Now taking the derivative of Eq.(2.23) and by using the relations given in Eq.(2.16) and (2.17) with a bit of manipulation we get:

$$\partial_\mu S^\mu = -\beta\Pi\theta - V_\mu\nabla^\mu\alpha + \beta\pi^{\mu\nu}\sigma_{\mu\nu}, \tag{2.24}$$

69

where Π is bulk viscous pressure, $\theta = \partial_\mu u^\mu$ which is the expansion scaler, V_μ is the diffusion current, $\beta = 1/T$ is the inverse temperature, $\sigma^{\mu\nu} = \Delta^{\mu\nu}_{\alpha\beta}\nabla^\alpha u^\beta$ is the symmetric, tranceless second-rank tensor corresponding to shear stress. Eq. (2.24) must satisfy the inequality condition $\partial_\mu S^\mu \geq 0$, stemming from the second law of thermodynamics. To ensure this, each component on the right-hand side of Eq. (2.24) should be positive definite. We can achieve this by expressing both the viscous pressures and diffusion current as follows:

$$\Pi = -\zeta\theta, \tag{2.25}$$

$$V^\mu = \kappa\nabla^\mu\alpha, \tag{2.26}$$

$$\pi^{\mu\nu} = 2\eta\sigma^{\mu\nu}, \tag{2.27}$$

where ζ, κ, and η are the coefficients of bulk, diffusion, and shear viscosity, respectively. Putting all these back into the Eq.(2.24) we get:

$$\partial_\mu S^\mu = \beta\zeta\Pi^2 - \frac{1}{\kappa}V_\mu V^\mu + \frac{\beta}{2\eta}\pi_{\mu\nu}\pi^{\mu\nu}. \tag{2.28}$$

Let us note that provided $\partial_\mu S^\mu$ is positive definite, the first term on the right-hand side of Eq. (2.28) should be positive with β and ζ being positive. The third term also requires η to be positive. However, in the second term, κ is positive, and the negative sign here is typically taken care of by the fact that the diffusion current (V^μ) is a space-like vector by construction. Thus, in short, ensuring positive definite entropy production requires that all transport coefficients be positive, which imposes a constraint on the range of values that they can take. The equations mentioned in Eq.(2.25), (2.26) and (2.27) represent the relativistic version of the Navier-Stokes relations. It is well known that in relativistic theory, the requirement that no signal should travel faster than the speed of light imposes an additional constraint. Consequently, to check this, we conduct a linear analysis of the aforementioned relations. Let's consider a small perturbation in the fluid's energy density and velocity from

an initial state of equilibrium and rest that is:

$$\epsilon = \epsilon_0 + \delta\epsilon(x, t), \tag{2.29}$$

$$u^\mu = (1, \mathbf{0}) + \delta u^\mu(x, t). \tag{2.30}$$

Here, ϵ_0 represents the equilibrium energy density, and $(1, \mathbf{0})$ denotes the unperturbed flow velocity with perturbations introduced through $\delta\epsilon$ and δu^μ. Considering the perturbations are of the form of plane waves that is $\delta\epsilon(x) = \delta\epsilon(k)e^{ik\cdot x}$ and similarly for δu^μ, we get a dispersion relation which gives a relation:

$$\omega \propto k^2, \tag{2.31}$$

where ω is the '0th' component of the four wave-vector k^μ and $\mathbf{k}$ is the spatial part of the four wave-vector with $|\mathbf{k}| = k$. Examining the group velocity derived from this dispersion relation, we find:

$$v_g(k) = \frac{d\omega}{dk} \propto k. \tag{2.32}$$

It's evident that the group velocity is unbounded. As the wave vector k approaches infinity, the group velocity also tends to infinity, which contradicts the principles of relativity. To address this, a causal theory is necessary. Thus, one turns to a higher-order derivative expansion initially proposed by Israel and Stewart [5, 6, 7]. Other formulations have also been proposed [8, 9, 10], but we will mainly focus on the Israel-Stewart-like causal theory formulation.

Israel-Stewart second-order causal theory

Israel and Stewart's development of a causal theory also relied on the notion of formulating the entropy four-current comprehensively, encompassing all primary fluid variables and incorporating dissipative currents. Thus, we express the generalized form of Eq.(2.23) as

follows [5, 11]:

$$S^\mu = P\beta^\mu + \beta_\nu T^{\mu\nu} - \alpha N^\mu - Q^\mu(\delta N^\mu, \delta T^{\mu\nu}), \tag{2.33}$$

where in Q^μ contains all the dissipative effects, with $\delta N^\mu = N^\mu - N_{(0)}^\mu$ and $\delta T^{\mu\nu} = T^{\mu\nu} - T_{(0)}^{\mu\nu}$. Utilizing Eqs.(2.16) and (2.17) in Eq.(2.33) and truncating up to the second-order in the derivative expansion we get:

$$\begin{aligned}
S^\mu &= su^\mu - \kappa V^\mu - \left(\beta_0\Pi^2 - \beta_1 V_\nu V^\nu + \beta_2\pi^{\alpha\beta}\pi_{\alpha\beta}\right)\frac{u^\mu}{2T} \\
&\quad - (\alpha_0\Pi\Delta^{\mu\nu} + \alpha_1\pi^{\mu\nu})\frac{V_\nu}{T} + O(\delta^3).
\end{aligned} \tag{2.34}$$

The α_i's and β_i's are complicated functions of temperature and chemical potential, often referred to as coupling terms. The β_i's represent diagonal coupling coefficients, indicating the coupling between dissipative stresses (bulk-bulk, shear-shear, diffusion-diffusion), while the α_i's denote cross-coupling coefficients between dissipative stresses and diffusion currents (bulk-diffusion and shear-diffusion). Upon differentiation of the aforementioned equation, we can get the form of $\partial_\mu S^\mu$ as shown in [5].

Ensuring $\partial_\mu S^\mu \geq 0$ according to the second law of thermodynamics, we thus get all the evolution equations for the dissipative stresses (bulk, shear, diffusion) which is given as:

$$\Pi = -\frac{1}{3}\zeta\left(\partial_\mu u^\mu + \beta_0\dot{\Pi} - \alpha_0\partial_\mu q^\mu\right), \tag{2.35}$$

$$q^\mu = \kappa T\Delta^{\mu\lambda}\left[(\partial_\lambda\alpha)nT/(\epsilon + P) - \beta_1\dot{q}_\lambda + \alpha_0\partial_\lambda\Pi + \alpha_1\partial_\nu\pi_\lambda^\nu\right], \tag{2.36}$$

$$\pi_{\mu\nu} = 2\eta\left(\nabla_{<\mu}u_{\nu>} - \beta_2\dot{\pi}_{\mu\nu} + \alpha_1\nabla_{<\mu}q_{\nu>}\right). \tag{2.37}$$

where spatial vector $q^\mu = h^\mu + \frac{V^\mu(\epsilon+P)}{n}$ (in Landau frame h^μ=0). $\dot{A}$ is just a different notation for DA that is mentioned above, where A can be any arbitrary quantity. The above set of equations are relaxation-type equations, implying that there is no instantaneous signal propagation but rather a delay achieved by relaxation times thus taking into account the causality issue posed at the leading order. It's worth noting that all the unknown β_i's should

be related to the relaxation time to ensure dimensional consistency and they do so in the following manner:

$$\tau_\Pi = \zeta\beta_0/3,$$

$$\tau_n = \kappa T\beta_1,$$

$$\tau_\pi = 2\eta\beta_2.$$

All the above relaxation times $\tau_\Pi, \tau_n, \tau_\pi$ are necessarily positive. With this, we now move on to the macroscopic relativistic magnetohydrodynamics formulation.

2.2 Relativistic MHD

Given our primary objective of investigating the influence of magnetic fields in heavy-ion collisions, it is evident that relativistic magnetohydrodynamics provides the most suitable theoretical framework for our study. To commence, let us present a textbook-style introduction to the relativistically covariant formulation of electrodynamics. Without sacrificing generality, we can define the second-rank antisymmetric electromagnetic field tensor $F^{\mu\nu}$ in terms of the electric E^μ and magnetic B^μ field four-vectors (defined below), along with the four-velocity u^μ, as is given in various references [12, 13, 14].

$$F^{\mu\nu} = E^\mu u^\nu - E^\nu u^\mu + \epsilon^{\mu\nu\alpha\beta}u_\alpha B_\beta. \tag{2.38}$$

Its Hodge dual is given by:

$$\tilde{F}^{\mu\nu} = B^\mu u^\nu - B^\nu u^\mu - \epsilon^{\mu\nu\alpha\beta}u_\alpha E_\beta, \tag{2.39}$$

where $E^\mu = F^{\mu\nu}u_\nu$ and $B^\mu = \tilde{F}^{\mu\nu}u_\nu = \frac{1}{2}\epsilon^{\mu\nu\alpha\beta}u_\nu F_{\alpha\beta}$. Additionally, using the antisymmetric property of $F^{\mu\nu}$, it becomes evident that both E^μ and B^μ are perpendicular to u^μ, meaning $E^\mu u_\mu = B^\mu u_\mu = 0$. Moreover, in the rest frame $u^\mu = (1, \mathbf{0})$, we find $E^\mu := (0, \mathbf{E})$

and $B^\mu := (0, \mathbf{B})$, where $\mathbf{E}$ and $\mathbf{B}$ represent the electric and magnetic field three-vectors, respectively, with $\mathrm{E}^i := F^{i0}$ and $\mathrm{B}^i := -\frac{1}{2}\epsilon^{ijk}F_{jk}$.

Maxwell's equations can be expressed covariantly as:

$$\partial_\mu F^{\mu\nu} = J^\nu, \tag{2.40}$$

$$\partial_\mu \tilde{F}^{\mu\nu} = 0, \tag{2.41}$$

where J^ν represents the electric charge four-current, acting as the source of the electromagnetic field. In a fluid with four-velocity u^μ, J^μ can be decomposed as follows:

$$J^\mu = j^\mu + d^\mu, \tag{2.42}$$

where j^μ denotes the conduction current and $d^\mu = \Delta^\mu_\nu J^\nu$ represents the charge diffusion current, with $n_q = u_\mu J^\mu$ being the proper net charge density. Assuming a linear constitutive relation between j^μ and E^μ (Ohm's law), we have $j^\mu = \sigma^{\mu\nu} E_\nu$, where $\sigma^{\mu\nu}$ denotes the conductivity tensor. It's important to note that $u_\mu j^\mu = 0$ indicates the fact that the conduction current exists even when the net charge vanishes. The solutions of equations (2.40) and (2.41), together with a given J^μ in equation (2.42), completely determine the evolution of the electromagnetic field. J^μ serves as a coupling between the fluid and the fields, as it contains information about the fluid, such as fluid conductivity $\sigma^{\mu\nu}$ and net charge density n_q, and acts as a source in Maxwell's equations. Incidentally, for a single-component gas as considered in the current thesis, the net charge density is equivalent to the net number density, and the following relation holds $n_q = q n_f$, where n_f corresponds to the net number density.

In the absence of polarization or magnetization, the stress-energy tensor for the electromagnetic field can be expressed as:

$$T^{\mu\nu}_{EM} = -F^{\mu\lambda}F^\nu_\lambda + \frac{1}{4}g^{\mu\nu}F^{\alpha\beta}F_{\alpha\beta}. \tag{2.43}$$

Differentiating the field stress-energy tensor, we obtain the equation of motion:

$$\partial_\mu T_{EM}^{\mu\nu} = -F^{\nu\lambda} J_\lambda. \tag{2.44}$$

Up to this point, no external sources have been considered. Therefore, the charge current density arises solely from the fluid, i.e., $J^\mu = J_f^\mu$. However, in the presence of an external source current J_{ext}^μ (e.g., spectator protons in heavy-ion collisions acting as an external source for the electromagnetic fields in the QGP), the total current consists of both conduction and external current densities:

$$J^\mu = J_f^\mu + J_{ext}^\mu. \tag{2.45}$$

In this scenario, the external current density serves as a source term in the energy-momentum conservation equation. In the ideal MHD limit (also to be discussed in chapter.(3)), which corresponds to a very large magnetic Reynolds number $R_m \gg 1$, the magnetic Reynolds number is given by $R_m = LU\sigma\mu$, where L represents the characteristic length or time scale of the QGP, U is the characteristic velocity of the flow, and μ is the magnetic permeability of the QGP. The large R_m limit is associated with a very large or infinite electrical conductivity. However, the induced charge density due to the electromagnetic field $J_{ind}^\mu = \sigma E^\mu$ (where σ is the isotropic electrical conductivity, i.e., $\sigma^{\mu\nu} = \sigma g^{\mu\nu}$) must be finite, leading to $E^\mu \to 0$ in this case. As a result, the electromagnetic tensor $F^{\mu\nu}$ takes the following form:

$$F^{\mu\nu} \to B^{\mu\nu} = \epsilon^{\mu\nu\alpha\beta} u_\alpha B_\beta. \tag{2.46}$$

Substituting equations (2.45) and (2.46) into Maxwell's equations (2.40), we obtain:

$$\epsilon^{\mu\nu\alpha\beta} \left(u_\alpha \partial_\mu B_\beta + B_\beta \partial_\mu u_\alpha \right) = J_f^\nu + J_{ext}^\nu. \tag{2.47}$$

Now, expressing the energy-momentum tensor for the electromagnetic case using equations (2.43) and (2.46), we have:

$$T_{EM}^{\mu\nu} \to T_B^{\mu\nu} = \frac{B^2}{2} \left(u^\mu u^\nu - \Delta^{\mu\nu} - 2b^\mu b^\nu \right), \tag{2.48}$$

where $B^\mu B_\mu = -B^2$ and $b^\mu = \frac{B^\mu}{B}$, with $b^\mu u_\mu = 0$ and $b^\mu b_\mu = -1$. Furthermore, from equation (2.46), one can show that $B^{\mu\nu} B_{\mu\nu} = 2B^2$, allowing us to introduce another anti-symmetric tensor defined as:

$$b^{\mu\nu} = -\frac{B^{\mu\nu}}{B}, \tag{2.49}$$

with the properties: $b^{\mu\nu} u_\nu = b^{\mu\nu} b_\nu = 0$ and $b^{\mu\nu} b_{\mu\nu} = 2$. When we relax the ideal MHD approximation and consider the effect of finite conductivity, the full $F^{\mu\nu}$ given in Eq.(2.38) is considered. The energy-momentum tensor for the electromagnetic field is expressed as:

$$
\begin{aligned}
T_{EM}^{\mu\nu} &= \left(\frac{B^2 + E^2}{2}\right) u^\mu u^\nu - \left(\frac{B^2 + E^2}{2}\right) \Delta^{\mu\nu} - B^2 b^\mu b^\nu \\
&\quad - E^2 e^\mu e^\nu + 2 Q^{(\mu} u^{\nu)},
\end{aligned} \tag{2.50}
$$

where $B^\mu = Bb^\mu$, $E^\mu = Ee^\mu$, $b^\mu b_\mu = -1$, $e^\mu e_\mu = -1$, $Q^\mu = \mathcal{E}^{\mu\lambda\rho} E_\lambda B_\rho$ with $\mathcal{E}^{\mu\lambda\rho} = \epsilon^{\mu\lambda\rho\tau} u_\tau$, and $b^\mu u_\mu = e^\mu u_\mu = 0$. We can now express the total $T^{\mu\nu}$ as $T^{\mu\nu} = T_{EM}^{\mu\nu} + T_f^{\mu\nu}$. For the non-dissipative fluid, $T_f^{\mu\nu} = \epsilon u^\mu u^\nu - P \Delta^{\mu\nu}$. Hence, the energy-momentum tensor for the non-dissipative fluid in the presence of the electromagnetic field takes the following form:

$$
\begin{aligned}
T_{tot(0)}^{\mu\nu} &= \left(\epsilon + \frac{B^2 + E^2}{2}\right) u^\mu u^\nu - \left(P + \frac{B^2 + E^2}{2}\right) \Delta^{\mu\nu} \\
&\quad - B^2 b^\mu b^\nu - E^2 e^\mu e^\nu + 2 Q^{(\mu} u^{\nu)}.
\end{aligned} \tag{2.51}
$$

For the dissipative fluid in the EM field, we have:

$$
\begin{aligned}
T_{tot}^{\mu\nu} &= \left(\epsilon + \frac{B^2 + E^2}{2}\right) u^\mu u^\nu - \left(P + \Pi + \frac{B^2 + E^2}{2}\right) \Delta^{\mu\nu} \\
&\quad + \pi^{\mu\nu} - B^2 b^\mu b^\nu - E^2 e^\mu e^\nu + 2 Q^{(\mu} u^{\nu)}.
\end{aligned} \tag{2.52}
$$

The relativistic magnetohydrodynamics equations thus consist of energy-momentum conservation equations for fluid and electromagnetic fields and Maxwell's equations. This set of conservation equations is closed with an Equation of State (EoS) relating fluid pressure, energy, and number density and a constitutive equation for the charge four current. In

the presence of an external electromagnetic field, there exists an external force on charged fluid, and the total energy-momentum conservation takes the following form

$$\partial_\mu T^{\mu\nu} = -F^{\nu\lambda} J_{\text{ext},\lambda}. \tag{2.53}$$

The conservation equation for electromagnetic fields can be rewritten using Eq.(2.44) and Eq.(2.45) as:

$$\partial_\mu T^{\mu\nu}_{EM} = -F^{\nu\lambda}(J_{f,\lambda} + J_{ext,\lambda}). \tag{2.54}$$

Now using Eq.(2.53) and Eq.(2.54) we land up at:

$$\partial_\mu T^{\mu\nu}_f = F^{\nu\lambda} J_{f,\lambda}. \tag{2.55}$$

Also, we know that the conservation of charge current of the fluid is conserved separately stating:

$$\partial_\mu J^\mu_f = 0 \tag{2.56}$$

Typically, the conservation of the total energy-momentum tensor in an isolated system holds. However, when an external source is present (such as an external charge current), conservation is only maintained by including an appropriate source term. This indicates that in such scenarios, the evolution of the fluid relies on the fluid charge current, as depicted in Eq.(2.55).

As previously discussed regarding Israel-Stewart-like second-order evolution equations for dissipative stresses in the context of viscous hydrodynamics, similar evolution equations exist for dissipative stresses in the presence of electromagnetic fields, which we will be deriving in the chapter.(3). Recalling our discussion on the Israel-Stewart type theory, which allowed for positive definite entropy current generation. We noted that the coupling terms associated with transport coefficients were unknown and were only constrained. To determine their values, we need an underlying theory, which we will be studying in the following section, specifically, the relativistic kinetic theory.

2.3   Relativistic Kinetic theory

Kinetic theory offers a way to understand the collective behavior by describing macroscopic quantities in terms of the distribution of individual particles in phase space. In relativistic systems, such as those in high-energy physics or astrophysics, we can derive formulations of dissipative hydrodynamics or magnetohydrodynamics using relativistic kinetic theory. In this approach, we employ a single-particle distribution function $f(x, p)$, where x denotes position space and p momentum of the particle. This function allows us to quantify the behavior of the system. For instance, the total number of particles (N) within the system can be represented as $\int_{-\infty}^{\infty} \int_{-\infty}^{\infty} d^4p d^4x f(x, p)$ where $d^4x d^4p$ is the phase-space volume element. Furthermore, all the fundamental quantities, such as the entropy current S^μ, the number current N^μ, and the energy-momentum tensor $T^{\mu\nu}$, can be expressed as various moments of this distribution function ($f(x, p)$). These moments provide insights into the overall dynamics of the system, shedding light on its macroscopic behavior. These are thus represented as:

$$T^{\mu\nu} = \int \frac{d^3p}{p^0} \sqrt{-g} p^\mu p^\nu f(x, p), \tag{2.57}$$

$$N^\mu = \int \frac{d^3p}{p^0} \sqrt{-g} p^\mu f(x, p), \tag{2.58}$$

$$S^\mu = -\int \frac{d^3p}{p^0} \sqrt{-g} p^\mu f(x, p)(ln f(x, p) - 1), \tag{2.59}$$

where $\frac{d^3p \sqrt{-g}}{p^0}$ is the Lorentz invariant quantity with $p^0 = \sqrt{|\mathbf{p}|^2 + m^2}$ and g being the det($g_{\mu\nu}$). The distribution function $f(x, p)$ represented above is a dynamical quantity and can be retrieved using the relativistic Boltzmann equation:

$$\frac{df}{d\mathcal{T}} = \frac{dx^\mu}{d\mathcal{T}} \partial_\mu f + \frac{dp^\mu}{d\mathcal{T}} \frac{\partial f}{\partial p^\mu} = C[f], \tag{2.60}$$

where $p^\mu = \frac{dx^\mu}{d\mathcal{T}}$ is the four-momentum of the individual particle, $\frac{df}{d\mathcal{T}}$ is the total derivative of the distribution function, and $F^\mu = \frac{dp^\mu}{d\mathcal{T}}$ is the external force applied. The first term here $\left(\frac{dx^\mu}{d\mathcal{T}}\partial_\mu f\right)$ represents the free-streaming term, while the second term takes into account the effects of all the external forces, and the right-hand side takes into account all the information about the collision dynamics taking place in the system. Here the $F^\mu = -\Gamma^\mu_{\alpha\beta}p^\alpha p^\beta$ or $qF^{\mu\nu}p_\nu$ are the forces corresponding to the curved space-time or the electromagnetic case, respectively with $\Gamma^\mu_{\alpha\beta}$ being the Christoffel symbol of second kind.

In the realm of hydrodynamics, we previously partitioned the total energy-momentum, number current, and entropy current into two distinct categories: ideal and dissipative. This categorization is based on the fact that we need to distinguish between ideal quantities, which do not contribute to entropy production, and those that lead to dissipation, consequently resulting in entropy production. Continuing in the same manner, we undertake a similar decomposition, presuming the presence of an equilibrium distribution function $f_0(x,p)$ alongside an off-equilibrium counterpart $\delta f(x,p)$. Consequently, we represent the distribution function $f(x,p) = f_0(x,p) + \delta f(x,p)$. Thus, we write the equilibrium and non-equilibrium quantities here as:

$$\epsilon \equiv u_\mu u_\nu T^{\mu\nu} = u_\mu u_\nu \int \frac{d^3p}{p^0}\sqrt{-g}p^\mu p^\nu \left(f_0 + \bar{f}_0\right), \tag{2.61}$$

$$n \equiv u_\mu N^\mu = u_\mu \int \frac{d^3p}{p^0}\sqrt{-g}p^\mu \left(f_0 - \bar{f}_0\right), \tag{2.62}$$

$$P \equiv -\frac{\Delta_{\mu\nu}}{3}T^{\mu\nu} = -\frac{\Delta_{\mu\nu}}{3}\int \frac{d^3p}{p^0}\sqrt{-g}p^\mu p^\nu \left(f_0 + \bar{f}_0\right), \tag{2.63}$$

$$s \equiv u_\mu S^\mu = -u_\mu \int \frac{d^3p}{p^0}\sqrt{-g}p^\mu(f_0 + \bar{f}_0)[ln(f_0 + \bar{f}_0) - 1], \tag{2.64}$$

$$dS^\mu \equiv \Delta^\mu_\nu S^\mu = -\Delta^\mu_\nu \int \frac{d^3p}{p^0}\sqrt{-g}p^\nu(\delta f + \delta\bar{f})[ln(\delta f + \delta\bar{f}) - 1], \tag{2.65}$$

$$V^\mu \equiv \Delta^\mu_\nu N^\nu = \Delta^\mu_\nu \int \frac{d^3p}{p^0}\sqrt{-g}p^\nu \left(\delta f - \delta\bar{f}\right), \tag{2.66}$$

$$\Pi \equiv -\frac{\Delta_{\mu\nu}}{3}\delta T^{\mu\nu} = -\frac{\Delta_{\mu\nu}}{3}\int \frac{d^3p}{p^0}\sqrt{-g}p^\mu p^\nu \left(\delta f + \delta\bar{f}\right), \tag{2.67}$$

$$\pi^{\mu\nu} \equiv \Delta^{\mu\nu}_{\alpha\beta}\delta T^{\mu\nu} = \Delta^{\mu\nu}_{\alpha\beta}\int \frac{d^3p}{p^0}\sqrt{-g}p^\alpha p^\beta \left(\delta f + \delta\bar{f}\right), \tag{2.68}$$

where $\bar{f}_0$ and $\delta\bar{f}$ denote the equilibrium and off-equilibrium parts from the anti-particles, where for anti-particles $q \to -q$ and $\mu \to -\mu$. For convenience, we express the integrals in Eq.(2.61) to Eq.(2.63) in terms of thermodynamic integrals $I^{(m)\pm}_{nq}$ (defined in Appendix A.1) as:

$$\epsilon = I^{(0)+}_{20}, \tag{2.69}$$

$$n = I^{(0)-}_{10}, \tag{2.70}$$

$$P = -I^{(0)+}_{21}, \tag{2.71}$$

here $\pm$ corresponds to the addition or subtraction of $\bar{f}$ (we will be using these notations also in the chapter.(3)). Again from the expression of entropy current in Eq.(2.59) and demanding $\partial_\mu S^\mu = 0$, we get that equilibrium distribution function to be of the following form:

$$f_0(x,p) = \mathcal{F}\left(\frac{p^\mu u_\mu}{T}\right). \tag{2.72}$$

In the case of fermions, bosons, or Boltzmann statistics, the equilibrium distribution is given as:

$$f_0(x,p) = \frac{1}{\exp\left(\frac{p^\mu u_\mu}{T} - \alpha\right) \pm l}, \tag{2.73}$$

where $l = 0, \pm 1$ for Boltzmann, fermions, and bosons, respectively. Here $u^\mu p_\mu$ is the scalar invariant and can be interpreted as the energy of the particle in the rest frame of the fluid. Along with the equilibrium quantities, the dissipative part of the distribution function $\delta f(x,p)$ is evaluated using the relativistic Boltzmann equation.(2.60). While doing so, it is very important to consider the form of the collision kernel. Over the years, there have been many advances toward taking care of the collision kernel [15, 16, 17]. One of

the most renowned and straightforward approaches is the RTA (relaxation time approximation), where we postulate $C[f] = -\frac{u \cdot p}{\tau_c} \delta f(x, p)$. Here, τ_c signifies the relaxation time, denoting the duration required for a particle in a non-equilibrium distribution state to transition to equilibrium. The negative sign's physical significance lies in its role in driving non-equilibrium particle distributions towards equilibrium. With this, we are ready with the final Boltzmann equation, that is:

$$p^\mu \partial_\mu f + F^\mu \frac{\partial f}{\partial p^\mu} = -\frac{u \cdot p}{\tau_c} \delta f(x, p), \tag{2.74}$$

which we will be using in the rest of the thesis.

In the next chapter, we use the above form of the Boltzmann equation given in Eq.(2.74) with external forces (electromagnetic fields) to derive the Israel-Stewart-like evolution equations for the dissipative stresses (Π, $\pi^{\mu\nu}$, V^μ) using the RTA as collision kernel.

References

[1] P. Romatschke, "New Developments in Relativistic Viscous Hydrodynamics," Int. J. Mod. Phys. E **19**, 1-53 (2010) doi:10.1142/S0218301310014613 [arXiv:0902.3663 [hep-ph]].

[2] C. Eckart, "The Thermodynamics of Irreversible Processes. 1. The Simple Fluid," Phys. Rev. **58**, 267-269 (1940) doi:10.1103/PhysRev.58.267

[3] C. Eckart, "The Thermodynamics of irreversible processes. 3.. Relativistic theory of the simple fluid," Phys. Rev. **58**, 919-924 (1940) doi:10.1103/PhysRev.58.919

[4] L.D. LANDAU and E.M. LIFSHITZ, "CHAPTER IX - SHOCK WAVES", in *Fluid Mechanics*, edited by L.D. LANDAU and E.M. LIFSHITZ, Pergamon, 1959, pp. 310-346, doi: 10.1016/B978-0-08-029142-0.50014-3,

[5] W. Israel and J. M. Stewart, "Transient relativistic thermodynamics and kinetic theory," Annals Phys. **118**, 341-372 (1979) doi: 10.1016/0003-4916(79)90130-1

[6] H. Grad, "On the kinetic theory of rarefied gases," Commun. Pure Appl. Math. **2**, no. 4, 331-407 (1949) doi: 10.1002/cpa.3160020403

[7] W. Israel, "Nonstationary irreversible thermodynamics: A Causal relativistic theory," Annals Phys. **100**, 310-331 (1976) doi: 10.1016/0003-4916(76)90064-6

[8] I. Muller, "Zum Paradoxon der Warmeleitungstheorie," Z. Phys. **198**, 329-344 (1967) doi: 10.1007/BF01326412

[9] I. Muller, "Speeds of propagation in classical and relativistic extended thermodynamics," Living Rev. Rel. **2**, 1 (1999) doi: 10.12942/lrr-1999-1

[10] M. Grmela and H. C. Ottinger, "Dynamics and thermodynamics of complex fluids. 1. Development of a general formalism," Phys. Rev. E **56**, 6620-6632 (1997) doi:10.1103/PhysRevE.56.6620

[11] A. Jaiswal, "Formulation of relativistic dissipative fluid dynamics and its applications in heavy-ion collisions," [arXiv:1408.0867 [nucl-th]].

[12] A. Lichnerowicz and Southwest Center for Advanced Studies, *Relativistic Hydrodynamics and Magnetohydrodynamics*, Mathematical physics monograph series, 1967, W. A. Benjamin, ISBN: 67018400, Lichnerowicz

[13] A. M. Anile, *Relativistic Fluids and Magneto-fluids*, Cambridge Monographs on Mathematical Physics, 2005, Cambridge University Press, ISBN: 9780521018128, Anile

[14] K. S. Thorne and R. D. Blandford, *Modern Classical Physics*, 2017, Princeton University Press, ISBN: 9781400848898, https://books.google.co.in/books?id=U1S6BQAAQBAJ

[15] P. L. Bhatnagar, E. P. Gross and M. Krook, "A Model for Collision Processes in Gases. 1. Small Amplitude Processes in Charged and Neutral One-Component Systems," Phys. Rev. **94**, 511-525 (1954) doi:10.1103/PhysRev.94.511.

[16] R. L. Anderson and B. R. Ikenberry, "A relativistic relaxation-time model for the Boltzmann equation," Physica **74**, 466-488 (1974) doi:10.1016/0031-8914(74)90355-3.

[17] Charles-Michel Marle, "Sur l'établissement des équations de l'hydrodynamique des fluides relativistes dissipatifs. I. — L'équation de Boltzmann relativiste," Annales De L Institut Henri Poincare-physique Theorique **10**, 67-126 (1969) url: `https://api.semanticscholar.org/CorpusID:124097847`.

Chapter 3

Relativistic non-resistive and resistive magnetohydrodynamics for dissipative systems

Here the terms "non-resistive" and "resistive" refers to different descriptions of magneto-hydrodynamics (MHD), a framework used to study the behavior of conducting mediums in the presence of magnetic fields. Let's explore these two descriptions: non-resistive MHD assumes that the medium is perfectly conducting, meaning there is no electrical resistance. In the previous chapter, we discussed that $E^\mu = F^{\mu\nu}u_\nu$, where the symbols have the usual meaning. In any arbitrarily boosted frame E^μ can be written as $(-\gamma\mathbf{E}\cdot\mathbf{v}, -\gamma(\mathbf{E}+\mathbf{v}\times\mathbf{B}))$. For a finite amount of charge, charge-current J^μ is finite and hence the limit of infinite conductivity leads to E^μ tending to 0 given that $J^\mu = \sigma E^\mu$. In this limit as E^μ is set to zero, it boils down to the condition that each element in the electric four-vector is zero, stating that the fluid velocity ($\mathbf{v}$) is perpendicular to the electric field ($\mathbf{E}$) and $\mathbf{E}+\mathbf{v}\times\mathbf{B}=0$, with $\mathbf{B}$ being the magnetic field vector. Thus in the ideal or non-resistive limit, Ohm's law takes the simplified form $\mathbf{E}+\mathbf{v}\times\mathbf{B}=0$. This approximation is often employed in astrophysics which results in a condition known as 'frozen-in' magnetic field lines, where the magnetic field evolves with the fluid, and its dynamics are completely determined by the fluid velocity. On the other hand, resistive MHD accounts for the presence of a finite electrical resistivity in the conducting medium. This is a more realistic scenario in which the Ohm's law is modified to include the resistive term: $\mathbf{E}+\mathbf{v}\times\mathbf{B}=\eta\mathbf{J}$, where η is the electrical resistivity and $\mathbf{J}$ is the electric current density. The resistive term accounts for the dissipation of magnetic energy due to the finite electrical resistivity of the medium.

In this chapter, we will discuss both resistive and non-resistive evolution equations for

the dissipative stresses for a conducting medium. It has been shown previously in chapter.(2) that Israel Stewart-like (IS-like) theories resolve the major problem of acausality in the first order. This theory is indeed known to be causal and stable but in a restricted manner [1, 2, 3, 4]. Many advancements in IS-like equations, excluding electromagnetic fields, have been derived directly from kinetic theory. These advancements were achieved by considering various moments, applying different counting schemes, or by incorporating non-local effects in collision terms etc [5, 6, 7, 8, 9, 10, 11, 12, 13, 14, 15]. Further, second-order causal magnetohydrodynamics equations were also derived for non-resistive in [16] and subsequently for resistive case in [17] for a single-component system of spinless particles (no antiparticle) using a 14-moment approximation.

Here, we will delve into the utilization of the relaxation time approximation in the collision kernel to derive the relativistic non-resistive and subsequently resistive, viscous second-order magnetohydrodynamic (MHD) equations that govern the dissipative quantities in the context of heavy-ion collisions. We should note that putting the limit of infinite conductivity or $E^\mu = 0$ in the resistive case, we should retrieve the non-resistive evolution equations of the dissipative stresses but to make sure that these are exactly the evolution equations in the non-resistive limit we derive both the cases one-by-one. To accomplish this, we solve the Boltzmann equation for a system of particles and antiparticles, employing a Chapman-Enskog-like gradient expansion of the single-particle distribution function truncated in the second order. Furthermore, in this chapter, we also derive the anisotropic transport coefficients in the Navier-Stokes limit. This will provide us with a comprehensive understanding of the behavior of the dissipative quantities considering the external electromagnetic field's effects on the system.

Firstly, we will review the MHD equations introduced in the previous chapter and briefly discuss these equations. Following that, in Section.(3.1), we will delve into the formalism utilized to derive Israel-Stewart-like equations for all the dissipative stresses, explicitly

considering the influence of external magnetic fields only in the non-resistive case. Additionally, this section will explore the new second-order transport coefficients arising from this formalism, examining their dependence on temperature and mass. In section.(3.2) we will derive the general expressions of Israel-Stewart-like evolution equations for dissipative stresses. This derivation will encompass contributions from electric and magnetic field vectors in a scenario of finite conductivity. Finally, in Section.(3.3), we will outline the conclusions drawn from the findings presented in this chapter. The time-like fluid's four-velocity u^μ satisfy $u_\mu u^\mu = 1$. Also, we use the following decomposition for the partial derivative: $\partial_\mu \equiv u_\mu u_\nu \partial^\nu + (g_{\mu\nu} - u_\mu u_\nu)\partial^\nu = u_\mu D + \nabla_\mu$. The $\nabla^\alpha u^\beta$ is decomposed as:

$$\nabla^\alpha u^\beta = \omega^{\alpha\beta} + \sigma^{\alpha\beta} + \frac{1}{3}\theta\Delta^{\alpha\beta}, \tag{3.1}$$

where $\omega^{\alpha\beta} = (\nabla^\alpha u^\beta - \nabla^\beta u^\alpha)/2$ is the anti-symmetric vorticity tensor, $\sigma^{\alpha\beta} \equiv \nabla^{\langle\alpha} u^{\beta\rangle} = \frac{1}{2}\left(\nabla^\alpha u^\beta + \nabla^\beta u^\alpha\right) - \frac{1}{3}\theta\Delta^{\alpha\beta}$ is the symmetric-traceless tensor and $\theta \equiv \partial_\mu u^\mu$ is the expansion scalar. The fourth-rank projection tensor is defined as $\Delta^{\mu\nu}_{\alpha\beta} = \frac{1}{2}\left(\Delta^\mu_\alpha \Delta^\nu_\beta + \Delta^\mu_\beta \Delta^\nu_\alpha\right) - \frac{1}{3}\Delta^{\mu\nu}\Delta_{\alpha\beta}$. In Chapter (2), we provided a brief overview of the relativistic MHD equations. We now proceed by rewriting the key equations that were previously introduced:

$$\partial_\mu T^{\mu\nu}_{EM} = -F^{\nu\lambda}\left(J_{f,\lambda} + J_{ext,\lambda}\right), \tag{3.2}$$

$$\partial_\mu T^{\mu\nu}_f = F^{\nu\lambda} J_{f,\lambda}, \tag{3.3}$$

$$\partial_\mu J^\mu_f = 0, \tag{3.4}$$

with $F^{\mu\nu} = E^\mu u^\nu - E^\nu u^\mu + B^{\mu\nu}$. All the terms have the usual meaning as defined previously. Considering the contributions from both the electric and magnetic fields we can further analyze these equations by taking the projection along and perpendicular to fluid four velocity. The parallel projection of Eq.(3.2) and Eq.(3.3) gives:

$$u_\nu \partial_\mu T^{\mu\nu}_{EM} = E^\lambda\left(J_{f,\lambda} + J_{ext,\lambda}\right), \tag{3.5}$$

$$u_\nu \partial_\mu T^{\mu\nu}_f = -E^\lambda J_{f,\lambda}. \tag{3.6}$$

It implies that the energy density of the fluid and the field is affected by the charge currents/electric field vector but in the Non-resistive limit $(E^\mu \to 0)$ we get the energy densities to be independent of both charge currents and the electromagnetic fields. The perpendicular projection of Eq.(3.2) and Eq.(3.3) using Eq.(2.45) gives

$$\Delta^\alpha_\nu \partial_\mu T^{\mu\nu}_{EM} = \left(-E^\alpha u^\lambda + Bb^{\alpha\lambda}\right)\left(J_{f,\lambda} + J_{ext,\lambda}\right), \qquad (3.7)$$

$$\Delta^\alpha_\nu \partial_\mu T^{\mu\nu}_f = \left(E^\alpha u^\lambda - Bb^{\alpha\lambda}\right)J_{f,\lambda}. \qquad (3.8)$$

This shows that though the momentum density of fluid depend on the diffusion current of the fluid/electromagnetic field but for fields, it additionally depends on the external current. Now using Eq.(3.4), Eq.(3.3) with the expression for $F^{\mu\nu}$ along with the equations for the fluid as is given in Eq.(2.16), Eq. (2.17) and using the thermodynamic integrals given in Eq. (A.7) and Eq. (A.8) we get the evolution equations for $\dot{\alpha}$, $\dot{\beta}$ and $\dot{u}^\mu$ which are of the following forms:

$$
\begin{aligned}
\dot{\alpha} &= \frac{1}{D_{20}}\left[J^{(0)-}_{20}\theta\left(\epsilon + P + \Pi\right) - J^{(0)+}_{30}\left(n_f\theta + \partial_\mu V^\mu_f\right) + J^{(0)-}_{20}\left(-\pi^{\mu\nu}\sigma_{\mu\nu} + qE^\mu V_{f\mu}\right)\right], \\
\dot{\beta} &= \frac{1}{D_{20}}\left[J^{(0)+}_{10}\theta\left(\epsilon + P + \Pi\right) - J^{(0)-}_{20}\left(n_f\theta + \partial_\mu V^\mu_f\right) + J^{(0)+}_{10}\left(-\pi^{\mu\nu}\sigma_{\mu\nu} + qE^\mu V_{f\mu}\right)\right], \\
\dot{u}^\mu &= \frac{1}{\epsilon + P}\left[\frac{n_f}{\beta}\left(\nabla^\mu\alpha - h\nabla^\mu\beta\right) - \Pi\dot{u}^\mu + \nabla^\mu\Pi - \Delta^\mu_\nu\partial_\rho\pi^{\rho\nu}\right] \\
&\quad + \frac{1}{\epsilon + P}\left[qn_f E^\mu - qBb^{\mu\nu}V_{f\nu}\right], \qquad (3.9)
\end{aligned}
$$

where $D_{20} = J^{(0)+}_{30}J^{(0)+}_{10} - J^{(0)-}_{20}J^{(0)-}_{20}$, $h = \frac{\epsilon+P}{n_f}$ and $\sigma^{\mu\nu} = \Delta^{\mu\nu}_{\alpha\beta}\nabla^\alpha u^\beta$. The above set of three equations gives us the equation of motion of the fluid variables. The first two equations however are the evolution equations for the chemical potential and temperature respectively which only depend on the external electric field vector, whereas the relativistic Navier-Stokes equation given in Eq.(3.9) depends both on the external electric and magnetic field vectors.

As previously discussed, the fluid variables represent the leading-order terms, also considered as the zeroth-order terms. Their derivatives form the first-order terms, typically

expressed by the constitutive equations of shear, bulk, and diffusion. However, the last term in the Navier-Stokes equation (as shown in Eq.(3.9)) is unique in that it depends on the magnetic fields and contributes to the Navier-Stokes equation at the next-to-leading order in the gradient expansion. This is because the diffusion current V_f^μ is itself a first-order term in the gradient expansion, which we are going to derive next for both resistive and non-resistive cases.

3.1 Non-Resistive MHD

Here we intend to derive order-by-order constitutive and evolution equations of all the dissipative stresses (bulk, diffusion and shear) for the ideal MHD conditions (infinite conductivity limit).

3.1.1 Formalism

In order to get the order-by-order expressions for all the dissipative stresses we will have to first find out the δf's at various orders upto $n = 2$, where n is the order of expansion, from the Boltzmann equation and putting these in the expressions for the dissipative stresses given in Eq.(2.66)-Eq.(2.68) we get all the results at various orders. Now we first start with the Boltzmann equation.

Relativistic Boltzmann Equation

In the relativistic Boltzmann equation (RBE), accounting for the influence of a non-zero force $\mathcal{F}^\nu$, as discussed in the preceding chapter, we have:

$$p^\mu \partial_\mu f + \mathcal{F}^\nu \frac{\partial}{\partial p^\nu} f = C[f]. \tag{3.10}$$

Here, $f(\mathbf{x}, \mathbf{p}, t)$ represents the one-particle distribution function, capturing the phase space density of particles, while $C[f]$ denotes the collision kernel. Notably, in the ideal magnetohydrodynamic (MHD) scenario, the electric field vanishes in the fluid's local rest frame.

Consequently, the sole contribution to the force term in the RBE stems from the magnetic field. This contribution is expressed as $\mathcal{F}^\nu := qF^{\nu\alpha}p_\alpha$ for particles, where q denotes the electric charge of the particles, and $F^{\mu\nu} = -Bb^{\mu\nu}$ (Eq.(2.46)).

As previously discussed, considerable simplification arises when we adopt the relaxation time approximation for the collision kernel. In non-relativistic systems, this approximation, introduced by Bhatnagar-Gross-Krook (BGK), and in relativistic systems, as proposed by Anderson and Witting in [18], takes the form:

$$C[f] = -\frac{u \cdot p}{\tau_c}\delta f,$$

where τ_c represents the relaxation time, indicating the duration particles take to deviate from equilibrium and reach an equilibrium state, and $\delta f = f - f_0$ represents the deviation from the equilibrium distribution f_0. Substituting this collision kernel into the relativistic Boltzmann equation (RBE), as given by Eq.(3.10), yields:

$$p^\mu\partial_\mu f + qF^{\sigma\nu}p_\nu\frac{\partial}{\partial p^\sigma}f = -\frac{u \cdot p}{\tau_c}\delta f. \tag{3.11}$$

Correspondingly, equations for antiparticles are derived by replacing $q \to -q$ and $f \to \bar{f}$. However, it's important to note that this approximation has its limitations. Notably, the relaxation time (τ_c) remains independent of the momentum of colliding particles. Furthermore, it assumes that the interaction between colliding particles results in mean free paths longer than the interaction length. In simpler terms, we assume that $f(\mathbf{x}, \mathbf{p}, t)$ varies smoothly over the duration of collisions and distances comparable to the interaction range.

Expansion in gradients

One can express Eq.(3.11) in the well-known hydrodynamic gradient expansion form, as discussed in [19], under the condition that the system approaches equilibrium, i.e., the collision kernel nearly vanishes ($C[f] \approx 0$). In the absence of an electromagnetic field, Eq.(3.11)

takes the form:

$$\left(\frac{\tau_c}{u \cdot p} p^\mu \partial_\mu + 1\right) f = (\mathcal{D} + 1) f = f_0, \tag{3.12}$$

where we define the operator $\mathcal{D} \equiv \frac{\tau_c}{u \cdot p} p^\mu \partial_\mu$. Multiplying the inverse operator $(\mathcal{D} + 1)^{-1}$ in the above equation and subsequently performing a power series expansion yields:

$$f = \sum_{n=0}^{\infty} (-\mathcal{D})^n f_0 = \sum_{n=0}^{\infty} \left(-\frac{\tau_c}{u \cdot p} p^\mu \partial_\mu\right)^n f_0. \tag{3.13}$$

This expansion holds true provided that the Knudsen number satisfies $\text{Kn} = \tau_c \partial \ll 1$, which serves as the relevant expansion parameter. If one assumes the typical gradient strength to be proportional to the temperature, $\partial \sim T$, then the expansion parameter becomes $\tau_c T$, and the series expansion remains valid for $\tau_c T \ll 1$. However, the naive gradient expansion breaks down in the presence of a magnetic field, as it introduces a new scale proportional to the strength of the magnetic field. By defining the operator $\mathcal{D}_B \equiv \frac{\tau_c}{u \cdot p} \left(p^\mu \partial_\mu + q F^{\sigma\nu} p_\nu \frac{\partial}{\partial p^\sigma}\right)$ and performing a similar power series expansion, we obtain:

$$
\begin{aligned}
f &= \sum_{n=0}^{\infty} (-\mathcal{D}_B)^n f_0, \\
&= \sum_{n=0}^{\infty} \left[-\frac{\tau_c}{u \cdot p} \left(p^\mu \partial_\mu + q F^{\sigma\nu} p_\nu \frac{\partial}{\partial p^\sigma}\right)\right]^n f_0.
\end{aligned} \tag{3.14}
$$

In addition to the previous assumption $\tau_c T \ll 1$, it's necessary to ensure $\tau_c / r_g \ll 1$, where $r_g = k_\perp / qB$ represents the gyroradius (Larmor radius), and $k_\perp$ denotes the component of momentum perpendicular to the magnetic field's direction. In plasma, the typical transverse momentum of a particle is $k_\perp \sim T$, thus satisfying the condition $\chi = qB\tau_c / T \ll 1$.

Here, we determine f by retaining terms up to the second-order, i.e., $n = 2$ in Eq.(3.14), resulting in:

$$f = f_0 + \delta f^{(1)} + \delta f^{(2)}, \tag{3.15}$$

where

$$\delta f^{(1)} = -\frac{\tau_c}{u \cdot p} \left(p^\mu \partial_\mu + q F^{\sigma\nu} p_\nu \frac{\partial}{\partial p^\sigma}\right) f_0, \tag{3.16}$$

and

$$\delta f^{(2)} \;=\; \frac{\tau_c}{u \cdot p}\left(p^\mu \partial_\mu + qF^{\sigma\nu}p_\nu \frac{\partial}{\partial p^\sigma}\right)\left[\frac{\tau_c}{u \cdot p}\left(p^\alpha \partial_\alpha + qF^{\rho\beta}p_\beta \frac{\partial}{\partial p^\rho}\right)f_0\right]. \quad (3.17)$$

This expression can be simplified using the relations $qBb^{\mu\nu}p_\nu \frac{\partial f_0}{\partial p^\mu} = 0$ and $F^{\mu\nu} = -Bb^{\mu\nu}$, resulting in:

$$f = f_0 + \delta\tilde{f}^{(1)} + \delta\tilde{f}^{(2)}, \quad (3.18)$$

where

$$\delta\tilde{f}^{(1)} = -\frac{\tau_c}{u \cdot p}p^\mu \partial_\mu f_0, \quad (3.19)$$

and

$$\delta\tilde{f}^{(2)} \;=\; \frac{\tau_c}{u \cdot p}p^\mu \partial_\mu \left[\frac{\tau_c}{u \cdot p}p^\alpha \partial_\alpha f_0\right] - \frac{\tau_c}{u \cdot p}qBb^{\sigma\nu}p_\nu \frac{\partial}{\partial p^\sigma}\left[\frac{\tau_c}{u \cdot p}p^\alpha \partial_\alpha f_0\right].$$

It's important to note that although the magnetic field does not explicitly enter the first term of $\delta\tilde{f}^{(2)}$, it does implicitly through the acceleration term $\dot{u}^\mu$, as shown in Eq.(3.9), when taking higher-order moments of such terms.

3.1.2   Results

With all the expressions for the off-equilibrium distribution function in place we can now just plug in all in the Eq.(2.66)-Eq.(2.68) and obtain the results for this case order-by-order.

First order equations

The term $\delta\tilde{f}^{(1)}$ does not depend explicitly or implicitly on the magnetic field, as the first-order equations retain terms up to $\mathcal{O}(\partial)$, as shown in all equations in Eq.(3.9). Nevertheless, for completeness, we discuss here the results for the first-order terms in the gradient expansion. The outcomes of this section coincide with those in [14], derived under the assumption of zero magnetic fields.

   We compute the dissipative part of the energy-momentum tensor (including shear, bulk viscosity, and diffusion) using $\delta\tilde{f}^{(1)}$ and $\delta\tilde{\tilde{f}}^{(1)}$, given by:

$$\pi_{(1)}^{\mu\nu} = \Delta_{\alpha\beta}^{\mu\nu} \int dp\, p^{\alpha} p^{\beta} \left(\delta\tilde{f}^{(1)} + \delta\tilde{\tilde{f}}^{(1)} \right), \tag{3.20}$$

$$\Pi_{(1)} = -\frac{\Delta_{\mu\nu}}{3} \int dp\, p^{\mu} p^{\nu} \left(\delta\tilde{f}^{(1)} + \delta\tilde{\tilde{f}}^{(1)} \right), \tag{3.21}$$

$$V_{(1)}^{\mu} = \Delta_{\alpha}^{\mu} \int dp\, p^{\alpha} \left(\delta\tilde{f}^{(1)} - \delta\tilde{\tilde{f}}^{(1)} \right). \tag{3.22}$$

The negative sign here in V^{μ} is from the conservation of net-number of charges. By substituting the expression for $\delta\tilde{f}^{(1)}$ from Eq.(3.19) into Eqs.(3.20)-(3.22) and performing some algebraic manipulations, we obtain the following relations. For the shear viscous pressure:

$$\pi_{(1)}^{\mu\nu} = 2\tau_c \beta_\pi \sigma^{\mu\nu}, \tag{3.23}$$

where $\beta_\pi = \beta J_{42}^{(1)+}$ and $\sigma^{\mu\nu} = \Delta_{\alpha\beta}^{\mu\nu} \nabla^{\alpha} u^{\beta}$.

For the bulk viscous pressure:

$$\Pi_{(1)} = -\tau_c \beta_\Pi \theta, \tag{3.24}$$

where $\theta = \partial_\mu u^\mu$ and

$$\beta_\Pi = \frac{5\beta}{3} J_{42}^{(1)+} + \mathcal{X} J_{31}^{(0)+} - \mathcal{Y} J_{21}^{(0)-}, \tag{3.25}$$

with $\mathcal{X}$ and $\mathcal{Y}$ given by

$$\begin{aligned}
\mathcal{X} &= \frac{J_{10}^{(0)+}(\epsilon + P) - J_{20}^{(0)-} n_f}{D_{20}}, \\
\mathcal{Y} &= \frac{J_{20}^{(0)-}(\epsilon + P) - J_{30}^{(0)+} n_f}{D_{20}}.
\end{aligned} \tag{3.26}$$

Finally, for the net particle diffusion current:

$$V_{(1)}^{\mu} = \tau_c \beta_V \nabla^{\mu} \alpha, \tag{3.27}$$

where $\beta_V = \frac{n_f}{\epsilon+P} J_{21}^{(0)-} - J_{21}^{(1)-}$. Here, β_π, β_Π, and β_V represent the transport coefficients of shear, bulk, and diffusion current, respectively, with their explicit expressions provided as well.

Second-order equations

Next we move onto the derivation for the second-order evolution equation for the dissipative stresses.

Shear stress:

The second-order contribution to the shear stress tensor is defined as:

$$\pi_{(2)}^{\mu\nu} = \Delta_{\alpha\beta}^{\mu\nu} \int dp\, p^\alpha p^\beta \left(\delta \tilde{f}^{(2)} + \delta \tilde{\tilde{f}}^{(2)} \right), \tag{3.28}$$

where $\delta \tilde{f}^{(2)}$ is provided in Eq.(3.20). It's important to note that the total shear stress includes both first and second-order terms:

$$\pi^{\mu\nu} = \pi_{(1)}^{\mu\nu} + \pi_{(2)}^{\mu\nu}. \tag{3.29}$$

By evaluating the integral in Eq.(3.28) (refer to Appendix.(A.5.3) for detailed calculations) and incorporating it into Eq.(3.29), we obtain the evolution equation for the shear stress tensor:

$$
\begin{aligned}
\frac{\pi^{\mu\nu}}{\tau_c} =\ & -\dot{\pi}^{\mu\nu} + 2\beta_\pi \sigma^{\mu\nu} + 2\pi_\gamma^{\langle\mu} \omega^{\nu\rangle\gamma} - \tau_{\pi\pi} \pi_\gamma^{\langle\mu} \sigma^{\nu\rangle\gamma} - \delta_{\pi\pi}\pi^{\mu\nu}\theta + \lambda_{\pi\Pi}\Pi\sigma^{\mu\nu} - \tau_{\pi V} V^{\langle\mu}\dot{u}^{\nu\rangle} \\
& + \lambda_{\pi V} V^{\langle\mu}\nabla^{\nu\rangle}\alpha + l_{\pi V}\nabla^{\langle\mu} V^{\nu\rangle} + \delta_{\pi B}\Delta_{\eta\beta}^{\mu\nu}qBb^{\gamma\eta}g^{\beta\rho}\pi_{\gamma\rho} - \tau_c qB\tau_{\pi VB}\dot{u}^{\langle\mu}b^{\nu\rangle\sigma}V_\sigma \\
& - \tau_c qB\lambda_{\pi VB}V_\gamma b^{\gamma\langle\mu}\nabla^{\nu\rangle}\alpha - q\tau_c\delta_{\pi VB}\nabla^{\langle\mu}\left(B^{\nu\rangle\gamma}V_\gamma\right),
\end{aligned}
\tag{3.30}
$$

where the resulting second-order transport coefficients are expressed in terms of thermodynamic integrals as shown in Table.(A.1). It's noteworthy that the coefficients $\tau_{\pi V}$ and $\lambda_{\pi V}$ involve derivatives of $l_{\pi V}$ [10], while $\tau_{\pi VB}$ and $\lambda_{\pi VB}$ include derivatives of $\delta_{\pi VB}$, respectively. It's observed that the last four terms explicitly incorporate the magnetic field,

which is a novel addition compared to the case of zero magnetic field [14]. In contrast to the 14-moment approximation employed in [16] for non-zero magnetic fields, only the first ten terms on the right-hand side exhibit a similar form or analogous structure. However, the last three terms are unique to this formulation and do not emerge in the 14-moment approximation. Further discussion on this matter is provided in Section.(3.1.2).

Bulk stress:

Similar to the derivation of shear viscosity, we proceed to derive the second-order evolution equation for bulk viscous stress. By definition:

$$
\Pi_{(2)} = -\frac{\Delta_{\alpha\beta}}{3} \int dp\, p^{\alpha} p^{\beta} \left(\delta \tilde{f}^{(2)} + \delta \tilde{\tilde{f}}^{(2)} \right). \tag{3.31}
$$

Evaluating the integral using $\delta \tilde{f}^{(2)}$ from Eq.(3.20), and noting that the total bulk stress is a combination of first and second-order terms, i.e., $\Pi = \Pi_{(1)} + \Pi_{(2)}$, we obtain, after some algebra (detailed calculations are provided in Appendix.(A.2.2)), the evolution equation for bulk stress:

$$
\begin{aligned}
\frac{\Pi}{\tau_c} =\ & -\dot{\Pi} - \delta_{\Pi\Pi}\Pi\theta + \lambda_{\Pi\pi}\pi^{\mu\nu}\sigma_{\mu\nu} - \tau_{\Pi V} V \cdot \dot{u} - \lambda_{\Pi V} V \cdot \nabla\alpha - l_{\Pi V}\partial \cdot V - \beta_{\Pi}\theta \\
& + \tau_c \tau_{\Pi V B} \dot{u}_{\alpha} q B b^{\alpha\beta} V_{\beta} - \tau_c q \delta_{\Pi V B} \nabla_{\mu}\left(Bb^{\mu\beta}V_{\beta}\right) - \tau_c q B \lambda_{\Pi V B} b^{\mu\beta} V_{\beta} \nabla_{\mu}\alpha, \tag{3.32}
\end{aligned}
$$

where the second-order transport coefficients are expressed in terms of thermodynamic integrals (see Table.(A.2)), and we utilize Eq.(3.26) for the expressions of $\mathcal{X}$ and $\mathcal{Y}$. The coefficients $\tau_{\Pi V}$ and $\lambda_{\Pi V}$ contain derivatives of $l_{\Pi V}$, while $\tau_{\Pi V B}$ and $\lambda_{\Pi V B}$ involve derivatives of $\delta_{\Pi V B}$. Notably, the last three terms of the equation are new compared to those in [14] and are dependent on the magnetic field. In comparison to the 14-moment approximation in [16] in the presence of a magnetic field, the bulk viscous relaxation equation did not include any magnetic field-dependent terms.

Diffusion current:

The expression for the second-order contribution to the diffusion current for the net charge is given by:

$$V_{(2)}^\mu = \Delta_\alpha^\mu \int dp \, p^\alpha \left(\delta \tilde{f}^{(2)} - \delta \bar{\tilde{f}}^{(2)} \right),$$ (3.33)

where $\delta \tilde{f}^{(2)}$ is taken from Eq.(3.20). Like other dissipative quantities, the total diffusion four-vector is composed of first and second-order terms, i.e., $V^\mu = V_{(1)}^\mu + V_{(2)}^\mu$. After evaluating the integral (for details see Appendix.(A.2.3)), we obtain the following second-order evolution equation for the diffusion current:

$$
\begin{aligned}
\frac{V^\mu}{\tau_c} = & -\dot{V}^{\langle\mu\rangle} - V_\nu \omega^{\nu\mu} - \lambda_{VV} V^\nu \sigma_\nu^\mu - \delta_{VV} V^\mu \theta + \lambda_{V\Pi} \Pi \nabla^\mu \alpha - \lambda_{V\pi} \pi^{\mu\nu} \nabla_\nu \alpha - \tau_{V\pi} \pi_\nu^\mu \dot{u}^\nu \\
& + \tau_{V\Pi} \Pi \dot{u}^\mu + l_{V\pi} \Delta^{\mu\nu} \partial_\gamma \pi_\nu^\gamma - l_{V\Pi} \nabla^\mu \Pi + \beta_V \nabla^\mu \alpha - qB \delta_{VB} b^{\mu\gamma} V_\gamma + \tau_c q B l_{V\pi B} b^{\sigma\mu} \partial^\kappa \pi_{\kappa\sigma} \\
& + \tau_c q B \tau_{V\Pi B} b^{\gamma\mu} \Pi \dot{u}_\gamma - \tau_c q B l_{V\Pi B} b^{\gamma\mu} \nabla_\gamma \Pi - q\tau_c \delta_{VVB} B b^{\mu\nu} V_\nu \theta - q\tau_c \lambda_{VVB} B b^{\gamma\nu} V_\nu \sigma_\gamma^\mu \\
& - q\tau_c \rho_{VVB} B b^{\gamma\nu} V_\nu \omega_\gamma^\mu - \tau_c q \tau_{VVB} \Delta_\gamma^\mu D \left(B b^{\gamma\nu} V_\nu \right).
\end{aligned}
$$ (3.34)

The second-order transport coefficients are expressed in terms of thermodynamic integrals, as detailed in Table.(A.3). Specifically, the coefficients $\tau_{V\pi}$ and $\lambda_{V\pi}$ involve the derivative of $l_{V\pi}$, while $\tau_{V\Pi}$ and $\lambda_{V\Pi}$ involve the derivative of $l_{V\Pi}$. Additionally, δ_{VVB} contains the derivative of τ_{VVB}. In deriving the final expression in Eq.(3.34), we utilize $\mathcal{X}$ and $\mathcal{Y}$ from Eq.(3.26). Comparing our result to the RTA calculation in [14] without a magnetic field reveals that the last eight terms on the RHS are new and dependent on the magnetic field. Similarly, comparing with the relaxation equation for diffusion in the presence of a magnetic field in [16] using the 14-moment approximation indicates that the first 13 terms share a similar form, while the last seven terms are absent in the moment method.

Analysis at the ultrarelativistic and weak field limit

In the ultra-relativistic limit ($m/T \to 0$), the transport coefficients for a classical Maxwell gas with a constant relaxation time τ_c can be analytically calculated using thermodynamic integrals. These coefficients can be categorized as follows: (i) Coefficients independent

Transport Coefficients	Denicol et al.	CE
β_π	$4P/5$	$4P/5$
$\tau_{\pi\pi}$	$10/7$	$10/7$
$\delta_{\pi\pi}$	$4/3$	$4/3$
$\tau_{\pi V}$	0	0
$\lambda_{\pi V}$	0	0
$l_{\pi V}$	0	0

(a)

Transport Coefficients	Denicol et al.	CE
$\delta_{\pi B}$	$2\beta/5$	$\beta/2$
δ_{VB}	$5\beta/12$	β
$\delta_{\pi VB}$	$-$	$2/5$
$\delta_{\Pi VB}$	$-$	$1/3$
$\tau_{\Pi VB}$	$-$	$2/3$
$l_{V\pi B}$	$-$	$\beta^2/12$
$\tau_{V\Pi B}$	$-$	$\beta^2/12$
$l_{V\Pi B}$	$-$	$\beta^2/12$
δ_{VVB}	$-$	$\beta/3$
λ_{VVB}	$-$	$3\beta/20$
ρ_{VVB}	$-$	$\beta/4$
τ_{VVB}	$-$	$\beta/4$

(c)

Transport Coefficients	Denicol et al.	CE
β_V	$n_f/12$	$n_f/12$
λ_{VV}	$3/5$	$3/5$
δ_{VV}	1	1
$\tau_{V\pi}$	$\beta/20$	$\beta/4$
$\lambda_{V\pi}$	$\beta/20$	$\beta/16$
$l_{V\pi}$	$\beta/20$	$\beta/4$

(b)

Table 3.1: (a) Comparison of coefficients for the shear-stress equation of a massless Boltzmann gas (particle only) calculated using the Chapman-Enskog (CE) method in this work and by Denicol et al. using the 14-moment method [17]. (b) Comparison of coefficients for the diffusion equation of a massless Boltzmann gas (particle only) calculated using the Chapman-Enskog (CE) method in this work and by Denicol et al. using the 14-moment method [17]. (c) Transport coefficients in the shear, bulk, and diffusion equations that couple the magnetic field and dissipative quantities for a massless Boltzmann gas (particles only).

of the magnetic field are listed in Tables.(3.1)(a) and (3.1)(b) for the shear and number diffusion, respectively. (ii) Magnetic field-dependent coefficients are presented in Table.(3.1)(c). In this limit, the bulk viscous pressure vanishes and is not considered. Additionally, Table.(3.1) includes results obtained from the 14-moment approximation in the presence of a magnetic field [16] in the ultra-relativistic limit. It's important to note that in this scenario, the coefficients $\delta_{\pi B}$ and δ_{VB} differ between the two approaches mentioned above.

In the regime of weak magnetic fields, characterized by temperatures much larger than the strength of the magnetic field ($T^2 \gg qB$), we introduce the dimensionless parameter $g_B = qB/T^2$, where $g_B \ll 1$. In the presence of a magnetic field, the relaxation-time approximation (RTA) expansion in Eq.(3.14) involves two power counting schemes: $\mathrm{Kn} = \tau_c T$ and $\chi = qB\tau_c/T$. However, in the weak field limit, the expansion parameter $\chi = g_B\tau_c T$ becomes small, and thus it is treated as a sub-leading contribution. Consequently, at second-order, one effectively retains terms up to $\mathcal{O}(\mathrm{Kn}^2)$ in spatial gradients and $\mathcal{O}(\chi \cdot \mathrm{Kn})$ for mixed terms [1]. In this limit, the relaxation equations reduces to the following forms:

$$
\dot{\pi}^{\mu\nu} = 2\beta_\pi \sigma^{\mu\nu} - \frac{\pi^{\mu\nu}}{\tau_c} + 2\pi_\gamma^{\langle\mu}\omega^{\nu\rangle\gamma} - \tau_{\pi\pi}\pi_\gamma^{\langle\mu}\sigma^{\nu\rangle\gamma} - \delta_{\pi\pi}\pi^{\mu\nu}\theta + \lambda_{\pi\Pi}\Pi\sigma^{\mu\nu}
$$
$$
- \tau_{\pi V}V^{\langle\mu}\dot{u}^{\nu\rangle} + \lambda_{\pi V}V^{\langle\mu}\nabla^{\nu\rangle}\alpha + l_{\pi V}\nabla^{\langle\mu}V^{\nu\rangle} + \delta_{\pi B}\Delta_{\eta\beta}^{\mu\nu}qBb^{\gamma\eta}g^{\beta\rho}\pi_{\gamma\rho}, \qquad (3.35)
$$

$$
\dot{\Pi} = -\beta_\Pi\theta - \frac{\Pi}{\tau_c} - \delta_{\Pi\Pi}\Pi\theta + \lambda_{\Pi\pi}\pi^{\mu\nu}\sigma_{\mu\nu} - \tau_{\Pi V}V \cdot \dot{u} - \lambda_{\Pi V}V \cdot \nabla\alpha - l_{\Pi V}\partial \cdot V, \qquad (3.36)
$$

$$
\dot{V}^{\langle\mu\rangle} = \beta_V\nabla^\mu\alpha - \frac{V^\mu}{\tau_c} - V_\nu\omega^{\nu\mu} - \lambda_{VV}V^\nu\sigma_\nu^\mu - \delta_{VV}V^\mu\theta + \lambda_{V\Pi}\Pi\nabla^\mu\alpha - \lambda_{V\pi}\pi^{\mu\nu}\nabla_\nu\alpha
$$
$$
- \tau_{V\pi}\pi_\nu^\mu\dot{u}^\nu + \tau_{V\Pi}\Pi\dot{u}^\mu + l_{V\pi}\Delta^{\mu\nu}\partial_\gamma\pi_\nu^\gamma - l_{V\Pi}\nabla^\mu\Pi - qB\delta_{VB}b^{\mu\gamma}V_\gamma. \qquad (3.37)
$$

The above set of simplified relaxation equations presented in Eqs.(3.35)-(3.37) corresponds to the relaxation equations derived in [16]. In the weak magnetic field limit, the

---

[1] We do not consider terms of $\mathcal{O}(\chi^2)$ since they do not contribute to the expansion in Eq.(3.14).
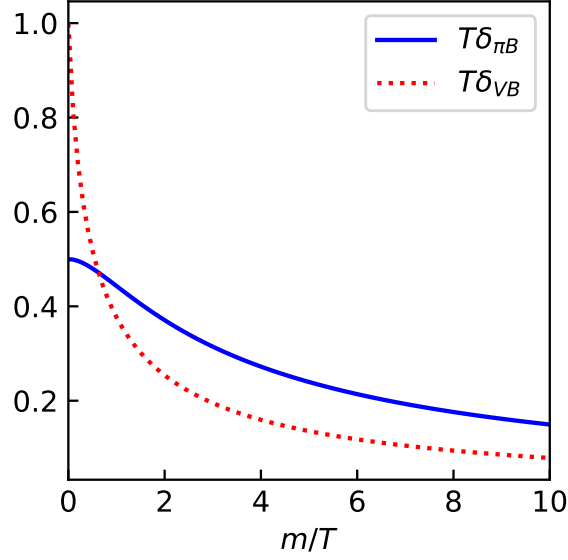
Figure 3.1: Dimensionless transport coefficients $T\delta_{VB}$ and $T\delta_{\pi B}$ that couple fluid to magnetic field as a function of m/T.

dimensionless magnetic field-dependent transport coefficients $T\delta_{\pi B}$ and $T\delta_{VB}$ are depicted in Fig.(3.1) as functions of m/T. As m/T approaches 0, these coefficients converge to the values obtained in Table.(3.1)(c).

Navier-Stokes limit

In the Navier-Stokes limit, we retain terms $\mathcal{O}(\text{Kn})$ and $\mathcal{O}(\chi \cdot \text{Kn})$, which results in the first and second terms on the right-hand side of Eqs.(3.35)-(3.37) being of first-order in gradients, along with the last term, which is both dependent on the magnetic field and first-order in gradients. Rearranging these terms, we obtain:

$$\frac{\Pi}{\tau_c} = \beta_\Pi \theta, \tag{3.38}$$

$$\left(\frac{g^{\mu\nu}}{\tau_c} + qB\delta_{VB}b^{\mu\gamma} \right) V_\gamma = \beta_V \nabla^\mu \alpha, \tag{3.39}$$

$$\left(\frac{g^{\mu\gamma}g^{\nu\rho}}{\tau_c} - \delta_{\pi B}\Delta_{\eta\beta}^{\mu\nu}qBb^{\gamma\eta}g^{\beta\rho} \right) \pi_{\gamma\rho} = 2\beta_\pi \sigma^{\mu\nu}. \tag{3.40}$$

Since the bulk viscous pressure remains independent of any magnetic field influence, the Navier-Stokes limit for bulk viscosity ζ is straightforwardly identical to the case without magnetic fields, i.e., $\zeta = \beta_\Pi \tau_c$. To proceed, we need to solve for the constitutive relations by inverting the coefficients multiplied on the left side of the remaining equations. The general solution for the remaining equations is given as follows:

$$V_\gamma = \left(\kappa_\parallel P_{\delta\gamma}^\parallel + \kappa_\perp P_{\delta\gamma}^\perp + \kappa_\times P_{\delta\gamma}^\times \right) \partial^\delta \alpha, \tag{3.41}$$

$$\pi_{\gamma\rho} = \left(\eta_0 P_{\alpha\beta\gamma\rho}^{(0)} + \eta_1 \left(P_{\alpha\beta\gamma\rho}^{(1)} + P_{\alpha\beta\gamma\rho}^{(-1)} \right) + i\eta_2 \left(P_{\alpha\beta\gamma\rho}^{(1)} - P_{\alpha\beta\gamma\rho}^{(-1)} \right) \right.$$
$$\left. + \eta_3 \left(P_{\alpha\beta\gamma\rho}^{(2)} + P_{\alpha\beta\gamma\rho}^{(-2)} \right) + i\eta_4 \left(P_{\alpha\beta\gamma\rho}^{(2)} - P_{\alpha\beta\gamma\rho}^{(-2)} \right) \right) \sigma^{\alpha\beta}. \tag{3.42}$$

Here, $P_{\delta\gamma}^\parallel$, $P_{\delta\gamma}^\perp$, and $P_{\delta\gamma}^\times$ are second-rank projection tensors, while $P_{\alpha\beta\gamma\rho}^{(n)}$, where $n = -2$ to $n = +2$, are fourth-rank projection tensors. The symbol i represents the imaginary unit. Further details on the definitions of these tensors can be found in Appendix.(A.3), and additional information is available in references [20, 21]. The transport coefficients $\kappa_\parallel$, $\kappa_\perp$, $\kappa_\times$, and η_0 to η_4 play crucial roles in characterizing the system's behavior. These coefficients can be determined by substituting the solutions derived earlier into the left-hand side of Eqs.(3.40) and (3.39), followed by the application of properties associated with projection tensors. The resulting expressions for the diffusion coefficients are as follows:

$$\kappa_\parallel = \beta_V \tau_c, \tag{3.43}$$

$$\kappa_\perp = \frac{\beta_V \tau_c}{1 + (qB\tau_c \delta_{VB})^2}, \tag{3.44}$$

$$\kappa_\times = \frac{\beta_V qB\tau_c^2 \delta_{VB}}{1 + (qB\tau_c \delta_{VB})^2} = \kappa_\perp qB\tau_c \delta_{VB}. \tag{3.45}$$

Similarly, the shear viscous coefficients are expressed as:

$$\eta_0 = 2\beta_\pi \tau_c, \tag{3.46}$$

$$\eta_1 = \frac{2\beta_\pi \tau_c}{1 + (2qB\tau_c\delta_{\pi B})^2}, \tag{3.47}$$

$$\eta_2 = \frac{4\beta_\pi qB\tau_c^2\delta_{\pi B}}{1 + (2qB\tau_c\delta_{\pi B})^2} = 2\eta_1 qB\tau_c\delta_{\pi B}, \tag{3.48}$$

$$\eta_3 = \frac{2\beta_\pi \tau_c}{1 + (qB\tau_c\delta_{\pi B})^2}, \tag{3.49}$$

$$\eta_4 = \frac{2\beta_\pi qB\tau_c^2\delta_{\pi B}}{1 + (qB\tau_c\delta_{\pi B})^2} = \eta_3 qB\tau_c\delta_{\pi B}. \tag{3.50}$$

Notably, η_1 and η_3 exhibit even functions concerning the magnetic field, while η_2 and η_4 may take either sign, representing odd functions of B. Fig.(3.2) illustrates the magnetic-field dependence of these coefficients, comparing results from the current work (solid lines) with those from reference [16] (dotted lines). In the limit of a vanishing magnetic field, i.e., $qB \to 0$, the diffusion coefficients reduce to $\kappa_\times \to 0$ and $\kappa_\parallel = \kappa_\perp$, whereas the shear viscous coefficients simplify to $\eta_2 = \eta_4 = 0$ and $\eta_1 = \eta_3 = \eta_0$, consistent with expectations. The transport coefficients identified in the Navier-Stokes limit in this study are denoted as $\kappa_\parallel$, $\kappa_\perp$, and $\kappa_\times$ for the diffusion coefficients, and $\eta_0, \eta_1, \eta_2, \eta_3, \eta_4$ for the shear viscous coefficients. In contrast, [16] labels them as $\kappa_{0\parallel}$, $\kappa_{0\perp}$, $\kappa_{0\times}$, $\eta_{00}, \eta_{01}, \eta_{02}, \eta_{03}, \eta_{04}$. Utilizing the same basis as [16], the following relations between the transport coefficients are established [22]:

$$\kappa_{0\parallel} \equiv \kappa_\parallel,$$

$$\kappa_{0\perp} \equiv \kappa_\perp,$$

$$\kappa_{0\times} \equiv \kappa_\times,$$

$$\tag{3.51}$$
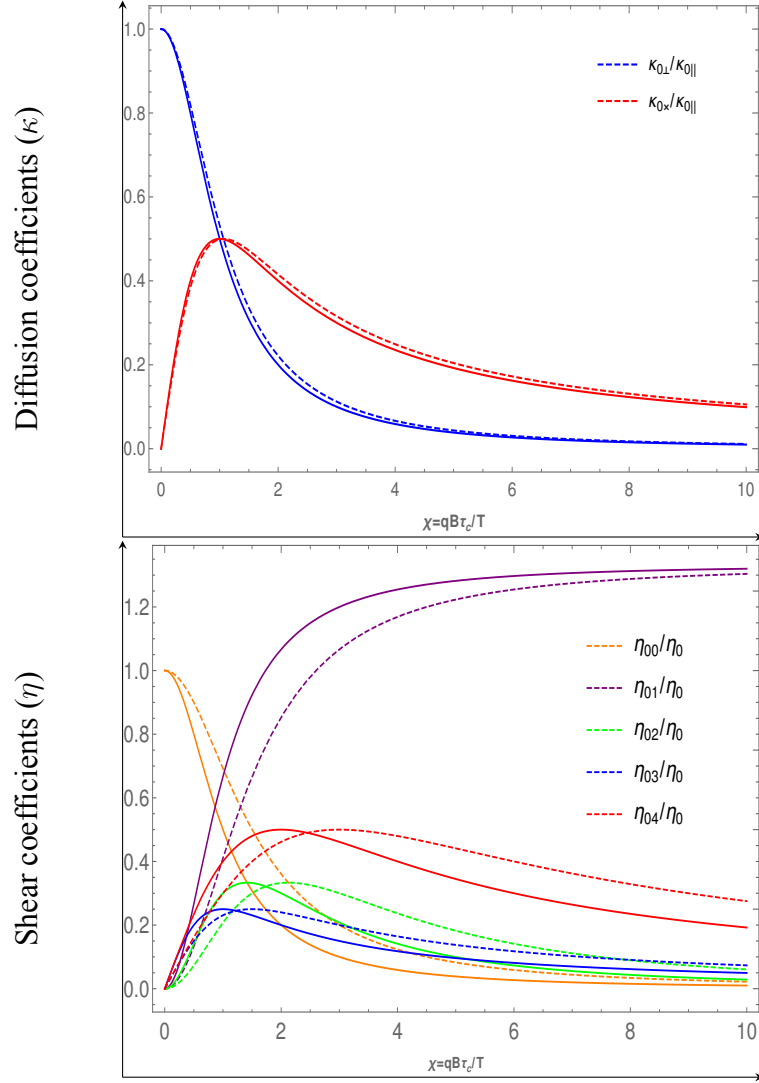
Figure 3.2: The magnetic-field dependence of the diffusion coefficients (top plot) and the shear-viscosity coefficients (bottom plot). The solid lines are the results from the current work while the dotted lines are from ref. [16].

$$\eta_{00} \equiv \eta_1,$$

$$\eta_{01} \equiv \frac{16(qB\tau_c\delta_{\pi B})^2}{3}\eta_1,$$

$$\eta_{02} \equiv \eta_3 - \eta_1,$$

$$\eta_{03} \equiv \frac{\eta_2}{2},$$

$$\eta_{04} \equiv \eta_4. \tag{3.52}$$

Mass Dependence — **Temperature Dependence**

Top left ($\delta_{\pi VB}$ vs mass): T = 120 MeV, T = 100 MeV, T = 80 MeV

Top right ($\delta_{\pi VB}$ vs temperature): m = 120 MeV, m = 100 MeV, m = 80 MeV

Middle left ($\delta_{\Pi VB}$ vs mass): T = 120 MeV, T = 100 MeV, T = 80 MeV

Middle right ($\delta_{\Pi VB}$ vs temperature): m = 120 MeV, m = 100 MeV, m = 80 MeV

Bottom left ($I_{V\pi B}, I_{V\Pi B}, \tau_{V\Pi B}$ vs mass): T = 120 MeV, T = 100 MeV, T = 80 MeV

Bottom right: m = 500 MeV, m = 250 MeV, m = 100 MeV
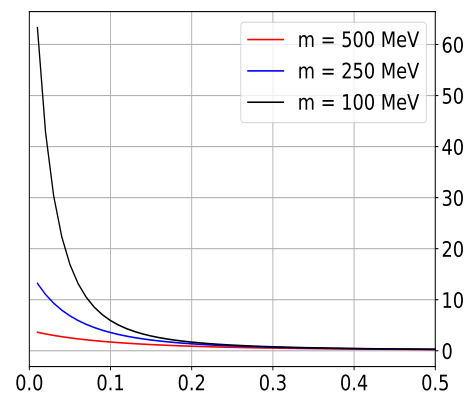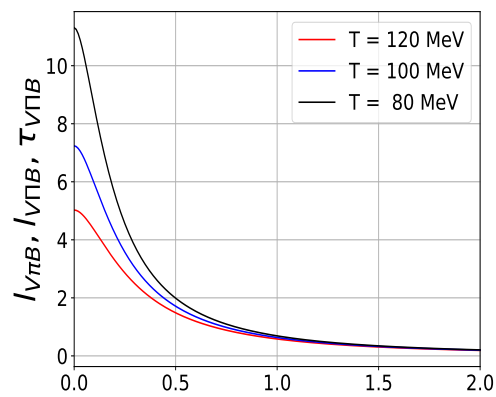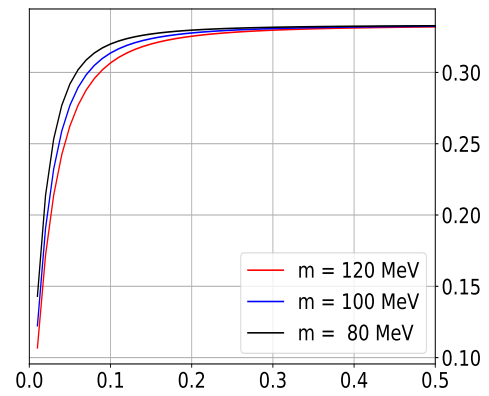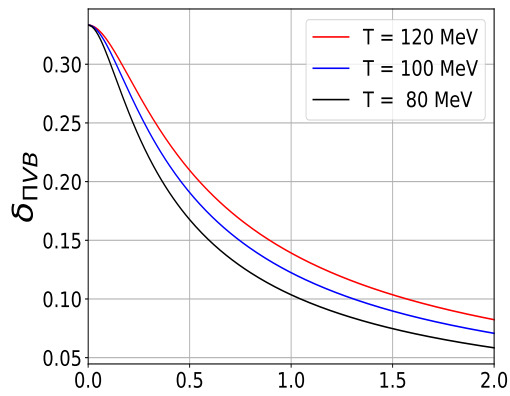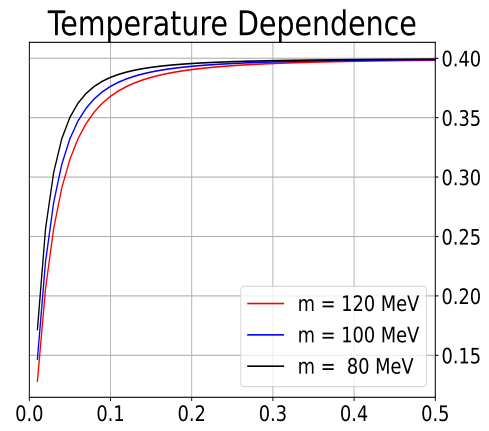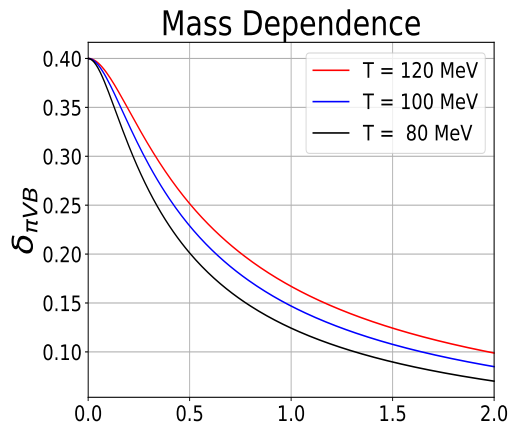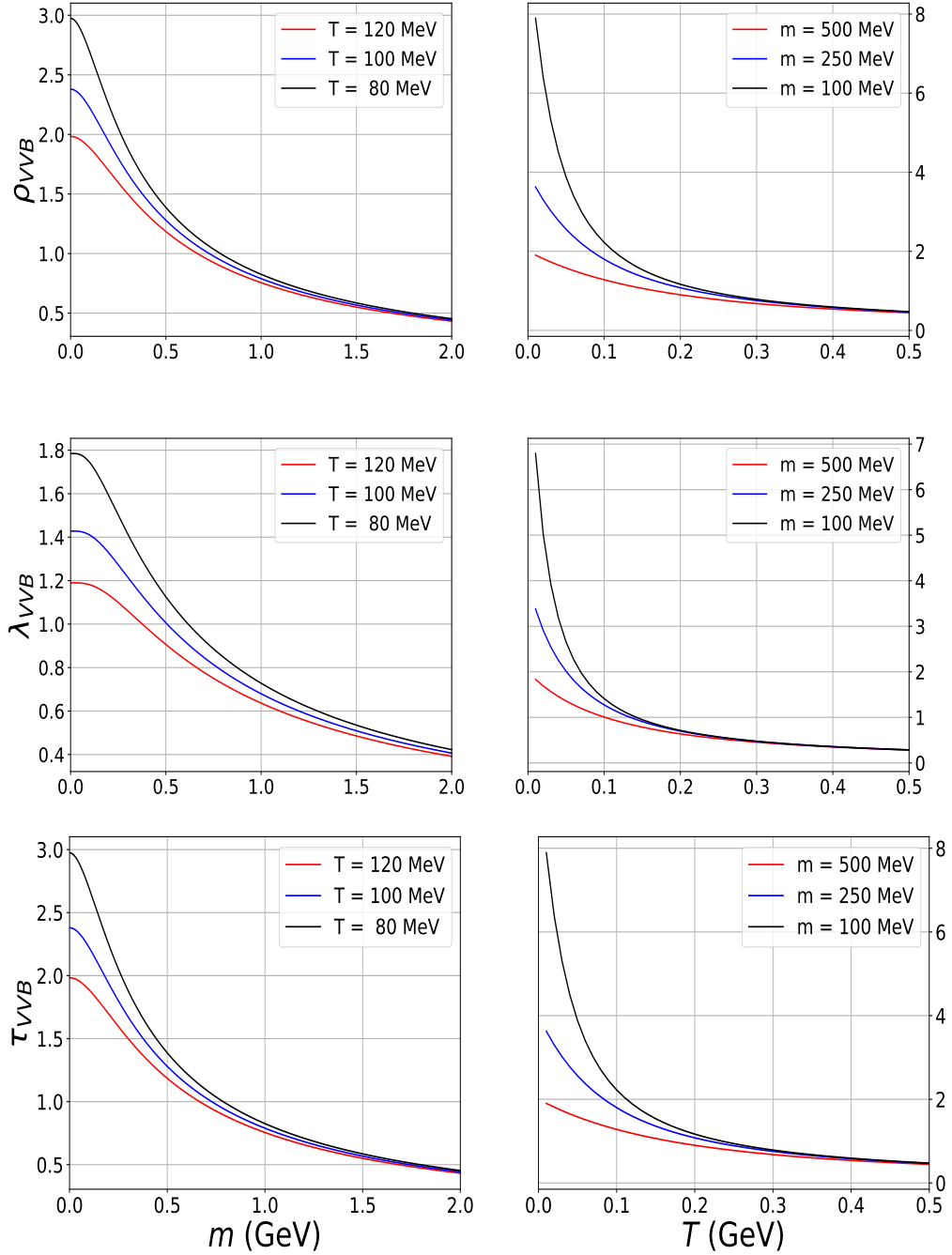
Figure 3.3: Mass and temperature variation of the transport coefficients arising due to external magnetic field at second-order.

A comparison of the transport coefficients obtained from both approaches in the $m = 0$ limit is depicted in Fig.(3.2), where they are plotted as functions of $\chi = qB\tau_c/T$. In this plot, the solid lines represent the results derived from the RTA method employed in our current study, while the dotted lines represent the outcomes obtained from the 14-moment approximation as reported in [16]. Notably, although there are quantitative discrepancies between the two sets of coefficients, they exhibit a similar qualitative behavior. These differences can be attributed to the distinct values of the transport coefficients $\delta_{\pi B}$ and δ_{VB} obtained in each approach.

Now we move onto the remaining transport coefficients. In Fig.(3.3), we plot the different transport coefficients with respect to mass or temperature. We observe that $\delta_{\pi VB}$ and $\delta_{\Pi VB}$ are sensitive to various temperatures at high mass (m), whereas for various masses, they are sensitive only at the low temperatures (T). We see that at increasing temperatures values of these transport coefficients are also increasing (clearly visible at high mass regions), whereas it is reverse in case of variation with masses. On the other hand, for other transport coefficients such as $l_{V\pi B}$, $l_{V\Pi B}$, $\tau_{V\Pi B}$, ρ_{VVB}, λ_{VVB}, and τ_{VVB}, they appear distinguishable for different temperatures at the low mass limit, while for various masses, they are distinguishable at the low-temperature limit.

3.2 Resistive MHD

Expanding on our previous analysis, we will now develop a more complete set of equations for dissipative stresses at different orders by relaxing the ideal MHD assumption of infinite conductivity.

3.2.1 Formalism

Following a similar procedure as in the previous case, we commence by deriving the off-equilibrium distribution function up to the second-order. Subsequently, utilizing the relation

between dissipative stresses and the distribution function, we derive the complete set of evolution equations.

Off-equilibrium correction to distribution functions upto second-order:

Utilizing a technique similar to that employed in the non-resistive scenario, we compute the δf corrections. Eq.(3.11) can be expressed as a power series expansion in the following manner:

$$f = \sum_{n=0}^{\infty} (-1)^n \left(\frac{\tau_c}{u.p} \right)^n \left(p^\mu \partial_\mu + q F^{\mu\nu} p_\nu \frac{\partial}{\partial p^\mu} \right)^n f_0. \tag{3.53}$$

In the scenario without electrical resistance, there were two expansion parameters: Kn $= \tau_c \partial_\mu$ and $\chi = q B \tau_c / T$. Here, the electric field wasn't treated as an independent degree of freedom; instead, it was linked to the magnetic field as $\mathbf{E} = -\mathbf{v} \times \mathbf{B}$. However, upon relaxing the assumption of infinite conductivity and explicitly incorporating the electric field's impact in our computations, an additional expansion parameter, $\xi = q E \tau_c / T$, alongside Kn and χ naturally arises. When truncating the expansion up to the second-order, we find:

$$f = f_0 + \delta f^{(1)} + \delta f^{(2)}, \tag{3.54}$$

where

$$\delta f^{(1)} = -\frac{\tau_c}{u \cdot p} \left(p^\mu \partial_\mu f_0 + \beta q E^\nu p_\nu f_0 \tilde{f}_0 \right), \tag{3.55}$$

$$\delta f^{(2)} = \mathcal{F}_1 + \mathcal{F}_2 + \mathcal{F}_3 + \mathcal{F}_4, \tag{3.56}$$

$$\mathcal{F}_1 = \frac{\tau_c}{u \cdot p} p^\mu \partial_\mu \left(\frac{\tau_c}{u \cdot p} p^\sigma \partial_\sigma f_0 \right),$$

$$\mathcal{F}_2 = \frac{\tau_c}{u \cdot p} p^\mu \partial_\mu \left(\frac{q \tau_c}{u \cdot p} f_0 \tilde{f}_0 \beta (E \cdot p) \right),$$

$$\mathcal{F}_3 = \frac{q \tau_c}{u.p} F^{\mu\nu} p_\nu \frac{\partial}{\partial p^\mu} \left(\frac{\tau_c}{u \cdot p} p^\sigma \partial_\sigma f_0 \right),$$

$$\mathcal{F}_4 = \frac{q^2 \tau_c}{u \cdot p} F^{\mu\nu} p_\nu \frac{\partial}{\partial p^\mu} \left(\frac{\tau_c}{u \cdot p} f_0 \tilde{f}_0 \beta (E \cdot p) \right).$$

Similarly the correction for anti-particles ($\delta \bar{f}$) are also calculated.

3.2.2 Results

After having these we will now move onto deriving the results for the first and second-order equations for shear, bulk and diffusion currents.

First order Constitutive relations

Having the δf's, now truncating upto $\mathcal{O}(\partial)$, $\mathcal{O}(\partial \chi)$ and $\mathcal{O}(\xi)$, we find the expressions for different dissipative stresses, here we will start with the bulk case.

Bulk Stress:

Utilizing Eq.(3.55), we compute the first-order dissipative fluxes. The first-order bulk stress is expressed as

$$\Pi_{(1)} = -\frac{\Delta_{\mu\nu}}{3} \int dp p^\mu p^\nu \left(\delta f^{(1)} + \delta \bar{f}^{(1)} \right) . \tag{3.57}$$

After some algebraic manipulation, we arrive at

$$\Pi_{(1)} = -\tau_c \beta_\Pi \theta, \tag{3.58}$$

where $\beta_\Pi = \frac{5\beta}{3} J_{42}^{(1)+} + \mathcal{X} J_{31}^{(0)+} - \mathcal{Y} J_{21}^{(0)-}$ with

$$\mathcal{X} = \frac{J_{10}^{(0)+} (\epsilon + P) - J_{20}^{(0)-} n_f}{D_{20}}$$

and

$$\mathcal{Y} = \frac{J_{20}^{(0)-} (\epsilon + P) - J_{30}^{(0)+} n_f}{D_{20}}$$

Diffusion Current:

The diffusion current for the first order is given by

$$V_{(1)}^\mu = \Delta_\alpha^\mu \int dp p^\alpha \left(\delta f^{(1)} - \delta \bar{f}^{(1)} \right) . \tag{3.59}$$

Using Eq. (3.55) we get

$$V_{(1)}^\mu = \tau_c \beta_V \left(\nabla^\mu \alpha + \beta q E^\mu \right) , \tag{3.60}$$

where $\beta_V = \frac{1}{h} J_{21}^{(0)-} - J_{21}^{(1)-}$.

Shear Stress:

The shear stress for the first order is given by

$$\pi_{(1)}^{\mu\nu} = \Delta_{\alpha\beta}^{\mu\nu} \int dp\, p^\alpha p^\beta \left(\delta f^{(1)} + \delta \bar{f}^{(1)} \right), \tag{3.61}$$

Using Eq.(3.55) we get

$$\pi_{(1)}^{\mu\nu} = 2\tau_c \beta_\pi \sigma^{\mu\nu}, \tag{3.62}$$

where $\beta_\pi = \beta J_{42}^{(1)+}$.

The first-order expressions reveal that both the bulk and shear stress cases yield identical results irrespective of any electromagnetic fields, consistent with the findings in the previous scenario. Conversely, the diffusion current exhibits contributions originating from E^μ.

Second-order evolution equations

The second-order evolution equations are found as follows.

Bulk Stress

In a manner akin to the first-order scenario, the expression for the second-order bulk stress is derived as follows:

$$\Pi_{(2)} = -\frac{\Delta_{\alpha\beta}}{3} \int dp\, p^\alpha p^\beta \left(\delta f^{(2)} + \delta \bar{f}^{(2)} \right). \tag{3.63}$$

Here, the total bulk stress encompasses contributions from both first and second-order terms, represented as:

$$\Pi = \Pi_{(1)} + \Pi_{(2)}. \tag{3.64}$$

The evolution equation governing the bulk stress is derived by considering Eq.(3.63) along with Eq.(3.64) (refer to Appendix.(A.5.1) for detailed derivation):

$$
\begin{aligned}
\frac{\Pi}{\tau_c} = {} & -\dot{\Pi} - \delta_{\Pi\Pi}\Pi\theta + \lambda_{\Pi\pi}\pi^{\mu\nu}\sigma_{\mu\nu} - \tau_{\Pi V} V \cdot \dot{u} - \lambda_{\Pi V} V \cdot \nabla\alpha \\
& - l_{\Pi V}\partial \cdot V - \beta_\Pi\theta - qB\lambda_{\Pi V B}b^{\mu\beta}V_\beta V_\mu \\
& + \tau_c\tau_{\Pi V B}\dot{u}_\alpha qB b^{\alpha\beta}V_\beta - q\delta_{\Pi V B}\nabla_\mu\left(\tau_c B b^{\mu\beta}V_\beta\right) - q^2\tau_c\chi_{\Pi E E}E^\mu E_\mu.
\end{aligned}
\tag{3.65}
$$

Here, the transport coefficients featured in Eq.(3.65) are cataloged in Table.(A.4), while the remaining coefficients retain their conventional interpretations as discussed for the ideal MHD (non-resistive) case.

Diffusion Current

The derivation of the diffusion current expression follows a similar approach, albeit with a key distinction: the particle and antiparticle contributions are no longer additive. We define the second-order diffusion current as:

$$
V^\mu_{(2)} = \Delta^\mu_\alpha \int dp\, p^\alpha \left(\delta f^{(2)} - \delta\bar{f}^{(2)}\right).
\tag{3.66}
$$

Combining the first and second-order terms, the total diffusion current is expressed as:

$$
V^\mu = V^\mu_{(1)} + V^\mu_{(2)}.
\tag{3.67}
$$

The second-order evolution equation for the diffusion current is derived from Eq.(3.66) and Eq.(3.67) (refer to Appendix.(A.5.2) for detailed derivation).

$$\frac{V^\mu}{\tau_c} = -\dot{V}^{\langle\mu\rangle} - V_\nu \omega^{\nu\mu} + \lambda_{VV} V^\nu \sigma^\mu_\nu - \delta_{VV} V^\mu \theta + \lambda_{V\Pi} \Pi \nabla^\mu \alpha - \lambda_{V\pi} \pi^{\mu\nu} \nabla_\nu \alpha$$

$$- \tau_{V\pi} \pi^\mu_\nu \dot{u}^\nu - qB \delta_{VB} b^{\mu\gamma} V_\gamma + \tau_{V\Pi} \Pi \dot{u}^\mu + l_{V\pi} \Delta^{\mu\nu} \partial_\gamma \pi^\gamma_\nu$$

$$- l_{V\Pi} \nabla^\mu \Pi + \beta_V \nabla^\mu \alpha + \tau_c qB l_{V\pi B} b^{\sigma\mu} \partial^\kappa \pi_{\kappa\sigma} - q\tau_c \lambda_{VVB} Bb^{\gamma\nu} V_\nu \sigma^\mu_\gamma$$

$$+ \tau_c qB \tau_{V\Pi B} b^{\gamma\mu} \Pi \dot{u}_\gamma - \tau_c qB l_{V\Pi B} b^{\gamma\mu} \nabla_\gamma \Pi - q\tau_c \delta_{VVB} Bb^{\mu\nu} V_\nu \theta$$

$$- q\tau_c \rho_{VVB} Bb^{\gamma\nu} V_\nu \omega^\mu_\gamma + \chi_{VE} qE^\mu + q\Delta^\mu_\alpha \chi_{VE} D\left(\tau_c E^\alpha\right)$$

$$- q\tau_c \rho_{VE} E^\mu \theta - q\tau_{VVB} \Delta^\mu_\gamma D\left(\tau_c Bb^{\gamma\nu} V_\nu\right). \tag{3.68}$$

The coefficients associated with the resistive case are detailed in Table.(A.5), while the remaining transport coefficients retain their properties as in the ideal MHD scenario.

Shear Stress

The second-order shear stress expression is derived using the following definition:

$$\pi^{\mu\nu}_{(2)} = \Delta^{\mu\nu}_{\alpha\beta} \int dp\, p^\alpha p^\beta \left(\delta f^{(2)} + \delta \bar{f}^{(2)}\right). \tag{3.69}$$

It's important to note that the total shear stress comprises both first and second-order terms:

$$\pi^{\mu\nu} = \pi^{\mu\nu}_{(1)} + \pi^{\mu\nu}_{(2)}. \tag{3.70}$$

Evaluating the integral in Eq.(3.69) (detailed in Appendix.(A.5.3)) and combining it with Eq.(3.70), we obtain the evolution equation for the shear stress:

$$\frac{\pi^{\mu\nu}}{\tau_c} = -\dot{\pi}^{\langle\mu\nu\rangle} + 2\beta_\pi \sigma^{\mu\nu} + 2\pi^{\langle\mu}_\gamma \omega^{\nu\rangle\gamma} - \tau_{\pi\pi} \pi^{\langle\mu}_\gamma \sigma^{\nu\rangle\gamma} - \delta_{\pi\pi} \pi^{\mu\nu} \theta$$

$$+ \lambda_{\pi\Pi} \Pi \sigma^{\mu\nu} - \tau_{\pi V} V^{\langle\mu} \dot{u}^{\nu\rangle} - \tau_c qB \tau_{\pi VB} \dot{u}^{\langle\mu} b^{\nu\rangle\sigma} V_\sigma$$

$$+ \lambda_{\pi V} V^{\langle\mu} \nabla^{\nu\rangle} \alpha - l_{\pi V} \nabla^{\langle\mu} V^{\nu\rangle} + \delta_{\pi B} \Delta^{\mu\nu}_{\eta\beta} qB b^{\gamma\eta} g^{\beta\rho} \pi_{\gamma\rho}$$

$$- qB \lambda_{\pi VB} V_\gamma b^{\gamma\langle\mu} V^{\nu\rangle} - q\delta_{\pi VB} \nabla^{\langle\mu}\left(\tau_c B^{\nu\rangle\gamma} V_\gamma\right) + q^2 \tau_c \chi_{\pi EE} \Delta^{\mu\nu}_{\sigma\rho} E^\sigma E^\rho. \tag{3.71}$$

The coefficients appearing only for the resistive case in Eq.(3.71) are listed in Table.A.6, while the remaining coefficients remain consistent with the ideal MHD scenario.

Transport Coefficients	CE	Denicol et al.
$\tau_{\Pi V}$	0	0
$\chi_{\Pi EE}$	$\beta^2 P/36$	–
$\lambda_{\Pi V}$	$1/(3\beta)$	0
$l_{\Pi V}$	0	0
$\lambda_{\Pi VB}$	$3/(\beta P)$	–

(a)

Transport Coefficients	CE	Denicol et al.
λ_{VV}	$2/5$	$3/5$
δ_{VV}	$22/3$	1
δ_{VB}	2β	$5\beta/12$
ρ_{VE}	$P\beta^2/18$	–
χ_{VE}	$P\beta^2/12$	$P\beta^2/12$

(b)

Transport Coefficients	CE	Denicol et al.
$\tau_{\pi V}$	$12/(5\beta)$	0
$l_{\pi V}$	$12/(5\beta)$	0
$\lambda_{\pi V}$	$11/5\beta$	0
$\lambda_{\pi VB}$	$24/5(\beta P)^{-1}$	–
$\chi_{\pi EE}$	$2\beta^2 P/15$	–

(c)

Table 3.2: (a) Transport coefficients for the bulk-stress for a massless Boltzmann gas (result for particles only and for zero chemical potential) calculated using CE method (this work) and compared with the results from the moment method [17] (b) same as Table.(3.2)(a) but for diffusion current (c) same as Table.(3.2)(a) but for shear stress.

Navier-stokes relations

Here, we isolate the terms that are only first-order in gradients in Eqs.(3.65), (3.68), and (3.71) to obtain the Navier-Stokes limit:

$$\frac{\Pi}{\tau_c} = -\beta_\Pi \theta, \tag{3.72}$$

$$V^\mu + qB\tau_c\delta_{VB}b^{\mu\nu}V_\nu - q\tau_c\beta\beta_V E^\mu = \tau_c\beta_V\nabla^\mu\alpha, \tag{3.73}$$

$$\left(\frac{g^{\mu\gamma}g^{\nu\rho}}{\tau_c} - \delta_{\pi B}\Delta^{\mu\nu}_{\eta\beta}qBb^{\gamma\eta}g^{\beta\rho}\right)\pi_{\gamma\rho} = 2\beta_\pi\sigma^{\mu\nu}. \tag{3.74}$$

In the power counting scheme, the electric field E^μ is considered $\mathcal{O}(\partial)$ as given in [23]. By employing the same projection operators as in the previous case, we obtain the coefficients for shear, bulk, and diffusion. Interestingly, the first-order transport coefficients for shear

and bulk viscosity remain the same as in the ideal MHD case. However, for diffusion, new transport coefficients emerge. Decomposing the diffusion four-current in terms of projectors, we have:

$$
\begin{aligned}
V_\nu = {} & \left(\kappa_\parallel P_{\delta\nu}^\parallel + \kappa_\perp P_{\delta\nu}^\perp + \kappa_\times P_{\delta\nu}^\times \right) \partial^\delta \alpha \\
& + \frac{1}{q} \left(\sigma_\parallel P_{\delta\nu}^\parallel + \sigma_\perp P_{\delta\nu}^\perp + \sigma_\times P_{\delta\nu}^\times \right) E^\delta.
\end{aligned}
$$

Utilizing Ohm's law for current in a conducting fluid:

$$
J_{\text{ind}}^\mu = \sigma_E^{\mu\nu} E_\nu,
$$

where $\sigma_E^{\mu\nu}$ is the electrical conductivity tensor. By substituting the above equation into Eq.(3.73), and leveraging the properties of projection operators, we find:

$$
\kappa_\parallel = \tau_c \beta_V,
$$
$$
\kappa_\perp = \frac{\tau_c \beta_V}{1 + (qB\tau_c \delta_{VB})^2},
$$
$$
\kappa_\times = \kappa_\perp qB\tau_c \delta_{VB}.
$$

Similarly, comparing coefficients of E^δ, we obtain:

$$
\sigma_E^\parallel = q^2 \tau_c \beta \beta_V,
$$
$$
\sigma_E^\perp = \frac{q^2 \tau_c \beta \beta_V}{1 + (qB\tau_c \delta_{VB})^2},
$$
$$
\sigma_E^\times = \frac{q^3 B \tau_c^2 \beta \beta_V \delta_{VB}}{1 + (qB\tau_c \delta_{VB})^2}.
$$

The relations presented above embody the kinetic interpretation of the Wiedemann-Franz law, which states that $\sigma = q^2 \beta \kappa$. Furthermore, setting all dissipative quantities to zero yields $\nabla^\mu \alpha = -q\beta E^\mu$. Notably, $\sigma_E^\parallel$ remains independent of the magnetic field and is proportional to T^2; $\sigma_E^\perp$ and $\sigma_E^\times$ decrease with increasing magnetic fields [24, 21, 25]. Again we can also decompose the $\delta f^{(1)}$ (as given in Eq.(3.55)) as

$$
\delta f^{(1)} = \frac{f_0 \bar{f}_0 \tau_c}{u \cdot p} \left(\mathcal{A}\Pi + \mathcal{B}^\beta V_\beta + \mathcal{C}^{\gamma\rho} \pi_{\gamma\rho} \right),
$$

where

$$
\mathcal{A} = -\frac{1}{\tau_c \beta_\Pi} \left[\frac{(u \cdot p)^2}{D_{20}} \left(J_{20}^{(0)-} \left(\epsilon + P \right) - J_{30}^{(0)+} n_f \right) \right.
$$
$$
\left. - \frac{(u \cdot p)}{D_{20}} \left(J_{10}^{(0)+} \left(\epsilon + P \right) - J_{20}^{(0)-} n_f \right) + \frac{\beta \Delta_{\mu\beta} p^\mu p^\beta}{3} \right],
$$
$$
\mathcal{B}^\beta = -\frac{p^\beta}{\tau_c \beta_V} + \frac{n_f (u \cdot p) p^\beta}{\tau_c \beta_V \left(\epsilon + P \right)}
$$
$$
- \left(1 - \frac{(u \cdot p)}{h} \right) \frac{q B p^\mu \delta_{VB} b_\mu^\beta}{\beta_V},
$$
$$
\mathcal{C}^{\gamma\rho} = \frac{\beta p^\beta p^\kappa}{2 \beta_\pi} \left(\frac{g_\kappa^\gamma g_\beta^\rho}{\tau_c} - \delta_{\pi B} \Delta_{\eta\tau}^{\mu\nu} q B b^{\gamma\eta} g^{\tau\rho} g_{\beta\nu} g_{\kappa\mu} \right).
$$

This formulation holds significant potential for applications such as the Cooper-Frye prescription, where the expression of δf corrections in terms of dissipative quantities could prove advantageous. It's important to note that while we've endeavored to represent δf in terms of powers of p^μ, it's not feasible for $\mathcal{B}^\beta$ and $\mathcal{C}^{\gamma\rho}$, where the corrections arising from magnetic fields manifest at the first order. In chapter.(6), we will exclusively utilize $\delta f^{(1)}$ for the electric fields case to investigate its various impact on flow harmonics and spectra.

3.3   Conclusion

For the first time, we derive the relativistic non-resistive and resistive, viscous second-order magnetohydrodynamics equations for the dissipative quantities using the relaxation time approximation by including the contributions from both particles and antiparticles. Assuming that the single-particle distribution function is close to equilibrium, we solve the Boltzmann equation in the presence of an external electromagnetic field using a Chapman-Enskog-like gradient expansion with three relevant expansion parameters: the Knudsen number $\text{Kn} = \tau_c T$, two dimensionless parameters $\chi = q B \tau_c / T$, and $\xi = q E \tau_c / T$, where the latter two depend on the strength of the electromagnetic fields. In the first order, dissipative quantities are independent of the magnetic field, whereas the diffusion current depends

on the electric field. Moreover, in the second order, we found new transport coefficients that couple the electromagnetic field to dissipative quantities, apart from the usual transport coefficients that one gets without any external field. Compared to the results of the 14-moment approximation, additional terms involving the electromagnetic field appear in the relaxation time approximation. However, in the weak field limit for the non-resistive case, the form of the relaxation equations is the same as that of the 14-moment approximation but with different values for the transport coefficients. Again, in the ultra-relativistic limit, the resulting transport coefficients from the two approaches were compared, and some of the coefficients were found to differ, and some new transport coefficients appeared. As the introduction of external fields breaks the isotropy of the transport coefficients, the shear splits into three independent components and the diffusion coefficients into two independent ones, whereas the bulk remains unaffected. Amongst the different transport coefficients, we found some are proportional to odd powers of the magnetic field, and some are not. The ones that are odd powers in the magnetic field are the Hall terms. These transport coefficients do not give rise to entropy, or, in other words, they do not contribute to entropy production. This is because the odd power of the magnetic field makes the transport coefficient odd under time-reversal symmetry, making it non-dissipative. Again, in the Navier-Stokes limit, we recovered the usual form of the transport coefficients, as was found before in the 14-moment approximation. Also, we retrieved the relativistic version of the Wiedemann-Franz law for the resistive case, which is the ratio of electrical to thermal conductivity of the fluid, which should be proportional to the inverse of the temperature. Lastly, we also delved into studying the behavior with varying temperature and mass for the new transport coefficients that appeared in the second order for the non-resistive case. Here, we found that some transport coefficients become insensitive to temperature at high or low m/T limits. The current chapter primarily examines the impact of external electromagnetic fields generated by spectators on transport coefficients and the evolution of

dissipative stresses up to the first and second orders in gradient expansion. Subsequently, our focus shifts to investigating the generation and evolution of such electromagnetic fields.

In the next chapter, we will explore the behavior of these electromagnetic fields originating from charged participants.

References

[1] S. Pu, T. Koide, and D. H. Rischke, "Does stability of relativistic dissipative fluid dynamics imply causality?," *Phys. Rev. D* **81**, 114039 (2010), doi: 10.1103/PhysRevD.81.114039 [arXiv:0907.3906 [hep-ph]].

[2] G. S. Denicol, T. Kodama, T. Koide, and P. Mota, "Shock propagation and stability in causal dissipative hydrodynamics," *Phys. Rev. C* **78**, 034901 (2008), doi: 10.1103/PhysRevC.78.034901 [arXiv:0805.1719 [hep-ph]].

[3] G. S. Denicol, T. Kodama, T. Koide, and P. Mota, "Stability and Causality in relativistic dissipative hydrodynamics," *J. Phys. G* **35**, 115102 (2008), doi: 10.1088/0954-3899/35/11/115102 [arXiv:0807.3120 [hep-ph]].

[4] S. Floerchinger and E. Grossi, "Causality of fluid dynamics for high-energy nuclear collisions," *JHEP* **08**, 186 (2018), doi: 10.1007/JHEP08(2018)186 [arXiv:1711.06687 [nucl-th]].

[5] B. Betz, D. Henkel, and D. H. Rischke, "From kinetic theory to dissipative fluid dynamics," *Prog. Part. Nucl. Phys.* **62**, 556-561 (2009), doi: 10.1016/j.ppnp.2008.12.018 [arXiv:0812.1440 [nucl-th]].

[6] Gabriel S. Denicol and Dirk H. Rischke, "Microscopic Foundations of Relativistic Fluid Dynamics," *Springer Nature Switzerland AG 2021*, doi: 10.1007/978-3-030-82077-0.

[7] G. S. Denicol, T. Koide, and D. H. Rischke, "Dissipative relativistic fluid dynamics: a new way to derive the equations of motion from kinetic theory," *Phys. Rev. Lett.* **105**, 162501 (2010), doi: 10.1103/PhysRevLett.105.162501 [arXiv:1004.5013 [nucl-th]].

[8] A. Muronga, "Relativistic Dynamics of Non-ideal Fluids: Viscous and heat-conducting fluids. II. Transport properties and microscopic description of relativistic nuclear matter," *Phys. Rev. C* **76**, 014910 (2007), doi: 10.1103/PhysRevC.76.014910 [arXiv:nucl-th/0611091 [nucl-th]].

[9] G. S. Denicol, H. Niemi, E. Molnar, and D. H. Rischke, "Derivation of transient relativistic fluid dynamics from the Boltzmann equation," *Phys. Rev. D* **85**, 114047 (2012), doi: 10.1103/PhysRevD.85.114047 [arXiv:1202.4551 [nucl-th]].

[10] G. S. Denicol, E. Molnár, H. Niemi, and D. H. Rischke, "Derivation of fluid dynamics from kinetic theory with the 14-moment approximation," *Eur. Phys. J. A* **48**, 170 (2012), doi: 10.1140/epja/i2012-12170-x [arXiv:1206.1554 [nucl-th]].

[11] B. Betz, D. Henkel, and D. H. Rischke, "Complete second-order dissipative fluid dynamics," *J. Phys. G* **36**, 064029 (2009), doi: 10.1088/0954-3899/36/6/064029.

[12] M. A. York and G. D. Moore, "Second order hydrodynamic coefficients from kinetic theory," *Phys. Rev. D* **79**, 054011 (2009), doi: 10.1103/PhysRevD.79.054011 [arXiv:0811.0729 [hep-ph]].

[13] A. Jaiswal, R. S. Bhalerao, and S. Pal, "New relativistic dissipative fluid dynamics from kinetic theory," *Phys. Lett. B* **720**, 347-351 (2013), doi: 10.1016/j.physletb.2013.02.025 [arXiv:1204.3779 [nucl-th]].

[14] A. Jaiswal, "Relativistic dissipative hydrodynamics from kinetic theory with relaxation time approximation," *Phys. Rev. C* **87**, no.5, 051901 (2013), doi: 10.1103/PhysRevC.87.051901 [arXiv:1302.6311 [nucl-th]].

[15] W. Florkowski and R. Ryblewski, "Highly-anisotropic and strongly-dissipative hydro-dynamics for early stages of relativistic heavy-ion collisions," *Phys. Rev. C* **83**, 034907 (2011), doi: 10.1103/PhysRevC.83.034907 [arXiv:1007.0130 [nucl-th]].

[16] G. S. Denicol, X. G. Huang, E. Molnár, G. M. Monteiro, H. Niemi, J. Noronha, D. H. Rischke, and Q. Wang, "Nonresistive dissipative magnetohydrodynamics from the Boltzmann equation in the 14-moment approximation," *Phys. Rev. D* **98**, no.7, 076009 (2018), doi: 10.1103/PhysRevD.98.076009 [arXiv:1804.05210 [nucl-th]].

[17] G. S. Denicol, E. Molnár, H. Niemi, and D. H. Rischke, "Resistive dissipative magne-tohydrodynamics from the Boltzmann-Vlasov equation," *Phys. Rev. D* **99**, no.5, 056017 (2019), doi: 10.1103/PhysRevD.99.056017 [arXiv:1902.01699 [nucl-th]].

[18] J. L. Anderson and H. R. Witting, "A relativistic relaxation-time model for the Boltz-mann equation," *Physica* **74** (3), 466-488 (1974), doi: 10.1016/0031-8914(74)90355-3.

[19] M. P. Heller, R. A. Janik and P. Witaszczyk, "Hydrodynamic Gradient Expansion in Gauge Theory Plasmas," *Phys. Rev. Lett.* **110**, no.21, 211602 (2013), doi: 10.1103/Phys-RevLett.110.211602 [arXiv:1302.0697 [hep-th]].

[20] S. Hess, "Tensors for Physics," *Undergraduate Lecture Notes in Physics*, Springer International Publishing, 2015, isbn: 9783319127873, url: `https://books.google.co.in/books?id=Nm26CAAAQBAJ`.

[21] A. Dash, S. Samanta, J. Dey, U. Gangopadhyaya, S. Ghosh and V. Roy, "Anisotropic transport properties of a hadron resonance gas in a magnetic field," Phys. Rev. D **102**, no.1, 016016 (2020) doi:10.1103/PhysRevD.102.016016 [arXiv:2002.08781 [nucl-th]].

[22] P. Mohanty, A. Dash and V. Roy, "One particle distribution function and shear viscosity in magnetic field: a relaxation time approach," Eur. Phys. J. A **55**, no. 3, 35 (2019) doi: 10.1140/epja/i2019-12705-7 [arXiv:1804.01788 [nucl-th]].

[23] J. Hernandez and P. Kovtun, JHEP **05**, 001 (2017) doi: 10.1007/JHEP05(2017)001 [arXiv:1703.08757 [hep-th]].

[24] G. Kremer, "Theory and applications of the relativistic Boltzmann equation," Int. J. Geom. Meth. Mod. Phys. **11**, (2014) doi: 10.1142/S0219887814600056.

[25] S. Satapathy, S. Ghosh and S. Ghosh, "Kubo estimation of the electrical conductivity for a hot relativistic fluid in the presence of a magnetic field," Phys. Rev. D **104**, no.5, 056030 (2021) doi: 10.1103/PhysRevD.104.056030 [arXiv:2104.03917 [hep-ph]].

Chapter 4

Electromagnetic fields by charged participants

In previous studies, extensive numerical investigations [1, 2, 3, 4, 5, 6, 7, 8] have explored the dynamics of the bulk medium, notably the Quark-Gluon Plasma (QGP), and its interplay with electromagnetic fields. However, within the realm of theoretical calculations, only a handful of works [9, 10, 11] have computed the evolution of electromagnetic fields generated by participants in the QGP and the hadronic phase but without taking into account the participant (fluid) flow velocity.

Given that charged participants constitute the bulk of the medium formation (predominantly in low-energy collisions), it is imperative to include fluid flow while calculating the fields they generate. Thus, understanding the electromagnetic fields generated by participants becomes crucial. This serves as the primary focus of this chapter's work. While the generic framework for studying the dynamics of charged participants is relativistic magnetohydrodynamics (RMHD), which often necessitates numerical simulations, our approach is more modest, focusing on analytical insights. To achieve this, we approximate the problem by studying Maxwell's equations in a charged background fluid flow, considering a simple one-dimensional Bjorken flow [12].

The structure of this chapter unfolds as follows: we commence with a review of the fundamental equations in Section.(4.1), followed by Section.(4.2), which outlines the background model and the associated assumptions. The solution to Green's function is presented in Section.(4.3). Subsequently, our findings are discussed in Section.(4.4), followed by the conclusion and outlook presented in Section (4.5). In this chapter, we will adhere to the

119

mostly positive metric assumption that is $g^{\mu\nu} = diag(-,+,+,+)$.

4.1 Basic equations

Let's review the fundamental equations required for our subsequent analysis, with their derivation outlined in [13, 14]. The energy-momentum tensor of the fluid, formulated in the Landau frame, is expressed as:

$$T_f^{\mu\nu} \equiv \varepsilon u^\mu u^\nu + p\Delta^{\mu\nu}, \tag{4.1}$$

where $\Delta^{\mu\nu}$ represents the spatial projection operator defined by:

$$\Delta^{\mu\nu} \equiv g^{\mu\nu} + u^\mu u^\nu, \tag{4.2}$$

and ε denotes the energy density, p signifies the isotropic pressure, and u^μ represents the fluid four-velocity. As customary, the fluid four-velocity is normalized such that $u^\mu u_\mu = -1$. The covariant derivative of u_μ can be decomposed using the four-velocity u_μ and the projection operator $\Delta_{\mu\nu}$ into basic irreducible kinematic quantities:

$$u_{\mu;\nu} = \sigma_{\mu\nu} + \omega_{\mu\nu} + \frac{\theta}{3}\Delta_{\mu\nu} - \dot{u}_\mu u_\nu, \tag{4.3}$$

where the shear tensor $\sigma_{\mu\nu}$, vorticity tensor $\omega_{\mu\nu}$, expansion scalar θ, and four-acceleration $\dot{u}_\mu$ are defined as follows:

$$\sigma_{\mu\nu} \equiv \frac{\Delta_\mu^\alpha \Delta_\nu^\beta}{2} \left(u_{\alpha;\beta} + u_{\beta;\alpha} \right) - \frac{\theta}{3}\Delta_{\mu\nu}, \tag{4.4}$$

$$\omega_{\mu\nu} \equiv \frac{\Delta_\mu^\alpha \Delta_\nu^\beta}{2} \left(u_{\alpha;\beta} - u_{\beta;\alpha} \right), \tag{4.5}$$

$$\theta \equiv u^\mu_{;\mu}, \tag{4.6}$$

$$\dot{u}_\mu \equiv u_{\mu;\nu} u^\nu. \tag{4.7}$$

It is noteworthy that $\sigma_{\mu\nu} u^\mu = \omega_{\mu\nu} u^\mu = \dot{u}^\mu u_\mu = 0$ by definition. Here ; represents the covariant derivative of a quantity. Let's examine the first set of Maxwell's equations, rep-

resented as follows:

$$F^{\mu\nu}{}_{;\mu} = -J^\nu \ , \tag{4.8}$$

where $J^\nu = J_f^\mu + J_{\text{ext}}^\nu$ represents the total charge four-current, encompassing both the charge current generated within the fluid J_f and that originating from an external source J_{ext}^ν, such as spectators. The fluid charge current adheres to the conservation law:

$$J_{f;\mu}^\mu = 0. \tag{4.9}$$

The second set of equations emerges as a direct consequence of the existence of a four-potential and is articulated as:

$$F_{\alpha\beta;\gamma} + F_{\beta\gamma;\alpha} + F_{\gamma\alpha;\beta} = 0 \ . \tag{4.10}$$

When observed from the perspective of fluid moving with four-velocity u_μ, the electromagnetic field tensor can be partitioned into 'electric' (E^μ) and 'magnetic' (B^μ) components, defined by:

$$E^\mu \equiv g^{\mu\alpha} F_{\alpha\nu} u^\nu \ , \tag{4.11}$$

and

$$B^\mu \equiv \frac{1}{2}\epsilon^{\mu\nu\alpha\beta} F_{\alpha\beta} u_\nu \ , \tag{4.12}$$

where $\epsilon_{\mu\nu\alpha\beta}$ signifies the totally antisymmetric tensor with $\epsilon_{0123} = \sqrt{-g}$. Utilizing the definitions provided in Eqs. (4.11) and (4.12), we readily deduce that

$$E_\mu u^\mu = 0 \ , \tag{4.13}$$

$$B_\mu u^\mu = 0 \ . \tag{4.14}$$

Using the provided definitions, we can express the electromagnetic tensor $F_{\mu\nu}$ in any arbitrary frame as follows:

$$F_{\mu\nu} \equiv u_\mu E_\nu - E_\mu u_\nu + \epsilon_{\mu\nu\alpha\beta} u^\alpha B^\beta. \tag{4.15}$$

Similarly, the charge current can be decomposed into the local charge density $\rho \equiv \rho_f = -J^\mu u_\mu$ and the charge diffusion current $V^\mu \equiv V_f^\mu = J^\nu \Delta_\nu{}^\mu$,

$$J^\mu \equiv J_f^\mu = \rho_f u^\mu + V_f^\mu \ . \tag{4.16}$$

It's noteworthy that as stated in the introduction, we will solely consider fluid-origin charges and currents here, neglecting any external contributions. For later convenience, we will omit the subscript 'f'. Maxwell's equations, Eq.(4.8) and Eq.(4.10), can be broken down into temporal and spatial components using u_μ and the projector $\Delta_{\mu\nu}$, yielding the following set of equations:

$$E^\mu{}_{;\mu} - B^{\mu\nu}\omega_{\mu\nu} - E^\nu \dot{u}_\nu = \rho \ , \tag{4.17}$$

$$B^\mu{}_{\nu;\mu} - u_\nu B_{\alpha\beta}\omega^{\alpha\beta} - E^\mu \left(\omega_{\mu\nu} + \sigma_{\mu\nu} - \frac{2\theta}{3}\Delta_{\mu\nu} \right) + \Delta_\nu{}^\alpha \dot{E}_\alpha = -V_\nu \ , \tag{4.18}$$

$$B^\mu{}_{;\mu} - E^{\mu\nu}\omega_{\mu\nu} - B^\nu \dot{u}_\nu = 0 \ , \tag{4.19}$$

$$E^\mu{}_{\nu;\mu} - u_\nu E_{\alpha\beta}\omega^{\alpha\beta} - B^\mu \left(\omega_{\mu\nu} + \sigma_{\mu\nu} - \frac{2\theta}{3}\Delta_{\mu\nu} \right) + \Delta_\nu{}^\alpha \dot{B}_\alpha = 0 \ , \tag{4.20}$$

where the antisymmetric tensors: $B_{\mu\nu} \equiv \epsilon_{\mu\nu\alpha\beta}u^\alpha B^\beta$, and $E_{\mu\nu} \equiv \epsilon_{\mu\nu\alpha\beta}u^\alpha E^\beta$.

As is mentioned in chapter.(2) the electromagnetic energy-momentum tensor is defined as

$$T_{em}^{\mu\nu} \equiv F^{\lambda\mu}F_\lambda{}^\nu - \frac{1}{4}g^{\mu\nu}F_{\alpha\beta}F^{\alpha\beta} \ , \tag{4.21}$$

and the total energy-momentum tensor of the system is given by

$$T^{\mu\nu} \equiv T_f^{\mu\nu} + T_{em}^{\mu\nu} \ . \tag{4.22}$$

The conservation law for $T^{\mu\nu}$ is expressed as

$$T^{\mu\nu}{}_{;\mu} = 0 \ . \tag{4.23}$$

The above equation is satisfied given that there are no external source present. These equations also imply

$$T_{f;\mu}^{\mu\nu} = F^{\nu\lambda}J_{f,\lambda}. \tag{4.24}$$

Projecting Eq.(4.24) along the directions of u_ν and $\Delta^\alpha{}_\nu$ yields the following equations of motion:

$$\dot{\varepsilon} = -((\varepsilon + p)\theta + E^\lambda V_\lambda), \tag{4.25}$$

$$\dot{u}^\alpha = \frac{1}{(\varepsilon + p)} \left(\nabla^\alpha p + E^\alpha \rho - B^{\alpha\lambda} V_\lambda \right). \tag{4.26}$$

The Lorentz forces in the second and third terms on the right-hand side of Eq.(4.26) contribute to the fluid's work, while dissipative forces from shear and bulk viscosity are neglected here. Eqs.(4.17)-(4.20) and (4.25)-(4.26), along with an equation of state for the fluid, completely describe the system under consideration, provided a consistent initial and boundary data are given. In the subsequent section, we simplify these equations by disregarding the back-reaction of electromagnetic fields on the fluid, as described in Eqs.(4.25)-(4.26). That is our fluid is not affected by the electromagnetic fields.

4.2 Background model and assumptions

The preceding analysis holds a broad applicability, as the Eqs.(4.17)–(4.20) are applicable to various physical scenarios once the background evolution is defined. For instance, when there are no matter sources, one can set the observer's acceleration to zero. Likewise, in cases where the fluid evolution is stationary and non-rotating, the expansion scalar and vorticity tensor can be assumed to be zero. In the subsequent discussion, we will consider a background fluid undergoing a longitudinal boost-invariant Bjorken expansion [12]. This choice is motivated by the well-known property of boost invariance being readily apparent in Milne coordinates compared to Minkowski coordinates. The line element in Milne coordinates (τ, x, y, η) is given by:

$$ds^2 = -d\tau^2 + dx^2 + dy^2 + \tau^2 d\eta^2 \tag{4.27}$$

This line element is invariant under the combined symmetry $SO(1,1) \otimes ISO(2) \otimes Z_2$, encompassing boost-invariance along the beam direction η, rotational and translational invariance in the transverse (x, y) coordinates, and reflection under $\eta \to -\eta$. The flow consistent with this combined symmetry property is $u^\mu = (1, 0, 0, 0)$. Similarly, the only non-vanishing Christoffel symbols are: $\Gamma^\tau_{\eta\eta} \equiv \tau$, $\Gamma^\eta_{\tau\eta} = \Gamma^\eta_{\eta\tau} \equiv 1/\tau$. Furthermore, Bjorken symmetry implies $\omega_{\mu\nu} = \dot{u}^\mu \equiv 0$, $\theta \equiv 1/\tau$, and $\sigma_{\mu\nu} \equiv \mathrm{diag}(0, -1/(3\tau), -1/(3\tau), 2\tau/3)$.

It's worth noting that the inherent anisotropy in the electromagnetic energy-momentum tensor clashes with the pronounced symmetry of the Milne metric. In the context of ideal Bjorken flow—where dissipation and electromagnetic effects are absent—Eq.(4.26) trivially reduces to zero. This arises from the boost invariance of the expansion, resulting in negligible acceleration. Similarly, Eq.(4.25) yields the well-established Bjorken scaling $\varepsilon \sim \tau^{-4/3}$ under the assumption of a squared speed of sound $c_s^2 = 1/3$. However, the presence of a back-reaction from the electromagnetic field onto the fluid introduces non-zero acceleration, thereby impacting the electromagnetic fields according to Eqs.(4.17)-(4.20). Furthermore, the electric field's influence leads to modifications in Eq.(4.25), deviating from the conventional Bjorken scaling. For example, in [2], the authors conducted a 1+1-dimensional resistive MHD calculation in transversely homogeneous settings, without neglecting any back-reaction. Their study elucidated how boost invariance is compromised due to the self-consistent dynamics of matter and electromagnetic fields.

A pivotal assumption underpins our analysis. Considering the expression on the right-hand side of Eq.(4.26), where the Lorentz forces are scaled by $1/(\varepsilon + P)$, we introduce the inverse plasma β-parameter: $\beta^{-1} \equiv B_0^2/(2p_0)$, which governs their relative strength. When the inverse plasma β-parameter $\beta^{-1} \ll 1$, we can safely disregard the back-reaction of the electromagnetic field on the fluid. Given that the strength of the electromagnetic field—originating from spectators in mid-central collisions—diminishes more rapidly with increasing collision energy compared to the energy density of the fluid, it's anticipated that

β^{-1} remains small at higher collision energies. Nonetheless, it's conceivable that certain regions within the fireball, such as its periphery, may exhibit large β^{-1} even at moderate energies. In the subsequent discussion, we will operate within this regime and neglect any influence of the electromagnetic fields on the background fluid.

Lastly, we make the assumption that the fluid behaves as an ideal insulator, characterized by a negligible conductivity, resulting in a diffusion current V_f^μ of zero according to Ohm's law. This assumption is not too bold, given that lattice simulations suggest a low conductivity for the plasma, with $\sigma/T = 8\pi\alpha_{\rm EM}/3 \simeq 0.06$ [15], where σ denotes conductivity, T represents temperature, and $\alpha_{\rm EM}$ refers to the fine structure constant. Nevertheless, for the sake of completeness, we retain this term in our subsequent derivation, although we omit it later when discussing specific cases (see Sec.(4.4)).

Under the aforementioned assumption, Eqs.(4.17)-(4.20) simplify to the familiar Gauss laws for electric and magnetic fields:

$$\partial_x E_x + \partial_y E_y + \tau^{-2}\partial_\eta E_\eta = \rho \, , \tag{4.28}$$

$$\partial_x B_x + \partial_y B_y + \tau^{-2}\partial_\eta B_\eta = 0 \, , \tag{4.29}$$

Similarly, the equations corresponding to Faraday's law become:

$$\partial_\tau\left(\tau B_x\right) = -(\partial_y E_\eta - \partial_\eta E_y) \, , \tag{4.30}$$

$$\partial_\tau\left(\tau B_y\right) = (\partial_x E_\eta - \partial_\eta E_x) \, , \tag{4.31}$$

$$\partial_\tau\left(\tau^{-1} B_\eta\right) = -(\partial_x E_y - \partial_y E_x) \, , \tag{4.32}$$

while Ampère's law is represented by:

$$\partial_\tau \left(\tau E_x \right) = (\partial_y B_\eta - \partial_\eta B_y) - \tau V^x \ , \tag{4.33}$$

$$\partial_\tau \left(\tau E_y \right) = -(\partial_x B_\eta - \partial_\eta B_x) - \tau V^y \ , \tag{4.34}$$

$$\partial_\tau \left(\tau^{-1} E_\eta \right) = (\partial_x B_y - \partial_y B_x) - \tau V^\eta \ . \tag{4.35}$$

In pursuit of deriving the wave equation governing electromagnetic fields within this expanding context, we begin by redefining the electromagnetic fields alongside the charges and currents. Specifically, we introduce the following transformations: $\tilde{E}_{(x,y)} = \tau E_{(x,y)}$, $\tilde{B}_{(x,y)} = \tau B_{(x,y)}$, $\tilde{E}_\eta = \tau^{-1} E_\eta$, $\tilde{B}_\eta = \tau^{-1} B_\eta$, $\tilde{\rho} = \tau \rho$, and $\tilde{V}^i = \tau^2 V^i$. With these redefinitions in place, Maxwell's equations given by Eq.(4.28)-(4.35) can be simplified to:

$$\partial_i \tilde{E}_i = \tilde{\rho} \ , \tag{4.36}$$

$$\partial_i \tilde{B}_i = 0 \ , \tag{4.37}$$

$$\partial_\tau \tilde{B}_x = \tau^{-1} \partial_\eta \tilde{E}_y - \tau \partial_y \tilde{E}_\eta \ , \tag{4.38}$$

$$\partial_\tau \tilde{B}_y = \tau \partial_x \tilde{E}_\eta - \tau^{-1} \partial_\eta \tilde{E}_x \ , \tag{4.39}$$

$$\partial_\tau \tilde{B}_\eta = \tau^{-1} \partial_y \tilde{E}_x - \tau^{-1} \partial_x \tilde{E}_y \ , \tag{4.40}$$

$$\partial_\tau \tilde{E}_x = \tau \partial_y \tilde{B}_\eta - \tau^{-1} \partial_\eta \tilde{B}_y - \tau^{-1} \tilde{V}^x \ , \tag{4.41}$$

$$\partial_\tau \tilde{E}_y = \tau^{-1} \partial_\eta \tilde{B}_x - \tau \partial_x \tilde{B}_\eta - \tau^{-1} \tilde{V}^y \ , \tag{4.42}$$

$$\partial_\tau \tilde{E}_\eta = \tau^{-1} \partial_x \tilde{B}_y - \tau^{-1} \partial_y \tilde{B}_x - \tau^{-1} \tilde{V}^\eta \ . \tag{4.43}$$

To derive the wave equations, we follow a systematic procedure. For instance, to obtain the wave equation for $\tilde{B}_x$, we utilize Eqs.(4.42) and (4.43), taking their partial derivatives with respect to η and y, respectively. Subsequently, we substitute the resultant expressions into the partial derivative with respect to τ in Eq.(4.38). This process is repeated for the remaining components of the electromagnetic fields, yielding the following set of wave equations:

$$\Box \tilde{E}_x = 2\partial_y \tilde{B}_\eta - (\partial_x \tilde{\rho} + \tau^{-1}\partial_\tau \tilde{V}^x) \, , \qquad (4.44)$$

$$\Box \tilde{E}_y = -2\partial_x \tilde{B}_\eta - (\partial_y \tilde{\rho} + \tau^{-1}\partial_\tau \tilde{V}^y) \, , \qquad (4.45)$$

$$\Box \tilde{E}_\eta = -\tau^{-1}\partial_\tau \tilde{V}^\eta - \tau^{-2}\partial_\eta \tilde{\rho} \, , \qquad (4.46)$$

$$\Box \tilde{B}_x = -2\partial_y \tilde{E}_\eta + \partial_y \tilde{V}^\eta - \tau^{-2}\partial_\eta \tilde{V}^y \, , \qquad (4.47)$$

$$\Box \tilde{B}_y = 2\partial_x \tilde{E}_\eta - \partial_x \tilde{V}^\eta + \tau^{-2}\partial_\eta \tilde{V}^x \, , \qquad (4.48)$$

$$\Box \tilde{B}_\eta = \tau^{-2}\partial_x \tilde{V}^y - \tau^{-2}\partial_y \tilde{V}^x \, , \qquad (4.49)$$

where $\Box$ represents the d'Alembert operator in Milne coordinates, defined as:

$$\Box \equiv \partial_\tau^2 + \tau^{-1}\partial_\tau - \tau^{-2}\partial_\eta^2 - \partial_x^2 - \partial_y^2. \qquad (4.50)$$

The Eqs.(4.44)-(4.49) constitute the primary findings of this study. In contrast to the standard source-free wave equation in Minkowski coordinates [11], these equations exhibit additional couplings between the field components on the right-hand side, which are absent in the former coordinate system. This discrepancy highlights an intriguing consequence: even in the absence of charge currents $\tilde{V}^i$, one can generate magnetic fields for stationary charges in an expanding medium. These magnetic fields are driven by the gradients of electric fields, which serve as sources. These phenomena, reminiscent of Jefimenko's equations or the Jefimenko-Feynman formula [16], will be briefly discussed in Sec.(4.4). The origin of these coupling terms can be traced back to the non-vanishing expansion scalar θ and shear stress tensor $\sigma^{\mu\nu}$ in Eqs.(4.17)-(4.20). It is crucial to note that the electromagnetic fields derived from the solutions of Eqs.(4.44)-(4.49) are not merely the coordinate-transformed solutions of electromagnetic fields in Minkowski coordinates. Unless one solves Eqs.(4.44)-(4.49) with a longitudinal fluid velocity $v^z \equiv u^z/u^t = \tanh\eta$ in the latter coordinate system, the solutions will differ. Here, u^z and u^t represent the components of the four-velocity in Minkowski coordinates. Since the velocity in Minkowski

coordinates is coordinate-dependent, the fields cannot be obtained simply by boosting from the rest frame to this frame. In the subsequent section, we will solve Eqs.(4.44)-(4.49) based on a mode decomposition of Green's equation.

4.3 Solution of the wave equations for electromagnetic fields

To tackle the system of non-linear coupled wave equations represented by Eqs.(4.44)-(4.49), we observe that the longitudinal components of the electromagnetic fields depend solely on external sources, while the transverse components rely on the gradients of the former. Consequently, we can adopt an iterative approach to solve the system, first addressing the longitudinal components and subsequently leveraging this solution to determine the transverse components. The equation governing the longitudinal components is a well-studied problem in the literature [17, 18, 19], frequently encountered in solving the Klein-Gordon equation in Milne coordinates. It is worth noting that various methods, such as the WKB procedure [20, 21] or mode decomposition of Green's function [22, 23], have been employed to address similar equations. However, in this study, we opt for the latter approach, which yields an exact solution.

Using the 2-point Green function $G(x_\mu; x'_\mu)$ between $x_\mu \equiv (\tau, \mathbf{x}_\perp, \eta)$ and $x'_\mu \equiv (\tau', \mathbf{x}'_\perp, \eta')$, we define the following:

$$G_r(x_\mu; x'_\mu) = -\Theta(\tau - \tau')G(x_\mu; x'_\mu) \,, \tag{4.51}$$

$$G_a(x_\mu; x'_\mu) = \Theta(\tau' - \tau)G(x_\mu; x'_\mu) \,, \tag{4.52}$$

$$\bar{G}(x_\mu; x'_\mu) = \frac{1}{2} \left[G_r(x_\mu; x'_\mu) + G_a(x_\mu; x'_\mu) \right] \,, \tag{4.53}$$

where $\Theta(\tau - \tau')$ is the Heaviside step function, and $G_r(x_\mu; x'_\mu)$, $G_a(x_\mu; x'_\mu)$, and $\bar{G}(x_\mu; x'_\mu)$ are the retarded, advanced, and symmetric propagators, respectively. Now, we decompose

the Green function into modes via a Fourier expansion:

$$G(x_\mu; x'_\mu) = \frac{1}{(2\pi)^3 \sqrt{\tau\tau'}} \int d^3k e^{i[\mathbf{k}_\perp \cdot (\mathbf{x}_\perp - \mathbf{x}'_\perp) + k_\eta(\eta - \eta')]} \left[a_{k_\eta}(\tau) b_{k_\eta}(\tau') - a_{k_\eta}(\tau') b_{k_\eta}(\tau) \right] ,$$

(4.54)

where $p_\mu \equiv (\mathbf{k}_\perp, k_\eta)$. Let $a_{k_\eta}(\tau)$ and $b_{k_\eta}(\tau)$ be particular solutions satisfying:

$$a_{k_\eta}(\tau) = 1 , \qquad\qquad \partial_\tau a_{k_\eta}(\tau) = 0 ,$$

$$b_{k_\eta}(\tau) = 0 , \qquad\qquad \partial_\tau b_{k_\eta}(\tau) = 1 , \qquad (4.55)$$

at $\tau = 1$. Then, it can be verified that the following relation holds for any τ:

$$a_{k_\eta}(\tau) \partial_\tau b_{k_\eta}(\tau) - \partial_\tau a_{k_\eta}(\tau) b_{k_\eta}(\tau) = 1. \qquad (4.56)$$

Given that the Green's function $G(x_\mu; x'_\mu)$ satisfies the homogeneous wave equation

$$\Box G(x_\mu; x'_\mu) = 0 \qquad (4.57)$$

together with the boundary conditions:

$$G(x_\mu; x'_\mu) = 0 , \qquad\qquad \partial_\tau G(x_\mu; x'_\mu) = -\frac{1}{\tau} \delta(x_i - x'_i) , \qquad (4.58)$$

at $\tau = \tau'$.

We can demonstrate that the symmetric propagator $\bar{G}(x_\mu; x'_\mu)$ satisfies the following inhomogeneous wave equation:

$$\Box \bar{G}(x_\mu; x'_\mu) = \frac{1}{\sqrt{\tau\tau'}} \delta^4(x_\mu - x'_\mu), \qquad (4.59)$$

where $\delta^4(x_\mu - x'_\mu) = \delta(\tau - \tau') \delta^3(x_i - x'_i)$. Using the definition of the d'Alembert operator from Eq.(4.50), it can be verified that the particular solution satisfies the following relations:

$$a_{k_\eta}(\tau) b_{k_\eta}(\tau') - a_{k_\eta}(\tau') b_{k_\eta}(\tau) = \frac{\pi\sqrt{\tau\tau'}}{2} \left[J_{ik_\eta}(k_\perp \tau) Y_{ik_\eta}(k_\perp \tau') - J_{ik_\eta}(k_\perp \tau') Y_{ik_\eta}(k_\perp \tau) \right] ,$$

(4.60)

where $J_{ik_\eta}(k_\perp \tau)$ and $Y_{ik_\eta}(k_\perp \tau)$ are the Bessel functions of the first and second kind, respectively, with $k_\perp \equiv |\mathbf{k}_\perp|$. Substituting Eq.(4.60) into Eq.(4.54), we arrive at the following equation for the Green's function:

$$G(x_\mu; x'_\mu) = -\frac{\epsilon(\tau - \tau')\theta(\lambda^2)}{4\pi} \int_0^\infty k_\perp dk_\perp J_0(\lambda k_\perp) J_0(r_\perp k_\perp) , \qquad (4.61)$$

$$= -\frac{\epsilon(\tau - \tau')}{2\pi}\delta(s^2), \qquad (4.62)$$

where $\lambda^2 = \tau^2 + \tau'^2 - 2\tau\tau' \cosh(\eta - \eta')$, $r_\perp^2 \equiv (x - x')^2 + (y - y')^2$, $s^2 = \lambda^2 - r_\perp^2$, and $\epsilon(\tau - \tau') = \Theta(\tau - \tau') - \Theta(\tau' - \tau)$ respectively. By substituting Eq.(4.61) into the definition of the symmetric propagator Eq.(4.53), we obtain:

$$\bar{G}(x_\mu; x'_\mu) = \frac{1}{4\pi}\delta(\tau^2 + \tau'^2 - 2\tau\tau' \cosh(\eta - \eta') - r_\perp^2). \qquad (4.63)$$

Eq.(4.61) closely resembles its counterpart in the usual representation in Minkowski spacetime, but the expression for s^2 in Eq.(4.61) (which has support only at the light cone) differs entirely from that in the latter.

Thus, for any field $\Phi(x_\mu)$ satisfying an equation of the form:

$$\Box\Phi(x_\mu) = S(x_\mu), \qquad (4.64)$$

with a generic source $S(x_\mu)$, the solution takes the form:

$$\Phi(x_\mu) = \int \bar{G}(x_\mu; x'_\mu) S(x'_\mu) \sqrt{g'} d^4 x'. \qquad (4.65)$$

4.4 Results

In this section, we unveil the outcomes concerning the electromagnetic fields produced by the participants. Initially, we scrutinize a straightforward scenario featuring a motionless point charge, where the fields correspond to those derived from the Liénard-Wiechert potential within the expanding fluid framework. This serves as a litmus test for our formulation

in a simplified setting. Following this, we proceed to a more practical scenario, wherein charged particles are arranged in a Gaussian distribution across the transverse plane while adhering to specific constraints on the region of participant charge allocation.

4.4.1   Field of a stationary point charge

Consider the charge density attributed to a stationary (co-moving) point particle in an expanding fluid, characterized by a four-velocity $u^\mu = (1, 0, 0, 0)$. This density is represented by:

$$\rho(\tau, \mathbf{x}) = Ze \frac{\delta^3(\mathbf{x} - \mathbf{x}_0)\Theta(\tau - \tau_0)}{\tau}. \tag{4.66}$$

Here, Ze signifies the charge magnitude, and $\mathbf{x}_0$ denotes its position. To mitigate the singularity of the Green's function at $\tau = 0$, we assume that the charge emerged at a finite time in the past, $\tau = \tau_0$. This assumption is common in heavy-ion collision hydrodynamics, where hydrodynamic evolution typically commences after a finite time, approximately $\sim 0.5 - 0.6$ fm. It's important to note that in this framework, there's no conservation law for charge, and charge can be spontaneously generated if sufficient energy is available. Additionally, considering the fluid as a perfect insulator implies a zero charge diffusion current V^μ. Consequently, the particular solution for the η component of the magnetic field (Eq.(4.49)) can be set to zero without loss of generality, effectively decoupling from other electromagnetic field components. Substituting the gradient of the point charge (Eq.(4.66)) as a source in the Green's function (Eq.(4.65)), we obtain:

$$\tilde{E}_\eta(\tau, \mathbf{x}) = -Ze \int \frac{1}{(\tau')^2} \bar{G}(\tau, \mathbf{x}; \tau', \mathbf{x}') \partial_\eta \tilde{\rho}(\tau', \mathbf{x}') \sqrt{g(\tau')} d^3\mathbf{x}' d\tau', \tag{4.67}$$

as a solution of Eq.(4.46). The integration of Eq.(4.67) with the symmetric Green's function (Eq.(4.63)) is straightforward, resulting in:

$$\tilde{E}_\eta(\tau, \mathbf{x}) = \begin{cases} Ze\dfrac{\tau\sinh(\eta-\eta_0)}{4\pi[(r_\perp-r_{\perp 0})^2+\tau^2\sinh^2(\eta-\eta_0)]^{3/2}}, & \text{if } \tau_0 < \tau_f(\mathbf{x};\mathbf{x}_0) < \tau \\ 0, & \text{otherwise} \end{cases} \tag{4.68}$$

where $\tau_f(\mathbf{x};\mathbf{x}_0) := \tau\cosh(\eta-\eta_0) - \sqrt{(r_\perp-r_{\perp 0})^2 + \tau^2\sinh^2(\eta-\eta_0)}$ and the inequality satisfies causality constraints. The transverse components of electric fields can be computed analogously, yielding:

$$\tilde{E}_x(\tau, \mathbf{x}) = \begin{cases} Ze\dfrac{\tau(x-x_0)\cosh(\eta-\eta_0)}{4\pi[(r_\perp-r_{\perp 0})^2+\tau^2\sinh^2(\eta-\eta_0)]^{3/2}}, & \text{if } \tau_0 < \tau_f(\mathbf{x};\mathbf{x}_0) < \tau \\ 0, & \text{otherwise} \end{cases} \tag{4.69}$$

$$\tilde{E}_y(\tau, \mathbf{x}) = \begin{cases} Ze\dfrac{\tau(y-y_0)\cosh(\eta-\eta_0)}{4\pi[(r_\perp-r_{\perp 0})^2+\tau^2\sinh^2(\eta-\eta_0)]^{3/2}}, & \text{if } \tau_0 < \tau_f(\mathbf{x};\mathbf{x}_0) < \tau \\ 0, & \text{otherwise} \end{cases} \tag{4.70}$$

As discussed in Section.(4.3), the transverse magnetic fields can be obtained by taking the gradients of the longitudinal component of the electric field, Eq.(4.68), acting as a source in Eq.(4.65), resulting in:

$$\tilde{B}_y(\tau, \mathbf{x}) = 2\int \bar{G}(\tau, \mathbf{x}; \tau', \mathbf{x}')\partial_{x'}\tilde{E}_\eta(\tau', \mathbf{x}')\sqrt{g(\tau')}d^3\mathbf{x}'d\tau', \tag{4.71}$$

as a solution of Eq.(4.48). The integration over τ' is straightforward, yielding:

$$\tilde{B}_y(\tau, \mathbf{x}) = \begin{cases} Ze\dfrac{3}{8\pi^2}\int d^3\mathbf{x}'\dfrac{\tau_f(\mathbf{x}';\mathbf{x})^2(x'-x_0)\sinh(\eta_0-\eta')}{[(r'_\perp-r_{\perp 0})^2+\tau_f(\mathbf{x}';\mathbf{x})^2\sinh^2(\eta'-\eta_0)]^{5/2}}\dfrac{1}{\sqrt{(r_\perp-r'_\perp)^2+\tau^2\sinh^2(\eta-\eta')}}, \\ \qquad \text{if } (\tau_0 < \tau_f(\mathbf{x}';\mathbf{x}_0) < \tau) \wedge (\tau_0 < \tau_f(\mathbf{x}';\mathbf{x}) < \tau), \\ 0, \qquad\qquad\qquad\qquad\qquad\qquad\qquad\qquad \text{otherwise} \end{cases} \tag{4.72}$$

where, $\tau_f(\mathbf{x}';\mathbf{x}) = \tau\cosh(\eta-\eta') - \sqrt{(r_\perp-r'_\perp)^2 + \tau^2\sinh^2(\eta-\eta')}$.

In the expression above, one of the constraints originates from the electric field in Eq.(4.68), while the other arises from the Green's function in Eq.(4.71). A similar approach

can be employed to obtain the x-component of the magnetic field. The spatial integration in Eq.(4.72) cannot be simplified into an elementary form; hence, we resort to numerical integration in the subsequent sections.
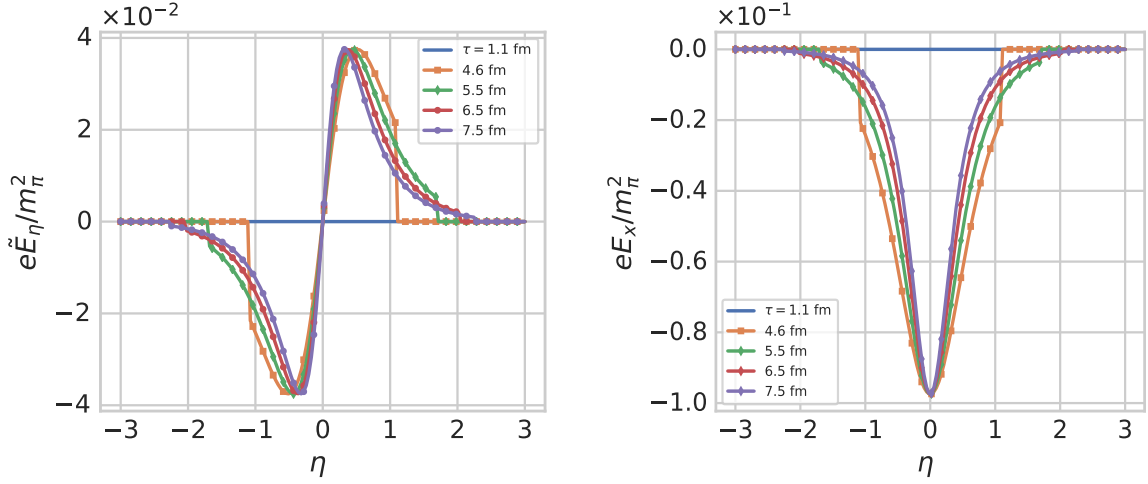
Figure 4.1: Electric-field components $e\tilde{E}_\eta$ (left) and eE_x (right) as functions of η for a stationary point source.

To examine the spatiotemporal behavior of the electromagnetic fields generated by the charged participants, we simplify by assuming that the charges are positioned at $\mathbf{x}_0 = (b/2, 0, 0)$ and the initial time $\tau_0 = 0.6$ fm, where b represents the coordinate of the source, taken as $b = 7$ fm. We compute the fields at points with transverse coordinates $\mathbf{x}_\perp = (0, 0)$, while allowing for varying rapidities η and times τ. The magnitude of the charge Ze is treated as a free parameter, and for our calculations, we set $Z = 79$, representing half of the total charged spectators in an Au-Au collision, although this is a simplification. With this setup, the only non-vanishing components of the electromagnetic fields are $\tilde{E}_\eta$, E_x, and B_y.

Fig.(4.1) illustrates the components $e\tilde{E}_\eta$ and eE_x of the electric field as functions of η. Different symbols in the plot correspond to distinct time frames. Notably, the x-component of the electric field exhibits even symmetry with respect to rapidity, with a magnitude approximately ten times greater than that of the η-component, which demonstrates odd sym-

metry. At any given η, the electric fields decay as $\sim \tau^{-3}$ (see Eqs.(4.68) and (4.69)). Preceding $\tau = 4.6$ fm, the electric field for both components is nonexistent due to retardation effects. Subsequently, only regions consistent with causality witness the electric field's presence, resulting in the piecewise behavior depicted in the figure. Naturally, this region of influence is contingent upon the initial time τ_0 and the relative distances $\mathbf{x} - \mathbf{x}_0$.
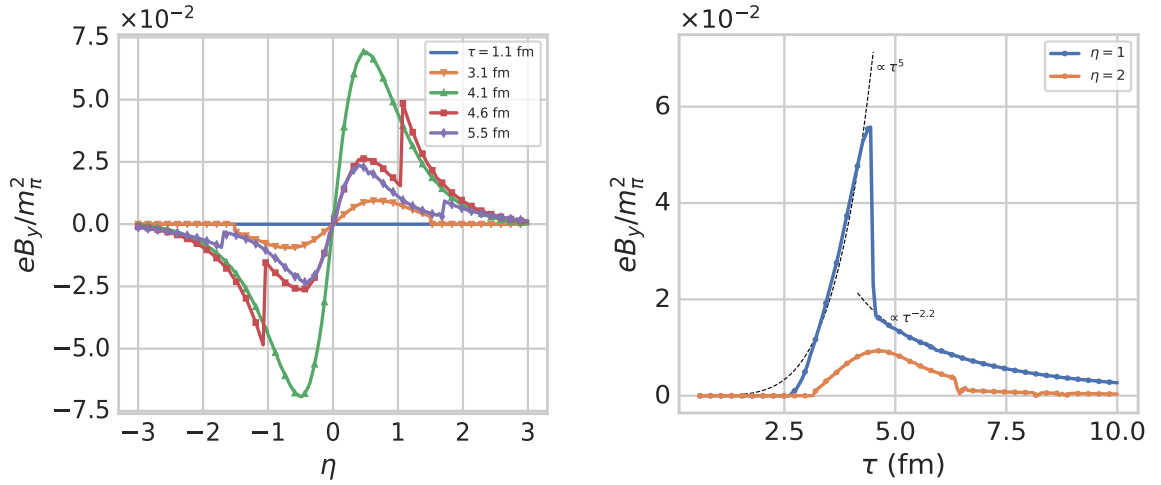
Figure 4.2: Left and right panels: Magnetic-field components eB_y as a function of η and time for a stationary point source respectively.

In Fig.(4.2) (left panel), the magnetic field component eB_y is depicted as a function of η, with various symbols denoting different time frames. Initially, at early times ($\tau < 3.1$ fm), the magnetic field is absent due to the initial causality constraint (refer to Eq.(4.72)), which is inherited from the electric field. However, unlike the electric field, which is confined to $\tau_f(\mathbf{x}; \mathbf{x}_0)$, the magnetic field's support extends to a broader space-time region, as evident in the left panel of Fig.(4.2). Here, the magnetic field attains non-zero values earlier than the corresponding electric field, which remains zero until $\tau = 4.6$ fm. Nevertheless, the magnetic field during this early period is confined to a narrower rapidity region due to this constraint. Subsequently, for 3.1 fm $< \tau < 4.6$ fm, the magnitude of the magnetic field intensifies and exhibits continuous evolution across the rapidity spectrum.
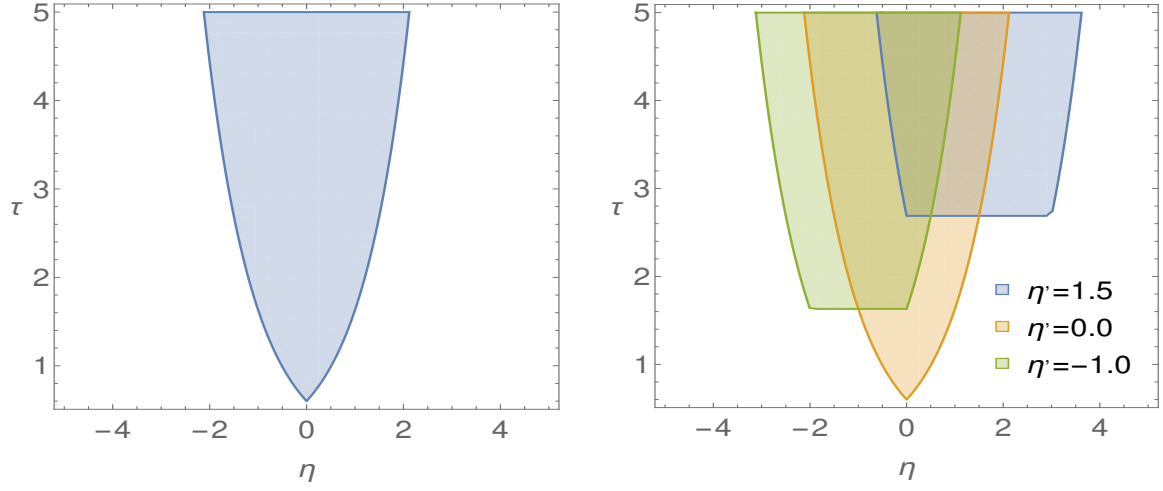
Figure 4.3: Left panel: Domain of influence $\tau_0 < \tau_f(\mathbf{x}; \mathbf{x}_0) < \tau$ for the electric field component $e\tilde{E}_\eta$. Right panel: Domain of influence for the magnetic field component eB_y, $\tau_0 < \tau_f(\mathbf{x}'; \mathbf{x}_0) < \tau \wedge \tau_0 < \tau_f(\mathbf{x}'; \mathbf{x}) < \tau$. The transverse coordinates and η_0 are set to zero ($r_\perp = r_{\perp 0} = \eta_0 = 0$) for simplicity.

The influence domains of both the electric and magnetic fields are determined by their respective equations. The electric field, denoted as $e\tilde{E}_\eta$ in Eq.(4.68), exhibits an influence domain defined as $\tau_0 < \tau_f(\mathbf{x}; \mathbf{x}_0) < \tau$, where $\tau_f(\mathbf{x}; \mathbf{x}_0)$ describes the causal boundary. On the other hand, the magnetic field, represented by eB_y in Eq.(4.72), extends its influence over the domain $\tau_0 < \tau_f(\mathbf{x}'; \mathbf{x}_0) < \tau \wedge \tau_0 < \tau_f(\mathbf{x}'; \mathbf{x}) < \tau$, where $\tau_f(\mathbf{x}'; \mathbf{x}_0)$ characterizes the extent of influence at each spatial point $\mathbf{x}'$ relative to the source at $\mathbf{x}_0$.

Examining Fig.(4.3) (left panel), which illustrates the domain of influence or causal region, it becomes evident that for smaller values of τ, the support of $\tau_f(\mathbf{x}; \mathbf{x}_0)$ is confined to narrower intervals in η for the electric field. Conversely, inspecting Fig.(4.3) (right panel) for the magnetic field, the support extends over larger areas depending on the specific value of η'. For instance, at $\eta' = 0$, the magnetic field's support closely resembles that of the electric field. However, for $\eta' = -1.0$ or $\eta' = 1.5$, the shaded region encompasses a broader area compared to the former scenario. As time progresses, both the electric and magnetic fields undergo an incremental expansion in their supportive domains.

Now turning our attention to Fig.(4.2) (right panel), showcasing the temporal evolution of the magnetic field for two distinct rapidity values, $\eta = 1$ and $\eta = 2$. For $\eta = 1$, we have additionally fitted the obtained numerical solution with a power law (indicated by black dotted lines). It's apparent that the entire time evolution can be categorized into two regimes: during early times, the magnetic field exhibits growth proportional to τ^5, while at later times, it decays as $\tau^{-2.2}$. In the intermediate region around $\tau \sim 4.6$ fm, a discontinuity is observed. Conversely, for larger rapidities, such as $\eta = 2$, the magnitude of the magnetic field is approximately an order of magnitude smaller compared to smaller rapidities, like $\eta = 1$. A noteworthy comparison can be made with the results obtained from spectators [11], where, at vanishing conductivity, the decay is simply proportional to τ^{-3}. However, during early times, the magnitude is significantly higher and depends on the collision energy. Nevertheless, a distinguishing characteristic of the magnetic field generated by the participants, unlike the spectators, is its sustained significance throughout the evolution, even at very late times. For instance, at $\tau = 10$ fm for a smaller rapidity $\eta = 1$, the magnitude is of the order of $\mathcal{O}(10^{-3})$ compared to $\mathcal{O}(10^{-5})$ (in units of m_π^2) for the spectators.

4.4.2   Fields for a transverse charge distribution

Now, let's delve into the investigation of fields induced by a stationary charge distribution. We adopt the convention that the charge density of both the target and projectile is distributed across the transverse plane while remaining localized in the rapidity direction. To simplify the analysis, we assume that the protons within a nucleus are uniformly distributed according to a Gaussian profile with mean $\mathbf{x}_0$ and standard deviation $\sigma_\perp$. Thus, the charge density takes the form:

$$\rho(\tau, \mathbf{x}) = Ze \frac{f_\perp(x, x_0; y, y_0)\delta(\eta - \eta_0)}{\tau} \Theta(\tau - \tau_0), \tag{4.73}$$

where $f_\perp(x, x_0; y, y_0)$ represents the charge distribution in the transverse direction, given by:

$$f_\perp(x, x_0; y, y_0) = \frac{1}{\pi\sigma_\perp^2} \left[\exp\left(-\frac{(x - x_0)^2 + (y - y_0)^2}{\sigma_\perp^2} \right) \right.$$
$$\left. + \exp\left(-\frac{(x + x_0)^2 + (y + y_0)^2}{\sigma_\perp^2} \right) \right] \Theta\left(1 - \frac{x^2}{r_a^2} - \frac{y^2}{r_b^2} \right). \quad (4.74)$$

Here, $x_0 = b/2$ and $y_0 = 0$, representing the centers of the nuclei in the transverse plane, with $\sigma_\perp = 5$ fm. The parameter b denotes the impact parameter, set to $b = 7$ fm. The semi-major and semi-minor axes of the elliptical region of the participants are determined by $r_a = R - x_0$ and $r_b = \sqrt{R^2 - x_0^2}$, where R signifies the radius of a nucleus ($R = 7$ fm). The unit step function in Eq.(4.74) ensures that only charges within the elliptical region in the transverse plane are considered.

Following a procedure akin to that for the point charge discussed in Section.(4.4.1), we can determine the various field components utilizing the Green's function given by Eq.(4.63) for the equations Eqs.(4.44) to (4.49). The integration over τ and η yields elementary results, leading to the following expressions for the electromagnetic field components:

$$\tilde{E}_\eta(\tau, \mathbf{x}) = \frac{Ze}{4\pi} \int d^2\mathbf{x}' \frac{\tau \sinh(\eta - \eta_0)}{\left[(x - x')^2 + (y - y')^2 + \tau^2 \sinh^2(\eta - \eta_0) \right]^{3/2}}$$
$$\times f_\perp(x', x_0; y', y_0) \Theta\left(1 - \frac{x'^2}{r_a^2} - \frac{y'^2}{r_b^2} \right), \quad (4.75)$$

$$\tilde{B}_y(\tau, \mathbf{x}) = Ze \frac{3}{8\pi^2} \int d^3\mathbf{x}' d^2\mathbf{x}'' \frac{\tau_f(\mathbf{x}'; \mathbf{x})^2 (x' - x'') \sinh(\eta_0 - \eta')}{\left[(x' - x'')^2 + (y' - y'')^2 + \tau_f(\mathbf{x}'; \mathbf{x})^2 \sinh^2(\eta_0 - \eta) \right]^{5/2}}$$
$$\times \frac{f_\perp(x'', x_0; y'', y_0)}{\sqrt{(x - x')^2 + (y - y')^2 + \tau^2 \sinh^2(\eta - \eta')}} \times \Theta\left(1 - \frac{x''^2}{r_a^2} - \frac{y''^2}{r_b^2} \right).$$
$$(4.76)$$

Here, the integration over $\mathbf{x}'$ is again confined to the causal region, satisfying the inequality $\tau_0 < \tau_f(\mathbf{x}'; \mathbf{x}) < \tau$, along with the physical boundary of the elliptical region expressed via the unit-step function. We explicitly present the expressions for $\tilde{E}_\eta$ and $\tilde{B}_y$,

noting that other components of the electromagnetic fields can be computed using a similar procedure, which we omit here.
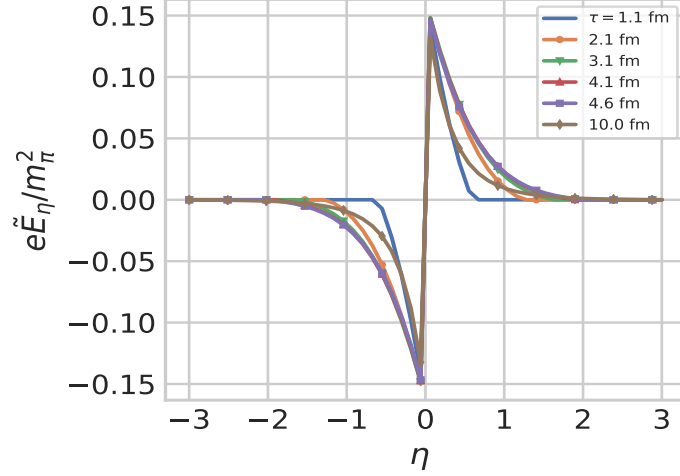
Figure 4.4: The electric-field component $e\tilde{E}_\eta$ as a function of η. Various symbols represent the values of electric field at different times.

Fig.(4.4) illustrates the behavior of $e\tilde{E}_\eta$ as a function of η at various time instances. In comparison to the electric field generated by a point charge distribution (see Fig.(4.1), top panel), the electric field arising from a charge distribution exhibits non-zero values even at early times, around $\tau \sim 1.1$ fm, albeit localized in space. As time progresses, the electric field gradually diminishes, asymptotically approaching zero at large rapidities. The magnitude of the electric field is approximately $\sim 0.1 m_\pi^2$, serving as the source for the magnetic field.

Fig.(4.5) depicts the temporal evolution of the transverse component of the magnetic field, eB_y, at rapidity $\eta = 0.5$, with the blue band representing an estimate of the numerical integration error. Due to the highly oscillatory nature of the integrand in Eq.(4.75), extrapolation to smaller time intervals was not feasible. Nonetheless, the qualitative behavior of the magnetic field at late times ($\tau_f > 4.6$ fm) resembles that of a point charge distribution (cf. Fig.(4.2), bottom panel), persisting for sufficiently long timescales in the context of
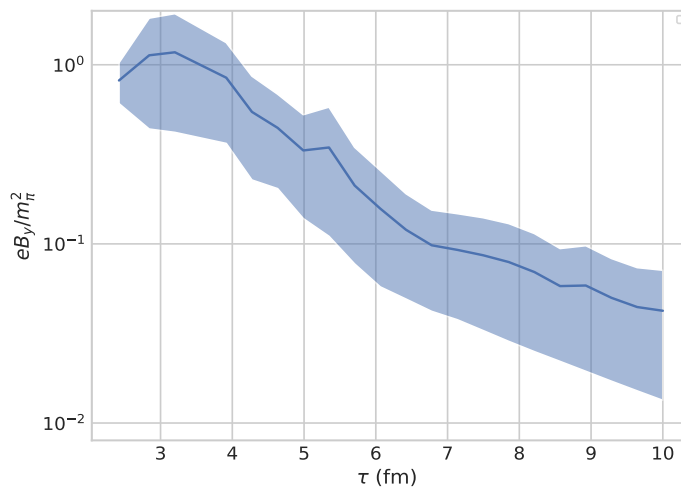
Figure 4.5: Time evolution of eB_y at rapidity $\eta = 0.5$. The blue band is the estimate of the error in the numerical integration.

heavy-ion collisions. This prolonged lifetime can be attributed to the retardation effect, evident from Fig.(4.3), highlighting that the support of the integral in Eq.(4.75) expands to larger spatial regions with non-vanishing gradients of electric field at late times.

4.5 Conclusion

Our investigation delved into the study of spatiotemporal dynamics of electromagnetic fields produced by charged particles within an expanding fluid governed by a background Bjorken flow. We addressed Maxwell's equations within this framework, assuming a negligible back-reaction to the fluid's flow. Introducing coupling to the fluid's shear and expansion scalar added complexity to the dynamics. Interestingly, we found that even without charged currents, gradients in the electric field could generate a magnetic field for a stationary charge distribution co-moving with the fluid. This resultant magnetic field undergoes an initial phase of vanishing, followed by growth and eventual decay. The principle of causality proves indispensable in describing the evolution of such charge distributions in space and time. We also examined a more realistic scenario involving continuous charge

distribution within the context of heavy-ion collisions. The resultant magnetic field retains significance even at temporal scales as large as ~ 10 fm. This observation supports prior studies discussing the magnetic field's influence during the hadronic stage of heavy-ion collisions [24, 25, 26]. However, our study has some limitations, primarily from the assumption of vanishing charged currents. Relaxing this assumption could yield intriguing consequences, particularly when considering non-equilibrium processes like charge diffusion and conductivity. These processes nullify existing gradients in the electric charge distribution, potentially leading to non-trivial alterations in the spatiotemporal evolution of dynamic electromagnetic fields. Unfortunately, our efforts to incorporate these terms into the analysis hindered our ability to find analytical solutions for Green's function, making the problem quite challenging. In the future we could explore flow patterns with non-zero vorticity and acceleration, offering promising paths for gaining deeper insights into the intricate dynamics of electromagnetic fields in expanding fluid media.

We now shift our focus to another aspect which is studying the behavior of all the components of electromagnetic fields taking into account the nuclear stopping. This phenomenon is particularly prominent in low-energy nuclear collisions, notably at FAIR energies.

References

[1] G. Inghirami, M. Mace, Y. Hirono, L. Del Zanna, D. E. Kharzeev and M. Bleicher, "Magnetic fields in heavy ion collisions: flow and charge transport," Eur. Phys. J. C **80**, no.3, 293 (2020) doi: 10.1140/epjc/s10052-020-7847-4 [arXiv:1908.07605 [hep-ph]].

[2] A. Dash, M. Shokri, L. Rezzolla and D. H. Rischke, "Charge diffusion in relativistic resistive second-order dissipative magnetohydrodynamics," Phys. Rev. D **107**, no.5, 056003 (2023) doi: 10.1103/PhysRevD.107.056003 [arXiv:2211.09459 [nucl-th]].

[3] K. Nakamura, T. Miyoshi, C. Nonaka and H. R. Takahashi, "Relativistic resistive magneto-hydrodynamics code for high-energy heavy-ion collisions," Eur. Phys. J. C **83**, no.3, 229 (2023) doi: 10.1140/epjc/s10052-023-11343-y [arXiv:2211.02310 [nucl-th]].

[4] E. R. Most, J. Noronha and A. A. Philippov, "Modelling general-relativistic plasmas with collisionless moments and dissipative two-fluid magnetohydrodynamics," Mon. Not. Roy. Astron. Soc. **514**, no.4, 4989-5003 (2022) doi: 10.1093/mnras/stac1435 [arXiv:2111.05752 [astro-ph.HE]].

[5] E. R. Most and J. Noronha, "Dissipative magnetohydrodynamics for nonresistive relativistic plasmas: An implicit second-order flux-conservative formulation with stiff relaxation," Phys. Rev. D **104**, no.10, 103028 (2021) doi: 10.1103/PhysRevD.104.103028 [arXiv:2109.02796 [astro-ph.HE]].

[6] K. Dionysopoulou, D. Alic, C. Palenzuela, L. Rezzolla and B. Giacomazzo, "General-Relativistic Resistive Magnetohydrodynamics in three dimensions: formulation and tests," Phys. Rev. D **88**, 044020 (2013) doi: 10.1103/PhysRevD.88.044020 [arXiv:1208.3487 [gr-qc]].

[7] A. Huang, D. She, S. Shi, M. Huang and J. Liao, "Dynamical magnetic fields in heavy-ion collisions," Phys. Rev. C **107**, no.3, 034901 (2023) doi: 10.1103/Phys-RevC.107.034901 [arXiv:2212.08579 [hep-ph]].

[8] A. Das, S. S. Dave, P. S. Saumia and A. M. Srivastava, "Effects of magnetic field on plasma evolution in relativistic heavy-ion collisions," Phys. Rev. C **96**, no.3, 034902 (2017) doi: 10.1103/PhysRevC.96.034902 [arXiv:1703.08162 [hep-ph]].

[9] D. E. Kharzeev, L. D. McLerran and H. J. Warringa, "The Effects of topological charge change in heavy ion collisions: 'Event by event P and CP violation'," Nucl. Phys. A **803**, 227-253 (2008) doi: 10.1016/j.nuclphysa.2008.02.298 [arXiv:0711.0950 [hep-ph]].

[10] U. Gursoy, D. Kharzeev and K. Rajagopal, "Magnetohydrodynamics, charged currents and directed flow in heavy ion collisions," *Phys. Rev. C* **89**(5), 054905 (2014) doi: 10.1103/PhysRevC.89.054905 [arXiv:1401.3805 [hep-ph]].

[11] U. Gürsoy, D. Kharzeev, E. Marcus, K. Rajagopal and C. Shen, "Charge-dependent Flow Induced by Magnetic and Electric Fields in Heavy Ion Collisions," Phys. Rev. C **98**, no.5, 055201 (2018) doi: 10.1103/PhysRevC.98.055201 [arXiv:1806.05288 [hep-ph]].

[12] J. D. Bjorken, "Highly Relativistic Nucleus-Nucleus Collisions: The Central Rapidity Region," Phys. Rev. D **27**, 140-151 (1983) doi: 10.1103/PhysRevD.27.140.

[13] Kip S. Thorne and Douglas MacDonald, "Electrodynamics in curved space-time: 3 + 1 formulation," Mon. Not. Roy. Astron. Soc. **198**, no.2, 339-343 (1982) doi: 10.1093/mnras/198.2.339 [https://academic.oup.com/mnras/article-pdf/198/2/339/9402846/mnras198-0339.pdf].

[14] C. G. Tsagas, "Electromagnetic fields in curved spacetimes," Class. Quant. Grav. **22**, 393-408 (2005) doi: 10.1088/0264-9381/22/2/011 [arXiv:gr-qc/0407080 [gr-qc]].

[15] G. Aarts and A. Nikolaev, "Electrical conductivity of the quark-gluon plasma: perspective from lattice QCD," Eur. Phys. J. A **57**, no.4, 118 (2021) doi: 10.1140/epja/s10050-021-00436-5 [arXiv:2008.12326 [hep-lat]].

[16] D. J. Griffiths, *Introduction to electrodynamics; 4th ed.*, Pearson, Boston, MA, 2013, https://cds.cern.ch/record/1492149, Re-published by Cambridge University Press in 2017, doi: 1108420419.

[17] H. Nariai and K. Tanabe, *Propagators for a Scalar Field in a Homogeneous Expanding Universe. I: Case of the Friedmann Universes*, Progress of Theoretical Physics **55** (1976) 1116–1132, Oxford University Press.

[18] T. Padmanabhan, *Physical interpretation of quantum field theory in noninertial coordinate systems*, Phys. Rev. Lett. **64** (1990) 2471–2474, doi: 10.1103/PhysRevLett.64.2471.

[19] D. Rindori, L. Tinti, F. Becattini, and D. H. Rischke, *Relativistic quantum fluid with boost invariance*, Phys. Rev. D **105** (2022) 056003, doi: 10.1103/PhysRevD.105.056003, eprint: arXiv:2102.09016 [hep-th].

[20] A. Sagnotti and B. Zwiebach, "Electromagnetic Waves in a Bianchi Type I Universe," Phys. Rev. D **24**, 305-319 (1981) doi: 10.1103/PhysRevD.24.305.

[21] S. V. Dhurandhar, C. V. Vishveshwara, and J. M. Cohen, *Electromagnetic, neutrino and gravitational fields in the Kasner space-time with rotational symmetry*, Classical and Quantum Gravity **1** (1984) 61, doi: 10.1088/0264-9381/1/1/009.

[22] L. M. Burko, A. I. Harte and E. Poisson, Phys. Rev. D **65**, 124006 (2002) doi: 10.1103/PhysRevD.65.124006 [arXiv:gr-qc/0201020 [gr-qc]].

[23] Eric Poisson, Adam Pound, and Ian Vega, *The motion of point particles in curved spacetime*, Living Reviews in Relativity **14** (2011) 1–190, Springer.

[24] A. Dash, S. Samanta, J. Dey, U. Gangopadhyaya, S. Ghosh and V. Roy, "Anisotropic transport properties of a hadron resonance gas in a magnetic field," Phys. Rev. D **102**, no.1, 016016 (2020) doi:10.1103/PhysRevD.102.016016 [arXiv:2002.08781 [nucl-th]].

[25] J. Dey, S. Samanta, S. Ghosh and S. Satapathy, "Quantum expression for the electrical conductivity of massless quark matter and of the hadron resonance gas in the presence of a magnetic field," Phys. Rev. C **106**, no.4, 044914 (2022) doi: 10.1103/PhysRevC.106.044914 [arXiv:2002.04434 [nucl-th]].

[26] S. Imaki, "Chiral magnetic effect in the hadronic phase," Phys. Rev. D **101**, no.7, 074024 (2020) doi: 10.1103/PhysRevD.101.074024 [arXiv:1906.08949 [hep-ph]].

Chapter 5

Effect of baryon stopping on the electromagnetic fields

It has been mentioned earlier that off-central relativistic heavy-ion collisions produce intense transient electromagnetic fields, which are predominantly produced due to the motion of spectators, reaching magnitudes of approximately $\sim 10 m_\pi^2$ at top RHIC energies [1, 2, 3, 4, 5, 6, 7, 8]. Notably, the peak values of the event-averaged electromagnetic field components generated in these collisions exhibit an approximate linear proportionality with the center-of-mass energy ($\sqrt{s_{NN}}$) [4]. These results, however, were obtained on the assumption of near-perfect transparency of the colliding nucleons, as described by the Glauber model [9]. For high $\sqrt{s_{NN}}$, such as top RHIC and LHC energies, the elastic or diffractive dissociation collisions lead to a minute loss of energy of the colliding nucleon, and hence it is a good approximation to consider that the colliding nucleons move in a straight line with almost constant velocity even after multiple collisions. However, for low $\sqrt{s_{NN}}$ collisions, baryon stopping can be sizeable [10, 11, 12, 13]. The baryon stopping must be considered while estimating the electromagnetic fields using the Glauber model at low $\sqrt{s_{NN}}$. Particularly, the temporal evolution of the fields post-collisions will be affected due to the decelerations of the protons after each binary collision.

Previous studies show that, on average, a proton loses half of its pre-collision energy, about one unit of rapidity in each binary collision [14]. The maximum value of the net baryon density at mid-rapidity is achieved for $\sqrt{s_{NN}} \approx 6 \, \text{GeV}$ [15, 16]. Above this collision energy, the mid-rapidity net baryon density decreases with increasing energy due to the higher transparency of the colliding nuclei. Hence, for higher collision energies, the effect

145

of deceleration in calculating electromagnetic fields is minimal. Some theoretical model studies, including models based on color glass condensate, could successfully describe the stopping effect [17, 18, 19]. However, in the current study, we do not use any of these models; instead, we take a more pedagogical approach and parameterize the decelerated motion of participants in the Monte-Carlo Glauber (MCG) model to mimic baryon stopping and then calculate the electromagnetic fields for $\sqrt{s_{NN}} = 4$-20 GeV.

This current chapter is organized as follows: In the first section, in Sec.(5.1), we discuss the theoretical formulation and the assumptions made for introducing the stopping of baryons after the collisions. Then, in Sec.(5.2), we briefly discuss the Monte-Carlo Glauber model. Next, in Sec.(5.3), we present the results. Finally, we conclude in Sec.(5.4).

5.1 Formulations

As mentioned in the introduction, we consider the deceleration of charged participants after they undergo binary collision. The electromagnetic fields for a point particle with charge Ze moving with velocity $\boldsymbol{\beta} = \frac{d\mathbf{r}}{dt}$ and a proper acceleration $\dot{\boldsymbol{\beta}} = \frac{d\boldsymbol{\beta}}{dt}$ can be calculated at position $\mathbf{r}_{\mathrm{obs}}$ at time t_{obs} from the well known formula [20].

$$
e\mathbf{B}(\mathbf{r}_{\mathrm{obs}}, t_{\mathrm{obs}}) = -\mathcal{C}Z\alpha_{EM}\left[\frac{\hat{\mathbf{R}} \times \boldsymbol{\beta}(t')}{\gamma^2 k^3 R^2} + \frac{(\hat{\mathbf{R}} \cdot \dot{\boldsymbol{\beta}}(t'))(\hat{\mathbf{R}} \times \boldsymbol{\beta}(t')) + k\hat{\mathbf{R}} \times \dot{\boldsymbol{\beta}}(t')}{k^3 R}\right]_{t'},
$$
$$
e\mathbf{E}(\mathbf{r}_{\mathrm{obs}}, t_{\mathrm{obs}}) = \mathcal{C}Z\alpha_{EM}\left[\frac{\hat{\mathbf{R}} - \boldsymbol{\beta}(t')}{\gamma^2 k^3 R^2} + \frac{\hat{\mathbf{R}} \times [(\hat{\mathbf{R}} - \boldsymbol{\beta}(t')) \times \dot{\boldsymbol{\beta}}(t')]}{k^3 R}\right]_{t'}, \tag{5.1}
$$

where e is electronic charge, the fields are all in units of m_π^2, and R is in fm. Here $\mathcal{C} = fm^{-2}/m_\pi^2 \sim 2$ is a numerical factor, $\alpha_{EM} = \frac{1}{137}$ is the fine structure constant, and Z is the atomic number of each nucleus (we consider symmetric collisions). The right-hand side of the above expressions is evaluated at retarded time t'. The relation between t' and

t_{obs} is given by

$$t' + \sqrt{(x_{\text{obs}} - x')^2 + (y_{\text{obs}} - y')^2 + (z_{\text{obs}} - z'(t'))^2} = t_{\text{obs}}. \qquad (5.2)$$

The relative position $\mathbf{R}(\mathbf{t'}) = \mathbf{r}_{\text{obs}} - \mathbf{r'}(\mathbf{t'})$, and the unit vector along it is defined as $\hat{\mathbf{R}} = \frac{\mathbf{R}}{R}$, the factor $k = 1 - \hat{\mathbf{R}} \cdot \boldsymbol{\beta}(t')$, and $\gamma = \frac{1}{\sqrt{1-\beta^2}}$ is the Lorentz factor.

To calculate the electromagnetic fields, we consider nucleons moving in a straight line with a constant velocity $\beta_{s_{NN}} = \left(1.0 - \frac{4m^2}{s_{NN}}\right)^{1/2}$, m is the mass of the proton. Depending on whether they are participants or spectators, we decelerate or let them continue moving with constant initial velocity for a given $\sqrt{s_{NN}}$. Below, we discuss a step-by-step process for evaluating the total electromagnetic field using an MC Glauber model and parameterized form for deceleration.

- We sample the positions of individual nucleons from the nuclear density distribution of the Wood-Saxon type (the details of which are discussed later). This will give us the initial positions $x_0'(t')$, $y_0'(t')$ and $z_0'(t')$ of the nucleons inside the right and left moving nucleus. We assume an Eikonal approximation where, even after binary collisions, individual nucleons will continue moving along the beam's direction. So far, the calculation of the fields is done at some retarded time t', and then we obtain the corresponding fields at t_{obs} using Eq.(5.2). Here, as we will be working with the collision of individual nucleons tracking its trajectory, it is more convenient to work in proper time τ where $\tau = \sqrt{t^2 - \mathbf{r}^2}$. Here, we choose $\tau = 0$ at $\mathbf{r} = 0$, corresponding to $t = 0$ when the centers of the two nuclei overlap. In this scenario, individual nucleon-nucleon collisions can occur for $\tau < 0$ or $\tau > 0$, assuming that just after the collision, the nucleons that take part in the collision process would decelerate.

- If the proton is a participant, we apply a deceleration with the following parametrized

form for the velocity profile as

$$\beta(\tau) = \mathcal{A} \left[1 - \tanh\left(\frac{\tau - \tau_h}{\Delta\tau} \right) \right],$$ (5.3)

where, $\mathcal{A} = \frac{\beta_{s_{NN}}}{2}$, $\Delta\tau$ is a parameter used to control the time interval for the deceleration, τ_h is a parameter to control the time scale of the deceleration such that at $\tau = \tau_h$ the initial velocity $\beta_{s_{NN}}$ is reduced to half of its original value. Further we define a starting time τ_s for individual nucleon-nucleon collision as the time when $\beta(\tau_s)/\beta_{s_{NN}} \sim 0.98$. As per our definition, τ_s could be positive or negative depending on the location of the participants inside the colliding nucleus. The choice of the starting time of collision, where velocity reduces to 98% of the initial velocity, is reasonable. Firstly, it helps us to handle the discontinuity in velocities at the onset of deceleration. Moreover, from a physical perspective, this reduction can be interpreted as arising from Coulombic repulsion or due to the composite structure of the nucleons. We further note that the definition τ_s is arbitrary. Still, it is a reasonable choice because we assume the nucleons in the MC Glauber model are hard spheres with radius given by the inelastic nucleon-nucleon cross section as given later in Eq.(5.5). A collision happens when they touch each other.

The starting time for individual nucleon-nucleon collisions in a given event is calculated based on their relative distances $\Delta z = z_{target} - z_{projectile}$ at $\tau = 0$, and considering straight line trajectories with velocity $\beta_{s_{NN}}$. In Fig.(5.1) we display the velocity profile $\beta(\tau)$ (solid lines) and the proper acceleration $\frac{d\beta}{d\tau}$ vs τ (dashed lines) for $\Delta\tau = 1$ fm (blue lines) and 3 fm (red lines) respectively.

- In Eq.(5.1), EM fields are evaluated at retarded time; hence we need to find the retarded time and corresponding positions of the nucleons from $\beta(\tau)$ using the relations

$$\frac{dt'(\tau)}{d\tau} = \frac{1}{\sqrt{1 - \beta^2(\tau)}}, \frac{dz'(\tau)}{d\tau} = \frac{\beta(\tau)}{\sqrt{1 - \beta^2(\tau)}}.$$
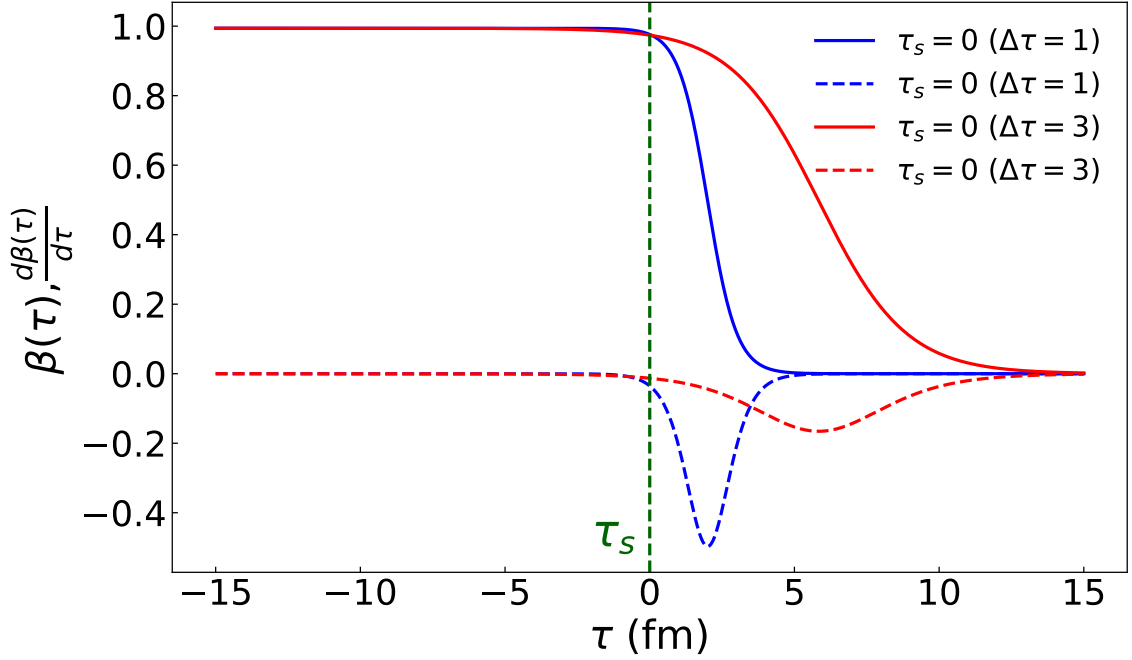
Figure 5.1: Parametrization of velocity $\beta\left(\tau\right)$ (solid lines) and the corresponding $\frac{d\beta}{d\tau}$ (dashed lines) as a function of τ for participants for $\Delta\tau = 1$ fm (blue curves) and 3 fm (red curves).

- Finally, we obtained the electromagnetic fields at observation point $\mathbf{r}_{\mathrm{obs}} \equiv (x, y, z)$ at present t_{obs} from Eq.(5.1). Calculating the electromagnetic field in an event-by-event case may result in some nucleons being very close to the point of observation, making $|\mathbf{R}| \approx 0$ leading to divergence for the fields. In practical calculations, different regularisation schemes have been used, and consistent results are obtained after taking the event average [1, 3, 4, 21]. To address this issue, here we introduce a cutoff at $|\mathbf{R}| \approx 1$ fm. This implies that the fields associated with nucleons within a distance of $|\mathbf{R}| = 1$ fm are discarded.

In this work, we calculate EM fields from an ensemble of a thousand events for a given collision centrality.

5.2 Monte-Carlo Glauber

As mentioned earlier, we use the MC Glauber model [9] to calculate the nucleon distributions, participants, spectators, and number of binary collisions for a given $\sqrt{s_{NN}}$ and impact parameter, here we briefly discuss the essential features and parameters used in our study. We sample the nucleon positions inside a given nucleus from the corresponding Wood-Saxon density distribution (assuming spherical symmetry):

$$\rho(r) \quad = \quad \frac{\rho_0}{1 + e^{\frac{r-R}{a}}}.$$ (5.4)

Where ρ_0 is the nucleon density in the center of the nucleus, R is the radius of the nucleus, a is the skin depth, and r is the radial distance from the center of the nucleus. For Au^{197} we use: $\rho_0 = 0.16$ fm^{-3}, $R = 6.34$ fm, a = 0.54 fm. We calculate participant for a given nucleon-nucleon inelastic cross section σ_{NN} by considering individual nucleons as a hard sphere; a collision takes place if the inter-nucleon transverse distance $r_\perp = \sqrt{(x_p - x_T)^2 + (y_p - y_T)^2} \leq r_c$, where

$$r_c \quad = \quad \sqrt{\frac{\sigma_{NN}}{\pi}}.$$ (5.5)

The (x_p, y_p) and (x_T, y_T) mentioned above are the transverse positions of projectile and target nucleons respectively. The experimentally measured values of σ_{NN} are available for selected energies, we fit the experimentally measured σ_{NN} vs $\sqrt{s_{NN}}$ with the following three parameters form,

$$\sigma_{NN}^f \quad = \quad A\left(\sqrt{s_{NN}}\right)^B + C.$$ (5.6)

Here, from the fit we obtain the values $A = 7.63$, $B = 0.22$, $C = 17.36$ with $\chi^2 \approx$ 0.05. The parametric fit and experimental data points (circles) are shown in Fig.(5.2). It is worthwhile noting that throughout the rest of the paper, we assume that the trajectory of the participants is governed by the Eq.(5.3) and each of the participants will eventually

lose much of its energy within a time interval $\Delta\tau$. However, the baryon usually loses about one unit of rapidity in each collision, and it will take multiple collisions before they lose a substantial amount of the initial energy [22, 23]. Such a realistic scenario of energy/rapidity loss is beyond the scope of the present work and can be implemented in a future study.
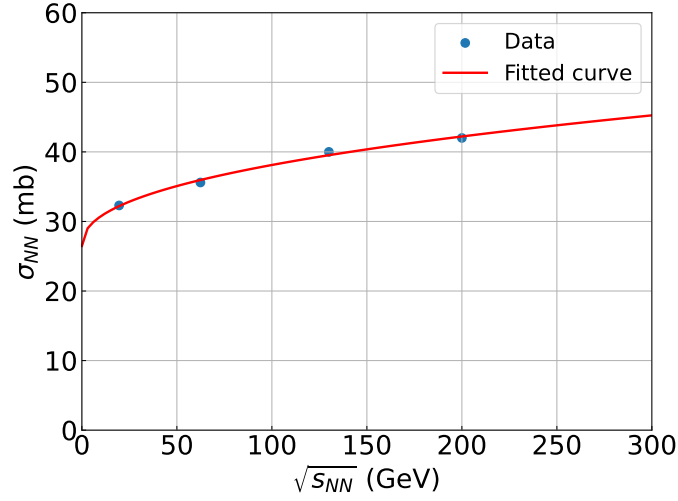
Figure 5.2: σ_{NN} (nucleon-nucleon inelastic cross-section) vs $\sqrt{s_{NN}}$ (circles) taken from [9]. The red line is a fit with a three-parameter function (Eq.(5.6)).
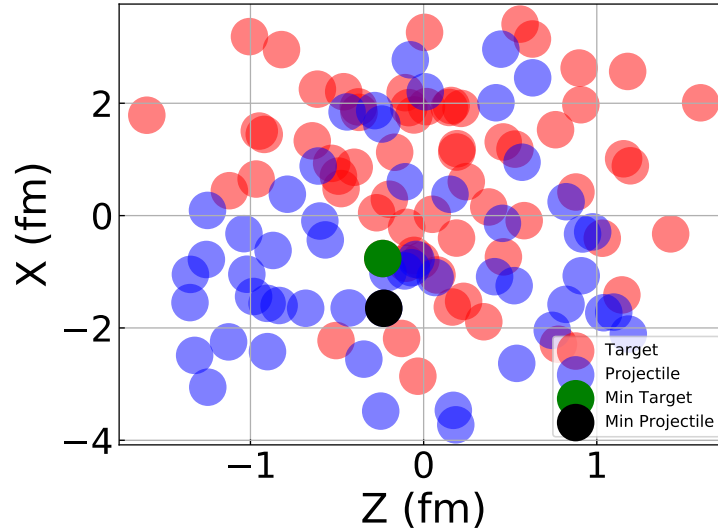
Figure 5.3: Snapshot of the participants in a given Au+Au collision event at $\tau = 0$ for $\sqrt{s_{NN}}$= 8 GeV and b=8 fm.

5.3   Results and Discussions

From now on, we denote 'electronic charge times the fields' simply as 'Fields' in our plots. We primarily focus on event-averaged values of the electric $\mathbf{E} \equiv (E_x, E_y, E_z) \equiv E_i$ and magnetic $\mathbf{B} \equiv (B_x, B_y, B_z) \equiv B_i$ field components to investigate the effect of baryon stopping on the electromagnetic fields unless stated otherwise. For the event-averaged case, we take ensemble of a thousand events, and to focus on the event-by-event contribution of each field component, we consider their absolute values so that the random phase cancellation during the averaging could be avoided.
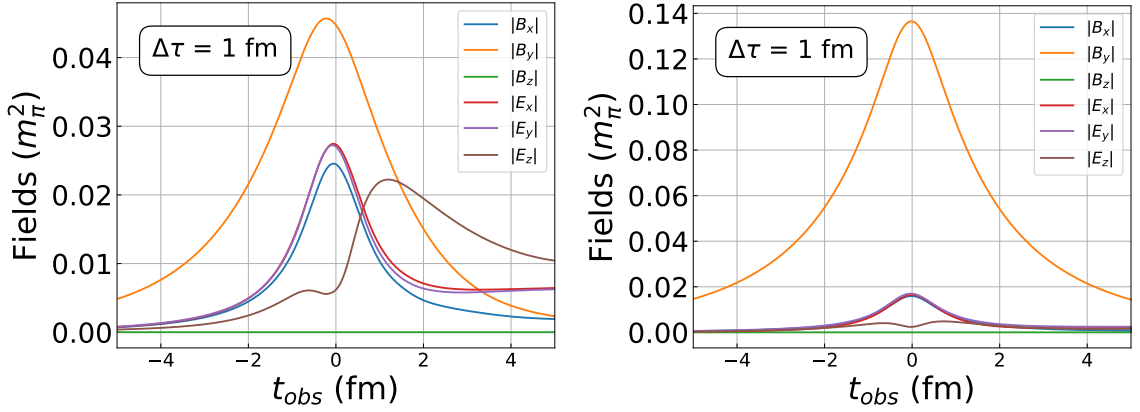
Figure 5.4: Evolution of $\mathbf{E}, \mathbf{B}$ at $\mathbf{r}_{\text{obs}} = (0, 0, 0)$ over time for $b = 3$ (left) and 12 fm (right) at $\sqrt{s_{NN}} = 4$ GeV, with $\Delta\tau = 1$ fm.

Since the number of participants/collisions decreases monotonically with the impact parameter/centrality of the collision, we expect the effects of baryon stopping with deceleration on the fields is minimal for peripheral collisions. Fig.(5.4) depicts the temporal evolution of $|E_i|$ and $|B_i|$ at the center of the collision zone $\mathbf{r}_{\text{obs}} = (0, 0, 0)$, for $\Delta\tau = 1$ fm at $\sqrt{s_{NN}} = 4$ GeV for two distinct impact parameters: 3 fm and 12 fm, respectively. Upon comparison of both plots, a notable distinction emerges, particularly evident in the more central collision (at $b = 3$ fm), showcasing the effect of deceleration being dominant at the most central collision which can be attributed to the increased number of participants.
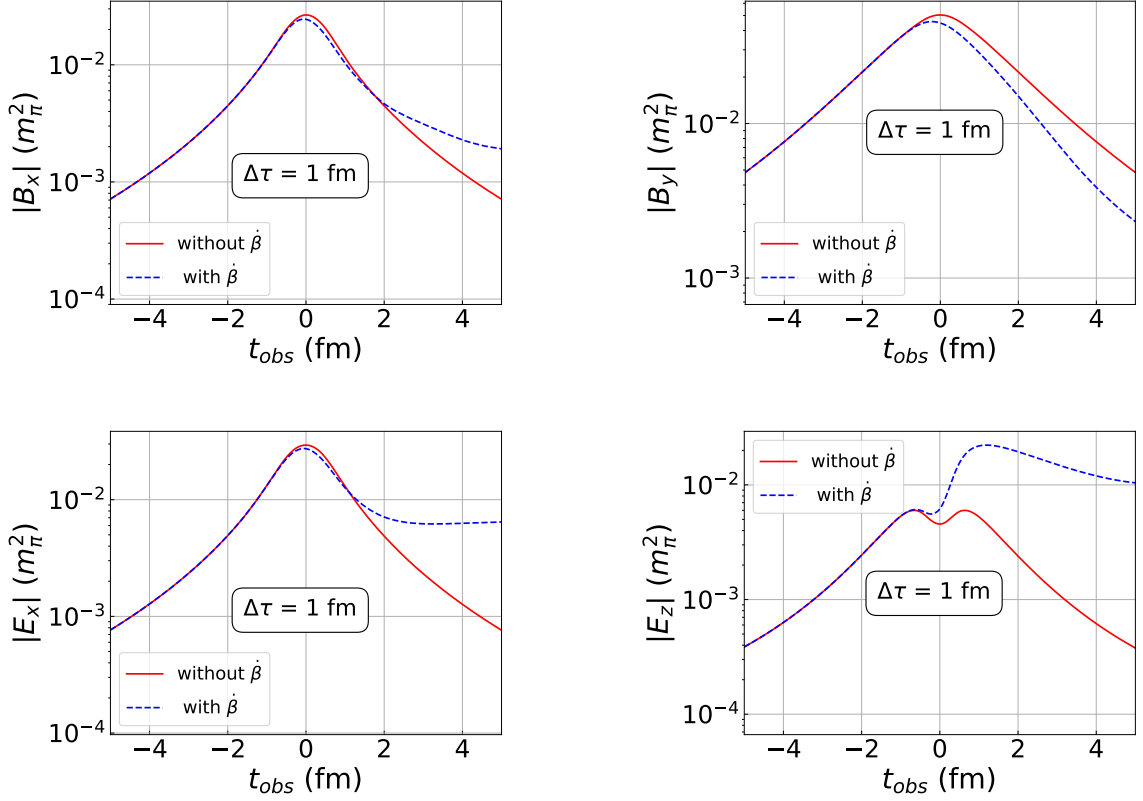
Figure 5.5: Comparison of $|B_x|, |B_y|$ (top panel), and $|E_x|, |E_z|$ (bottom panel) with (blue dashed lines) and without deceleration (red solid lines) at $\sqrt{s_{NN}} = 4$ GeV with $b = 3$ fm at $\mathbf{r}_{\text{obs}} = (0, 0, 0)$.

In the presence of deceleration the magnitude of $|B_x|, |E_x|, |E_y|$, and $|E_z|$ are enhanced in the presence of deceleration after $\tau \sim 2$ fm. Furthermore, electric fields seem to asymptotically reach a constant value for $t_{\text{obs}} \gtrsim 4$ fm. This late-time behavior arises from the dominance of Coulombic fields as deceleration drives participant velocities towards non-relativistic limits, and they may eventually come to rest. Additionally, a slight shift in the peak values of $|B_x|, |B_y|, |E_x|$, and $|E_y|$ is noticeable in the left plot compared to the right, primarily attributed to the velocity profile of participants which start decelerating slightly before the collision, i.e., $\tau < 0$. To see the effect of baryon stopping, we show the comparison of the temporal evolution of the electromagnetic fields with and without baryon stopping at $\sqrt{s_{NN}} = 4$ GeV for $b = 3$ fm in Fig.(5.5). The solid red lines correspond to

no stopping, and the blue dashed lines correspond to baryon stopping. It is evident that $|E_x|$ and $|E_z|$ are significantly higher for the stopping scenario at late times (after 3-4 fm). Whereas $|B_y|$ does not show this type of asymptotic behavior at late times, as seen from the right plot of the top panel in Fig.(5.5). This is understood as charges at rest won't give rise to any magnetic fields, unlike the Coulombic contribution to the electric fields.
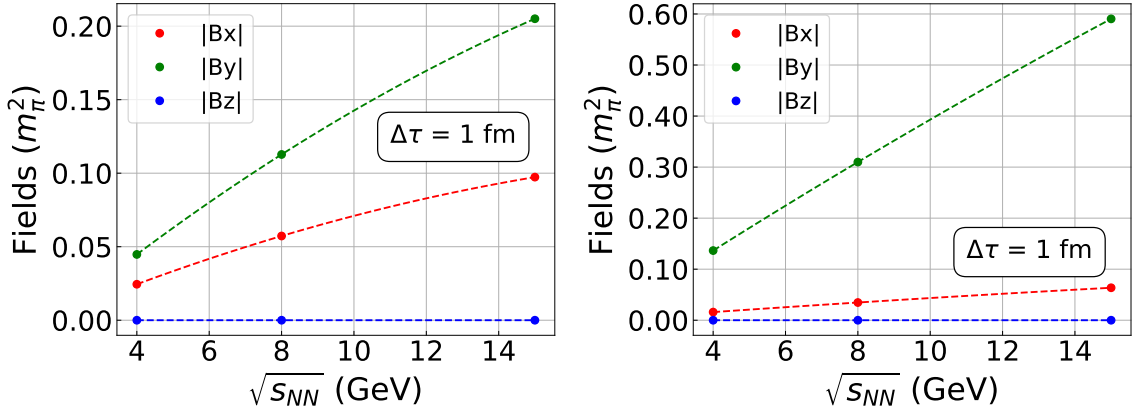
Figure 5.6: Variation of magnetic fields with $\sqrt{s_{NN}}$ for b= 3 (left panel), 12 fm (right panel) at $\mathbf{r}_{obs}$ = (0,0,0).

We found $|E_z|$ is most sensitive to deceleration and is enhanced substantially after collisions for the baryon stopping scenario compared to the other components of the electric fields. In case of no baryon stopping, the peak value of event averaged electromagnetic field rises almost linearly as a function of $\sqrt{s_{NN}}$ [4]. To investigate whether this approximate linear dependency on $\sqrt{s_{NN}}$ still holds for baryon stopping scenario, we plot $|B_i|$'s at $(\mathbf{r}_{obs}, t_{obs}) = 0$ as a function of $\sqrt{s_{NN}}$ in Fig.(5.6). The left panel is for $b = 3$ fm, and the right is for $b = 12$ fm. From the comparison of these two plots, a clear dependence is observed as we go from central to peripheral collisions. However, the approximate linear proportionality with $\sqrt{s_{NN}}$ holds for peripheral collisions while the effect of baryon stopping seems to break the apparent linearity. We found deceleration introduces a small quadratic dependence. Fig.(5.7) on the other hand illustrates the impact parameter depen-

dence of $|E_i|, |B_i|$'s at $(\mathbf{r}_{\mathrm{obs}}, t_{\mathrm{obs}}) = (\mathbf{0}, 0)$ for baryon stopping (dashed lines) and without stopping (solid lines). The change in the number of participants with impact parameters causes the observed difference between the two cases.
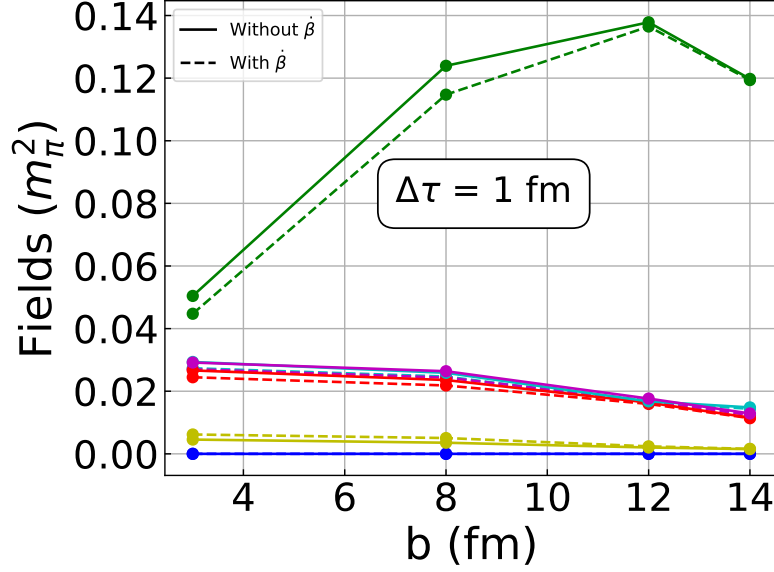
Figure 5.7: Variation of B_x (red), B_y (green), B_z (blue), E_x (cyan), E_y (magenta), E_z (yellow) with b for $\sqrt{s_{NN}} = 4$ at $(t, \mathbf{r}_{\mathrm{obs}}) = (0, \mathbf{0})$ with (dashed lines) and without deceleration (solid lines).

The parameter $\Delta\tau$ used in Eq.(5.3) controls the timescale for the deceleration of the participants. We study the effect of varying $\Delta\tau$ on the electromagnetic field in Fig.(5.8). The results for $(|B_x|, |B_y|)$ (top two panels) and $(|E_x|$ and $|E_z|)$ (bottom two panels), are shown for $\Delta\tau = 1$ fm (solid red lines) and $\Delta\tau = 3$ fm (solid blue lines). We kept $b = 3$ fm and $\sqrt{s_{NN}} = 4$ GeV constant in all these cases. We checked that $|E_y|$ is quite similar to that of $|E_x|$ and hence not shown here. These results show a clear dependence of the field strength and its time-evolution on $\Delta\tau$. For comparison, we also show no deceleration results by dashed red lines.
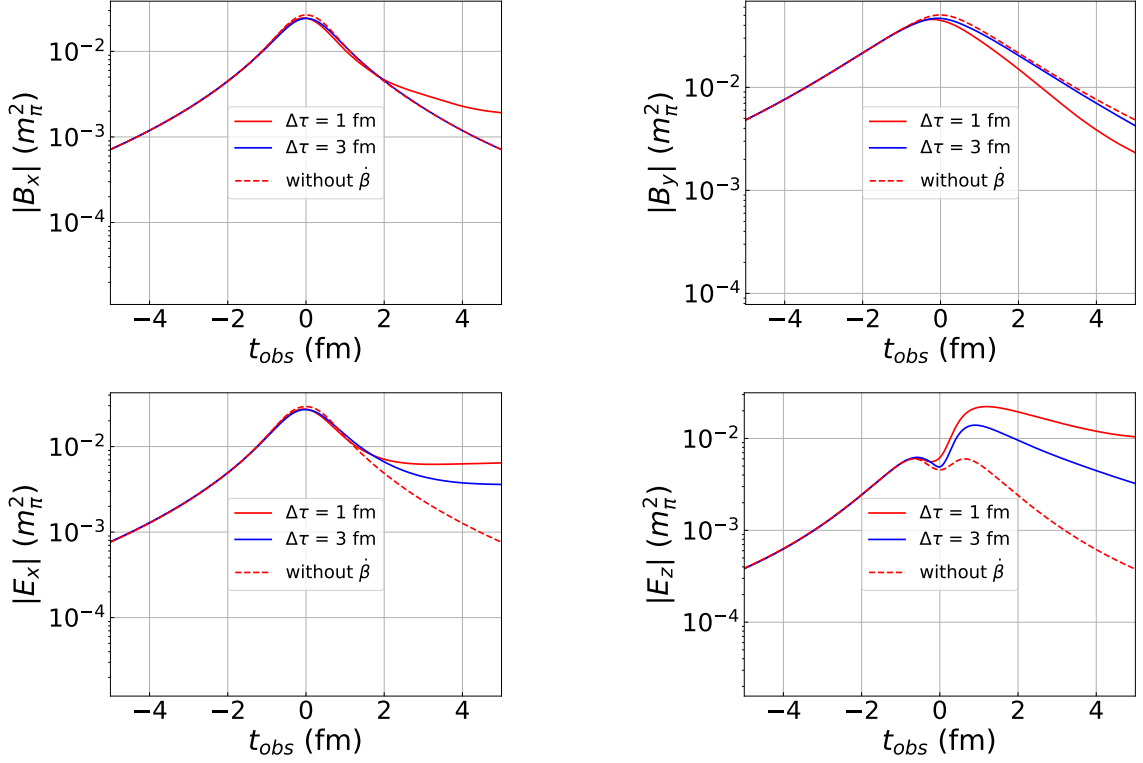
Figure 5.8: Comparison of the components of the fields for $\Delta\tau = 1$ (solid red lines), $\Delta\tau = 3$ fm (solid blue lines), and without $\dot{\beta}$ (red dashed lines) at $\sqrt{s_{NN}} = 4$ GeV and $b = 3$ fm at $\mathbf{r}_{\text{obs}} = (0, 0, 0)$.

Naively, one would expect a large $\Delta\tau$ correspond to longer deceleration time results in longer-living fields, but we do not expect any dependency of the peak magnitude of the electromagnetic fields on $\Delta\tau$ for $\tau \leq 0$. However, in Fig.(5.8), we found an apparent deviation from this expectation, particularly evident in the bottom panel. The peak magnitude of $|E_z|$ appears to be higher for $\Delta\tau = 1$ fm compared to $\Delta\tau = 3$ fm. This disparity primarily arises from the fact that in our parametrization for velocity Eq.(5.3) a larger $\Delta\tau$ corresponds to a smaller proper deceleration and vice versa and hence varying contribution in the production of EM fields. Moreover, the lumpy charge distribution along the longitudinal direction and the accumulation of these charges around the observation point $\mathbf{r}_{\text{obs}} = (0, 0, 0)$ after collision also depend on $\Delta\tau$. The influence of $\Delta\tau$ seems to be more prominent on the electric

fields, particularly on $|E_z|$ shown in right most plot in the bottom panel of Fig.(5.8).
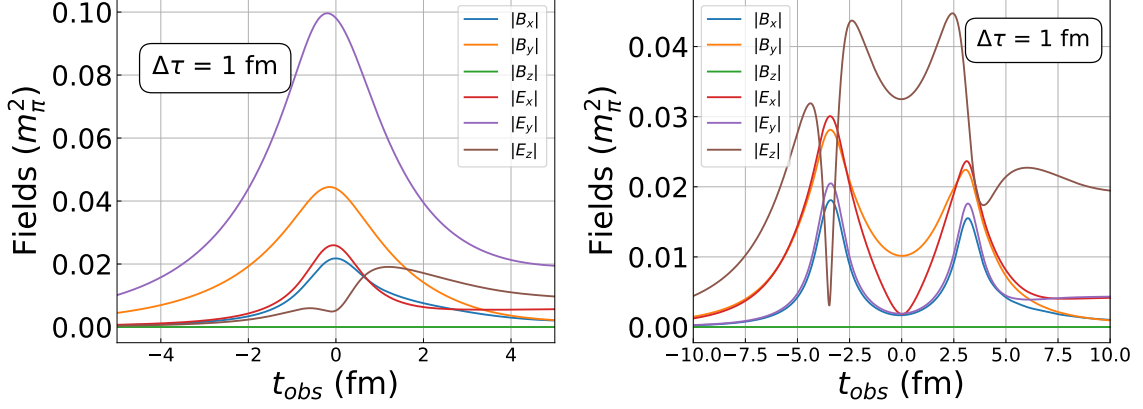
Figure 5.9: Left panel: Fields at $\mathbf{r}_{\text{obs}} = (0, 3, 0)$ for $\sqrt{s_{NN}}$ = 4 GeV and $\Delta\tau = 1$ fm. Right panel: same as left panel but for $\mathbf{r}_{\text{obs}} = (0, 0, 3)$.

Up until now, all the results shown were for $\mathbf{r}_{\text{obs}}$ = (0,0,0). In Fig.(5.9) we show the temporal variation of the fields at two different observation locations $\mathbf{r}_{\text{obs}} = (0, 3, 0)$ (left panel) and $(0, 0, 3)$ (right panel) for $\sqrt{s_{NN}}$ = 4 GeV and $\Delta\tau = 1$ fm. We found the temporal evolution of fields is almost identical for the observation point located on the y axis in the central transverse plane (left panel) as what was observed at $\mathbf{r}_{\text{obs}} = (0, 0, 0)$ (Fig.(5.4)). The only exception is $|E_y|$, which is larger due to the the coherent superposition from the target and projectile.

The passing of target and projectile nuclei through the observation point $\mathbf{r}_{\text{obs}} = (0, 0, 3)$ on the z axis is expected to give rise to double-peaked (symmetrically situated around $\tau = 0$) structure of the temporal evolution of field components which is apparent from the right panel of Fig.(5.9). $|E_z|$ seems to dominate in this case compared to other components. The asymmetry in the field values around $t_{\text{obs}} = 0$ fm in Fig.(5.9) arises due to the post-collision deceleration of nucleons.

So far, all the results shown here have been obtained by taking averages of the field components over many (thousand) events. We plotted all six field components for a randomly
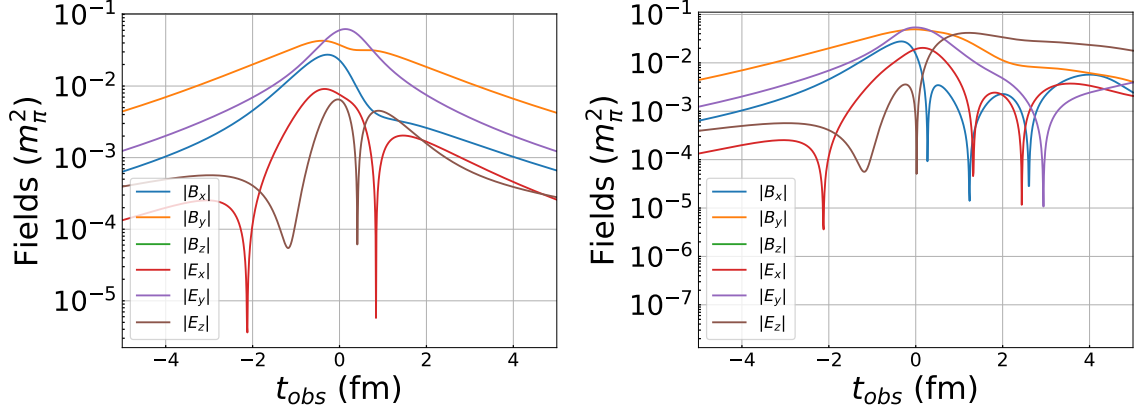
Figure 5.10: Fields in a randomly selected event. Left panel: without deceleration at $\mathbf{r}_{\text{obs}} = (0, 0, 0)$ for $\sqrt{s_{NN}}$= 4 GeV and b= 3 fm. Right panel: same as left panel but with deceleration and for the same event as above.

chosen event for $\sqrt{s_{NN}}$= 4 GeV and b= 3 fm in Fig.(5.10). The fact that field variations with time is non-trivial due to the lumpy charge distribution and similar magnitude of the components of electric and magnetic fields at $\mathbf{r}_{\text{obs}} = (0, 0, 0)$ is apparent from the figure. The left panel corresponds to no deceleration, and the right panel corresponds to deceleration case with $\Delta \tau$ = 1 fm.

5.4 Conclusion

In this chapter, we use the Monte-Carlo Glauber model with post-collision baryon stopping to investigate the vacuum space-time evolution of electromagnetic fields in low-energy heavy-ion collisions. Several observations are in order: First, upon incorporating baryon stopping via a parameterized form of the velocity of the colliding nucleons, with the key parameter being the time interval for deceleration ($\Delta \tau$), visible effects are observed for $t_{\text{obs}} \geq 0$. Secondly, as observed earlier for event-by-event calculations, due to the quantum fluctuations in the nucleon positions, all components of the electromagnetic fields become comparable in high-energy heavy-ion collisions at ($\tau = 0$); in the present study, we found temporal evolution of these electromagnetic fields retains this trend before and after the

collision. Specific field components dominate for a given collision impact parameter only when taking the event average. One of the novel findings of the present investigation is that even without any medium effects the deceleration enhances electric fields at late times compared to the case of no deceleration; the effect of deceleration is most significant for the longitudinal component of the electric fields at late times.

The presence of deceleration mostly reduces the strength of the magnetic fields post-collisions. However, contrary to the other two components, we found B_x increases at late times compared to the scenario of zero deceleration. We observed a slight shift of the peak position of EM fields from $\tau = 0$ for the baryon stopping scenario, perhaps akin to the particular form of the parameterized velocity used in this study. For higher $\sqrt{s_{NN}}$, when the nucleons move with almost constant velocity after each binary collision, a linear proportionality of the peak value of magnetic fields (at $\tau = 0$) with $\sqrt{s_{NN}}$ is observed. However, in the presence of deceleration, this approximate linearity seems to be broken slightly at lower energies. Owing to the lower velocities of the colliding nucleons for smaller $\sqrt{s_{NN}}$ the crossing time for the two nuclei becomes longer and additionally, the fluctuating nucleon positions along the longitudinal direction give rise to a non-trivial variation of the EM field when measured on an event-by-event basis.

Lastly, in the concluding chapter of the present thesis (chapter.(6)), we will be investigating the impact of electric fields on bulk observables such as spectra and flow harmonics.

References

[1] V. Skokov, A. Y. Illarionov and V. Toneev, "Estimate of the magnetic field strength in heavy-ion collisions," Int. J. Mod. Phys. A **24**, 5925-5932 (2009) doi:10.1142/S0217751X09047570 [arXiv:0907.1396 [nucl-th]].

[2] U. Gursoy, D. Kharzeev and K. Rajagopal, "Magnetohydrodynamics, charged currents and directed flow in heavy ion collisions," Phys. Rev. C **89**, no.5, 054905 (2014) doi:10.1103/PhysRevC.89.054905 [arXiv:1401.3805 [hep-ph]].

[3] V. Voronyuk, V. D. Toneev, W. Cassing, E. L. Bratkovskaya, V. P. Konchakovski and S. A. Voloshin, "(Electro-)Magnetic field evolution in relativistic heavy-ion collisions," Phys. Rev. C **83**, 054911 (2011) doi:10.1103/PhysRevC.83.054911 [arXiv:1103.4239 [nucl-th]].

[4] W. T. Deng and X. G. Huang, "Event-by-event generation of electromagnetic fields in heavy-ion collisions," Phys. Rev. C **85**, 044907 (2012) doi:10.1103/PhysRevC.85.044907 [arXiv:1201.5108 [nucl-th]].

[5] D. E. Kharzeev, L. D. McLerran and H. J. Warringa, "The Effects of topological charge change in heavy ion collisions: 'Event by event P and CP violation'," Nucl. Phys. A **803**, 227-253 (2008) doi:10.1016/j.nuclphysa.2008.02.298 [arXiv:0711.0950 [hep-ph]].

[6] V. Roy and S. Pu, "Event-by-event distribution of magnetic field energy over initial fluid energy density in $\sqrt{s_{\mathrm{NN}}}$= 200 GeV Au-Au collisions," Phys. Rev. C **92**, 064902 (2015) doi:10.1103/PhysRevC.92.064902 [arXiv:1508.03761 [nucl-th]].

[7] S. N. Alam, V. Roy, S. Ahmad and S. Chattopadhyay, "Electromagnetic field fluctuation and its correlation with the participant plane in Au+Au and iso-

baric collisions at sNN=200 GeV," Phys. Rev. D **104**, no.11, 114031 (2021) doi:10.1103/PhysRevD.104.114031 [arXiv:2107.01552 [hep-ph]].

[8] X. L. Zhao, G. L. Ma and Y. G. Ma, "Impact of magnetic-field fluctuations on measurements of the chiral magnetic effect in collisions of isobaric nuclei," Phys. Rev. C **99**, no.3, 034903 (2019) doi:10.1103/PhysRevC.99.034903 [arXiv:1901.04151 [hep-ph]].

[9] M. L. Miller, K. Reygers, S. J. Sanders and P. Steinberg, "Glauber modeling in high energy nuclear collisions," Ann. Rev. Nucl. Part. Sci. **57**, 205-243 (2007) doi:10.1146/annurev.nucl.57.090506.123020 [arXiv:nucl-ex/0701025 [nucl-ex]].

[10] H. Appelshauser *et al.* [NA49], "Baryon stopping and charged particle distributions in central Pb + Pb collisions at 158-GeV per nucleon," Phys. Rev. Lett. **82**, 2471-2475 (1999) doi:10.1103/PhysRevLett.82.2471 [arXiv:nucl-ex/9810014 [nucl-ex]].

[11] I. G. Bearden *et al.* [BRAHMS], "Nuclear stopping in Au + Au collisions at s(NN)**(1/2) = 200-GeV," Phys. Rev. Lett. **93**, 102301 (2004) doi:10.1103/PhysRevLett.93.102301 [arXiv:nucl-ex/0312023 [nucl-ex]].

[12] I. C. Arsene *et al.* [BRAHMS], "Nuclear stopping and rapidity loss in Au+Au collisions at s(NN)**(1/2) = 62.4-GeV," Phys. Lett. B **677**, 267-271 (2009) doi:10.1016/j.physletb.2009.05.049 [arXiv:0901.0872 [nucl-ex]].

[13] L. Adamczyk *et al.* [STAR], "Bulk Properties of the Medium Produced in Relativistic Heavy-Ion Collisions from the Beam Energy Scan Program," Phys. Rev. C **96**, no.4, 044904 (2017) doi:10.1103/PhysRevC.96.044904 [arXiv:1701.07065 [nucl-ex]].

[14] W. Busza, K. Rajagopal and W. van der Schee, "Heavy Ion Collisions: The Big Picture, and the Big Questions," Ann. Rev. Nucl. Part. Sci. **68**, 339-376 (2018) doi:10.1146/annurev-nucl-101917-020852 [arXiv:1802.04801 [hep-ph]].

[15] J. Cleymans and H. Satz, "Thermal hadron production in high-energy heavy ion collisions," Z. Phys. C **57**, 135-148 (1993) doi:10.1007/BF01555746 [arXiv:hep-ph/9207204 [hep-ph]].

[16] J. Randrup and J. Cleymans, "Exploring high-density baryonic matter: Maximum freeze-out density," Eur. Phys. J. **52**, 218-219 (2016) doi:10.1140/epja/i2016-16218-7 [arXiv:0905.2824 [nucl-th]].

[17] J. Mohs *et al.* [SMASH], "Particle Production via Strings and Baryon Stopping within a Hadronic Transport Approach," J. Phys. G **47**, no.6, 065101 (2020) doi:10.1088/1361-6471/ab7bd1 [arXiv:1909.05586 [nucl-th]].

[18] M. Li and J. I. Kapusta, "Large Baryon Densities Achievable in High Energy Heavy Ion Collisions Outside the Central Rapidity Region," Phys. Rev. C **99**, no.1, 014906 (2019) doi:10.1103/PhysRevC.99.014906 [arXiv:1808.05751 [nucl-th]].

[19] L. D. McLerran, S. Schlichting and S. Sen, "Spacetime picture of baryon stopping in the color-glass condensate," Phys. Rev. D **99**, no.7, 074009 (2019) doi:10.1103/PhysRevD.99.074009 [arXiv:1811.04089 [hep-ph]].

[20] David Tong, "David Tong: Lectures on Electromagnetism," `https://www.damtp.cam.ac.uk/user/tong/em/el5.pdf`.

[21] W. T. Deng and X. G. Huang, "Electric fields and chiral magnetic effect in Cu+Au collisions," Phys. Lett. B **742**, 296-302 (2015) doi: 10.1016/j.physletb.2015.01.050 [arXiv:1411.2733 [nucl-th]].

[22] C. Y. Wong, "BARYON DISTRIBUTION IN RELATIVISTIC HEAVY ION COLLISIONS," Phys. Rev. Lett. **52**, 1393-1396 (1984) doi: 10.1103/PhysRevLett.52.1393.

[23] C. Y. Wong and Z. D. Lu, "Multiple Collision Model for High-energy Nucleus-nucleus Collisions," Phys. Rev. D **39**, 2606-2616 (1989) doi: 10.1103/PhysRevD.39.2606.

Chapter 6

Effect of electric fields on bulk observables

It is well known that medium properties are inferred from the experimental results via indirect probes, as discussed in chapter.(1). Out of which transverse momentum (p_T) spectra and flow harmonics (specifically elliptic flow v_2) are the most prominent ones. In the current chapter, our focus remains on these two key observables. It is known that blast-wave model incorporating one-particle distribution in Cooper-Frye prescription has proven to be successful in describing the experimental findings [1, 2, 3, 4, 5, 6, 7]. Also on the other hand, the influence of electric fields on bulk observables like p_T spectra and flow coefficients of charged hadrons have received limited attention, with only a few studies available [8, 9]. Moreover, developing a Relativistic dissipative resistive magnetohydrodynamics (RDRMHD) numerical code presents a substantial challenge [10, 11], yet holds immense potential for comprehensively studying all electromagnetic effects.

Hence, our approach here will be simple yet effective. Therefore, by using the blast-wave model, we here intend to explore the effect of electric fields on spectra and flow harmonics for charged pions and protons. We incorporate the first-order correction to the single-particle distribution function due to the electric fields and the dissipative effects while calculating the invariant yields of hadrons in the Cooper-Frye prescription at the freezeout hypersurface. Further, the splitting of particles and antiparticles' elliptic flow due to electric fields is also discussed.

The current chapter is structured as follows: First, the blast-wave model is explored in Section.(6.1). This is followed by a discussion on the Cooper-Frye prescription and

164

associated formulas, along with the setup, detailed in Sections.(6.2) and (6.3), respectively. Section.(5.3) is dedicated to discussing results, while Section.(6.5) presents the summary and conclusion of our study.

6.1   Blast-wave model

The blast-wave model represents a theoretical framework that considers the collective motion of the matter produced in heavy-ion collisions and parameterizes its four-velocity. It further assumes that hadrons are produced from a constant-temperature freeze-out hypersurface, with the freeze-out temperature being a free parameter. The invariant yields of hadrons are obtained from the Cooper-Frye formalism, which is described later. Despite its simplicity, the blast-wave model can successfully describe experimental data of identified hadrons, transverse-momentum spectra, and elliptic flow [1, 2, 3, 4, 5, 6]. In heavy-ion collisions, one popular parametrization of the fluid's four-velocity is inspired by the Bjorken model of boost-invariant expansion in the longitudinal direction of the fluid. In this work, we use the Milne coordinate (τ, η, r, ϕ), where τ is the proper time, η is the space-time rapidity, r is the radial distance from the center of the fireball, and lastly, ϕ is the azimuthal angle. The metric used here is $g_{\mu\nu} = \text{diag}\,(1, -\tau^2, -1, -r^2)$, and the transformation between the Cartesian and Milne coordinates is given as:

$$\begin{bmatrix} t \\ x \\ y \\ z \end{bmatrix} = \begin{bmatrix} cosh\eta & 0 & 0 & 0 \\ 0 & 0 & cos\phi & 0 \\ 0 & 0 & sin\phi & 0 \\ sinh\eta & 0 & 0 & 0 \end{bmatrix} \begin{bmatrix} \tau \\ \eta \\ r \\ \phi \end{bmatrix}.$$

Where

$$\tau = \sqrt{t^2 - z^2},$$

$$\eta = \tanh^{-1} z/t,$$

$$r = \sqrt{x^2 + y^2},$$

$$\phi = arctan2(y, x).$$

The parameterized form of the velocity four vector with longitudinal boost-invariance is given as

$$u^r = u_0 \frac{r}{R} \left[1 + 2 \sum_{n=1}^{\infty} c_n \cos n \left[\phi - \psi_n \right] \right] \Theta \left(R - r \right),$$

$$u^\phi = u^\eta = 0,$$

$$u^\tau = \sqrt{1 + (u^r)^2}. \tag{6.1}$$

Where $u^\tau, u^r, u^\phi, u^\eta$ are the components of the fluid's four velocity; u_0 and c_n's are free parameters used to reproduce the p_T spectra (invariant yield) and the flow harmonics of charged hadrons. $\Theta \left(R - r \right)$ is the Heaviside function, which imposes the condition that if $r > R$, $u^r = 0$. R is the radius of the freezeout hypersurface, ϕ is the azimuthal angle in coordinate space, and ψ_n is the *n-th* order participant plane angle. As we do not consider event-by-event fluctuations in this work, we set $\psi_n = 0$, i.e., the minor axis of the participant planes coincides with the direction of the impact parameter. We parametrized the temperature to

$$T \left(\tau, \eta, r, \phi \right) = T_0 \Theta \left(R - r \right),$$

where T_0 denotes the temperature at the freezeout hypersurface.

6.2 Cooper-frye formalism

As mentioned earlier, the invariant yield of hadrons is obtained from the Cooper-Frye formula [12], which assumes that the freeze-out hypersurface is a timelike vector $d\Sigma_\mu$ given by $(\tau d\eta dr r d\phi, 0, 0, 0)$. The invariant yield is given by the following equation:

$$\frac{dN}{d^2 p_T dy} = \frac{\mathcal{G}}{(2\pi)^3} \int p^\mu d\Sigma_\mu f(x, p). \tag{6.2}$$

Here, $f(x, p)$ is the single-particle distribution function, and x and p are the position and momentum four-vectors of the particles, respectively. $\mathcal{G}$ is the degeneracy factor.

Suppose the system is not in local thermal equilibrium. In that case, as is the case for a rapidly expanding fireball, the single-particle distribution function must consider the deviation from equilibrium when calculating hadron yields using the Cooper-Frye prescription. The distribution function is usually decomposed into an equilibrium part f_0 and a small non-equilibrium part δf, so the total distribution function becomes $f = f_0 + \delta f$. The second-order correction to f gives rise to new transport coefficients due to the external magnetic field. The temperature and mass dependence of the transport coefficients' were also discussed in chapter (3).

However, this work considers terms up to first-order in gradients, as is presented in chapter.(3). In this case, the invariant yield (Eq. (6.2)) becomes

$$\frac{dN}{d^2 p_T dy} = \frac{\mathcal{G}}{(2\pi)^3} \int p^\mu d\Sigma_\mu \left(f_0 + \delta f^1 \right). \tag{6.3}$$

Where $\delta f^1 \ll f_0$. In chapter.(3), δf^1 is calculated using the Boltzmann equation using the Relaxation Time Approximation (RTA). We give the expression for δf^1 in Appendix.(B.2) for the sake of completeness.

6.3 Setup

For the current study, we consider only $n = 2$ in the expression for u^r (Eq.(6.1)), resulting in

$$u^r = u_0 \frac{r}{R}[1 + 2c_2 \cos(2\phi)]\Theta\left(R - r\right).$$

The equilibrium distribution is $f_0 = \left(e^{\beta u \cdot p - \alpha} + l\right)^{-1}$, where β is the inverse temperature, $l = \pm 1$ corresponds to fermions and bosons, respectively. We use the parameters given in Table (6.1) to obtain the invariant yield of π^+ that matches the ALICE measurement shown as red circles in the top panel of Fig.(6.1)[13]. Earlier hydrodynamic model studies [14] have shown that it is not possible to simultaneously describe π^+ and p spectra for zero baryon chemical potential, so we use a different set of values for u_0, c_2, and T (given in the rightmost column of Table (6.1)) to explain the proton spectra. The blast-wave model with these parameters reasonably well explains the experimental data [2, 3, 4, 5, 6]. The bottom panel of Fig. (6.1) shows the blast-wave results for v_2 of π^+ and p. It is clear from the bottom panel of Fig. (6.1) that the ideal blast-wave model over-predicts the experimental data (shown by circles), as was also observed for ideal hydrodynamics results [15, 16]. It is known that the inclusion of shear viscosity improves the agreement between theoretical and experimental results.

After setting up the parameters for the ideal case (zero viscosity), we can now explore the effect of viscosity (through the relaxation time τ_c) and electric fields on spectra and flow harmonics by comparing the corresponding results with the ideal results. In our model, τ_c and the electric field qE appear in δf^1, giving rise to additional corrections to the invariant yields and flow harmonics of charged hadrons. We compute the p_T differential n-th order flow coefficient using the usual formula:

$$v_n(p_T, y) \quad = \quad \frac{\int_{-\pi}^{\pi} d\varphi \cos(n\varphi) \frac{dN}{d^2 p_T dy}}{\int_{-\pi}^{\pi} d\varphi \frac{dN}{d^2 p_T dy}}. \qquad (6.4)$$
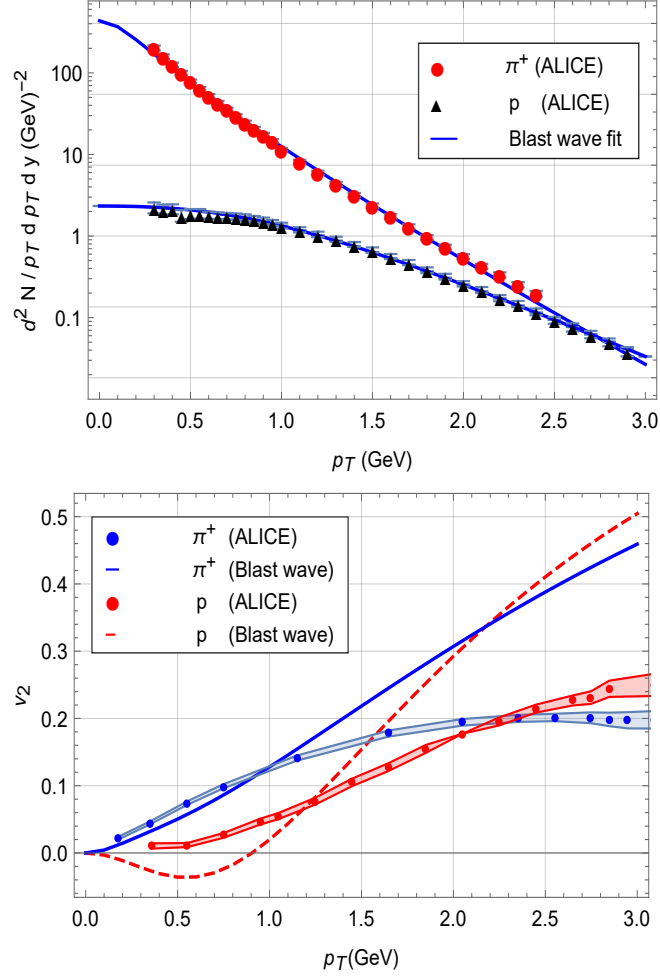
Figure 6.1: Top plot is the comparison of the experimentally measured π^+ (red filled circles) and protons (black triangles) for Pb+ Pb collision at $\sqrt{s} = 2.76$ TeV for 20-30 % centrality with the ideal blast-wave results (lines) for the parameters in Table 6.1. The lower panel shows the corresponding v_2 vs p_T for π^+ (blue line) and protons (red dashed line) from Blastwave with the Data points (ALICE [13]) are plotted with Blue (for π^+) and Red (for proton) with the bands showing the experimental errors.

 As we need the electric field distribution on the freezeout hypersurface to be used in the

Cooper-Frye formula (Eq.(6.2)), we use a parameterized form of the EM field. In principle,

the fields generated in the initial stages of heavy-ion collisions due to the charged protons

inside the two colliding nuclei would evolve with the QGP fluid, but the blast-wave model

does not allow any such self-consistent dynamical evolution of fields. Here we use param-

	π^+	p
u_0	1.2	1.22
T	130 MeV	140 MeV
R	10 fm	10 fm
τ	6 fm	6 fm
m	139.5 MeV	938 MeV
c_2	0.1	0.15

Table 6.1: The fit parameters for π^+ and p respectively at mid-rapidity.

eterized electric fields of four different configurations in the transverse plane (XY plane) while calculating the invariant yields.
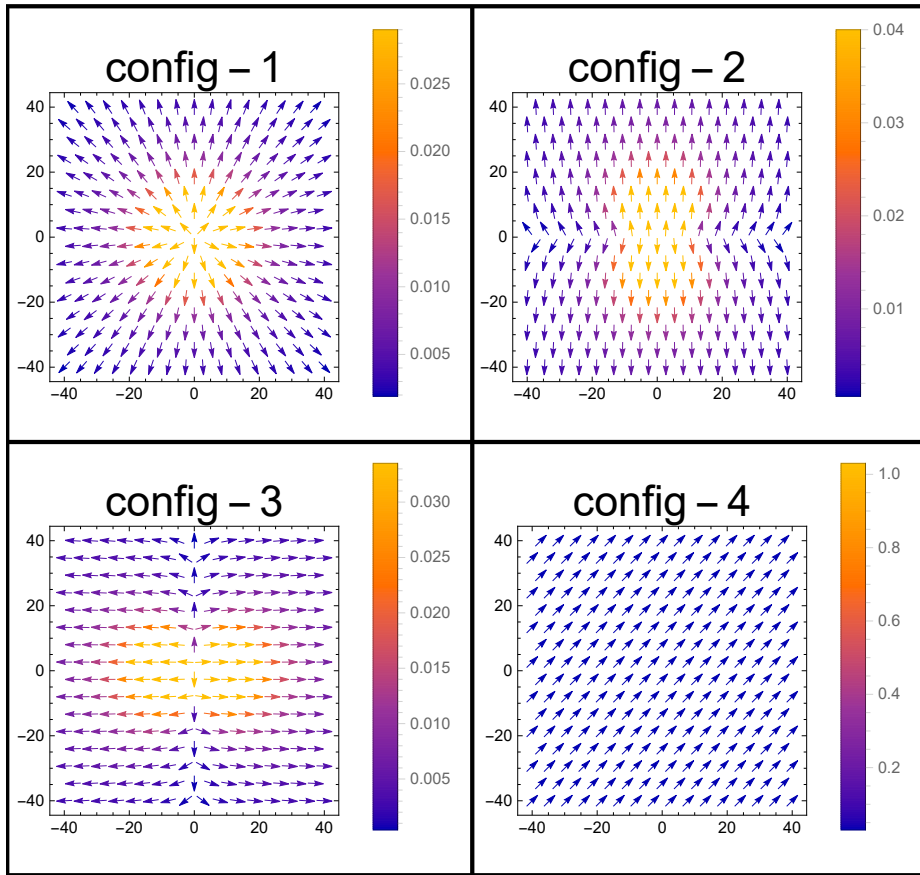
Figure 6.2: Electric field configurations in the transverse plane. Detailed expressions for different configurations are given in Appendix-(B.3). Magnitude of electric fields (in GeV^2) are shown using colour map.

Some of these configurations do not represent the actual scenario encountered in heavy-ion collisions, but we use them for exploratory purposes. Here we discuss the different configurations used in the calculations, as shown in Fig.(6.2).

- **config-1**: The top left panel of Fig.(6.2) represents isotropic ($E_y = E_x$) Coulomb fields due to a point charge of large magnitude at the origin. The elliptic flow harmonic is expected to be mostly unaltered due to the symmetry of the field in the transverse plane.

- **config-2**: The top right panel of Fig.(6.2) closely resembles the field configuration expected in a symmetric heavy-ion collision which gives rise to an approximately prolate-like field ($E_y > E_x$) configuration. Due to the larger force from the electric field along the out-of-plane direction, we expect a decrease in the elliptic flow for this case.

- **config-3**: The bottom left panel of Fig.(6.2) represents the rotated version of **config-2** by an angle $\pi/2$ in the plane, which represents approximately an oblate-like field ($E_x > E_y$) configuration. Following the same logic as **config-2**, we expect an increase in the elliptic flow in this case.

- **config-4**: The bottom right panel of Fig.(6.2) represents a constant unidirectional electric field (making an angle 45^0 with the x axis); this configuration mimics upto some extent an asymmetric nuclear collision such d+Au or p+Pb collisions. This configuration is sometimes denoted as directional fields in the text, and we expect it to alter the directed flow for the apparent reason.

6.4 Results

Here we discuss our main results for different configurations of electric fields (described in the previous section) on the spectra and v_2 for pions and protons.
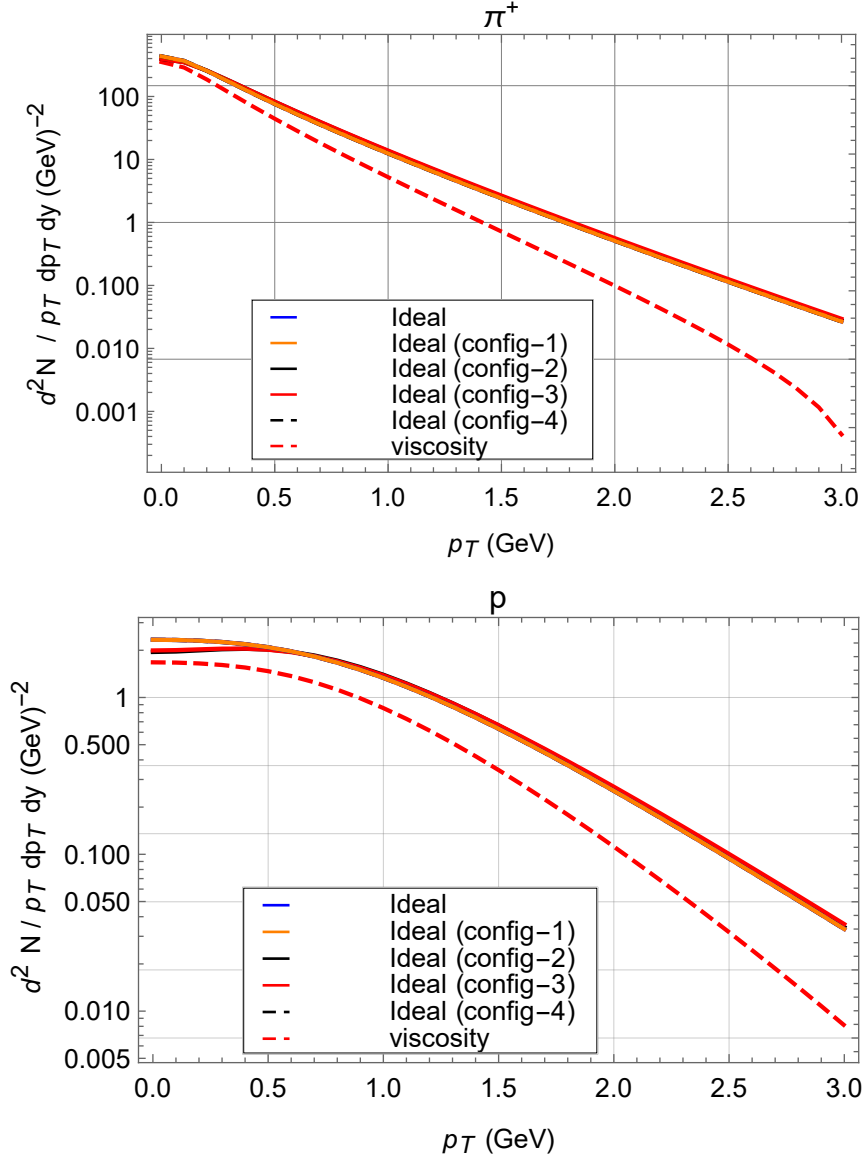
Figure 6.3: Upper panel represents the p_T spectra for π^+ and lower panel for protons with different transverse field configurations as in Fig.(6.2) and for the case of viscosity for $t_c = 1$ fm.

The top panel of Fig.(6.3) shows the dependence of the p_T spectra of π^+ on the electric

fields for the ideal case, for comparison we also show the results for non-zero viscosity but with no electric fields. The magnitude of viscosity in our model is controlled through t_c, which is set to 1 fm for the results shown here. Here we see that the p_T spectra hardly show any dependence on different transverse electric field configurations (solid orange, black, and red lines correspond to **config-1**, **config-2**, and **config-3** respectively). As expected, the effect of finite viscosity is comparatively more prominent on the p_T spectra; we see a suppression at higher p_T regions for the viscous case. Since both bulk and shear viscosity are present, In our case, the slope of the spectra is determined by the relative contributions of these two viscosities [17, 18]. The bottom panel of Fig.(6.3) shows the p_T spectra for protons for ideal (with electric fields) and viscous (without electric field) cases, where we see a small suppression in the lower p_T region for the case of **config-2** and **config-3** for the ideal case. We also see a suppression at higher p_T for the viscous case, as was seen for π^+. At this point, we would like to clarify a few points regarding the relative contributions of various corrections to the p_T spectra of identified hadrons. We note that both viscosity and electric fields may alter fluid velocity and the single-particle distribution function, which is used in converting the fluid elements into particles (hadrons) on the freeze-out hypersurface. Since in the blast-wave model we fix the flow profile by choosing appropriate parameterization, the corrections due to electric field and viscosity only appear in the freeze-out distribution function δf. From the expression of δf (as given in Appendix-(B.2)), we see that the correction due to the electric field is $\propto p_T$ while the viscous correction is $\propto p_T^2$. Hence, at low p_T, the correction due to the electric field dominates, whereas the viscous corrections are large for high p_T. For mid p_T the two effects compete, and the result depends on the exact values of the coefficient appearing in the corresponding corrections.

Before discussing the differential v_2 for different cases, it is worthwhile to explore the dependence of p_T integrated (0-3 GeV) $dN/d\phi$ on different field configurations and viscosities. In the top panel of Fig.(6.4), we show the $dN/d\phi$ of π^+ as a function of ϕ for
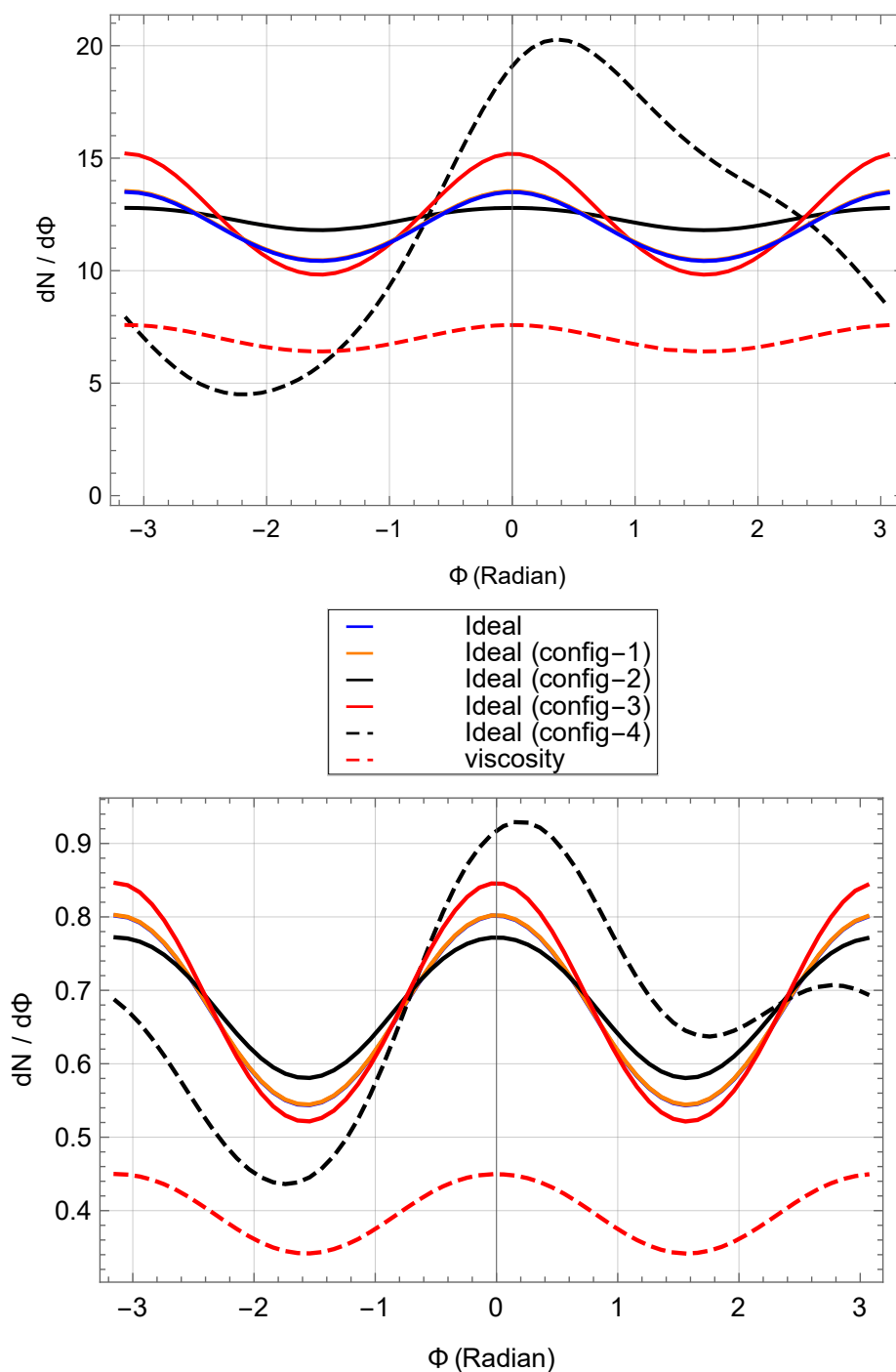
Figure 6.4: Top panel: $dN/d\phi$ as a function of ϕ for π^+ for various field configurations. Bottom panel: Same as the top panel but for protons.

various cases. As expected, we have a pure cosine-like dependence of $dN/d\phi$ for the ideal case (shown by the solid blue line); the viscosity reduces the multiplicity as well as the amplitude (shown by the red dashed line). **config-1** the isotropic field configuration (solid orange line) almost coincides with the ideal result, but we see a noticeable change in the amplitude of $dN/d\phi$ for **config-2**, **config-3** as expected. Things become more interesting for **config-4** (black dashed line); here, we generate finite directed flow-like behavior; this is understood from the fact that a unidirectional force shifts the center of mass of the distribution. Similar behavior was observed for protons also shown in the bottom panel of Fig.(6.4).

A more concrete way to study the angular dependence of $dN/d\phi$ for **config-4** can be achieved by using a finite Fourier series decomposition of $dN/d\phi$ as shown in Eq.(6.5).

$$f(\Phi) = N \left[1 + 2 \sum_{n=1}^{3} v_n cos(n\Phi) + 2 \sum_{n=1}^{3} w_n sin(n\Phi) \right]. \tag{6.5}$$

Using a non-linear least squares fit with v_n, w_n, and N as free parameters, we obtain the best fit for $dN/d\phi$ with the values of these parameters given in Table (6.2). Here we note that the directional force v_1 is larger than v_2 for π^+, and they are similar in magnitude for protons. Moreover, we notice that, unlike other cases, the azimuthal distribution breaks reflection symmetry with respect to the Y axis, which gives rise to the non-zero w_n shown in Table (6.2). We also observe a mass dependence of the directional flow as π^+ has a larger v_1 compared to the protons.

To have a visual understanding of the goodness of fit, we show a comparison of the fitted values (using Eq.(6.5)) (solid blue line) and the $dN/d\phi$ from the blast-wave model (dotted-dash orange line) for π^+ (top panel) and proton (bottom panel) in Fig.(6.5).

More familiar and useful observables in experiments are centrality and p_T dependent flow harmonics. In Fig. (6.6), we show the dependence of the second-order flow harmonics v_2 (a.k.a. elliptic flow) for different configurations. Here we see that there is almost no

	π^+	p
N	$11.907 \pm 2.7e\text{-}05$	$0.672 \pm 7.1e\text{-}08$
v_1	$0.218 \pm 1.0e\text{-}07$	$0.081 \pm 7.9e\text{-}08$
v_2	$0.064 \pm 9.8e\text{-}08$	$0.096 \pm 7.9e\text{-}08$
v_3	$0.017 \pm 9.7e\text{-}08$	$0.005 \pm 7.8e\text{-}08$
w_1	$0.213 \pm 1.0e\text{-}07$	$0.081 \pm 7.9e\text{-}08$
w_2	$0.000 \pm 9.8e\text{-}08$	$0.000 \pm 7.8e\text{-}08$
w_3	$0.017 \pm 9.8e\text{-}08$	$0.005 \pm 7.8e\text{-}08$

Table 6.2: Fit parameters for π^+ and proton for **config-4** from Eq.(6.5).

deviation from the ideal case for the isotropic (**config-1**) and directed field cases (**config-4**). However, the situation is different for the other two cases; we can clearly see an increase in v_2 for **config-3** and a suppression for **config-2**. We also note that viscosity suppresses the elliptic (red dashed line) flow for π^+ and elavates that for proton.

The effect of electric fields becomes more interesting when we examine the difference in v_2 for particles (π^+, p) and antiparticles ($\pi^-, \bar{\text{p}}$). This difference $\Delta v_2 = v_2(\text{h}) - v_2(\bar{\text{h}})$ is shown in Fig.(6.8) as a function of p_T. We observe a non-monotonic variation in Δv_2 as a function of p_T for both pions and protons. Interestingly, a similar observation was made in [19].

If we refer to Fig.(6.3) and (6.6), we see that the effect of electric field and viscosity show different behavior for p_T spectra and v_2. For the p_T spectra, the effect of viscosity is visible for both π^+ and p, but it appears as though the electric field barely modifies the spectra relative to the ideal case. On the other hand, the effect of viscosity on v_2 is marginal for p, while for π^+, it shows a significant deviation from the ideal case at high p_T. In contrast, electric field effects on v_2 are substantial for both π^+ and p. We can understand these nontrivial features if we refer to the expressions for the correction to the freeze-out distribution function as given in Appendix-(B.2). When we consider both the corrections (field and viscous), as mentioned above, they show different dependencies at different p_Ts. If we calculate the percentage correction by the electric field, it is about 7-8 % for pions,
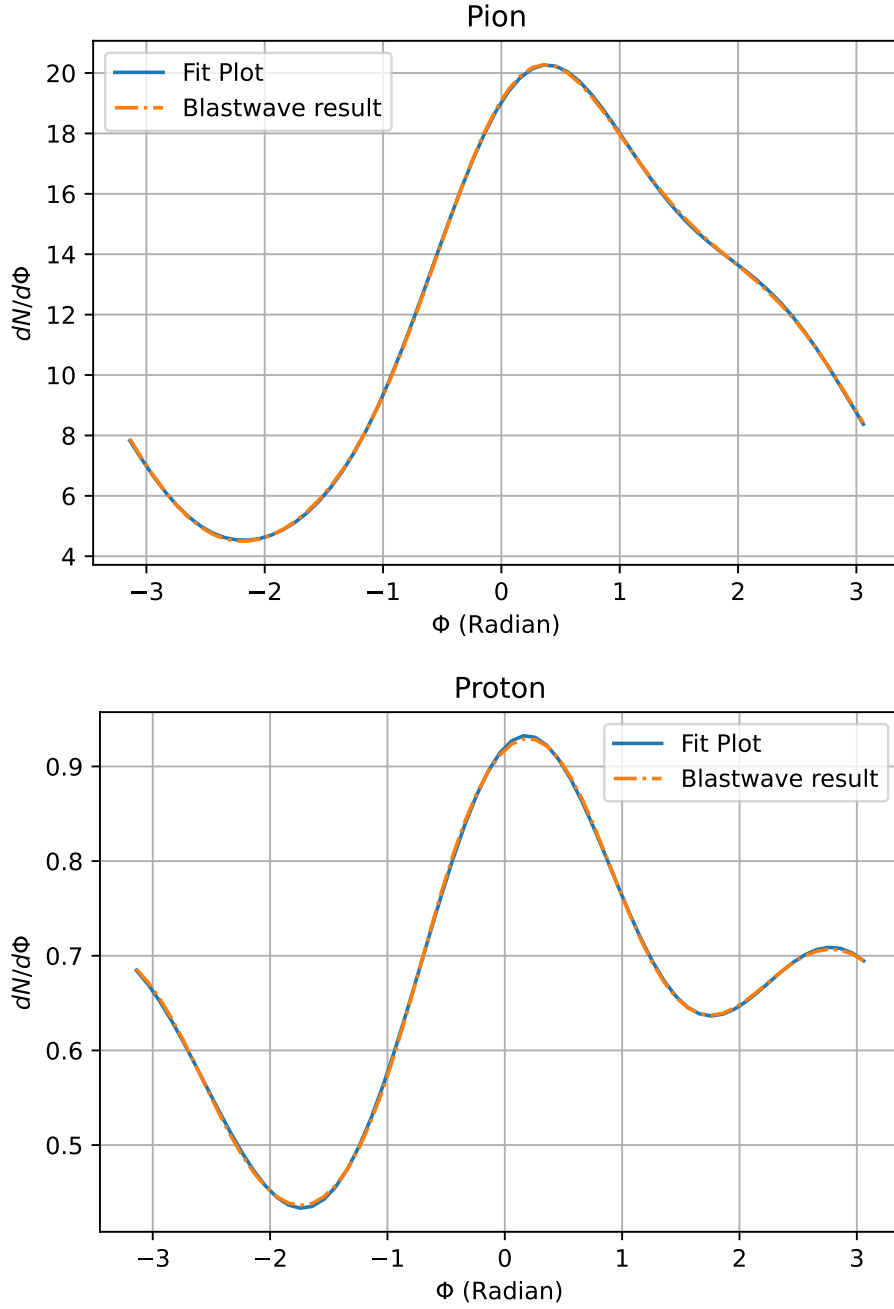
Figure 6.5: Blast-wave results and the fitted curves using Eq.(6.5) for **config-4** for π^+ (top panel) and proton (bottom panel).

but at lower p_T, whereas the viscous correction dominates at high p_T. In spectra, the log scaling on the y-axis gives us the impression that the field is not affecting the spectra at
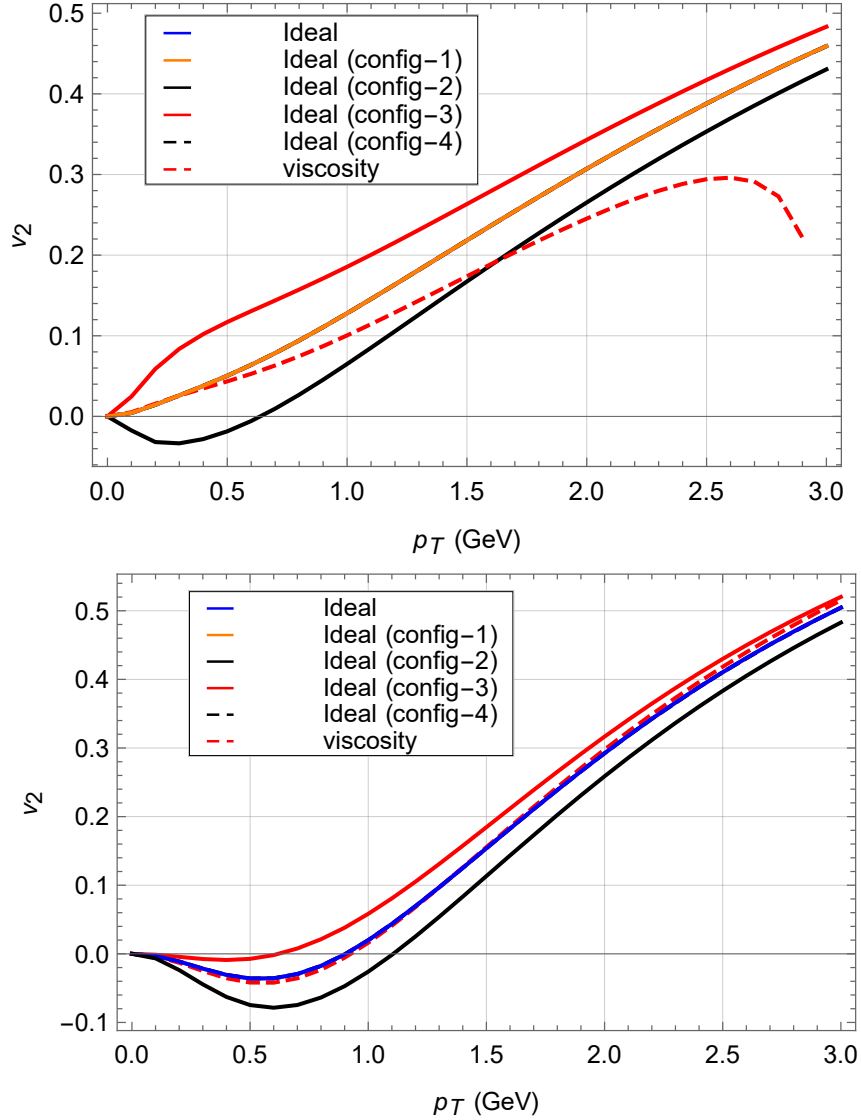
Figure 6.6: v_2 vs p_T for π^+ (top panel) and proton (bottom panel) for the transverse electric field configurations shown in Fig.(6.2).

all. This can again be verified from Fig.(6.4), which shows the p_T integrated azimuthal variation of multiplicity, where we can clearly see a sizeable correction due to the fields. Note that the p_T spectra do not contain information about the azimuthal dependency of the distribution, whereas v_2 ($\langle\cos(2\varphi)\rangle$) measures azimuthal variation in the flow. Hence, the effect in spectra might not be as prominent as in flow. Also, the δf contains contributions
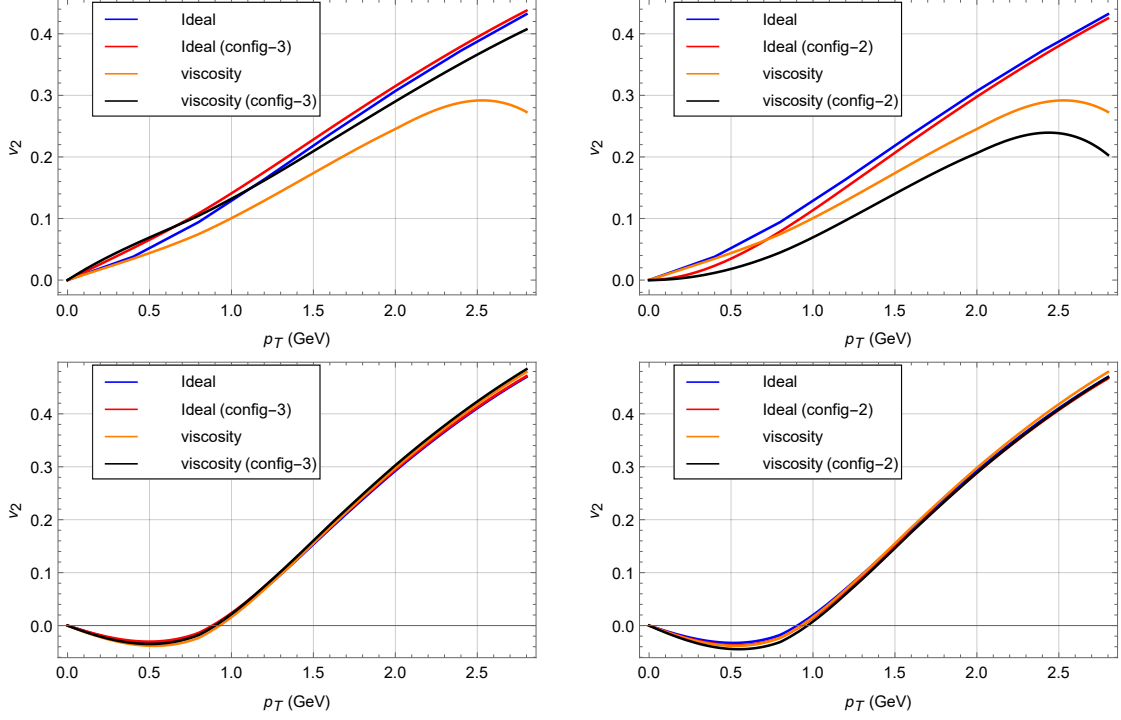
Figure 6.7: v_2 vs p_T for π^+ (top panel) and proton (bottom panel) for the viscosity and transverse electric field configurations shown in Fig.(6.2) taken individually and also simultaneously.

from both shear and bulk viscosity together, and they are known to suppress and enhance v_2 at large p_T, respectively. The viscous correction also depends on the mass; hence, the cancellation of bulk and shear corrections is more prominent for proton than for pion.

If we now consider the effects of viscosity and electric field simultaneously, as shown in Fig.(6.7), we see that there is competition between the corrections due to viscosity and electric field. In Fig.(6.7) **config-3**, independently, electric field enhances v_2 and viscosity suppresses v_2. The combined effect puts a v_2 value in between the independent contributions. Whereas in **config-2**, both electric field and viscosity suppress v_2, and their combined effect suppresses v_2 further. We also observe that the relative corrections for the proton are smaller than those for the pion. This is because the value of these corrections is a function of $m_T = \sqrt{m^2 + p_T^2}$, which can be readily seen from the δf in Appendix.(B.2).

Throughout this study, we only consider the effect of electric fields and the first-order correction in the δf. As mentioned earlier, it has been shown that there are new transport coefficients at higher order corrections to f, which may alter the results obtained here and can be further studied.
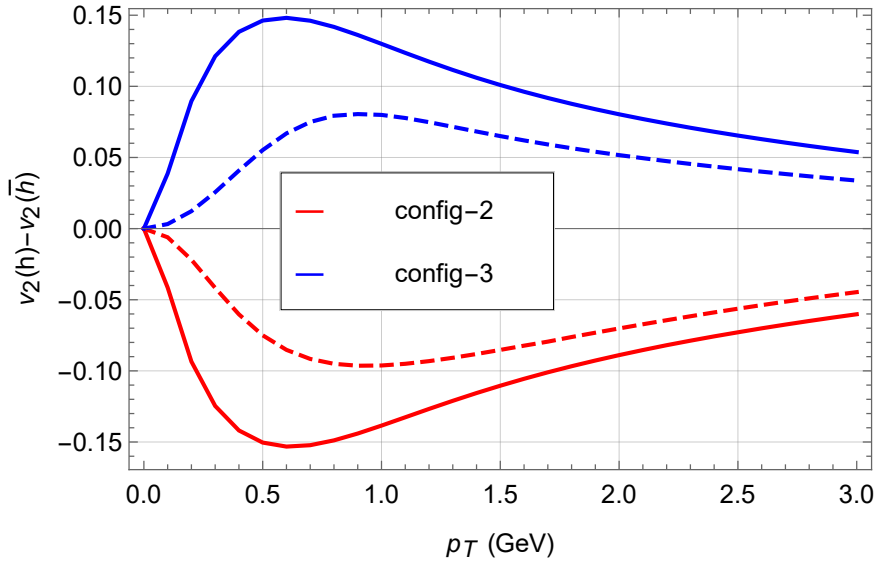
Figure 6.8: $v_2(\mathrm{h}) - v_2(\bar{\mathrm{h}})$ as a function of p_T for **config-2** (red) and **config-3** (blue). Solid and dashed lines correspond to π and p respectively.

6.5 Conclusion

Here in this chapter, we have studied the effect of electric fields on the bulk observables in heavy-ion collisions, such as p_T spectra and the directed and elliptic flow of charged pions and protons. We use the blast-wave model and different configurations of electric fields on the transverse plane to carry out this exploratory study. The p_T spectra of hadrons in the blast-wave model are obtained using the Cooper-Frye prescription, where we incorporate non-equilibrium correction δf due to the viscosity and the electric fields. Since the blast-wave model does not include space-time evolution, the fluid velocity, and the electric fields are parameterized on the freezeout hypersurface to calculate experimental observables. In

our case, fluid velocity fields are modulated to dominantly generate the elliptic flow. We use four different configurations of transverse electric fields: isotropic fields ($E_x = E_y$), prolate-like fields ($E_y > E_x$), oblate-like fields ($E_x > E_y$), and directed fields ($E_x = E_y =$ constant). The typical maximum electric field value for all these configurations is $\sim m_\pi^2$. Flow harmonics for isotropic fields remain unchanged for both pions and protons. Both prolate and oblate-like field configurations alter the flow harmonics, and the directed field gives rise to large directed flow v_1 for both pions and protons. The directed field case is particularly interesting as it breaks the mirror symmetry of the azimuthal distribution of the spectra and gives rise to parity odd-terms (terms proportional to $\sin(\varphi)$), along with the directed flows. This is of importance for the Chiral Magnetic Effect (CME) search, especially considering that it has already been reported earlier in the literature for Cu+Au collisions, showing that the effect of electric fields leads to the suppression of the $\Delta\gamma$ correlator [20]. We also observed a mass dependence of v_1 generated due to the electric fields and calculated the Δv_2 vs. p_T. This Δv_2 vs. p_T might be important to constrain the strength of the electromagnetic fields that can be measured in heavy-ion collisions.

References

[1] K. S. Lee, U. W. Heinz, and E. Schnedermann, "Search for Collective Transverse Flow Using Particle Transverse Momentum Spectra in Relativistic Heavy Ion Collisions," Z. Phys. C **48**, 525-541 (1990) doi: 10.1007/BF01572035.

[2] P. Huovinen, P. F. Kolb, U. W. Heinz, P. V. Ruuskanen, and S. A. Voloshin, "Radial and elliptic flow at RHIC: Further predictions," Phys. Lett. B **503**, 58-64 (2001) doi: 10.1016/S0370-2693(01)00219-2 [arXiv:hep-ph/0101136 [hep-ph]].

[3] C. Adler *et al.* [STAR], "Identified particle elliptic flow in Au + Au collisions at s(NN)**(1/2) = 130-GeV," Phys. Rev. Lett. **87**, 182301 (2001) doi: 10.1103/PhysRevLett.87.182301 [arXiv:nucl-ex/0107003 [nucl-ex]].

[4] D. Teaney, "The Effects of viscosity on spectra, elliptic flow, and HBT radii," Phys. Rev. C **68**, 034913 (2003) doi: 10.1103/PhysRevC.68.034913 [arXiv:nucl-th/0301099 [nucl-th]].

[5] Z. Tang, Y. Xu, L. Ruan, G. van Buren, F. Wang, and Z. Xu, "Spectra and radial flow at RHIC with Tsallis statistics in a Blast-Wave description," Phys. Rev. C **79**, 051901 (2009) doi: 10.1103/PhysRevC.79.051901 [arXiv:0812.1609 [nucl-ex]].

[6] X. Sun, H. Masui, A. M. Poskanzer, and A. Schmah, "Blast Wave Fits to Elliptic Flow Data at $\sqrt{s_{NN}}$ = 7.7–2760 GeV," Phys. Rev. C **91**, no.2, 024903 (2015) doi: 10.1103/PhysRevC.91.024903 [arXiv:1410.1947 [hep-ph]].

[7] Z. Yang and R. J. Fries, "Parameterizing smooth viscous fluid dynamics with a viscous blast wave," J. Phys. G **51**, no.1, 015102 (2024) doi:10.1088/1361-6471/ad0914 [arXiv:2007.11777 [nucl-th]].

[8] U. Gursoy, D. Kharzeev, and K. Rajagopal, "Magnetohydrodynamics, charged currents and directed flow in heavy ion collisions," Phys. Rev. C **89**, no.5, 054905 (2014) doi: 10.1103/PhysRevC.89.054905 [arXiv:1401.3805 [hep-ph]].

[9] U. Gürsoy, D. Kharzeev, E. Marcus, K. Rajagopal, and C. Shen, "Charge-dependent Flow Induced by Magnetic and Electric Fields in Heavy Ion Collisions," Phys. Rev. C **98**, no.5, 055201 (2018) doi: 10.1103/PhysRevC.98.055201 [arXiv:1806.05288 [hep-ph]].

[10] K. Nakamura, T. Miyoshi, C. Nonaka, and H. R. Takahashi, "Relativistic resistive magneto-hydrodynamics code for high-energy heavy-ion collisions," Eur. Phys. J. C **83**, no.3, 229 (2023) doi: 10.1140/epjc/s10052-023-11343-y [arXiv:2211.02310 [nucl-th]].

[11] G. Inghirami, L. Del Zanna, A. Beraudo, M. H. Moghaddam, F. Becattini, and M. Bleicher, "Numerical magneto-hydrodynamics for relativistic nuclear collisions," Eur. Phys. J. C **76**, no.12, 659 (2016) doi: 10.1140/epjc/s10052-016-4516-8 [arXiv:1609.03042 [hep-ph]].

[12] F. Cooper and G. Frye, "Comment on the Single Particle Distribution in the Hydrodynamic and Statistical Thermodynamic Models of Multiparticle Production," Phys. Rev. D **10**, 186 (1974) doi:10.1103/PhysRevD.10.186.

[13] B. Abelev *et al.* [ALICE], "Centrality dependence of π, K, p production in Pb-Pb collisions at $\sqrt{s_{NN}}$ = 2.76 TeV," Phys. Rev. C **88**, 044910 (2013) doi: 10.1103/PhysRevC.88.044910 [arXiv:1303.0737 [hep-ex]].

[14] V. Roy and A. K. Chaudhuri, "Lattice based equation of state and transverse momentum spectra of identified particles in ideal and viscous hydrodynamics," DAE Symp. Nucl. Phys. **55**, 624-625 (2010) [arXiv:1003.1195 [nucl-th]].

[15] V. Roy and A. K. Chaudhuri, "Bulk viscosity in heavy ion collision," [arXiv:1201.4230 [nucl-th]].

[16] R. Snellings, "Elliptic Flow: A Brief Review," New J. Phys. **13**, 055008 (2011) doi: 10.1088/1367-2630/13/5/055008 [arXiv:1102.3010 [nucl-ex]].

[17] J. Noronha-Hostler, J. Noronha and F. Grassi, "Bulk viscosity-driven suppression of shear viscosity effects on the flow harmonics at energies available at the BNL Relativistic Heavy Ion Collider," Phys. Rev. C **90**, no.3, 034907 (2014) doi: 10.1103/PhysRevC.90.034907 [arXiv:1406.3333 [nucl-th]].

[18] G. S. Denicol, T. Kodama and T. Koide, "The effect of shear and bulk viscosities on elliptic flow," J. Phys. G **37**, 094040 (2010) doi: 10.1088/0954-3899/37/9/094040 [arXiv:1002.2394 [nucl-th]].

[19] G. Inghirami, M. Mace, Y. Hirono, L. Del Zanna, D. E. Kharzeev and M. Bleicher, "Magnetic fields in heavy ion collisions: flow and charge transport," Eur. Phys. J. C **80**, no.3, 293 (2020) doi: 10.1140/epjc/s10052-020-7847-4 [arXiv:1908.07605 [hep-ph]].

[20] W. T. Deng and X. G. Huang, "Electric fields and chiral magnetic effect in Cu+Au collisions," Phys. Lett. B **742**, 296-302 (2015) doi: 10.1016/j.physletb.2015.01.050 [arXiv:1411.2733 [nucl-th]].

Chapter 7

Summary and Outlook

This thesis mainly delves into various aspects such as generation and effects due to electromagnetic fields on the QGP medium in the context of high-energy heavy-ion collisions. Firstly we developed a causal second-order ideal and resistive MHD formalism where we evaluated the various evolution equations governing the dissipative stresses such as bulk, diffusion, and shear within the QGP medium for both particles and anti-particles. These evolution equations are of paramount importance as they are used in hydrodynamical codes for evaluating these dissipative stresses, which again acts as an input for evaluating various observables (spectra and flow-harmonics).

The derivation of these second-order evolution equations, akin to the Israel-Stewart formalism, serves as a vital methodology to circumvent the causality issues inherent in the Navier-Stokes limit for all dissipative stresses. This was done by employing relativistic magnetohydrodynamics (RMHD) with the underlying microscopic theory which is a relativistic kinetic theory, central to which is the relativistic Boltzmann equation, along with the contribution from external forces. The collision kernel on the right-hand side of the Boltzmann equation is taken to be a relaxation time approximation (RTA). Here we derived all these macroscopic evolution equations by calculating the off-equilibrium distribution function (f) employing the Boltzmann equation. This derivation is based on the approximation that the system is very close to the equilibrium state which is given by equilibrium distribution function f_0, with off-equilibrium distribution function defined as $f = f_0 + \delta f$, where δf is defined as a small deviation from the equilibrium distribution function. This approximation is mainly taken care of via the Knudsen number ($\tau_c T$) and other dimensionless

quantities ($\chi = \frac{qB\tau_c}{T}$, $\xi = \frac{qE\tau_c}{T}$) which serve as the expansion parameter. These dimensionless quantities also ensure that the formalism works pretty well in the weak field limit (qE and $qB \to 0$) as opposed to the strong field approximation.

It is known that in any interacting medium consisting of microscopic particles, collide against each other, there is a momentum, heat, and mass transfer taking place. Hence, any external force applied to the medium gets transferred within it carrying important information about the way the medium responds to the applied force. This response is generally captured via the transport coefficients. As was discussed in the chapter.(1) and (3) the thermodynamic flux can be related to the thermodynamic forces via:

$$\mathbf{J} \;=\; \gamma \mathbf{X}, \tag{7.1}$$

where $\mathbf{X}$ is the thermodynamic force which acts on the medium and $\mathbf{J}$ is the flux generated, with γ being the transport coefficient. This transport coefficient in general can be a tensor, which can be further expanded in terms of the available basis (or projection tensors) in the following manner:

$$\gamma^{\alpha\beta} \;=\; \left(\gamma_\parallel P^\parallel_{\delta\gamma} + \gamma_\perp P^\perp_{\delta\gamma} + \gamma_\times P^\times_{\delta\gamma} \right), \tag{7.2}$$

where the $\gamma_\parallel$, $\gamma_\perp$, $\gamma_\times$, $P^\parallel_{\delta\gamma}$, $P^\perp_{\delta\gamma}$, $P^\times_{\delta\gamma}$ are the parallel, perpendicular and hall terms corresponding to the transport coefficients and projection tensors respectively. This can be however generalized to higher rank tensors (given in Appendix.(A)). For the isotropic case $\gamma_\parallel = \gamma_\perp$ and $\gamma_\times$ is zero without external fields. However, the introduction of external forces disrupts this isotropy, leading to directional preferences. Hence in this thesis, we investigated the influence of the external electromagnetic fields, predominantly generated from spectator charges, on the transport coefficients. To gain insights into the behavior of the primary transport coefficients in the presence of external fields we study the Navier-Stokes limit where we found that the longitudinal components (along the direction of the

external magnetic fields) and bulk viscosity are not affected by the external EM fields at all. Other components like the transverse and Hall components (denoted by $\perp$ and $\times$ respectively) are however affected. The transverse terms were found to be even functions of magnetic fields, whereas the Hall terms were odd functions of magnetic fields (that is $\propto$ B in our case). These Hall coefficients are indeed found to be non-dissipative which can be readily verified by simply applying time reversal symmetry transformations on the relation $J^\mu = \sigma^{\mu\nu} E_\nu$ and studying $\sigma^{\mu\nu}$. We further found that at second-order in gradient expansion, the dissipative stresses contain many additional transport coefficients that couple to the external electromagnetic fields apart from the usual second-order transport coefficients that were found previously. To get some insights into the behavior of the transport coefficients we also studied its variation against the mass, temperature, and EM fields. Additionally, the values of these transport coefficients were also evaluated for a massless Boltzmann gas. Lastly, we also retrieved the Wiedemann-Franz law from our theory, which states that $\sigma = q^2 \beta \kappa$, where σ and κ represent the electrical and thermal conductivity, respectively, and q denotes the electrical charge.

Moving forward the calculation of the electromagnetic fields was previously done assuming both the spectators and participants move with a constant velocity before and after the collisions. Most of the calculations have considered participants taken from the geometric overlap region of the collision and with a constrain on their rapidity coverage (that is less than the beam rapidity Y_b) [1] due to some rapidity loss by the participants. However, many model calculations take care of the participants in a variety of other ways [2, 3, 3]. Since participants contribute to the bulk of the medium formation and flow with a velocity (fluid velocity) that is different from that of the initial velocity calculated using $v = \left(1.0 - \frac{4m^2}{\left(\sqrt{s_{NN}}\right)^2}\right)^{1/2}$, m is the mass of the proton and $\sqrt{s_{NN}}$ is the center of mass energy of the colliding nucleus. It is thus imperative to take into account the fluid velocity (specifically at low-energies) while calculating the electromagnetic fields for the charged

participants using Maxwell's equations. Hence, in chapter.(4), a comprehensive examination of the complete 3+1D spatio-temporal evolution of electromagnetic fields generated by participants in heavy-ion collisions was conducted, assuming a Bjorken expansion of the fluid with no back reaction from electromagnetic fields on fluid velocity. We adopt the Bjorken flow assumption primarily for its mathematical convenience in understanding the behavior of the generated fields. While this assumption can be violated in practice, hence we introduce a parameter, denoted by $\beta^{-1} = \frac{B^2}{2P}$, to quantify the deviation from this assumption. This parameter represents the ratio of pressure induced by magnetic fields to that induced by the fluid. A value less than 1 provides an optimal scenario for our formalism to excel.

In this formalism we neglected the dissipative effects due to diffusion; that is, we set V^μ(diffusion current) $= 0$. Our analysis revealed that the fields generated by participants exhibit distinct temporal behavior compared to those generated by spectators. Here, fields generated after the collisions grow and then decay with time, as opposed to the decaying nature of the electromagnetic fields in the case of spectators. A naive comparison of the strength of the fields produced at late times at $\tau = 10$ fm at space-time rapidity $\eta = 1$, gives the values of the order of $\mathcal{O}(10^{-3})$ (for participants) compared to $\mathcal{O}(10^{-5})$ (in units of m_π^2) for the spectators at $\tau \approx 2$ fm [1]. This gives us the impression that at the initial stage, the field strengths are mainly due to the spectators, but at a later stage, the strength is primarily governed by the participant charges.

Continuing on the same line of investigation that is calculating the various components of electromagnetic fields, in chapter.(5), we turn towards low-energy nuclear collisions, where the phenomenon of baryon stopping has been experimentally observed. Previous theoretical studies have also indicated that electromagnetic fields persist for a longer duration in such collisions (low-energies) compared to high-energy collisions, such as those at $\sqrt{s_{NN}} \approx 200$ GeV or 2.76 TeV, even in a vacuum. Thus, we focus on two key aspects: the

nuclear stopping effect and the prolonged existence of electromagnetic fields in low-energy collisions. Making an amalgamation of both things, we investigated the impact of baryon stopping on electromagnetic fields at low center-of-mass energy collisions by parametrizing the velocities of participant charges in a Monte-Carlo Glauber model calculation. Our analysis reveals distinct effects of stopping on various components of electromagnetic fields, particularly during or after collisions. We mainly calculated the behavior of the electromagnetic fields for $\sqrt{s_{NN}}$ between 4 to 20 GeV. Here are a few of the observations that we made:

- We found that even without any medium effects the deceleration enhances electric fields at late times (at $t_{\mathrm{obs}} \geq 4$ fm) compared to the case of no deceleration.

- The effects of deceleration are most significant for the longitudinal component of the electric fields, which can be mainly attributed to the fact that the particles continue to be in the z-direction even after the collisions where the deceleration seems to dominate.

- The linear proportionality of the values of magnetic fields at $\tau = 0$ with $\sqrt{s_{NN}}$ is found to be slightly broken in the presence of deceleration.

- In more central collisions the number of participants experiencing the deceleration effects is more in number. Hence while estimating the behavior of all the field components with impact parameter for two different scenarios with and without deceleration, we found a notable difference between the two mainly at most central collisions.

In high-energy heavy-ion collisions, studies primarily focus on the two most important experimental observables that is the flow harmonics and transverse spectra measurements. In chapter.(6), we conducted a detailed investigation into the influence of electric fields on these bulk observables by taking various configurations of fields on the transverse plane.

Utilizing a blast-wave model, our analysis revealed substantial effects of electric fields on the bulk-observables for identified particles (pions and protons) with transverse momentum (p_T). One interesting observation was in the case of directed fields (especially relevant in the case of asymmetric collisions like d+Au, p+Au, etc.). Here, such fields break the symmetry in the azimuthal distribution of the charged multiplicities. This symmetry breaking thus generates new odd flow harmonics and introduces new parity odd terms in the Fourier series expansion of the multiplicities in the azimuthal plane, which may be relevant for the search for CME signals. Moreover, we investigated the difference between particle and antiparticle's elliptic flow, denoted as Δv_2, as a function of transverse momentum (p_T), where $\Delta v_2 = v_2(h^+) - v_2(h^-)$. We found that Δv_2 initially increases and reaches a saturation around $p_T = 3$ GeV.

In summary, this thesis tries to deepen our understanding of how electromagnetic fields influence the evolution of quark-gluon plasma and how it gets affected by the QGP medium, thereby contributing to the overall advancement in our knowledge of the behavior of these fields in the context of heavy-ion collisions.

However, there are several promising avenues for further exploration beyond the scope of our current investigations.

- At ultra-relativistic energies, the colliding nuclei carry a large initial global angular momentum of the order of 10^4 to $10^5\hbar$, accompanied by the formation of an intense electromagnetic field. Hence, taking both the global rotation of the medium along with the electromagnetic fields into account and studying their relative effects on the transport coefficients could offer valuable insights into the behavior of fields and angular momentum on the QGP medium.

- Measuring the effect of EM fields via the bulk observables has been quite challenging, though several advancements have been made in this direction. A very inter-

esting work in this direction could be in constraining or putting an upper bound on the strength of the fields that can be measured in such collisions. One possible way of doing this is by comparing Δv_2 vs. p_T results from various model calculations, including the electromagnetic fields, with the available or forthcoming STAR data.

- It has been seen previously that in asymmetric collisions (d+Au, Cu+Au, etc) the $\Delta\gamma$ correlator (defined in chapter.(1)) value is suppressed in the presence of electric fields in such scenarios. Hence, a comprehensive exploration of the significance of electric fields in probing the Chiral Magnetic Effect (CME) is imperative.

All these phenomena mentioned above can be further explored by a consistent magnetohydrodynamics (MHD) code; however, developing such a consistent code is pretty challenging. Still, several attempts have been made in this direction [5, 6, 7, 8].

- Further considering conserved charges beyond electric charges, such as baryons and strangeness, it would be intriguing to investigate the interplay of all these conserved charges on final bulk observables specifically in low-energy heavy-ion collisions. Also, a comparative analysis between the effects of electromagnetic fields and baryon diffusion could enhance our understanding of their impact on medium properties, particularly on the splitting of flow harmonics with transverse momentum (p_T), rapidity (y) and impact parameter (b). This may further clarify the limitations of the above proposed observable for seeing the effects of the electromagnetic fields in these low-energy heavy-ion collisions.

- In chapter.(5), where stopping is introduced via velocity parametrization, several improvements are conceivable. One of them can be relaxing the assumption that nucleons come to a halt within a few femtometers post-collision. This could lead to a more realistic scenario where nucleons attain a reduced velocity, possibly experiencing further energy loss or maintaining this diminished velocity depending on the

circumstances. This adjustment could improve the model's agreement with experimentally measured net baryon density with rapidity, enabling an accurate estimation of $\Delta\tau$. Additionally, studying the behavior of electromagnetic fields by considering both the medium and stopping effects could provide fascinating insights.

References

[1] U. Gursoy, D. Kharzeev and K. Rajagopal, "Magnetohydrodynamics, charged currents and directed flow in heavy ion collisions," Phys. Rev. C **89**, no.5, 054905 (2014) doi:10.1103/PhysRevC.89.054905 [arXiv:1401.3805 [hep-ph]].

[2] V. Skokov, A. Y. Illarionov and V. Toneev, "Estimate of the magnetic field strength in heavy-ion collisions," Int. J. Mod. Phys. A **24**, 5925-5932 (2009) doi:10.1142/S0217751X09047570 [arXiv:0907.1396 [nucl-th]].

[3] V. Voronyuk, V. D. Toneev, W. Cassing, E. L. Bratkovskaya, V. P. Konchakovski and S. A. Voloshin, "(Electro-)Magnetic field evolution in relativistic heavy-ion collisions," Phys. Rev. C **83**, 054911 (2011) doi:10.1103/PhysRevC.83.054911 [arXiv:1103.4239 [nucl-th]].

[4] H. Taya, T. Nishimura and A. Ohnishi, "Estimation of the electromagnetic field in intermediate-energy heavy-ion collisions," [arXiv:2402.17136 [hep-ph]].

[5] G. Inghirami, L. Del Zanna, A. Beraudo, M. H. Moghaddam, F. Becattini and M. Bleicher, "Numerical magneto-hydrodynamics for relativistic nuclear collisions," Eur. Phys. J. C **76**, no.12, 659 (2016) doi:10.1140/epjc/s10052-016-4516-8 [arXiv:1609.03042 [hep-ph]].

[6] A. Dash, M. Shokri, L. Rezzolla and D. H. Rischke, "Charge diffusion in relativistic resistive second-order dissipative magnetohydrodynamics," Phys. Rev. D **107**, no.5, 056003 (2023) doi:10.1103/PhysRevD.107.056003 [arXiv:2211.09459 [nucl-th]].

[7] K. Nakamura, T. Miyoshi, C. Nonaka and H. R. Takahashi, "Relativistic resistive magneto-hydrodynamics code for high-energy heavy-ion collisions," Eur. Phys. J. C **83**, no.3, 229 (2023) doi:10.1140/epjc/s10052-023-11343-y [arXiv:2211.02310 [nucl-th]].

[8] M. Mayer, L. Rezzolla, H. Elfner, G. Inghirami and D. H. Rischke, "BHAC-QGP: three-dimensional MHD simulations of relativistic heavy-ion collisions, II. Application to Au-Au collisions," [arXiv:2403.08669 [hep-ph]].

Chapter 8

Units and conversions

In the study of heavy-ion collisions, it is often advantageous to work with natural units. In natural units, fundamental physical constants such as the speed of light, Planck's constant, and the gravitational constant are set to unity, simplifying mathematical expressions and theoretical calculations. This choice of units eliminates the need to carry around cumbersome numerical factors and allows physicists to focus on the underlying physics of the system. In this current chapter, we will briefly review most of the conversions and units that are used in the context of heavy ion collisions.

8.1   Conversion

Natural units assume that certain values are constants which are mentioned below and using those we get proper conversion factors. Here we consider: $\hbar = c = k_B = \mu_0 = \epsilon_0 = 1$. That means $3 \times 10^8 m/s = 1$, hence:

$$1m \;\; = \;\; 0.333 \times 10^{-8} s. \tag{8.1}$$

Also, we know that 1.055×10^{-34}Js =1.

$$\implies \;\; 1J = 0.947867299 \times 10^{34} s^{-1}. \tag{8.2}$$

Now employing Eq.(8.1), Eq.(8.2) we can get the relationship between Joule and meter which is given as:

$$\implies \;\; 1J = \frac{0.947867299 \times 10^{34}}{3 \times 10^8} m^{-1} = 0.31595 \times 10^{26} m^{-1}. \tag{8.3}$$

Again we know that 1 eV = 1.6 $\times 10^{-19}$ J. Hence the relationship between Joule and eV is given as:

$$\implies 1J = 0.625 \times 10^{19} eV. \tag{8.4}$$

Equating Eq.(8.3) and Eq.(8.4) we get:

$$
\begin{aligned}
0.625 \times 10^{19} eV &= 0.31595 \times 10^{26} m^{-1}, \\
1 eV &= 0.50552 \times 10^{7} m^{-1}, \\
1 GeV &= 0.50552 \times 10^{16} m^{-1}. \tag{8.5}
\end{aligned}
$$

We also know that:

$$
\begin{aligned}
1 fm &= 10^{-15} m, \\
1 GeV &= 5 fm^{-1}, \\
5 fm^{-1} &= 1000 MeV, \\
1 fm^{-1} &= 200 MeV.
\end{aligned}
$$

Using the equations in (8.5) and Eq.(8.1) we get:

$$
\begin{aligned}
1 GeV &= \frac{0.50552 \times 10^{16}}{0.333 \times 10^{-8}} s^{-1}, \\
1 GeV &= 1.5180 \times 10^{24} s^{-1}. \tag{8.6}
\end{aligned}
$$

The relation between GeV and Kg can be found using Eq.(8.1), Eq.(8.6) as given below:

$$
\begin{aligned}
\hbar &= 1.055 \times 10^{-34} kg \frac{m^2}{s} = 1, \\
&\quad 1.055 \times 10^{-34} kg \frac{(0.333 \times 10^{-8} s)^2}{s} = 1, \\
&\quad 0.11698 \times 10^{-50} Kg = 1 s^{-1}, \\
&\quad 0.11698 \times 10^{-50} Kg = 0.6587 \times 10^{-24} GeV, \\
&\quad 1 GeV = 0.17776 \times 10^{-26} Kg. \tag{8.7}
\end{aligned}
$$

The cosmological constant $\Lambda = 1.1056 \times 10^{-52} m^{-2}$ can also be written in GeV units in the following way by using Eq.(8.1):

$$\Lambda = \frac{1.1056 \times 10^{-52} \times (10^{-32})}{(0.50552)^2} GeV^2.$$

8.2 Units of Quantities

Here, we have summarized all the quantities used in this thesis with their notations, units, and formulas below:

Quantities	Notations	Formula	Units
Fluid velocity	u	$g_{\mu\nu} u^\mu u^\nu = 1$	Dimensionless
Energy density	ϵ	$\epsilon = T^{\mu\nu} u_\mu u_\nu$	$\frac{GeV}{fm^3}$
Isotropic pressure	P	$P = c_s^2 \epsilon$	$\frac{GeV}{fm^3}$
Shear viscosity	η	$\pi^{\mu\nu} = \eta \nabla^{<\mu} u^{\nu>}$	$\frac{GeV}{fm^2}$
Bulk viscosity	ζ	$-\zeta \nabla_\mu u^\mu$	$\frac{GeV}{fm^2}$
Chemical potential	α	$\alpha = \frac{\mu}{T}$	Dimensionless
Net-number density	n	$N^\mu = n u^\mu + V^\mu$	$\frac{1}{fm^3}$
Diffusion	V	$V^\mu = \kappa \nabla^\mu \alpha$	$\frac{1}{fm^3}$
Diffusion coefficient	κ	$\kappa = \frac{V^\mu}{\nabla^\mu \alpha}$	$\frac{1}{fm^2}$
Charge	q	Potential energy$= \frac{1}{4\pi r} q_1 q_2$	Dimensionless
Electric field	E	Lorentz force: $\frac{dp}{dt} = q(E + v \times B)$	$(GeV)^2$
Magnetic field	B	Lorentz force: $\frac{dp}{dt} = q(E + v \times B)$	$(GeV)^2$
Electrical conductivity	σ	$J^\mu = qV^\mu = \sigma^{\mu\nu} E_\nu$	$\frac{1}{(GeV)^2(fm)^3}$
Entropy density	s	Entropy current: $S^\mu = su^\mu$	$\frac{1}{fm^3}$
Rapidity	η_s	Space-time rapidity: $\eta_s = \frac{1}{2} ln \left(\frac{t+z}{t-z} \right)$	Dimensionless
Mometum rapidity	y_p	$y_p = \frac{1}{2} \ln \left(\frac{E+p}{E-p} \right)$	Dimensionless
rigidity	-	$\frac{momentum\ of\ the\ particle}{charge}$	GeV

Appendix A

(Chapter-3 appendix)

A.1   Thermodynamic Integrals

The n-th moments integral for the distribution function is defined as:

$$I^{(m)\pm}_{\mu_1\mu_2\cdots\mu_n} = \int \frac{dp}{(u\cdot p)^m} p_{\mu_1} p_{\mu_2} \cdots p_{\mu_n} \left(f_0 \pm \bar{f}_0\right), \tag{A.1}$$

which can be docomposed as:

$$I^{(m)\pm}_{\mu_1\mu_2\ldots\mu_n} = I^{(m)\pm}_{n0} u_{\mu_1} \cdots u_{\mu_n} + I^{(m)\pm}_{n1} \left(\Delta_{\mu_1\mu_2} u_{\mu_3} \cdots u_{\mu_n} + \text{perm.}\right) + \cdots$$

$$\cdots + I^{(m)\pm}_{nq} \left(\Delta_{\mu_1\mu_2}\Delta_{\mu_3\mu_4} \cdots \Delta_{\mu_{n-1}\mu_n} + \text{perm.}\right). \tag{A.2}$$

where $n \geq 2q$.

Similarly the auxiliary moments integral

$$J^{(m)\pm}_{\mu_1\mu_2\cdots\mu_n} = \int \frac{dp}{(u\cdot p)^m} p_{\mu_1} p_{\mu_2} \cdots p_{\mu_n} \left(f_0\tilde{f}_0 \pm \bar{f}_0\tilde{\bar{f}}_0\right), \tag{A.3}$$

can be decomposed as:

$$J^{(m)\pm}_{\mu_1\mu_2\ldots\mu_n} = J^{(m)\pm}_{n0} u_{\mu_1} \cdots u_{\mu_n} + J^{(m)\pm}_{n1} \left(\Delta_{\mu_1\mu_2} u_{\mu_3} \cdots u_{\mu_n} + \text{perm.}\right) + \cdots \tag{A.4}$$

$$\cdots + J^{(m)\pm}_{nq} \left(\Delta_{\mu_1\mu_2}\Delta_{\mu_3\mu_4} \cdots \Delta_{\mu_{n-1}\mu_n} + \text{perm.}\right). \tag{A.5}$$

where $\tilde{f}_0 = 1 - r f_0$. Here we define the thermodynamic integrals as follows:

$$I^{(m)\pm}_{nq} = \frac{1}{(2q+1)!!} \int dp(u\cdot p)^{n-2q-m} (\Delta_{\alpha\beta}p^\alpha p^\beta)^q \left(f_0 \pm \bar{f}_0\right), \tag{A.6}$$

and

$$J^{(m)\pm}_{nq} = \frac{1}{(2q+1)!!} \int dp(u\cdot p)^{n-2q-m} (\Delta_{\alpha\beta}p^\alpha p^\beta)^q \left(f_0\tilde{f}_0 \pm \bar{f}_0\tilde{\bar{f}}_0\right). \tag{A.7}$$

One can write the J in terms of I as:

$$J_{nq}^{(0)\pm} = \frac{1}{\beta}\left[-I_{n-1,q-1}^{(0)\pm} + (n-2q)I_{n-1,q}^{(0)\pm}\right]. \tag{A.8}$$

The general expression of D_{nq} used in eq. (3.9) and eq. (3.9) is given by: $D_{nq} = J_{n+1,q}^{(0)+}J_{n-1,q}^{(0)+} - J_{nq}^{(0)-}J_{nq}^{(0)-}$.

A.2   Second order relaxation equation for dissipative stresses

In this appendix we discuss the detail calculation of the second order dissipative stresses. The contribution due to the antiparticles are not shown explicitly for simplicity but they appear in the final expressions.

A.2.1   Shear stress

The second order shear stress $\pi_{(2)}^{\mu\nu}$ is given by eq. (3.69):

$$\pi_{(2)}^{\mu\nu} = \Delta_{\alpha\beta}^{\mu\nu}\int dp\, p^\alpha p^\beta \left(\frac{\tau_c}{u\cdot p}p^\rho \partial_\rho\left[\frac{\tau_c}{u\cdot p}p^\sigma \partial_\sigma f_0\right] + \frac{\tau_c}{u\cdot p}qF^{\gamma\eta}p_\eta\frac{\partial}{\partial p^\gamma}\left[\frac{\tau_c}{u\cdot p}p^\sigma \partial_\sigma f_0\right]\right)(A.9)$$

For convenience, we write them into two parts as:

$$\pi_{(2)}^{\mu\nu} = \mathcal{I}_1 + \mathcal{I}_2. \tag{A.10}$$

Here

$$\mathcal{I}_1 = \Delta_{\alpha\beta}^{\mu\nu}\int dp\, p^\alpha p^\beta \left(\frac{\tau_c}{u\cdot p}p^\rho \partial_\rho\left[\frac{\tau_c}{u\cdot p}p^\sigma \partial_\sigma f_0\right]\right), \tag{A.11}$$

$$\mathcal{I}_2 = \Delta_{\alpha\beta}^{\mu\nu}\int dp\, p^\alpha p^\beta \left(\frac{\tau_c}{u\cdot p}qF^{\gamma\eta}p_\eta\frac{\partial}{\partial p^\gamma}\left[\frac{\tau_c}{u\cdot p}p^\sigma \partial_\sigma f_0\right]\right), \tag{A.12}$$

Let us first evaluate the integral $\mathcal{I}_1$:

$$\mathcal{I}_1 = \Delta_{\alpha\beta}^{\mu\nu}\int dp\, p^\alpha p^\beta \left(\frac{\tau_c}{u\cdot p}p^\rho \partial_\rho\left[\frac{\tau_c}{u\cdot p}p^\sigma \partial_\sigma f_0\right]\right),$$
$$= \mathcal{A} + \mathcal{B} + \mathcal{C}, \tag{A.13}$$

where

$$\mathcal{A} = \Delta^{\mu\nu}_{\alpha\beta} \int dp\, p^\alpha p^\beta \tau_c D \left[\frac{\tau_c}{u \cdot p} p^\sigma \partial_\sigma f_0 \right],$$

$$\mathcal{B} = \Delta^{\mu\nu}_{\alpha\beta} \int dp\, p^\alpha p^\beta \frac{\tau_c}{u \cdot p} p^\rho \nabla_\rho \left[\tau_c \dot{f_0} \right],$$

$$\mathcal{C} = \Delta^{\mu\nu}_{\alpha\beta} \int dp\, p^\alpha p^\beta \frac{\tau_c}{u \cdot p} p^\rho \nabla_\rho \left[\frac{\tau_c}{u \cdot p} p^\sigma \nabla_\sigma f_0 \right].$$

A straight forward calculation gives:

$$\mathcal{A} = -\Delta^{\mu\nu}_{\alpha\beta} \int dp\, f_0 \tilde{f}_0 p^\alpha p^\beta \tau_c D \left[\frac{\tau_c}{u \cdot p} p^\sigma \left\{ \beta p^\gamma \partial_\sigma u_\gamma + (u \cdot p)\, \partial_\sigma \beta - \partial_\sigma \alpha \right\} \right].$$

We can rewrite the above expression in terms of the thermodynamic integrals given in Appendix A.1 and eq. (3.9) as:

$$\mathcal{A} = -\tau_c \dot{\pi}^{\langle\mu\nu\rangle} - 2\tau_c^2 \left(\frac{n_f}{\epsilon + P} J^{(0)-}_{31} - J^{(1)-}_{31} \right) \dot{u}^{\langle\mu} \nabla^{\nu\rangle} \alpha + \tau_c^2 \Delta^{\mu\nu}_{\alpha\beta} J^{(0)+}_{31} \dot{u}^\beta \left[\frac{\beta q B b^{\alpha\sigma}}{\epsilon + P} V_\sigma \right]$$

$$+ \tau_c^2 \Delta^{\mu\nu}_{\alpha\beta} J^{(0)+}_{31} \dot{u}^\alpha \left[\frac{\beta q B b^{\beta\sigma}}{\epsilon + P} V_\sigma \right]. \tag{A.14}$$

Similarly for $\mathcal{B}$ we have:

$$\mathcal{B} = \Delta^{\mu\nu}_{\alpha\beta} \int dp\, p^\alpha p^\beta \frac{\tau_c}{u \cdot p} p^\rho \nabla_\rho \left[\tau_c \dot{f_0} \right],$$

$$= -\Delta^{\mu\nu}_{\alpha\beta} \int dp\, f_0 \tilde{f}_0 p^\alpha p^\beta \frac{\tau_c}{u \cdot p} p^\rho \nabla_\rho \tau_c \left[\beta p^\gamma \dot{u}_\gamma + (u \cdot p)\dot{\beta} - \dot{\alpha} \right].$$

Using the thermodynamics integral discussed in Appendix A.1 we get:

$$\mathcal{B} = -2\tau_c^2 \left[\left(J^{(0)+}_{31} + J^{(1)+}_{42} \right) \dot{\beta} - \left(J^{(1)-}_{31} + J^{(2)-}_{42} \right) \dot{\alpha} \right] \sigma^{\mu\nu} - 2\tau_c^2 \nabla^{\langle\mu} \left(\dot{u}^{\nu\rangle} \beta J^{(1)+}_{42} \right),$$

$$= -2\tau_c^2 \left[\left(J^{(0)+}_{31} + J^{(1)+}_{42} \right) \mathcal{X} - \left(J^{(1)-}_{31} + J^{(2)-}_{42} \right) \mathcal{Y} \right] \theta \sigma^{\mu\nu} - 2\tau_c^2 \nabla^{\langle\mu} \left(\dot{u}^{\nu\rangle} \beta J^{(1)+}_{42} \right), \tag{A.15}$$

where in the last line we have used the expression for $\dot{\alpha}$ and $\dot{\beta}$ given in eq. (3.9) and eq. (3.9). The $\mathcal{X}$ and $\mathcal{Y}$ are same as eq. (3.26). Finally, for $\mathcal{C}$ we have

$$\mathcal{C} = \Delta^{\mu\nu}_{\alpha\beta} \int dp\, p^\alpha p^\beta \frac{\tau_c}{u \cdot p} p^\rho \nabla_\rho \left[\frac{\tau_c}{u \cdot p} p^\sigma \nabla_\sigma f_0 \right],$$

$$= -\Delta^{\mu\nu}_{\alpha\beta} \int dp\, f_0 \tilde{f}_0 p^\alpha p^\beta \frac{\tau_c}{u \cdot p} p^\rho \nabla_\rho \left[\frac{\tau_c}{u \cdot p} p^\sigma \left(\beta p^\gamma \nabla_\sigma u_\gamma + (u \cdot p) \nabla_\sigma \beta - \nabla_\sigma \alpha \right) \right].$$

Like the previous cases we use the thermodynamic integrals given in Appendix A.1 along with eq. (3.9) and eq. (3.1) to rewrite the above expression:

$$
\begin{aligned}
\mathcal{C} &= 2\nabla^{\langle\mu}\left(\dot{u}^{\nu\rangle}\beta\tau_c^2 J_{42}^{(1)+}\right) + 2\nabla^{\langle\mu}\left[\nabla^{\nu\rangle}\alpha\tau_c^2\left(J_{42}^{(2)-} - \frac{1}{h}J_{42}^{(1)-}\right)\right] - 4\beta\tau_c^2\left(2J_{63}^{(3)+} + J_{42}^{(1)+}\right)\sigma_\rho^{\langle\mu}\sigma^{\nu\rangle\rho} \\
&\quad -\frac{20}{3}\beta\tau_c^2 J_{42}^{(1)+}\theta\sigma^{\mu\nu} - \frac{28}{3}\beta\tau_c^2 J_{63}^{(3)+}\theta\sigma^{\mu\nu} - 4\beta\tau_c^2\left(J_{42}^{(1)+} + 2J_{63}^{(3)+}\right)\sigma^{\langle\mu\rho}\omega_\rho^{\nu\rangle} \\
&\quad +2\tau_c^2\nabla^{\langle\mu}\left[J_{42}^{(1)+}\left(\frac{\beta q B b^{\nu\rangle\gamma}V_\gamma}{\epsilon + P}\right)\right],
\end{aligned}
\tag{A.16}
$$

Now let us evaluate the second integral $\mathcal{I}_2$:

$$
\begin{aligned}
\mathcal{I}_2 &= -\Delta_{\alpha\beta}^{\mu\nu}\int dp\, p^\alpha p^\beta\left(\left(\frac{\tau_c}{u\cdot p}\right)^2 qBb^{\gamma\eta}p_\eta\frac{\partial}{\partial p^\gamma}\left[p^\sigma\partial_\sigma f_0\right]\right), \\
&= \Delta_{\alpha\beta}^{\mu\nu}\int dp\, f_0\tilde{f}_0 p^\alpha p^\beta\left(\left(\frac{\tau_c}{u\cdot p}\right)^2 qBb^{\gamma\eta}p_\eta\left((\beta p^\rho\partial_\sigma u_\rho + (u\cdot p)\partial_\sigma\beta - \partial_\sigma\alpha)\Delta_\gamma^\sigma\right) + \beta\partial_\sigma u_\rho p^\sigma\Delta_\gamma^\rho\right), \\
&= 2\tau_c^2 qBb^{\gamma\eta}\beta J_{42}^{(2)-}\left(\Delta_{\eta\beta}^{\mu\nu}g^{\beta\rho} + \Delta_{\alpha\eta}^{\mu\nu}g^{\alpha\rho}\right)\sigma_{\gamma\rho},
\end{aligned}
\tag{A.17}
$$

where we have used $\frac{\partial}{\partial p^\gamma}p^\sigma\partial_\sigma f_0 = \partial_\sigma f_0\Delta_\gamma^\sigma + p^\sigma\frac{\partial}{\partial p^\gamma}\partial_\sigma f_0$ and the expression for $\partial_\sigma f_0$ to arrive at the final expression.

Now using eqs. (A.14)-(A.17) we get the final expression:

$$
\begin{aligned}
\pi_{(2)}^{\mu\nu} &= -\tau_c\dot{\pi}^{\langle\mu\nu\rangle} - 2\tau_c^2\dot{u}^{\langle\mu}\nabla^{\nu\rangle}\alpha\left(\frac{n_f}{\epsilon + P}J_{31}^{(0)-} - J_{31}^{(1)-}\right) + \tau_c^2\Delta_{\alpha\beta}^{\mu\nu}J_{31}^{(0)+}\dot{u}^\beta\left[\frac{\beta q B b^{\alpha\sigma}}{\epsilon + P}V_\sigma\right] \\
&\quad +\tau_c^2\Delta_{\alpha\beta}^{\mu\nu}J_{31}^{(0)+}\dot{u}^\alpha\left[\frac{\beta q B b^{\beta\sigma}}{\epsilon + P}V_\sigma\right] - 2\tau_c^2\left[\left(J_{31}^{(0)+} + J_{42}^{(1)+}\right)\mathcal{X} - \left(J_{31}^{(1)-} + J_{42}^{(2)-}\right)\mathcal{Y}\right]\theta\sigma^{\mu\nu} \\
&\quad -2\tau_c^2\nabla^{\langle\mu}\left(\dot{u}^{\nu\rangle}\beta J_{42}^{(1)+}\right) + 2\nabla^{\langle\mu}\left(\dot{u}^{\nu\rangle}\beta\tau_c^2 J_{42}^{(1)+}\right) + 2\nabla^{\langle\mu}\left[\nabla^{\nu\rangle}\alpha\tau_c^2\left(J_{42}^{(2)-} - \frac{n_f}{\epsilon + P}J_{42}^{(1)-}\right)\right] \\
&\quad -\frac{20}{3}\beta\tau_c^2 J_{42}^{(1)+}\theta\sigma^{\mu\nu} - 4\beta\tau_c^2\left(2J_{63}^{(3)+} + J_{42}^{(1)+}\right)\sigma_\rho^{\langle\mu}\sigma^{\nu\rangle\rho} - \frac{28}{3}\beta\tau_c^2 J_{63}^{(3)+}\theta\sigma^{\mu\nu} \\
&\quad -4\beta\tau_c^2\left(J_{42}^{(1)+} + 2J_{63}^{(3)+}\right)\sigma^{\langle\mu\rho}\omega_\rho^{\nu\rangle} + 2\tau_c^2\nabla^{\langle\alpha}\left[J_{42}^{(1)+}\left(\frac{\beta q B b^{\beta\rangle\gamma}V_\gamma}{\epsilon + P}\right)\right] \\
&\quad +2\tau_c^2 qBb^{\gamma\eta}\beta J_{42}^{(2)-}\left(\Delta_{\eta\beta}^{\mu\nu}g^{\beta\rho} + \Delta_{\alpha\eta}^{\mu\nu}g^{\alpha\rho}\right)\sigma_{\gamma\rho}.
\end{aligned}
\tag{A.18}
$$

Here we kept terms only upto second-order in gradients.

A.2.2 Bulk stress

Let us now consider the bulk viscous case. From eq. (3.63) we get:

$$
\begin{aligned}
\Pi_{(2)} &= -\frac{1}{3}\Delta_{\alpha\beta}\int dp p^\alpha p^\beta \left(\frac{\tau_c}{u\cdot p}p^\mu\partial_\mu\left[\frac{\tau_c}{u\cdot p}p^\rho\partial_\rho f_0\right] + \frac{\tau_c}{u\cdot p}qF^{\mu\nu}p_\nu\frac{\partial}{\partial p^\mu}\left[\frac{\tau_c}{u\cdot p}p^\rho\partial_\rho f_0\right]\right), \\
&= \mathcal{I}_1 + \mathcal{I}_2,
\end{aligned}
\tag{A.19}
$$

where

$$
\begin{aligned}
\mathcal{I}_1 &= -\frac{\Delta_{\alpha\beta}}{3}\int dp p^\alpha p^\beta \frac{\tau_c}{u\cdot p}p^\mu\partial_\mu\left[\frac{\tau_c}{u\cdot p}p^\rho\partial_\rho f_0\right], \\
\mathcal{I}_2 &= -\frac{\Delta_{\alpha\beta}}{3}\int dp p^\alpha p^\beta \frac{\tau_c}{u\cdot p}qF^{\mu\nu}p_\nu\frac{\partial}{\partial p^\mu}\left[\frac{\tau_c}{u\cdot p}p^\rho\partial_\rho f_0\right].
\end{aligned}
$$

Note that for our case $F^{\mu\nu} = -Bb^{\mu\nu}$. Let us first evaluate $\mathcal{I}_1$ by breaking it into three parts $\mathcal{I}_1 = \mathcal{A} + \mathcal{B} + \mathcal{C}$ where

$$
\begin{aligned}
\mathcal{A} &= -\frac{\Delta_{\alpha\beta}}{3}\int dp p^\alpha p^\beta \tau_c D\left[\frac{\tau_c}{u\cdot p}p^\rho\partial_\rho f_0\right], \\
\mathcal{B} &= -\frac{\Delta_{\alpha\beta}}{3}\int dp p^\alpha p^\beta \frac{\tau_c}{u\cdot p}p^\mu\nabla_\mu\left(\tau_c\dot{f}_0\right), \\
\mathcal{C} &= -\frac{\Delta_{\alpha\beta}}{3}\int dp p^\alpha p^\beta \frac{\tau_c}{u\cdot p}p^\mu\nabla_\mu\left(\frac{\tau_c p^\rho}{u\cdot p}\nabla_\rho f_0\right).
\end{aligned}
$$

We evaluate each of the above integrals one-by-one:

$$
\begin{aligned}
\mathcal{A} &= -\frac{\Delta_{\alpha\beta}}{3}\int dp p^\alpha p^\beta \tau_c D\left[\frac{\tau_c}{u\cdot p}p^\rho\partial_\rho f_0\right], \\
&= \frac{\Delta_{\alpha\beta}}{3}\int dp f_0\tilde{f}_0 p^\alpha p^\beta \tau_c D\left[\frac{\tau_c}{u\cdot p}p^\rho\left(\beta p^\gamma\partial_\rho u_\gamma + (u\cdot p)\partial_\rho\beta - \partial_\rho\alpha\right)\right], \\
&= -\tau_c\dot{\Pi} + \frac{2\tau_c^2}{3}J_{31}^{(0)-}\frac{n_f}{\epsilon+P}\nabla^\alpha\alpha\dot{u}_\alpha - \frac{2\tau_c^2}{3}J_{21}^{(0)-}\nabla^\alpha\alpha\dot{u}_\alpha - \frac{2\tau_c^2\beta}{3(\epsilon+P)}J_{31}^{(0)+}\dot{u}_\alpha qBb^{\alpha\beta}V_\beta
\end{aligned}
\tag{A.20}
$$

We have used the thermodynamic integrals given in Appendix.A.1 along with eq. (A.2) and eq. (3.9) to arrive at the final expression eq. (A.20). Now let us evaluate $\mathcal{B}$ with the help of

thermodynamic integrals and its properties given in Appendix A.1:

$$
\begin{aligned}
\mathcal{B} &= -\frac{\Delta_{\alpha\beta}}{3} \int dp\, p^\alpha p^\beta \frac{\tau_c}{u \cdot p} p^\mu \nabla_\mu(\tau_c \dot{f}_0), \\
&= \frac{5\tau_c^2}{3} \nabla_\mu \left(\beta J_{42}^{(1)+} \dot{u}^\mu \right) + \frac{5\tau_c^2}{3} \theta \left[\left(J_{31}^{(0)+} + J_{42}^{(1)+} \right) \dot{\beta} - \left(J_{31}^{(1)-} + J_{42}^{(2)-} \right) \dot{\alpha} \right].
\end{aligned}
$$

$$(A.21)$$

Similarly for $\mathcal{C}$ we have

$$
\begin{aligned}
\mathcal{C} &= -\frac{\Delta_{\alpha\beta}}{3} \int dp\, p^\alpha p^\beta \frac{\tau_c}{u \cdot p} p^\mu \nabla_\mu \left(\frac{\tau_c p^\rho}{u \cdot p} \nabla_\rho f_0 \right), \\
&= \frac{\Delta_{\alpha\beta}}{3} \int dp\, f_0 \tilde{f}_0 p^\alpha p^\beta \frac{\tau_c}{u \cdot p} p^\mu \nabla_\mu \left(\frac{\tau_c p^\rho}{u \cdot p} \left(\beta p^\gamma \nabla_\rho u_\gamma + (u \cdot p) \nabla_\rho \beta - \nabla_\rho \alpha \right) \right), \\
&= \frac{5\tau_c^2 \beta}{9} \left(7 J_{63}^{(3)+} + \frac{23}{3} J_{42}^{(1)+} \right) \theta^2 + \frac{5\tau_c^2}{3} \nabla_\mu \left[\nabla^\mu \alpha \left(J_{42}^{(1)-} \frac{n_f}{\epsilon + P} - J_{42}^{(2)-} \right) \right] \\
&\quad + \frac{\tau_c^2 \beta}{3} \left(7 J_{63}^{(3)+} + J_{42}^{(1)+} \right) \sigma^{\mu\nu} \sigma_{\mu\nu} + \frac{5\tau_c^2}{3} \nabla_\mu \left[-J_{42}^{(1)+} \beta \dot{u}^\mu - \frac{J_{42}^{(1)+} \beta q B b^{\mu\nu} V_\nu}{\epsilon + P} \right].
\end{aligned}
$$

$$(A.22)$$

Needless to say, here we kept only terms upto the second-order. The remaining integral $\mathcal{I}_2$ is evaluated in a similar fashion,

$$
\begin{aligned}
\mathcal{I}_2 &= \frac{\Delta_{\alpha\beta}}{3} \int dp\, p^\alpha p^\beta \frac{\tau_c}{u \cdot p} q B b^{\mu\nu} p_\nu \frac{\partial}{\partial p^\mu} \left[\frac{\tau_c}{u \cdot p} p^\rho \partial_\rho f_0 \right], \\
&= -\frac{\Delta_{\alpha\beta}}{3} \int dp\, f_0 \tilde{f}_0 p^\alpha p^\beta \frac{\tau_c}{u \cdot p} q B b^{\mu\nu} p_\nu \frac{\partial}{\partial p^\mu} \left[\frac{\tau_c}{u \cdot p} p^\rho \left(p^\gamma \beta \partial_\rho u_\gamma + (u \cdot p) \partial_\rho \beta - \partial_\rho \alpha \right) \right], \\
&= -\frac{\Delta_{\alpha\beta}}{3} \tau_c^2 q B b_\nu^\mu \left(\beta J_{(2)-}^{\alpha\beta\nu\gamma} \nabla_\mu u_\gamma + \beta J_{(2)-}^{\alpha\beta\nu\rho} \partial_\rho u_\mu \right),
\end{aligned}
$$

$$(A.23)$$

using the expansion given in eq. (A.2) and the anti-symmetric property of $b^{\mu\nu}$ we get:

$$
\mathcal{I}_2 = -\frac{q B \tau_c^2}{3} \beta J_{42}^{(2)-} \left(5 b^{\mu\gamma} \nabla_\mu u_\gamma + 5 b^{\mu\rho} \nabla_\rho u_\mu \right) = 0.
$$

$$(A.24)$$

Finally using eqs. (A.20)-(A.22) and eq. (A.24) we have:

$$
\begin{aligned}
\Pi_{(2)} &= -\tau_c \dot{\Pi} + \frac{2\tau_c^2}{3h} J_{31}^{(0)-} \dot{u}_\alpha \nabla^\alpha \alpha - \frac{2\tau_c^2}{3} J_{21}^{(0)-} \dot{u}_\alpha \nabla^\alpha \alpha - \frac{2\tau_c^2 \beta}{3(\epsilon + P)} J_{31}^{(0)+} \dot{u}_\alpha q B b^{\alpha\beta} V_\beta \\
&\quad + \frac{5\tau_c^2 \beta}{9} \left(7 J_{63}^{(3)+} + \frac{23}{3} J_{42}^{(1)+} \right) \theta^2 + \frac{5\tau_c^2}{3} \left[\left(J_{31}^{(0)+} + J_{42}^{(1)+} \right) \dot{\beta} - \left(J_{31}^{(1)-} + J_{42}^{(2)-} \right) \dot{\alpha} \right] \theta \\
&\quad + \frac{\tau_c^2 \beta}{3} \left(7 J_{63}^{(3)+} + J_{42}^{(1)+} \right) \sigma^{\mu\nu} \sigma_{\mu\nu} + \frac{5\tau_c^2}{3} \nabla_\mu \left[\left(\frac{1}{h} J_{42}^{(1)-} - J_{42}^{(2)-} \right) \nabla^\mu \alpha \right] \\
&\quad - \frac{5\tau_c^2}{3} \nabla_\mu \left[\frac{J_{42}^{(1)+} \beta q B b^{\mu\nu} V_\nu}{\epsilon + P} \right].
\end{aligned}
\tag{A.25}
$$

eq. (A.25) is the second-order relaxation equation for the bulk-viscous stress.

A.2.3 Diffusion current

In this section we discuss the detail derivation of the diffusion current. From eq. (3.33) we get:

$$
V_{(2)}^\mu = \Delta_\alpha^\mu \int dp p^\alpha \left(\frac{\tau_c}{u \cdot p} p^\sigma \partial_\sigma \left[\frac{\tau_c}{u \cdot p} p^\rho \partial_\rho f_0 \right] + \frac{\tau_c}{u \cdot p} q F^{\sigma\nu} p_\nu \frac{\partial}{\partial p^\sigma} \left[\frac{\tau_c}{u \cdot p} p^\rho \partial_\rho f_0 \right] \right),
\tag{A.26}
$$

where

$$
\begin{aligned}
\mathcal{I}_1 &= \Delta_\alpha^\mu \int dp p^\alpha \frac{\tau_c}{u \cdot p} p^\sigma \partial_\sigma \left[\frac{\tau_c}{u \cdot p} p^\rho \partial_\rho f_0 \right], \\
\mathcal{I}_2 &= \Delta_\alpha^\mu \int dp p^\alpha \frac{\tau_c}{u \cdot p} q F^{\sigma\nu} p_\nu \frac{\partial}{\partial p^\sigma} \left[\frac{\tau_c}{u \cdot p} p^\rho \partial_\rho f_0 \right].
\end{aligned}
$$

Let us first calculate the $\mathcal{I}_1$ by breaking it up into three parts as: $\mathcal{I}_1 = \mathcal{A} + \mathcal{B} + \mathcal{C}$ where

$$
\begin{aligned}
\mathcal{A} &= \Delta_\alpha^\mu \int dp p^\alpha \tau_c D \left[\frac{\tau_c}{u \cdot p} p^\rho \partial_\rho f_0 \right], \\
\mathcal{B} &= \Delta_\alpha^\mu \int dp p^\alpha \frac{\tau_c}{u \cdot p} p^\sigma \nabla_\sigma \left(\tau_c \dot{f}_0 \right), \\
\mathcal{C} &= \Delta_\alpha^\mu \int dp p^\alpha \frac{\tau_c}{u \cdot p} p^\sigma \nabla_\sigma \left(\frac{\tau_c p^\rho}{u \cdot p} \nabla_\rho f_0 \right).
\end{aligned}
$$

For $\mathcal{A}$ we get:

$$
\begin{aligned}
\mathcal{A} &= -\Delta_\alpha^\mu \int dp f_0 \tilde{f}_0 p^\alpha \tau_c D \left[\frac{\tau_c}{u \cdot p} p^\rho \left(\beta p^\gamma \partial_\rho u_\gamma + (u \cdot p) \partial_\rho \beta - \partial_\rho \alpha \right) \right], \\
&= -\Delta_\alpha^\mu D \left[\int dp f_0 \tilde{f}_0 p^\alpha \tau_c \frac{\tau_c}{u \cdot p} p^\rho \left(\beta p^\gamma \partial_\rho u_\gamma + (u \cdot p) \partial_\rho \beta - \partial_\rho \alpha \right) \right], \\
&= -\tau_c \dot{V}^{\langle \mu \rangle} - \tau_c^2 \Delta_\gamma^\mu D \left[\frac{n_f q B b^{\gamma\nu} V_\nu}{\epsilon + P} \right].
\end{aligned}
\tag{A.27}
$$

We have used the thermodynamic integrals and its expansion given in the Appendix A.1, along with eqs. (3.9) and (3.9) to arrive at the final expression. Similarly for $\mathcal{B}$ we get:

$$
\begin{aligned}
\mathcal{B} &= \Delta_\alpha^\mu \int dp p^\alpha \frac{\tau_c}{u \cdot p} p^\sigma \nabla_\sigma \left(\tau_c \dot{f}_0 \right), \\
&= \Delta_\alpha^\mu \nabla_\sigma \left(\int dp p^\alpha \frac{\tau_c}{u \cdot p} p^\sigma \tau_c \dot{f}_0 \right) + \Delta_\alpha^\mu \nabla_\sigma u_\gamma \left(\int dp p^\alpha p^\gamma \frac{\tau_c}{(u \cdot p)^2} p^\sigma \tau_c \dot{f}_0 \right), \\
&= -\tau_c^2 \nabla^\mu \left(J_{21}^{(0)-} \dot{\beta} - J_{21}^{(1)+} \dot{\alpha} \right) - \tau_c^2 \beta \dot{u}^\mu \theta \left(\frac{4}{3} J_{21}^{(0)-} + \frac{5}{3} J_{42}^{(2)-} \right) - \tau_c^2 \beta J_{21}^{(0)-} \dot{u}_\gamma \omega^{\gamma\mu} \\
&\quad - \tau_c^2 \beta \dot{u}_\gamma \sigma^{\gamma\mu} \left(J_{21}^{(0)-} + 2 J_{42}^{(2)-} \right).
\end{aligned}
\tag{A.28}
$$

Lastly for $\mathcal{C}$ we get:

$$
\begin{aligned}
\mathcal{C} &= \Delta_\alpha^\mu \int dp p^\alpha \frac{\tau_c^2}{u \cdot p} p^\sigma \nabla_\sigma \left(\frac{p^\rho}{u \cdot p} \nabla_\rho f_0 \right), \\
&= \Delta_\alpha^\mu \nabla_\sigma \left(\int dp p^\alpha \frac{\tau_c^2}{u \cdot p} p^\sigma \frac{p^\rho}{u \cdot p} \nabla_\rho f_0 \right) + \Delta_\alpha^\mu \nabla_\sigma u_\gamma \left(\int dp p^\alpha p^\gamma \frac{\tau_c^2}{(u \cdot p)^2} p^\sigma \frac{p^\rho}{u \cdot p} \nabla_\rho f_0 \right).
\end{aligned}
$$

Substituting the expression for $\nabla_\rho f_0$ and using the usual thermodynamic integrals and their expansion along with eq. (3.9) and eq. (3.1) the above expression takes the following form:

$$
\begin{aligned}
\mathcal{C} = {}& -\frac{4\tau_c^2}{3}\left(\frac{J_{21}^{(0)+}n_f}{\epsilon+P} - J_{21}^{(1)+}\right)(\nabla^\mu\alpha)\,\theta + \frac{4\tau_c^2}{3}J_{21}^{(0)-}\beta\dot{u}^\mu\theta + \tau_c^2 J_{21}^{(0)-}\beta\dot{u}^\gamma\sigma_\gamma^\mu \\
& -\tau_c^2\left(\frac{J_{21}^{(0)+}n_f}{\epsilon+P} - J_{21}^{(1)+}\right)(\nabla^\gamma\alpha)\,\sigma_\gamma^\mu - \tau_c^2\left(\frac{J_{21}^{(0)+}n_f}{\epsilon+P} - J_{21}^{(1)+}\right)(\nabla^\gamma\alpha)\,\omega_\gamma^\mu + \tau_c^2 J_{21}^{(0)-}\beta\dot{u}^\gamma\omega_\gamma^\mu \\
& +\tau_c J_{21}^{(0)-}\omega_\gamma^\mu\left[\frac{\beta q B b^{\gamma\nu}V_\nu}{\epsilon+P}\right] - 2\tau_c^2\left(\frac{J_{42}^{(2)+}n_f}{\epsilon+P} - J_{42}^{(3)+}\right)(\nabla^\gamma\alpha)\,\sigma_\gamma^\mu + 2\tau_c^2 J_{42}^{(2)-}\beta\dot{u}^\gamma\sigma_\gamma^\mu \\
& -\frac{5\tau_c^2}{3}\left(\frac{J_{42}^{(2)+}n_f}{\epsilon+P} - J_{42}^{(3)+}\right)(\nabla^\mu\alpha)\,\theta + \frac{5\tau_c^2}{3}J_{42}^{(2)-}\beta\dot{u}^\mu\theta - 2\tau_c^2\Delta_\rho^\mu\nabla_\gamma\left(\beta J_{42}^{(2)-}\sigma^{\rho\gamma}\right) \\
& -\frac{5\tau_c^2}{3}\nabla^\mu\left[\beta J_{42}^{(2)-}\theta\right] + \frac{4\tau_c}{3}J_{21}^{(0)-}\theta\left[\frac{\beta q B b^{\mu\nu}V_\nu}{\epsilon+P}\right] + \tau_c J_{21}^{(0)-}\sigma_\gamma^\mu\left[\frac{\beta q B b^{\gamma\nu}V_\nu}{\epsilon+P}\right] \\
& +2\tau_c J_{42}^{(2)-}\sigma_\gamma^\mu\left[\frac{\beta q B b^{\gamma\nu}V_\nu}{\epsilon+P}\right] + \frac{5\tau_c}{3}J_{42}^{(2)-}\theta\left[\frac{\beta q B b^{\mu\nu}V_\nu}{\epsilon+P}\right].
\end{aligned}
\tag{A.29}
$$

Now let us calculate the integral $\mathcal{I}_2$:

$$
\begin{aligned}
\mathcal{I}_2 = {}& -\Delta_\alpha^\mu\int dp\, f_0\tilde{f}_0 p^\alpha\frac{\tau_c}{u\cdot p}qF^{\sigma\nu}p_\nu\frac{\partial}{\partial p^\sigma}\left[\frac{\tau_c}{u\cdot p}p^\rho\left(\beta p^\gamma\partial_\rho u_\gamma + (u\cdot p)\partial_\rho\beta - \partial_\rho\alpha\right)\right], \\
= {}& \tau_c^2 qB\left[\frac{1}{h}J_{21}^{(1)-}b^{\gamma\mu}\nabla_\gamma\alpha - J_{21}^{(2)-}b^{\gamma\mu}\nabla_\gamma\alpha - \frac{\beta J_{21}^{(1)+}b^{\gamma\mu}\Delta_\gamma^\sigma\partial^k\pi_{k\sigma}}{\epsilon+P} - \frac{\beta J_{21}^{(1)+}b^{\gamma\mu}\Pi\dot{u}_\gamma}{\epsilon+P}\right. \\
& \left. +\frac{\beta J_{21}^{(1)+}b^{\gamma\mu}\nabla_\gamma\Pi}{\epsilon+P}\right].
\end{aligned}
\tag{A.30}
$$

Adding eqs. (A.27)-(A.30) together we get the final expression for the diffusion current (which after simplification becomes eq.(3.34)) :

$$
\begin{aligned}
V_{(2)}^{\mu} = &-\tau_c \dot{V}^{\langle\mu\rangle} - \tau_c^2 \Delta_\gamma^\mu D \left[\frac{n_f q B b^{\gamma\nu} V_\nu}{\epsilon + P} \right] - \tau_c^2 \nabla^\mu \left(J_{21}^{(0)-} \dot{\beta} - J_{21}^{(1)+} \dot{\alpha} \right) - \tau_c^2 \beta \dot{u}^\mu \theta \left(\frac{4}{3} J_{21}^{(0)-} + \frac{5}{3} J_{42}^{(2)-} \right) \\
&- \tau_c^2 \beta J_{21}^{(0)-} \dot{u}_\gamma \omega^{\gamma\mu} - \tau_c^2 \beta \dot{u}_\gamma \sigma^{\gamma\mu} \left(J_{21}^{(0)-} + 2 J_{42}^{(2)-} \right) - \frac{4\tau_c^2}{3} \left(\frac{J_{21}^{(0)+} n_f}{\epsilon + P} - J_{21}^{(1)+} \right) (\nabla^\mu \alpha) \theta \\
&+ \frac{4\tau_c^2}{3} J_{21}^{(0)-} \beta \dot{u}^\mu \theta - \tau_c^2 \left(\frac{J_{21}^{(0)+} n_f}{\epsilon + P} - J_{21}^{(1)+} \right) (\nabla^\gamma \alpha) \sigma_\gamma^\mu + \tau_c^2 J_{21}^{(0)-} \beta \dot{u}^\gamma \sigma_\gamma^\mu + 2\tau_c^2 J_{42}^{(2)-} \beta \dot{u}^\gamma \sigma_\gamma^\mu \\
&- \tau_c^2 \left(\frac{J_{21}^{(0)+} n_f}{\epsilon + P} - J_{21}^{(1)+} \right) (\nabla^\gamma \alpha) \omega_\gamma^\mu + \tau_c^2 J_{21}^{(0)-} \beta \dot{u}^\gamma \omega_\gamma^\mu - 2\tau_c^2 \left(\frac{J_{42}^{(2)+} n_f}{\epsilon + P} - J_{42}^{(3)+} \right) (\nabla^\gamma \alpha) \sigma_\gamma^\mu \\
&- \frac{5\tau_c^2}{3} \left(\frac{J_{42}^{(2)+} n_f}{\epsilon + P} - J_{42}^{(3)+} \right) (\nabla^\mu \alpha) \theta + \frac{5\tau_c^2}{3} J_{42}^{(2)-} \beta \dot{u}^\mu \theta - 2\tau_c^2 \Delta_\rho^\mu \nabla_\gamma \left(\beta J_{42}^{(2)-} \sigma^{\rho\gamma} \right) \\
&- \frac{5\tau_c^2}{3} \nabla^\mu \left[\beta J_{42}^{(2)-} \theta \right] + \frac{4\tau_c}{3} J_{21}^{(0)-} \theta \left[\frac{\beta q B b^{\mu\nu} V_\nu}{\epsilon + P} \right] + \tau_c J_{21}^{(0)-} \sigma_\gamma^\mu \left[\frac{\beta q B b^{\gamma\nu} V_\nu}{\epsilon + P} \right] \\
&+ 2\tau_c J_{42}^{(2)-} \sigma_\gamma^\mu \left[\frac{\beta q B b^{\gamma\nu} V_\nu}{\epsilon + P} \right] + \frac{5\tau_c}{3} J_{42}^{(2)-} \theta \left[\frac{\beta q B b^{\mu\nu} V_\nu}{\epsilon + P} \right] + \tau_c J_{21}^{(0)-} \omega_\gamma^\mu \left[\frac{\beta q B b^{\gamma\nu} V_\nu}{\epsilon + P} \right] \\
&+ \tau_c^2 q B \left[\frac{J_{21}^{(1)-} b^{\gamma\mu}}{h} \nabla_\gamma \alpha - J_{21}^{(2)-} b^{\gamma\mu} \nabla_\gamma \alpha - \frac{\beta J_{21}^{(1)+} b^{\gamma\mu} \Delta_\gamma^\sigma \partial^k \pi_{k\sigma}}{\epsilon + P} - \frac{\beta J_{21}^{(1)+} b^{\gamma\mu} \Pi \dot{u}_\gamma}{\epsilon + P} \right. \\
&\left. + \frac{\beta J_{21}^{(1)+} b^{\gamma\mu} \nabla_\gamma \Pi}{\epsilon + P} \right] .
\end{aligned}
$$

$$
(A.31)
$$

A.3 Projection tensors

The definition of the second and fourth rank projection tensors used in the text is shown in this section.

A general antisymmetric second rank tensor $b_{\mu\nu}$ can be defined by

$$
b_{\mu\nu} \equiv \varepsilon_{\mu\lambda\nu} b^\lambda,
\tag{A.32}
$$

where b_μ is a unit axial four vector. The second rank projection tensors are then defined as

$$
\begin{aligned}
P^{(0)}_{\mu\nu} &= b_\mu b_\nu, \\
P^{(+1)}_{\mu\nu} &= \frac{1}{2}\left(\Delta_{\mu\nu} - b_\mu b_\nu - ib_{\mu\nu}\right), \\
P^{(-1)}_{\mu\nu} &= \frac{1}{2}\left(\Delta_{\mu\nu} - b_\mu b_\nu + ib_{\mu\nu}\right).
\end{aligned}
$$

where $i = \sqrt{-1}$. They satisfy the following properties

$$
P^{(\mathrm{m})}_{\mu\kappa} P^{(\mathrm{m}'),\kappa}_{\nu} = \delta_{\mathrm{mm}'} P^{(\mathrm{m})}_{\mu\nu}, \tag{A.33}
$$

$$
\left(P^{(\mathrm{m})}_{\mu\nu}\right)^{\dagger} = P^{(-\mathrm{m})}_{\mu\nu} = P^{(\mathrm{m})}_{\nu\mu}, \tag{A.34}
$$

$$
\sum_{\mathrm{m}=-1}^{1} P^{(\mathrm{m})}_{\mu\nu} = \Delta_{\mu\nu}, \quad P^{(\mathrm{m})}_{\mu\mu} = 1, \tag{A.35}
$$

where $\mathrm{m}, \mathrm{m}' = 0, \pm 1$. The projection tensors $P^{(\mathrm{m})}_{\mu\nu}$ satisfy the following eigenvalue equation (see ref. [20])

$$
P^{(\mathrm{m})}_{\mu\kappa} b^{\kappa}_{\nu} = i\mathrm{m} P^{(\mathrm{m})}_{\mu\nu}, \tag{A.36}
$$

where m is the eigenvalue. Also $b_{\mu\nu}$ can be represented as a linear combination of the projection tensors

$$
b_{\mu\nu} = \sum_{\mathrm{m}=-1}^{1} i\mathrm{m} P^{(\mathrm{m})}_{\mu\nu}. \tag{A.37}
$$

It is also easy to generalize them to the fourth rank projection tensor which are defined in terms of the second rank projection tensor as

$$
P^{(\mathrm{m})}_{\mu\nu,\mu'\nu'} = \sum_{\mathrm{m}_1=-1}^{1} \sum_{\mathrm{m}_2=-1}^{1} P^{(\mathrm{m}_1)}_{\mu\mu'} P^{(\mathrm{m}_2)}_{\nu\nu'} \delta\left(\mathrm{m}, \mathrm{m}_1 + \mathrm{m}_2\right), \tag{A.38}
$$

where $\delta\left(\mathrm{m}, \mathrm{m}_1 + \mathrm{m}_2\right) = 1$ for $\mathrm{m} = \mathrm{m}_1 + \mathrm{m}_2$ and zero otherwise. Notice that $\mathrm{m}_1 + \mathrm{m}_2$ assumes the five values $\mathrm{m} = -2, -1, 0, 1, 2$ which in turn result in the five shear viscous coefficients dicussed in the text. A generalization to higher ranks is also possible using the above basis if need arises.

A.4 General expressions of transport coefficients

$\tau_{\pi\pi}$	$\frac{2\beta}{\beta_\pi}\left(2J_{63}^{(3)+} + J_{42}^{(1)+}\right)$
$\delta_{\pi\pi}$	$\frac{\beta}{3\beta_\pi}\left(7J_{63}^{(3)+} + 5J_{42}^{(1)+}\right)$
$\lambda_{\pi\Pi}$	$\frac{2}{\beta_\Pi}\left[\left(J_{31}^{(0)+} + J_{42}^{(1)+}\right)\mathcal{X} - \left(J_{31}^{(1)-} + J_{42}^{(2)-}\right)\mathcal{Y} + \frac{\beta}{3}\left(7J_{63}^{(3)+} + 5J_{42}^{(1)+}\right)\right]$
$l_{\pi V}$	$\frac{2}{\beta_V}\left(J_{42}^{(2)-} - \frac{n_f}{\epsilon+P}J_{42}^{(1)-}\right)$
$\delta_{\pi B}$	$2J_{42}^{(2)-}/J_{42}^{(1)+}$
$\delta_{\pi VB}$	$2\beta J_{42}^{(1)+}/(\epsilon + P)$

Table A.1: Transport coefficients appearing in shear-stress equation eq. (3.30).

$\delta_{\Pi\Pi}$	$\frac{5}{3\beta_\Pi}\left[(J_{31}^{(0)+} + J_{42}^{(1)+})\mathcal{X} - (J_{31}^{(1)-} + J_{42}^{(2)-})\mathcal{Y} + \frac{\beta}{3}(7J_{63}^{(3)+} + \frac{23}{3}J_{42}^{(1)+})\right]$
$\lambda_{\Pi\pi}$	$\frac{\beta}{3\beta_\pi}\left(7J_{63}^{(3)+} + J_{42}^{(1)+}\right)$
$l_{\Pi V}$	$\frac{5}{3\beta_V}\left(J_{42}^{(2)-} - \frac{n_f}{\epsilon+P}J_{42}^{(1)-}\right)$
$\delta_{\Pi VB}$	$\frac{5J_{42}^{(1)+}\beta}{3(\epsilon+P)}$

Table A.2: Transport coefficients appearing in bulk equation eq. (3.32).

λ_{VV}	$1 + \frac{2}{\beta_V}\left(\frac{n_f}{\epsilon+P}J_{42}^{(2)+} - J_{42}^{(3)+}\right)$
δ_{VV}	$\frac{4}{3} + \frac{5}{3\beta_V}\left(\frac{n_f J_{42}^{(2)+}}{\epsilon+P} - J_{42}^{(3)+}\right)$
$l_{V\pi}$	$-\frac{\beta}{\beta_\pi}J_{42}^{(2)-}$
$\tau_{V\pi}$	$-\beta\frac{\partial}{\partial\beta}l_{V\pi}$
$\lambda_{V\pi}$	$-\frac{1}{h}\frac{\partial}{\partial\beta}l_{V\pi}$
$l_{V\Pi}$	$-\frac{1}{\beta_\Pi}\left(\mathcal{X}J_{21}^{(0)-} - \mathcal{Y}J_{21}^{(1)+} + \frac{5\beta}{3}J_{42}^{(1)-}\right)$
δ_{VB}	$-\left(\frac{n_f J_{21}^{(1)-}}{\epsilon+P} - J_{21}^{(2)-}\right)/\beta_V$
$l_{V\pi B}$	$-\beta J_{21}^{(1)+}/(\epsilon+P)$
$\tau_{V\Pi B}$	$-\beta J_{21}^{(1)+}/(\epsilon+P)$
$l_{V\Pi B}$	$-\beta J_{21}^{(1)+}/(\epsilon+P)$
λ_{VVB}	$-\frac{\beta}{\epsilon+P}\left(J_{21}^{(0)-} + 2J_{42}^{(2)-}\right)$
ρ_{VVB}	$-\beta J_{21}^{(0)-}/(\epsilon+P)$
τ_{VVB}	$n_f/(\epsilon+P)$

Table A.3: Transport coefficients appearing in diffusion equation eq. (3.34).

A.5 Second order relaxation equations for resistive case

Here we give the detailed calculations of the second order dissipative quantities. The explicit dependence of the anti-particles is not shown in the calculation, but they appear in our

final results.

A.5.1 Bulk stress

Let us consider the bulk viscous case first. From Eq. (3.63) we get:

$$\Pi = -\frac{\Delta_{\alpha\beta}}{3} \int dp p^\alpha p^\beta \left(\delta f^{(2)} + \delta \bar{f}^{(2)} \right), \tag{A.39}$$

$$\Pi = \mathcal{I}_1 + \mathcal{I}_2 + \mathcal{I}_3 + \mathcal{I}_4. \tag{A.40}$$

For convenience we split $\mathcal{I}_1$ into three terms as follows:

$$\mathcal{I}_1 = \mathcal{A} + \mathcal{B} + \mathcal{C}, \tag{A.41}$$

where

$$\mathcal{A} = -\frac{\Delta_{\alpha\beta}}{3} \int dp p^\alpha p^\beta \tau_c D \left[\frac{\tau_c}{u \cdot p} p^\rho \partial_\rho f_0 \right],$$

$$\mathcal{B} = -\frac{\Delta_{\alpha\beta}}{3} \int dp p^\alpha p^\beta \frac{\tau_c}{u \cdot p} p^\mu \nabla_\mu \left(\tau_c \dot{f}_0 \right),$$

$$\mathcal{C} = -\frac{\Delta_{\alpha\beta}}{3} \int dp p^\alpha p^\beta \frac{\tau_c}{u \cdot p} p^\mu \nabla_\mu \left(\frac{\tau_c p^\rho}{u \cdot p} \nabla_\rho f_0 \right).$$

We carry out these integrals one-by-one and we get:

$$\begin{aligned}
\mathcal{A} &= -\tau_c \dot{\Pi} + \frac{2\tau_c^2}{3h} J_{31}^{(0)+} \dot{u}_\alpha \nabla^\alpha \alpha - \frac{2\tau_c^2}{3} J_{21}^{(0)-} \dot{u}_\alpha \nabla^\alpha \alpha \\
&\quad - \frac{2\tau_c^2 \beta}{3h} J_{31}^{(0)+} \dot{u}_\alpha q B b^{\alpha\beta} V_\beta + \frac{2\tau_c^2 \beta}{3(\epsilon + P)} J_{31}^{(0)+} \dot{u}_\alpha q E^\alpha, \\
\mathcal{B} &= \frac{5\tau_c^2}{3} \nabla_\mu \left(\beta J_{42}^{(1)+} \dot{u}^\mu \right) + \frac{5\tau_c^2}{3} \theta \left[\left(J_{31}^{(0)+} + J_{42}^{(1)+} \right) \dot{\beta} - \left(J_{31}^{(1)-} + J_{42}^{(2)-} \right) \dot{\alpha} \right], \\
\mathcal{C} &= \frac{5\tau_c^2 \beta}{9} \left(7 J_{63}^{(3)+} + \frac{23}{3} J_{42}^{(1)+} \right) \theta^2 + \frac{5\tau_c^2}{3} \nabla_\mu \left[\nabla^\mu \alpha \left(\frac{1}{h} J_{42}^{(1)-} - J_{42}^{(2)-} \right) \right] \\
&\quad + \frac{\tau_c^2 \beta}{3} \left(7 J_{63}^{(3)+} + J_{42}^{(1)+} \right) \sigma^{\mu\nu} \sigma_{\mu\nu} + \frac{5\tau_c^2}{3} \nabla_\mu \left[-J_{42}^{(1)+} \beta \dot{u}^\mu - \frac{J_{42}^{(1)+} \beta q B b^{\mu\nu} V_\nu}{\epsilon + P} \right] \\
&\quad + \frac{5\tau_c^2}{3} \nabla_\mu \left[\frac{J_{42}^{(1)-} \beta q E^\mu}{h} \right]. \tag{A.42}
\end{aligned}$$

For the rest three terms after some algebra we get:

$$
\begin{aligned}
\mathcal{I}_2 &= -\frac{2}{3}\tau_c^2 q\beta E_\mu J_{31}^{(1)-}\dot{u}^\mu - \frac{5}{3}\tau_c^2 q\nabla_\mu(\beta J_{42}^{(2)-}E^\mu), \\
\mathcal{I}_3 &= -q\tau_c^2\Big[\frac{1}{3h}\left(5J_{42}^{(2)-} + 2J_{31}^{(1)-} - 5J_{42}^{(3)+} - 2J_{31}^{(2)+}\right)E^\mu\nabla_\mu\alpha + \frac{q\beta}{3h}\left(5J_{42}^{(2)-} + 2J_{31}^{(1)-}\right)E^\mu E_\mu \\
&\quad + \frac{q\beta}{3hn_f}\left(5J_{42}^{(2)-} + 2J_{31}^{(1)-}\right)E^\mu B_{\mu\nu}V_f^\nu\Big], \\
\mathcal{I}_4 &= \frac{q^2\tau_c^2}{3}\left(5\beta J_{42}^{(3)+} + 2\beta J_{31}^{(2)+}\right)E_\mu E^\mu.
\end{aligned}
\tag{A.43}
$$

A.5.2 Diffusion

The second order diffusion current $V_{(2)}^\mu$ is given by Eq. (3.66):

$$
\begin{aligned}
V_{(2)}^\mu &= \Delta_\alpha^\mu \int dp\, p^\alpha \left(\delta f^{(2)} - \delta\bar{f}^{(2)}\right), \\
V_{(2)}^\mu &= \mathcal{I}_1 + \mathcal{I}_2 + \mathcal{I}_3 + \mathcal{I}_4.
\end{aligned}
\tag{A.44}
$$

Like the previous case we split $\mathcal{I}_1$ into three terms as follows:

$$
\mathcal{I}_1 = \mathcal{A} + \mathcal{B} + \mathcal{C},
\tag{A.45}
$$

where

$$
\begin{aligned}
\mathcal{A} &= \Delta_\alpha^\mu \int dp\, p^\alpha \tau_c D\left[\frac{\tau_c}{u\cdot p}p^\rho\partial_\rho f_0\right], \\
\mathcal{B} &= \Delta_\alpha^\mu \int dp\, p^\alpha \frac{\tau_c}{u\cdot p}p^\sigma\nabla_\sigma\left(\tau_c\dot{f}_0\right), \\
\mathcal{C} &= \Delta_\alpha^\mu \int dp\, p^\alpha \frac{\tau_c}{u\cdot p}p^\sigma\nabla_\sigma\left(\frac{\tau_c p^\rho}{u\cdot p}\nabla_\rho f_0\right).
\end{aligned}
$$

After integrating we have:

$$
\mathcal{A} = -\tau_c \dot{V}^{\langle \mu \rangle} - \tau_c^2 \Delta_\gamma^\mu D \left[\frac{q n_f B b^{\gamma\nu} V_\nu}{\epsilon + P} \right] - \Delta_\nu^\mu D \left[q\beta \tau_c^2 E^\nu J_{21}^{(1)-} \right],
$$

$$
\mathcal{B} = -\tau_c^2 \nabla^\mu \left(J_{21}^{(0)-} \dot{\beta} - J_{21}^{(1)+} \dot{\alpha} \right) - \frac{\tau_c^2 \beta \dot{u}^\mu \theta}{3} \left(4 J_{21}^{(0)-} + 5 J_{42}^{(2)-} \right) - \tau_c^2 \beta J_{21}^{(0)-} \dot{u}_\gamma \omega^{\gamma\mu}
$$
$$
\qquad - \tau_c^2 \beta \dot{u}_\gamma \sigma^{\gamma\mu} \left(J_{21}^{(0)-} + 2 J_{42}^{(2)-} \right),
$$

$$
\mathcal{C} = -\frac{4\tau_c^2}{3} \theta \left(\frac{1}{h} J_{21}^{(0)+} - J_{21}^{(1)+} \right) \nabla^\mu \alpha + \frac{4\tau_c^2}{3} J_{21}^{(0)-} \beta \dot{u}^\mu \theta - \tau_c^2 \left(\frac{1}{h} J_{21}^{(0)+} - J_{21}^{(1)+} \right) \sigma_\gamma^\mu \nabla^\gamma \alpha
$$
$$
\qquad + \tau_c^2 J_{21}^{(0)-} \beta \dot{u}^\gamma \sigma_\gamma^\mu - \tau_c^2 \left(\frac{1}{h} J_{21}^{(0)+} - J_{21}^{(1)+} \right) \omega_\gamma^\mu \nabla^\gamma \alpha + \tau_c^2 J_{21}^{(0)-} \beta \dot{u}^\gamma \omega_\gamma^\mu
$$
$$
\qquad + \tau_c J_{21}^{(0)-} \omega_\gamma^\mu \left[\frac{\beta q B b^{\gamma\nu} V_\nu}{\epsilon + P} \right] - 2\tau_c^2 \left(\frac{1}{h} J_{42}^{(2)+} - J_{42}^{(3)+} \right) \sigma_\gamma^\mu \nabla^\gamma \alpha
$$
$$
\qquad + 2\tau_c^2 J_{42}^{(2)-} \beta \dot{u}^\gamma \sigma_\gamma^\mu - \frac{5\tau_c^2}{3} \theta \left(\frac{1}{h} J_{42}^{(2)+} - J_{42}^{(3)+} \right) \nabla^\mu \alpha + \frac{5\tau_c^2}{3} J_{42}^{(2)-} \beta \dot{u}^\mu \theta
$$
$$
\qquad - 2\tau_c^2 \Delta_\rho^\mu \nabla_\gamma \left(\beta J_{42}^{(2)-} \sigma^{\rho\gamma} \right) - \frac{5\tau_c^2}{3} \nabla^\mu \left(\beta J_{42}^{(2)-} \theta \right)
$$
$$
\qquad + \frac{4\tau_c^2}{3} J_{21}^{(0)-} \theta \left[\frac{\beta q B b^{\mu\nu} V_\nu}{\epsilon + P} \right] + \tau_c^2 J_{21}^{(0)-} \sigma_\gamma^\mu \left[\frac{\beta q B b^{\gamma\nu} V_\nu}{\epsilon + P} \right]
$$
$$
\qquad + 2\tau_c^2 J_{42}^{(2)-} \sigma_\gamma^\mu \left[\frac{\beta q B b^{\gamma\nu} V_\nu}{\epsilon + P} \right] + \frac{5\tau_c^2}{3} J_{42}^{(2)-} \theta \left[\frac{\beta q B b^{\mu\nu} V_\nu}{\epsilon + P} \right]
$$
$$
\qquad - \tau_c^2 \left(\frac{4}{3} J_{31}^{(1)+} + \frac{5}{3} J_{42}^{(2)+} \right) \theta \left(\frac{q\beta n_f E^\mu}{\epsilon + P} \right)
$$
$$
\qquad - 2\tau_c^2 J_{42}^{(2)+} \sigma_\gamma^\mu \left(\frac{q\beta n_f E^\gamma}{\epsilon + P} \right) - \tau_c^2 J_{31}^{(1)+} \left(\omega_\gamma^\mu + \sigma_\gamma^\mu \right) \frac{q\beta n_f E^\gamma}{\epsilon + P}. \tag{A.46}
$$

The rest of the terms give:

$$
\mathcal{I}_2 = q\tau_c^2 D \left(\beta J_{21}^{(1)+} E^\mu \right) + q\tau_c^2 \beta J_{21}^{(1)+} E^\alpha u^\mu \dot{u}_\alpha + q\tau_c^2 \beta J_{31}^{(2)+} \left(E_\nu \left(\omega^{\nu\mu} + \sigma^{\nu\mu} + \frac{\Delta^{\nu\mu}}{3} \theta \right) + E^\mu \theta \right)
$$
$$
\qquad + q\tau_c^2 \beta J_{42}^{(3)+} \left(E^\mu \theta + 2 E_\rho \left(\sigma^{\mu\rho} + \frac{\Delta^{\mu\rho}}{3} \theta \right) \right),
$$

$$
\mathcal{I}_3 = q\tau_c^2 \left(\beta J_{31}^{(2)+} B^{\mu\nu} \left(\frac{1}{\epsilon + P} \left[\frac{n_f}{\beta} (\nabla_\nu \alpha) - \Pi \dot{u}_\nu + \nabla_\nu \Pi - \Delta_{\nu\mu} \partial_\rho \pi^{\rho\mu} + q n_f E_\nu - q B b_\nu^\mu V_{f\mu} \right] \right) \right)
$$
$$
\qquad + q\tau_c^2 \left(\beta J_{31}^{(2)+} E^\mu \theta + J_{20}^{(1)+} E^\mu \dot{\beta} \right) + q\tau_c^2 \left(-J_{20}^{(2)+} E^\mu \dot{\alpha} - J_{21}^{(2)+} B_\nu^\mu \nabla^\nu \alpha \right)
$$
$$
\qquad + q\tau_c^2 \left(\beta E_\nu J_{42}^{(3)+} \left(2\sigma^{\mu\nu} + \frac{5}{3} \Delta^{\mu\nu} \theta \right) + E^\mu J_{31}^{(2)+} \dot{\beta} \right) - q\tau_c^2 \left(E^\mu J_{31}^{(3)+} \dot{\alpha} \right),
$$

$$
\mathcal{I}_4 = -\beta q^2 \tau_c^2 J_{21}^{(2)-} E^\nu B_\nu^\mu. \tag{A.47}
$$

A.5.3 Shear stress

The second order shear stress $\pi^{\mu\nu}_{(2)}$ is given by Eq. (3.69):

$$
\begin{aligned}
\pi^{\mu\nu}_{(2)} &= \Delta^{\mu\nu}_{\alpha\beta} \int dp p^\alpha p^\beta \left(\delta f^{(2)} + \delta \bar{f}^{(2)} \right) \\
&= \mathcal{I}_1 + \mathcal{I}_2 + \mathcal{I}_3 + \mathcal{I}_4.
\end{aligned} \tag{A.48}
$$

Again the first term can be divided into three parts and is given by :

$$
\mathcal{I}_1 = \mathcal{A} + \mathcal{B} + \mathcal{C}, \tag{A.49}
$$

where

$$
\begin{aligned}
\mathcal{A} &= \Delta^{\mu\nu}_{\alpha\beta} \int dp p^\alpha p^\beta \tau_c D \left[\frac{\tau_c}{u \cdot p} p^\sigma \partial_\sigma f_0 \right], \\
\mathcal{B} &= \Delta^{\mu\nu}_{\alpha\beta} \int dp p^\alpha p^\beta \frac{\tau_c}{u \cdot p} p^\rho \nabla_\rho \left[\tau_c \dot{f}_0 \right], \\
\mathcal{C} &= \Delta^{\mu\nu}_{\alpha\beta} \int dp p^\alpha p^\beta \frac{\tau_c}{u \cdot p} p^\rho \nabla_\rho \left[\frac{\tau_c}{u \cdot p} p^\sigma \nabla_\sigma f_0 \right].
\end{aligned}
$$

$$
\begin{aligned}
\mathcal{A} &= -\tau_c \dot{\pi}^{\langle\mu\nu\rangle} - 2\tau_c^2 \left(\frac{n_f}{\epsilon + P} J^{(0)-}_{31} - J^{(1)-}_{31} \right) \dot{u}^{\langle\mu} \nabla^{\nu\rangle} \alpha + \tau_c^2 \Delta^{\mu\nu}_{\alpha\beta} J^{(0)+}_{31} \dot{u}^\beta \left[\frac{\beta q B b^{\alpha\sigma}}{\epsilon + P} V_\sigma \right] \\
&\quad + \tau_c^2 \Delta^{\mu\nu}_{\alpha\beta} J^{(0)+}_{31} \dot{u}^\alpha \left[\frac{\beta q B b^{\beta\sigma}}{\epsilon + P} V_\sigma \right] - \tau_c^2 \Delta^{\mu\nu}_{\alpha\beta} J^{(0)-}_{31} \dot{u}^\beta \left[\frac{q \beta E^\alpha n_f}{\epsilon + P} \right] - \tau_c^2 \Delta^{\mu\nu}_{\alpha\beta} J^{(0)-}_{31} \dot{u}^\alpha \left[\frac{q \beta E^\beta n_f}{\epsilon + P} \right], \\
\mathcal{B} &= -2\tau_c^2 \left[\left(J^{(0)+}_{31} + J^{(1)+}_{42} \right) \dot{\beta} - \left(J^{(1)-}_{31} + J^{(2)-}_{42} \right) \dot{\alpha} \right] \sigma^{\mu\nu} - 2\tau_c^2 \nabla^{\langle\mu} \left(\dot{u}^{\nu\rangle} \beta J^{(1)+}_{42} \right), \\
\mathcal{C} &= 2\nabla^{\langle\mu} \left(\dot{u}^{\nu\rangle} \beta \tau_c^2 J^{(1)+}_{42} \right) + 2\nabla^{\langle\mu} \left[\nabla^{\nu\rangle} \alpha \tau_c^2 \left(J^{(2)-}_{42} - \frac{1}{h} J^{(1)-}_{42} \right) \right] - 4\beta \tau_c^2 \left(2 J^{(3)+}_{63} + J^{(1)+}_{42} \right) \sigma^{\langle\mu}_\rho \sigma^{\nu\rangle\rho} \\
&\quad - \frac{20}{3} \beta \tau_c^2 J^{(1)+}_{42} \theta \sigma^{\mu\nu} - \frac{28}{3} \beta \tau_c^2 J^{(3)+}_{63} \theta \sigma^{\mu\nu} - 4\beta \tau_c^2 \left(J^{(1)+}_{42} + 2 J^{(3)+}_{63} \right) \sigma^{\langle\mu\rho} \omega^{\nu\rangle}_\rho \\
&\quad + 2\tau_c^2 \nabla^{\langle\mu} \left[J^{(1)+}_{42} \left(\frac{\beta q B b^{\nu\rangle\gamma} V_\gamma}{\epsilon + P} \right) \right] - 2\tau_c^2 \nabla^{\langle\mu} \left[J^{(1)-}_{42} \left(\frac{\beta q E^{\nu\rangle} n_f}{\epsilon + P} \right) \right]. \tag{A.50}
\end{aligned}
$$

The rest of the terms give:

$$\mathcal{I}_2 = q\tau_c^2\beta J_{31}^{(1)-}\Delta_{\alpha\beta}^{\mu\nu}\left(E^\alpha\dot{u}^\beta + E^\beta\dot{u}^\alpha\right) + \nabla^{\langle\mu}\left(q\tau_c^2\beta E^{\nu\rangle}J_{42}^{(2)-}\right),$$

$$\mathcal{I}_3 = \Delta_{\alpha\beta}^{\mu\nu}q\tau_c^2\left(J_{31}^{(1)-}\left(\dot{\beta}\left(B^{\alpha\beta} + B^{\beta\alpha}\right) + E^\beta\nabla^\alpha\beta + E^\alpha\nabla^\beta\beta\right)\right)$$
$$+\Delta_{\alpha\beta}^{\mu\nu}q\tau_c^2\left(J_{42}^{(2)-}\left(E^\beta\nabla^\alpha\beta + E^\alpha\nabla^\beta\beta\right) + \beta J_{41}^{(2)-}E^\alpha\dot{u}^\beta\right)$$
$$+\Delta_{\alpha\beta}^{\mu\nu}q\tau_c^2\left(\beta J_{42}^{(2)-}\left(\theta B^{\alpha\beta} + B_\nu^\alpha\nabla^\beta u^\nu + B_\nu^\alpha\nabla^\nu u^\beta\right)\right)$$
$$+\Delta_{\alpha\beta}^{\mu\nu}q\tau_c^2\left(\beta J_{41}^{(2)-}E^\beta\dot{u}^\alpha + \beta J_{42}^{(2)-}\left(\theta B^{\beta\alpha} + B_\nu^\beta\nabla^\alpha u^\nu + B_\nu^\beta\nabla^\nu u^\alpha\right)\right)$$
$$-\Delta_{\alpha\beta}^{\mu\nu}q\tau_c^2\ J_{31}^{(2)-}\left(\dot{\alpha}B^{\alpha\beta} + E^\alpha\nabla^\beta\alpha + \dot{\alpha}B^{\beta\alpha} + E^\beta\nabla^\alpha\alpha\right)$$
$$+\Delta_{\alpha\beta}^{\mu\nu}q\tau_c^2\beta J_{52}^{(3)-}\left(E^\beta\dot{u}^\alpha + E^\alpha\dot{u}^\beta\right) - \Delta_{\alpha\beta}^{\mu\nu}q\tau_c^2 J_{42}^{(3)-}\left(E^\alpha\nabla^\beta\alpha + E^\beta\nabla^\alpha\alpha\right),$$

$$\mathcal{I}_4 = -2\Delta_{\alpha\beta}^{\mu\nu}q^2\tau_c^2\beta E^\alpha E^\beta\left(J_{42}^{(3)+} + J_{31}^{(2)+}\right).$$

A.6   General expressions of transport coefficients

$\tau_{\Pi V}$	$-\beta \frac{\partial}{\partial \beta} \left[\frac{5}{3\beta_V} \left(J_{42}^{(2)-} - \frac{n_f}{\epsilon+P} J_{42}^{(1)-} \right) \right]$ $-$ $\left[\frac{2}{3\beta_V} \left(\frac{J_{31}^{(0)-}}{h} - J_{31}^{(1)-} \right) - \beta \frac{\partial}{\partial \beta} \left(\frac{5}{3h\beta_V} J_{42}^{(1)-} - \frac{5}{3\beta_V} J_{42}^{(2)-} \right) \right]$
$\lambda_{\Pi V}$	$\left(\frac{\partial}{\partial \alpha} + h^{-1} \frac{\partial}{\partial \beta} \right) \left[\frac{5}{3\beta_V} \left(J_{42}^{(2)-} - \frac{n_f}{\epsilon+P} J_{42}^{(1)-} \right) \right]$ $-$ $\frac{1}{3\beta\beta_V} \left(5 J_{42}^{(3)+} - \frac{5}{h} J_{42}^{(2)-} + 2 J_{31}^{(2)+} - \frac{2}{h} J_{31}^{(1)-} \right)$ $-$ $\left(\frac{\partial}{\partial \alpha} + h^{-1} \frac{\partial}{\partial \beta} \right) \left[\frac{5}{3h\beta_V} J_{42}^{(1)-} - \frac{5}{3\beta_V} J_{42}^{(2)-} \right]$
$l_{\Pi V}$	$\frac{5}{3\beta_V} \left(J_{42}^{(2)-} - \frac{n_f}{\epsilon+P} J_{42}^{(1)-} \right) - \frac{1}{\beta\beta_V} \left[\frac{5\beta}{3h} J_{42}^{(1)-} - \frac{5}{3}\beta J_{42}^{(2)-} \right]$
$\lambda_{\Pi V B}$	$\frac{1}{\beta_V} \left(\frac{\partial}{\partial \alpha} + h^{-1} \frac{\partial}{\partial \beta} \right) \left[\frac{5 J_{42}^{(1)+} \beta}{3(\epsilon+P)} \right] + \frac{1}{\beta_V} \left[\frac{-1}{3(\epsilon+p)} \left(5 J_{42}^{(2)-} + 2 J_{31}^{(1)-} \right) \right]$
$\chi_{\Pi E E}$	$\frac{-\beta}{3} \left(5 J_{42}^{(3)+} + 2 J_{31}^{(2)+} - \frac{5}{h} J_{42}^{(2)+} - \frac{2}{h} J_{31}^{(1)+} \right)$

Table A.4: Transport coefficients appearing in bulk-stress equation Eq. (3.65).

λ_{VV}	$-\left(1 + \frac{2}{\beta_V}\left(\frac{n_f}{\epsilon+P}J_{42}^{(2)+} - J_{42}^{(3)+}\right) - \frac{1}{\beta_V}\left\{\left(J_{31}^{(2)+} + 4J_{42}^{(3)+}\right) - \frac{1}{h}\left(2J_{42}^{(2)+} + J_{31}^{(1)+}\right)\right\}\right)$
δ_{VV}	$\frac{4}{3} + \frac{5}{3\beta_V}\left(\frac{n_f J_{42}^{(2)+}}{\epsilon+P} - J_{42}^{(3)+}\right) + \frac{1}{\beta\beta_V}\left[\frac{\beta}{h}\left(\frac{4}{3}J_{31}^{(1)+} + \frac{5}{3}J_{42}^{(2)+}\right)\right] -$ $\frac{1}{\beta\beta_V}\left[\beta\left(\frac{7}{3}J_{31}^{(2)+} + \frac{10}{3}J_{42}^{(3)+}\right) - \left(J_{20}^{(1)+} + J_{21}^{(1)+}\right)\mathcal{X} - \left(J_{20}^{(2)+} + J_{21}^{(2)+}\right)\mathcal{Y}\right]$
δ_{VB}	$\left(\frac{n_f J_{21}^{(1)-}}{\epsilon+P} - J_{21}^{(2)-}\right)/\beta_V + \frac{1}{\beta_V}\left(\frac{J_{21}^{(1)-}}{h} - J_{21}^{(2)-}\right)$
χ_{VE}	$\beta\beta_V$
ρ_{VE}	$-\left(\frac{n_f}{D_{20}}\left[\left(J_{20}^{(0)+}\frac{\partial\chi_{VE}}{\partial\alpha} + J_{10}^{(0)+}\frac{\partial\chi_{VE}}{\partial\beta}\right)h - \left(J_{30}^{(0)+}\frac{\partial\chi_{VE}}{\partial\alpha} + J_{20}^{(0)+}\frac{\partial\chi_{VE}}{\partial\beta}\right)\right]\right)$

Table A.5: Transport coefficients appearing in Diffusion evolution equation Eq. (3.68).

$\tau_{\pi V}$	$\beta\frac{\partial}{\partial\beta}\left[\frac{2}{\beta_V}\left(J_{42}^{(2)-} - \frac{n_f}{\epsilon+P}J_{42}^{(1)-}\right)\right] - \frac{2}{\beta_V}\left[J_{31}^{(1)-} - \frac{J_{31}^{(0)-}}{h}\right] -$ $\beta\frac{\partial}{\partial\beta}\frac{1}{\chi_{VE}}\left[-\beta J_{42}^{(2)-} + 2J_{42}^{(1)-}\left(\frac{\beta}{h}\right)\right]$
$\lambda_{\pi V}$	$\left(\frac{\partial}{\partial\alpha} + h^{-1}\frac{\partial}{\partial\beta}\right)\left[\frac{2}{\beta_V}\left(J_{42}^{(2)-} - \frac{n_f}{\epsilon+P}J_{42}^{(1)-}\right)\right] + \frac{2}{h\beta\beta_V}\left(J_{31}^{(1)-} + J_{42}^{(2)-}\right) -$ $\frac{2}{\beta\beta_V}\left(J_{31}^{(2)-} + J_{42}^{(3)-}\right) - \left(\frac{\partial}{\partial\alpha} + h^{-1}\frac{\partial}{\partial\beta}\right)\frac{1}{\chi_{VE}}\left[-\beta J_{42}^{(2)-} + 2J_{42}^{(1)-}\left(\frac{\beta}{h}\right)\right]$
$l_{\pi V}$	$-\frac{2}{\beta_V}\left(J_{42}^{(2)-} - \frac{n_f}{\epsilon+P}J_{42}^{(1)-}\right) + \frac{1}{\chi_{VE}}\left[-\beta J_{42}^{(2)-} + 2J_{42}^{(1)-}\left(\frac{\beta}{h}\right)\right]$
$\lambda_{\pi VB}$	$\frac{1}{\beta_V}\left(\frac{\partial}{\partial\alpha} + h^{-1}\frac{\partial}{\partial\beta}\right)\left[2\beta J_{42}^{(1)+}/(\epsilon+P)\right] + \frac{1}{\beta\beta_V}\left[-\frac{2\beta}{(\epsilon+P)}\left(J_{31}^{(1)-} + J_{42}^{(2)-}\right)\right]$
$\chi_{\pi EE}$	$2\beta\left(\frac{\left(J_{31}^{(1)-} + J_{42}^{(2)-}\right)}{h} - \left(J_{42}^{(3)+} + J_{31}^{(2)+}\right)\right)$

Table A.6: Transport coefficients appearing in shear-stress evolution equation Eq. (3.71).

Appendix B

(Chapter-6)

B.1   Formulas and Conversions used in Chapter-6

In Chapter 6 of the thesis, we have used the Milne coordinate system (τ, η, r, ϕ), where

$$\tau = \sqrt{t^2 - z^2},$$

$$r = \sqrt{x^2 + y^2},$$

$$\eta = \tanh^{-1}(z/t),$$

$$\phi = \tan^{-1}(y/x).$$

Due to the coordinate transformation, various equations changed forms compared to the Cartesian coordinates. Here, we give the details about the Jacobian and Christoffel symbols used in this study due to the above coordinate transformation: the Jacobian for the volume element is $\sqrt{-g} = \tau r$, and the non-vanishing Christoffel symbols are

$$\Gamma^{\tau}_{\eta\eta} = \tau, \qquad\qquad \Gamma^{\eta}_{\tau\eta} = \frac{1}{\tau},$$

$$\Gamma^{r}_{\phi\phi} = -r, \qquad\qquad \Gamma^{\phi}_{r\phi} = \frac{1}{r}.$$

The space-like projection is defined as $\Delta^{\mu\nu} = g^{\mu\nu} - u^{\mu}u^{\nu}$; for the Milne coordinate system, different components of $\Delta^{\mu\nu}$ are

$$\Delta^{\tau\tau} = -\left(u^r\right)^2, \qquad\qquad \Delta^{\eta\eta} = -\frac{1}{\tau^2},$$

$$\Delta^{rr} = -1 - \left(u^r\right)^2, \qquad\qquad \Delta^{\phi\phi} = -\frac{1}{r^2},$$

$$\Delta^{\tau\eta} = \Delta^{\tau\phi} = \Delta^{\eta r} = \Delta^{\eta\phi} = \Delta^{r\phi} = 0,$$

$$\Delta^{\tau r} = -\sqrt{1 + (u^r)^2}\, u^r.$$

The expansion scalar is given by $\theta = D_\mu u^\mu = \partial_\mu u^\mu + \Gamma^\mu_{\mu\alpha} u^\alpha$.

We consider real particles, and the on-shell condition is given by $g_{\mu\nu} p^\mu p^\nu = (p^\tau)^2 - \tau^2(p^\eta)^2 - (p^r)^2 - r^2(p^\phi)^2 = m^2$. Following the convention used in heavy-ion collisions, we express the components of the four-momentum p^μ as:

$(E, p^x, p^y, p^z) = (m_T \cosh y, p_T \cos\varphi, p_T \sin\varphi, m_T \sinh y)$, where $p_T = \sqrt{p_x^2 + p_y^2}$, $m_T = \sqrt{m^2 + p_T^2}$, and $y = \tanh^{-1}(p_z/E)$. The components of the four-momentum in Milne coordinates are

$$p^\tau = m_T \cosh(y - \eta), \qquad\qquad \tau p^\eta = m_T \sinh(y - \eta),$$
$$p^r = p_T \cos(\varphi - \phi), \qquad\qquad r p^\phi = p_T \sin(\varphi - \phi). \qquad\text{(B.1)}$$

Here, $(p^\tau, p^\eta, p^r, p^\phi)$ are the momentum components in the Milne coordinate with y being the rapidity in momentum space, η being the space-time rapidity, ϕ being the azimuthal angle in coordinate space, and φ being the azimuthal angle of the particle in momentum space.

In Eq. (6.2), we have the term $p^\mu d\Sigma_\mu$, which in our case is given by $p^\mu d\Sigma_\mu = g_{\mu\nu} p^\mu d\Sigma^\nu = m_T \cosh(y - \eta) \tau d\eta r dr d\phi$.

B.2   First-order (δf) Correction to the Single-Particle Distribution

In Eq. (6.3), we introduced the first-order correction to the single-particle distribution while calculating the invariant yield using the Cooper-Frye formula. Here, we give the detailed expression of δf in terms of gradients of fluid variables and fields:

$$
\begin{aligned}
\delta f &= -\frac{\tau_c}{u \cdot p} \left(p^\mu \partial_\mu f_0 + q F^{\mu\nu} p_\nu \frac{\partial f_0}{\partial p^\mu} \right) \\
&= \frac{\tau_c f_0 \tilde{f}_0}{u \cdot p} \left(\beta p^\mu p^\alpha D_\mu u_\alpha + (u \cdot p) p^\mu \partial_\mu \beta - p^\mu \partial_\mu \alpha \right) - \frac{\tau_c f_0 \tilde{f}_0}{u \cdot p} q \beta E^\nu p_\nu \\
&= \frac{\tau_c f_0 \tilde{f}_0}{u \cdot p} \left(\beta p^\mu p^\alpha \left[u_\mu \dot{u}_\alpha + \sigma_{\mu\alpha} + \omega_{\mu\alpha} + \frac{\Delta_{\mu\alpha}\theta}{3} \right] + (u \cdot p) p^\mu \partial_\mu \beta - p^\mu \partial_\mu \alpha \right) - \frac{\tau_c f_0 \tilde{f}_0}{u \cdot p} q \beta E^\nu p_\nu \\
&= \frac{\tau_c f_0 \tilde{f}_0}{u \cdot p} \left(\beta p^\mu p^\alpha \partial_\mu u_\alpha + \beta p^\phi p^\phi r u_r - \beta p^\eta p^\eta \tau u_\tau + (u \cdot p) p^\mu \partial_\mu \beta - p^\mu \partial_\mu \alpha \right) - \frac{\tau_c f_0 \tilde{f}_0}{u \cdot p} q \beta E^\nu p_\nu \\
&= \frac{\tau_c f_0 \tilde{f}_0}{u \cdot p} \left(\beta p^\phi p^\phi r u_r - \beta p^\eta p^\eta \tau u_\tau + (u \cdot p) p^\mu \partial_\mu \beta - p^\mu \partial_\mu \alpha \right) - \frac{\tau_c f_0 \tilde{f}_0}{u \cdot p} q \beta E^\nu p_\nu \\
&\quad + \frac{\tau_c f_0 \tilde{f}_0}{u \cdot p} \left(\beta p^\tau p^r \partial_\tau u_r + \beta p^r p^r \partial_r u_r + \beta p^\phi p^r \partial_\phi u_r \right) \\
&\quad + \frac{\tau_c f_0 \tilde{f}_0}{u \cdot p} \left(\beta p^\tau p^\tau \partial_\tau u_\tau + \beta p^r p^\tau \partial_r u_\tau + \beta p^\phi p^\tau \partial_\phi u_\tau \right) . \\
&= \frac{\tau_c f_0 \tilde{f}_0}{u \cdot p} \left(\beta \left(\frac{p_T \sin(\varphi - \phi)}{r} \right)^2 r u_r - \beta \left(\frac{m_T \sinh(y - \eta)}{\tau} \right)^2 \tau u_\tau + (u \cdot p) p^\mu \partial_\mu \beta - p^\mu \partial_\mu \alpha \right) \\
&\quad - \frac{\tau_c f_0 \tilde{f}_0}{u \cdot p} q \beta E^\nu p_\nu + \frac{\tau_c f_0 \tilde{f}_0}{u \cdot p} \left(\beta m_T \cosh(y - \eta) p_T \cos(\varphi - \phi) \frac{(u^r)^2}{r u^\tau} - \beta (p_T \cos(\varphi - \phi))^2 \frac{u^r}{r} \right) \\
&\quad + \frac{\tau_c f_0 \tilde{f}_0}{u \cdot p} \beta \frac{p_T \sin(\varphi - \phi)}{r} p_T \cos(\varphi - \phi) u_0 \frac{2r}{R} \sum n c_n \sin n \left[\phi - \psi_n \right] \\
&\quad + \frac{\tau_c f_0 \tilde{f}_0}{u \cdot p} \left(-\beta (m_T \cosh(y - \eta))^2 \frac{(u^r)^3}{r(u^\tau)^2} + \beta m_T \cosh(y - \eta) p_T \cos(\varphi - \phi) \frac{(u^r)^2}{r u^\tau} \right) \\
&\quad - \frac{\tau_c f_0 \tilde{f}_0}{u \cdot p} \beta \frac{p_T \sin(\varphi - \phi)}{r} m_T \cosh(y - \eta) \frac{u^r}{u^\tau} u_0 \frac{2r}{R} \sum n c_n \sin n \left[\phi - \psi_n \right] .
\end{aligned}
$$

$$\delta f = \frac{\tau_c f_0 \tilde{f}_0}{u \cdot p} \beta \left(\frac{u_r}{r} + \frac{\sin(\varphi - \phi)\cos(\varphi - \phi)}{r} u_0 \frac{2r}{R} \sum c_n n \sin n \left[\phi - \psi_n \right] \right) p_T^2$$

$$- \frac{\tau_c f_0 \tilde{f}_0}{u \cdot p} q \beta E^\nu p_\nu + \frac{\tau_c f_0 \tilde{f}_0}{u \cdot p} \left((u \cdot p) p^\mu \partial_\mu \beta - p^\mu \partial_\mu \alpha \right)$$

$$+ \frac{\tau_c f_0 \tilde{f}_0}{u \cdot p} \beta \left(2 \cosh(y - \eta) \cos(\varphi - \phi) \frac{(u^r)^2}{r u^\tau} \right.$$

$$\left. - \cosh(y - \eta) \sin(\varphi - \phi) \frac{u^r}{r u^\tau} u_0 \frac{2r}{R} \sum c_n n \sin n \left[\phi - \psi_n \right] \right) m_T p_T$$

$$- \frac{\tau_c f_0 \tilde{f}_0}{u \cdot p} \beta \left(\sinh^2(y - \eta) \frac{u_\tau}{\tau} + \cosh^2(y - \eta) \frac{(u^r)^3}{r(u^\tau)^2} \right) m_T^2, \tag{B.2}$$

where $\beta = \frac{1}{T}$ and $\alpha = \frac{\mu}{T}$ with $\Gamma^\tau_{\eta\eta} = \tau$ along with $\Gamma^r_{\phi\phi} = -r$. The contribution due to the electric field $E \cdot p$ in the above equation, when expanded, takes the following form:

$$\delta f = -\frac{\tau_c f_0 \tilde{f}_0}{u \cdot p} q \beta E \cdot p,$$

$$\delta f = -\frac{\tau_c f_0 \tilde{f}_0}{u \cdot p} q \beta \left(E^\tau p^\tau - \tau^2 E^\eta p^\eta - E^r p^r - r^2 E^\phi p^\phi \right).$$

B.3 Co-ordinate transformation of Electric four vector

The electric field components in Milne-coordinates $(E^\tau, E^\eta, E^r, E^\phi)$ are connected to the Cartesian components (E^t, E^x, E^y, E^z) through the following transformation

$$\begin{bmatrix} E^\tau \\ E^r \\ E^\phi \\ E^\eta \end{bmatrix} = \begin{bmatrix} Cosh[\eta] & 0 & 0 & -Sinh[\eta] \\ 0 & Cos[\phi] & Sin[\phi] & 0 \\ 0 & \frac{-Sin[\phi]}{r} & \frac{Cos[\phi]}{r} & 0 \\ \frac{-Sinh[\eta]}{\tau} & 0 & 0 & \frac{Cosh[\eta]}{\tau} \end{bmatrix} \begin{bmatrix} E^t \\ E^x \\ E^y \\ E^z \end{bmatrix}.$$

We also note $E.u = 0$ and this gives rise to :

$$
E^t = \frac{E^z Sinh\eta}{cosh\eta} + \frac{(cos\phi E^x + sin\phi E^y)u^r}{cosh\eta u^\tau},
$$

$$
E^\eta = \frac{E^z}{\tau Cosh\eta} - \frac{tanh\eta E^r u^r}{\tau u^\tau}.
$$

As mentioned in the main text we use four different configuration of transverse electric fields, they are parameterised as :

$$
eE_x = \frac{\mathcal{B} Z \alpha_{em}(x - x_0)Cosh[\eta - \eta_0]}{((x - x_0)^2 + (y - y_0)^2 + (\tau Sinh[\eta - \eta_0])^2)^{3/2}},
$$

$$
eEy = \frac{\mathcal{A} Z \alpha_{em}(y - y_0)Cosh[\eta - \eta_0]}{((x - x_0)^2 + (y - y_0)^2 + (\tau Sinh[\eta - \eta_0])^2)^{3/2}},
$$

$$
eEz = 0,
$$

where Z is the atomic number (for our case we choose Z=82), $\alpha_{em}=\frac{1}{137}$, $\mathcal{A}$ and $\mathcal{B}$ are the modulation factors which controls the spatial configuration of the field in the transverse plane, and α is the fine structure constant. We get the first 3 configurations in Fig.(6.2) by choosing (i) $\mathcal{A}=\mathcal{B}=10$ for **config-1**, (ii) $\mathcal{A}=20$, $\mathcal{B}=1$ for **config-2** (iii) $\mathcal{A}=1$, $\mathcal{B}=20$ for **config-3**, and $qE_x = qE_y = m_\pi^2$ for **config-4**.